7-17-2008

Investigation of Fundamental Black Hole Properties of AGN through Optical Variability

Wesley Thomas Ryle

Investigation of Fundamental Black Hole Properties of AGN Through Optical Variability

by

Wesley Thomas Ryle

Under the Direction of H. Richard Miller

Abstract

Active galactic nuclei (AGN) are known to vary in brightness in all regions of the electromagnetic spectrum and over a wide range of timescales. Many methods have been utilized to transform this observed variability into meaningful information about the central engines of AGN. One such technique, adapted from time series analysis of galactic x-ray binary systems, has been used to detect a characteristic break timescale in the power density spectra of x-ray variability of Seyfert galaxies. This timescale, thought to be related to instabilities in the accretion disk, appears to scale with black hole mass over many orders of magnitude.

This dissertation performs similar times series analyses with the optical data of eight blazars. The majority of these objects also display a characteristic break timescale. In cases where a black hole mass estimate is known, the timescales are in good agreement with the relationship observed for galactic x-ray binary systems and Seyfert galaxies. For objects of unknown mass, this relationship can be used to provide a mass estimate

of the supermassive black hole. Comparisons are made between the structure function and power density spectrum for each object, and the implications for the connection between the accretion disk and relativitic jet in AGN are discussed.

Index Words: astronomy, active galactic nuclei, blazars, time series analysis, power density spectrum, structure function, supermassive black hole

Investigation of Fundamental Black Hole Properties of AGN Through Optical Variability

by

Wesley Thomas Ryle

A Dissertation Presented in Partial Fulfillment of Requirements for the Degree of

Doctor of Philosophy

in the College of Arts and Sciences

Georgia State University

2008

Investigation of Fundamental Black Hole Properties of AGN Through Optical Variability

by

Wesley Thomas Ryle

Major Professor:	H. Richard Miller
Committee:	Michael T. Carini
	D. Michael Crenshaw
	Douglas R. Gies
	William H. Nelson
	Paul J. Wiita

Electronic Version Approved:

Office of Graduate Studies
College of Arts & Sciences
Georgia State University
August 2008

Contents

Tables

Figures

If you want to make an apple pie from scratch, you must first create the Universe.

—— *Carl Sagan*

– 1 –

Introduction

Over half a century has passed since the appearance of active galactic nuclei (AGN) as a research field. The evolution of this branch of astronomy has seen its share of obstacles, but it has progressed nonetheless. In the beginning, with the work of astronomers like Carl Seyfert and Maarten Schmidt, it was difficult to understand the connection between their observations and the astronomical phenomenon that they represented. The understanding of AGN, from the nearby Seyfert galaxies to the most distant quasars, has slowly coalesced into a single picture. All AGN are now believed to contain a supermassive black hole surrounded by an accretion disk and clouds of high velocity, hot gas. With the unification of the AGN class at hand, it has become a matter of importance to distinguish how this central engine functions and how differences in the mechanics or viewing angle create the various subgroups we observe. Today, almost all AGN research seeks to describe the environment near the central black hole and the enigma of how such enormous energies are generated in a relatively compact region.

A variety of methods have been developed to probe the inner regions of AGN utilizing new and improved technologies. There is a great deal of excitement arising from the launch of satellites to explore regions of the electromagnetic spectrum with improved sensitivity. Such missions, combined with observations obtained at other

wavelengths, provide additional key insights into the physics of the AGN central engine. In the present study, we have expanded on a traditional technique, time series analysis of optical data, in an effort to understand more fully the nature of AGN.

1.1 AGN Background and History

The earliest detection of an AGN is usually traced back to an optical spectrum of NGC 1068 taken at Lick Observatory in 1908 (Fath 1908). The spectrum of this object and many subsequent others were notable because of the width of their emission lines, which were in some cases $>$ 5,000 km s^{-1}. The large velocities, combined with the unresolved, highly luminous central core of the galaxy, were the first clues regarding the incredible power emitted from the nuclei of these objects. These distinctive spiral galaxies became the prototypes of the Seyfert class (Seyfert 1943).

Beginning in the late 1950's and 1960's, numerous radio surveys of the sky were made. Many of the objects in the radio sky were found to be associated with optical images of galaxies. However, with more precise radio positions, there were numerous optical counterparts identified with compact, point-like objects (Hazard et al. 1963). Even more intriguing were the spectra of these objects, which were clearly non-stellar and showed emission lines at unexpected wavelengths. The revelation came when it was realized that the emission lines were the familiar hydrogen Balmer series, but shifted to substantially redder wavelengths (Schmidt 1963). The consequences of

this discovery were multi-fold. First, the large redshift indicated that these objects were located far outside our galaxy (assuming the Hubble law applied to this class of objects). Second, at these distances, the objects must be extremely luminous (each more than the combined light of a galaxy), yet they appear as compact, stellar-like sources in the sky, which were referred to as quasi-stellar objects or quasars.

Initially Seyfert galaxies and quasars were not thought to be related classes of objects. The two classes were discovered by very different methods and at different times. However, by the late 1960's, the similarities in the spectra and emission processes of Seyfert galaxies and quasars strongly suggested that these two classes were related. Over time, additional classes of AGN were observed, such as low ionization nuclear emission line region (LINER) galaxies, radio galaxies, and blazars. A major goal of AGN researchers during the 1990's was to investigate if the many different types of AGN could be understood using a single, relatively simple, model.

That model, affectionately called the 'exploding bagel model' by colleagues at Georgia State University, was initially established by Antonucci & Miller (1985) and reviewed by Urry & Padovani (1995). A representation of this model can be seen in Figure 1.1. In this model, all AGN contain supermassive black holes at their centers, with masses typically in the range of 10^6 to 10^9 $M_\odot$. The large amounts of energy are produced via an accretion disk of matter surrounding the black hole. The gravitational potential energy of the supermassive black hole is converted to radiation primarily through viscous heating of the accretion disk. Depending on the nature of

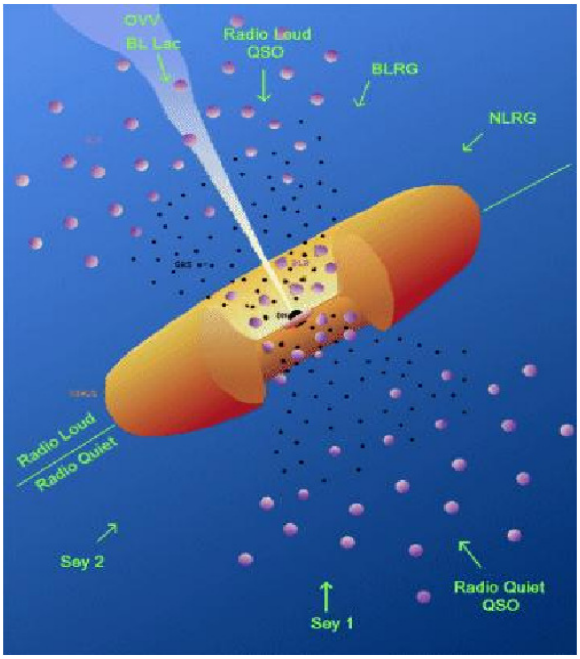

Figure. 1.1: A representation of the unified AGN model presented by Urry & Padovani (1995).

the accretion disk, and perhaps on the spin of the black hole, substantial amounts of this infalling matter may be ejected as a relativistic jet, thereby producing the radio loud classes of AGN. In order to explain the broad and narrow lines seen in the spectra of Seyfert galaxies, clouds of gas are assumed to be in motion about the black hole, with clouds close to the black hole producing the broad line region (BLR) and clouds further from the black hole producing the narrow line region (NLR). Finally, it is believed that the black hole, accretion disk, and BLR are all surrounded by an obscuring material that is distributed roughly as in a torus and contains a substantial amount of dust.

The role of the obscuring torus is vital, despite the fact that its properties are still relatively unknown. The key to almost all favored AGN unification models is the line

of sight of the observer relative to the axis of the dust torus. Intrinsically, the central engines of all AGN are thought to be very similar, with their powers depending upon the SMBH mass and the accretion rate onto it. Depending on the observers' line of sight, however, the interior portion of the AGN may become partially or completely obscured by the dusty torus.

The observational consequences of this scenario are most easily demonstrated with the Seyfert class. Seyfert type 1 galaxies show both narrow and broad emission lines, while Seyfert type 2 galaxies exhibit only the narrow lines, as seen in Figure 1.2. In terms of the model, this can be explained if the line of sight to the core of a Seyfert 2 galaxy passes through the torus, while Seyfert 1 galaxies are seen at a larger angle to the plane of the torus. In this way, the BLR is obscured by the torus for Seyfert 2 galaxies, eliminating the broad component of the spectral lines. This concept is further supported by observations of some Seyfert 2 galaxies in polarized light, where the hidden broad components are revealed by light scattered into the line of sight (Antonucci & Miller 1985; Miller et al. 1991).

While the unified models do explain the differences in spectra between many AGN, they do not immediately address the problem that AGN can also be broken into two apparently different luminosity classes based on their radio loudness. Aside from their very different radio outputs, radio-loud and radio-quiet active galaxies behave in very similar fashions with respect to orientation angle. Broad line radio galaxies (BLRGs) and narrow line radio galaxies (NLRGs) are the analogs of Seyfert 1 and 2 galaxies,

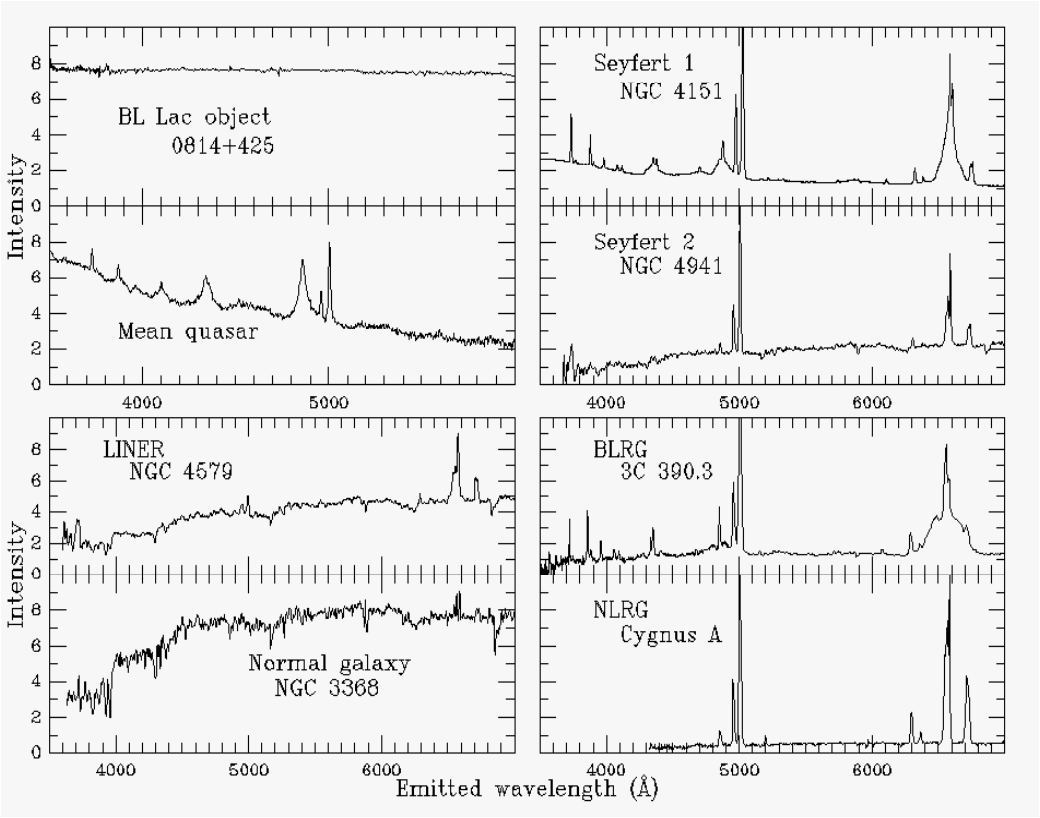

Figure. 1.2: A variety of spectra representing the many types of AGN. Taken from Bill Keel's website on Quasars and AGN, available at http://www.astr.ua.edu/keel/agn/

respectively. Blazars are thought to be an extreme case, where the viewing angle is very near the axis of relativistic jet of material. The properties and origins of these jets will be discussed in Section 1.5.

The time series analysis techniques presented in this dissertation have been performed on a wide variety of objects, from stellar mass black hole binary systems to Seyfert galaxies. The sample of objects investigated in this study, listed in Table 1.1, is composed mainly of blazars. This selection is due almost solely to the fact that these are the objects which have been steadily monitored by the Program for Extragalactic Astronomy (PEGA) group at Georgia State University for more than

three decades.

Table. 1.1: Object Sample for this Dissertation.

Object	R.A.	Dec.	Redshift	Classification
AO 0235+164	02:38:39.0	+16:36:59.4	0.940	BL Lacertae
3C 120	04:33:11.1	+05:21:15.7	0.033	Seyfert 1 (Radio galaxy)
PKS 0735+178	07:38:07.5	+17:42:18.9	0.424	BL Lacertae
OJ 287	08:54:48.9	+20:06:30.5	0.306	BL Lacertae
3C 279	12:56:11.2	−05:47:21.8	0.536	Blazar/OVV
PKS 1510−089	15:12:50.6	−09:06:00.0	0.361	Blazar/OVV
BL Lac	22:02:43.4	+42:16:40.0	0.069	BL Lacertae
3C 454.3	22:53:57.8	+16:08:53.7	0.859	Blazar/OVV

Blazars can be subdivided into two main groups, optically violent variables (OVV) and BL Lacertae (BL Lac) objects. In both cases, the emission from the object is thought to be highly beamed through the relativistic jet. Both classes are also highly variable on short timescales and display high polarizations. OVV objects, also often called flat-spectrum radio quasars or high polarization quasars, are characterized by strong emission and absorption lines, while BL Lac objects have weak, if any, noticeable discrete features in their spectra. In general, it is believed that the BL Lac objects are intrinsically weaker radio sources than OVV objects, though both fall into the radio-loud category (Peterson 1997; Kembhavi & Narlikar 1999).

1.2 The Nature of Blazar Variability

Variability must be at the center of any discussion of blazars. It is one of their defining characteristics and has been noted since the discovery of the class. In the case of BL

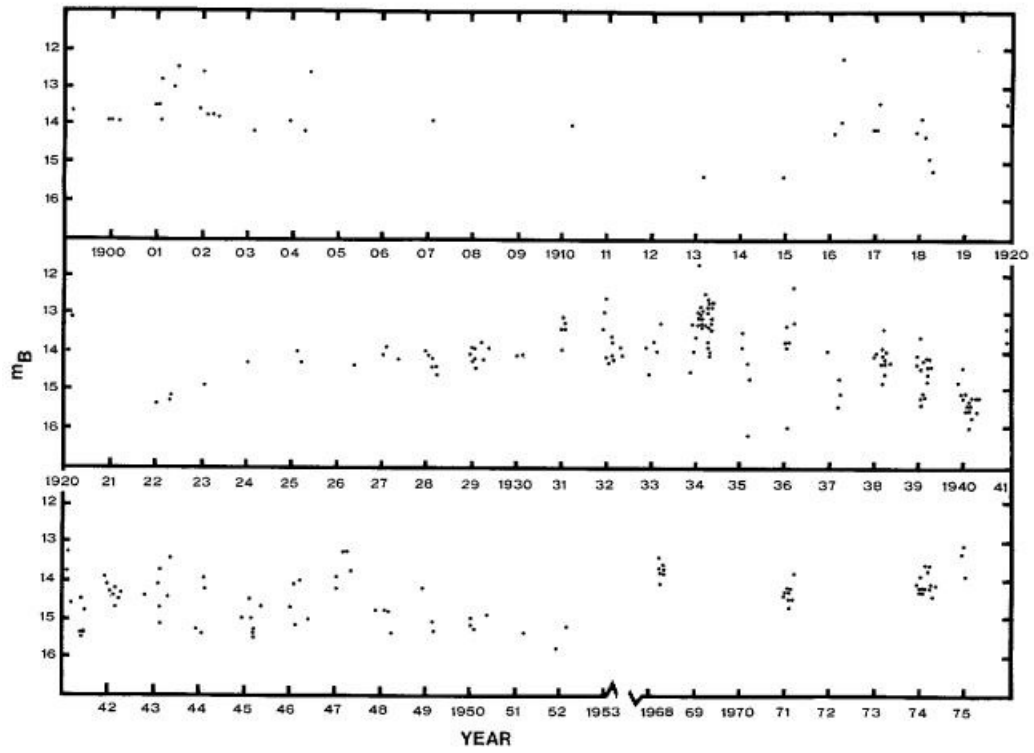

Figure. 1.3: An example of the long-term variability in the BL-Lac object Mkn 421. Data are collected from the archival plates of the Harvard College Observatory (Miller 1975).

Lac itself, the object was originally misidentified as a variable star. The fact that blazars vary in brightness over many timescales is integral to this study, because it is from these changes that we hope to gain some understanding of the central engine. Simultaneous monitoring campaigns at multiple wavelengths have been a primary source of information for blazar researchers over the past few decades. It has led to a better understanding of the underlying physics of the AGN mechanism, but has also created many intriguing questions about the source of the variability.

The first indication of variability for AGN came early with the studies of quasars such as 3C 48 (Matthews & Sandage 1963). Even as many new objects were being

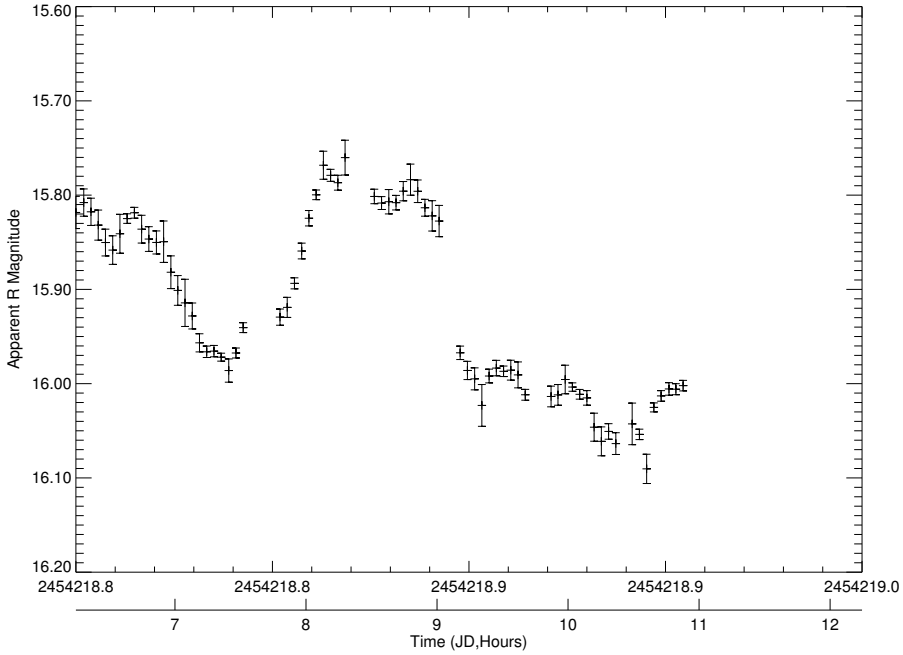

Figure. 1.4: An example of the microvariability in the blazar PKS 1633+382. Data were collected at the Perkins telescope at Lowell Observatory.

discovered, long-term monitoring campaigns were initiated in both the optical (Smith 1996) and radio regimes (Aller et al. 1996). In some cases, archival plates could be used to trace back optical variability over the past century (Miller 1975). Modern day monitoring campaigns can involve dozens of observatories in a worldwide network, such as those performed by the Whole Earth Blazar Telescope (WEBT) (Villata et al. 2000, 2002). An example of the long-term optical flux variability in the BL Lac object Mkn 421 can be seen in Figure 1.3.

For the blazar class in particular, more intensive monitoring led to variability being discovered on smaller and smaller timescales. Although Racine (1970) reported that the prototype of this class, BL Lacertae, varied significantly on timescales as

short as hours to minutes, the validity of those results was questioned. Subsequently, observations of this "microvariability" in BL Lac were supported (Miller et al. 1974; Miller 1981) and were observed for many other blazars (Miller 1988; Miller et al. 1989; Carini 1990; Carini & Miller 1992). An example of the short-term microvariability seen in the object PKS 1633+382 can be seen in Figure 1.4.

1.3 Multiwavelength Campaigns

Compared with spectroscopy and polarimetry, the measurement of variability through photometry is a relatively straightforward method of investigation. For this reason, multiwavelength variability studies have been a major tool utilized by blazar researchers over the past few decades. Variations measured at radio, infrared (IR), optical, ultraviolet (UV), and x-ray wavelengths can be compared to gain a better understanding of the physics of the source. Another form of photometric study, time series analysis, will be discussed in the next section and in further detail in Chapter 3. This section gives a brief review of multiwavelength studies of AGN conducted over the past two decades and their successes and failures in providing an insight into the physical processes responsible for emission and variability of these objects.

The goal for any multiwavelength campaign is to find correlations or relationships between variations in different wavelength regimes. In a fundamental way, this informs the observer of how the central engine of an AGN functions, based on assumptions of where the radiation in each waveband originates. For example, if an event, such as

a spike in the light curve, is seen to propagate from x-rays through optical to radio, this has been interpreted as arising from a blob of material or shock traveling down the relativistic jet of a blazar. The presence or absence of a correlation, combined with the lead/lag of the correlation, are key diagnostics of the emission processes.

Large multiwavelength campaigns for a number of AGN were first organized in the 1980's. A true multiwavelength campaign, which encompasses all available regions of the electromagnetic spectrum, requires the use of many ground and space based observatories. Despite the numerous resources required, such large scale programs have been carried out for a modest number of blazars, some over multiple epochs. Results from these campaigns have not produced definitive results.

One example is the BL-Lac object AO 0235+164. During a campaign over long timescales, the object displayed very clear evidence for correlation between radio and optical data, as seen in Figure 1.5 from Raiteri et al. (2001). In this study, the optical variations where discovered to lead the radio variations by up to 60 days. However, during smaller timescales and lower flux states, there appears to be a complete lack of correlation, as seen in Figure 1.6 from Takalo et al. (1998). It becomes more difficult to explain the mechanism for variability when the results of the multiwavelength campaigns do not produce consistent results over time and flux level. The benefits of additional campaigns will, no doubt, be advantageous in improving our understanding of the emission mechanism.

Recent work by Osterman (2006) has shown that the degree of correlation between

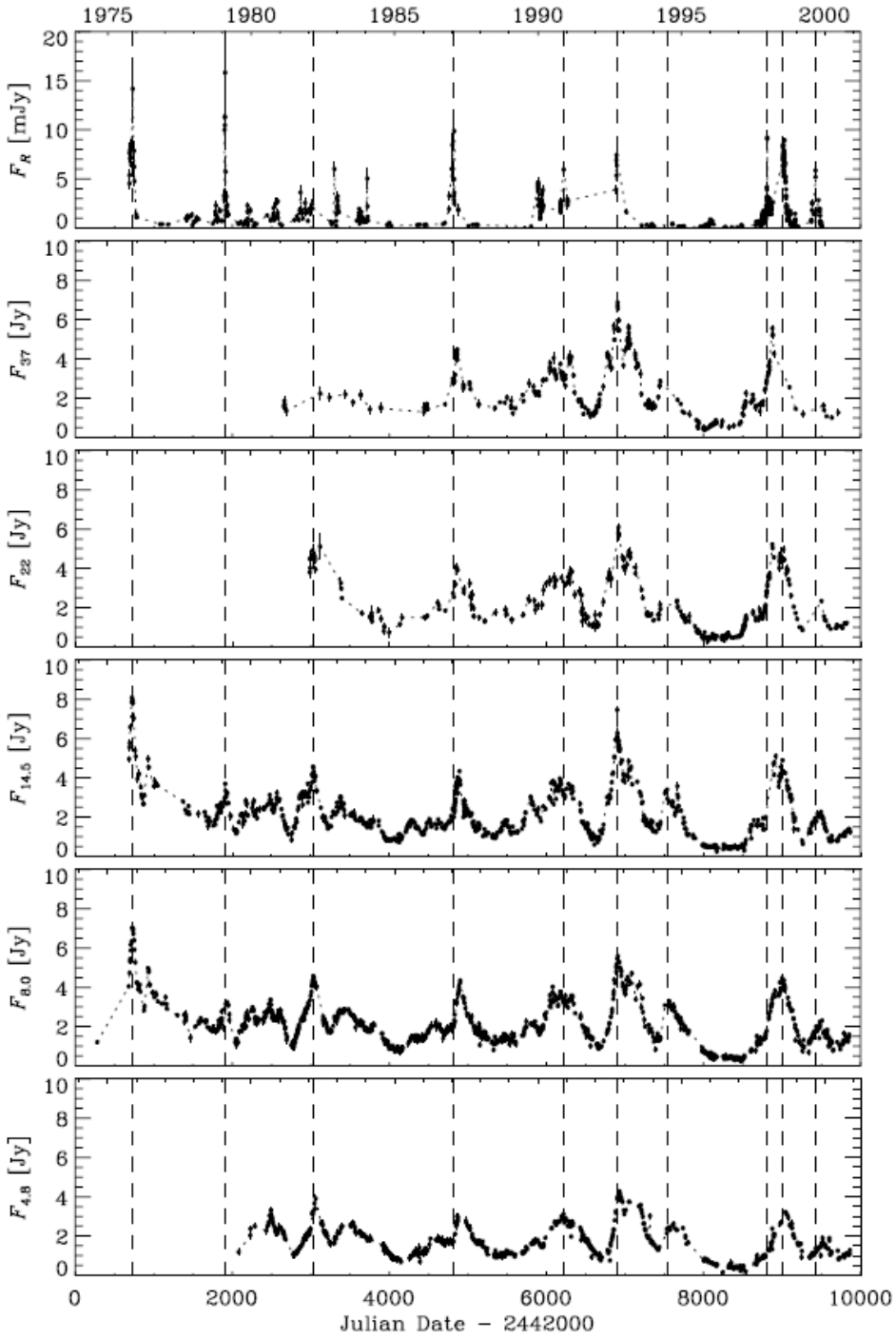

Figure. 1.5: An example of radio-optical correlation in the long-term light curve of the BL-Lac object AO 0235+164, taken from Raiteri et al. (2001).

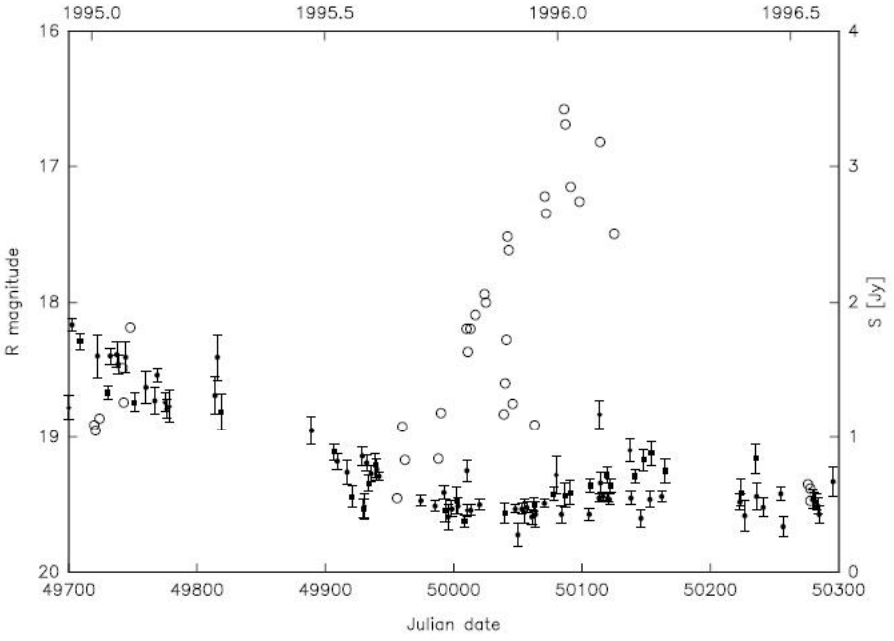

Figure. 1.6: An example of a lack of radio-optical correlation in the light curve of the BL-Lac object AO 0235+164 at a relative low flux state, with open circles as optical data, black dots and squares as 22 Ghz and 37 Ghz data, respectively (Takalo et al. 1998).

variations at different wavelengths may be dependent on the relative flux level of the object, somewhat similar to what is seen for the blazar AO 0235+164 in Figures 1.5 and 1.6. According to Osterman et al. (2007), a similar relationship is also seen in the blazar PKS 2155-304, demonstrated by Figure 1.7. In this scheme, at elevated, high flux states, blazars show a high degree of correlation between their optical and x-ray light curves. As the flux level decreases, the lag between light curves becomes greater and the correlation weaker until no significant correlation is detected.

A key aspect of multiwavelength studies, aside from correlation analysis, is the spectral shape of the AGN emission. The spectral energy distribution (SED) of an object gives the general shape of flux versus frequency of an object and can provide

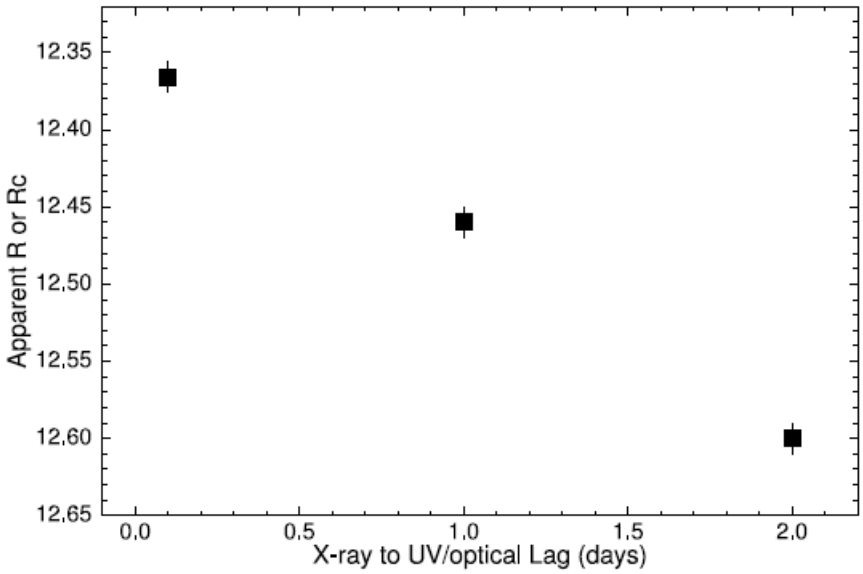

Figure. 1.7: Brightness level of the blazar PKS 2155-304 versus the lag between optical and x-ray light curves (Osterman 2006).

insight into the nature of the emission process. Also, changes in the SED of an AGN over time may reveal how current activity, such as an optical flare, is related to the broadband emission process of the object as a whole.

A typical blazar SED is described by two large, broad features with one peaking somewhere in the IR to extreme UV (EUV) frequency range and the other component peaking at much higher energies, such as hard x-ray to gamma ray frequencies. The lower energy peak is almost certainly due to synchrotron emission while the higher energy peak is likely produced by a Compton up-scattering of photons. As already mentioned, multiwavelength campaigns allow blazar researchers to monitor the shape of the SED over time. An example of these changes can be seen in Figure 1.8 from Villata et al. (2006). In this figure, it is easily seen that during the flaring state of

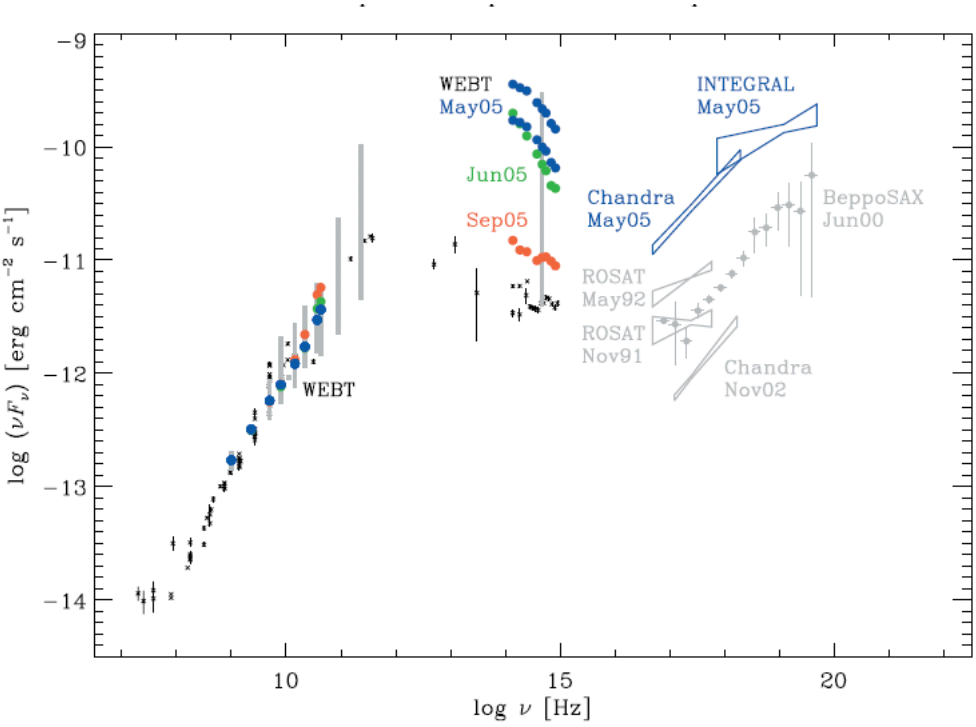

Figure. 1.8: The SED of the blazar 3C454.3 taken during relative quiescent periods and during the flaring state of the 2005 season (Villata et al. 2006).

2005, the SED peaks of 3C 454.3 changed drastically in both peak frequency and amplitude.

1.4 Time Series Analysis of AGN Light Curves

The primary focus of this dissertation will be on the time series analysis of blazar light curves at optical wavelengths. Time series analysis is, in general, the analysis of a process which varies over time. It is obvious why this type of analysis is useful in astronomy, especially when dealing with photometric light curves of variable objects. Time series analysis seeks to characterize the variability process in a quantitative fashion. The simplest way this is employed is through period searching algorithms

for variable stars. If the brightness of a variable star with a period of 5 days is sampled randomly over a sufficient span of time, time series analysis of the light curve can reveal the period.

There is still some debate over whether the variability of blazars is in any way periodic. Some investigations have claimed periodicities on a wide range of timescales (Fan & Lin 2000), although in most cases, this behavior is neither reliable nor reproducible. For a select few blazars, the claim of periodicity is better supported, but still open to question. The most notable case is that of OJ 287, which has a purported 11-12 year cycle (e.g., Kidger 2000) that many have tried to model with a binary supermassive black hole system (e.g., Valtaoja et al. 2000). In general, there has been no convincing evidence found demonstrating that blazar variability is periodic.

Although blazar light curves do not appear periodic, there are still many benefits to the use of time series analysis. In the case of compact accreting systems, like AGN and galactic x-ray binary (GXRB) systems, the variability has been best described by a noise process. There are many types of noise and time series analysis is one of the best methods for discerning the different varieties.

In this study, the analysis of variability behavior will be carried out through the use of the structure function (SF) and the power density spectrum (PDS). The PDS is the technique which most clearly defines the character of variability by defining the amount of variability power at a given frequency. The shape of the PDS is a key clue to the nature of the variability process.

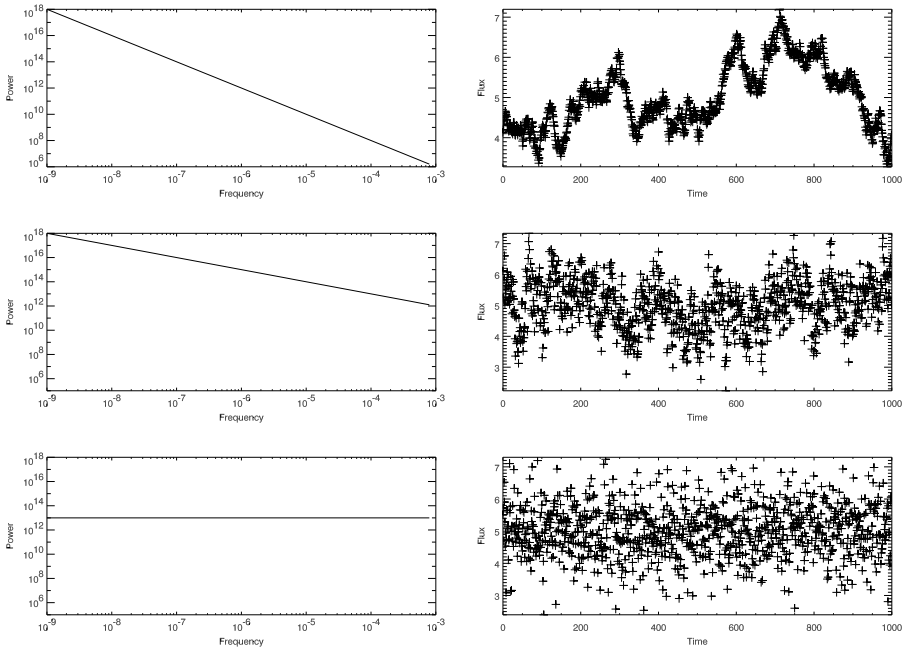

Figure. 1.9: A demonstration of different PDS slopes and resultant light curves. The top plots show a red noise PDS with a slope of -2, the middle plots show pink noise PDS with a slope of -1, and the bottom plots show a white noise PDS with a slope of 0.

Noise processes will show a distinct shape in their PDS, namely a power law with a constant slope. The value of this slope separates the different types of noise into three well known groups. A slope of -2 is referred to as red noise, -1 as pink or flicker noise, and a slope of zero as white noise. Each slope produces a slightly different form of variability, each with implications for the physical processes possibly responsible for producing the variations. An example of the PDS and simulated light curve for each type of slope is shown in Figure 1.9.

In the case of zero slope or white noise, the result is equal variability power at all frequencies. This case is clearly not physical, as the observed light curve would appear to vary equally on all timescales, infinitely long or short. For a slope -2, longer term

variations are preferred over shorter, high frequency changes, producing a light curve with a smooth, slowly changing nature. The middle case, a slope of -1 or flicker noise, is a mix of the two, showing smaller, short timescale changes superimposed on a smoother long term light curve.

In terms of a physical representation of nature for AGN, none of these well-defined cases can actually match the observational results. In order to account for the observed high frequency variability and to not diverge at the lower frequencies, the slope of the PDS must change from steep at high frequencies to shallow at low frequencies. Fortunately, there are examples within our own galaxy that have been monitored sufficiently in order ascertain the shape of the PDS for accreting systems. A discussion of these objects and further extrapolation to AGN will be discussed in Section 1.6.

1.5 Methods of Mass Determination for AGN

The understanding of the physics of the AGN central engine begins with one of the simplest and most common characteristics of astronomical objects. Assuming that a supermassive black hole is at the core of every AGN, the mass of that black hole must be a fundamental parameter that controls the emission of the object. In order to examine how variability and black hole mass are interlinked, we begin with estimates of the mass that are independent of variability. This section describes the techniques employed thus far in determining the supermassive black hole masses of AGN.

In an ideal situation, one would be able to resolve the central regions of AGN

and directly resolve the BLR or perhaps even the accretion disk. Unfortunately, such measurements are not possible at the present time. Instead, all determinations of supermassive black hole mass estimates must rely on indirect techniques. It is also very clear that the more indirect the technique, the larger the scatter in mass estimate. The measurement of supermassive black hole mass is still a relatively new field and with time and better facilities, these estimates will become much more reliable.

$$M_{\rm SMBH} = \frac{f v^2 R_{\rm BLR}}{G} \tag{1.1}$$

The most reliable measurements of SMBH mass come from estimates of the size of the BLR. In this scenario, it is believed that the BLR clouds are gravitationally bound to the SMBH and that their motion has become virialized, such that they follow the relationship seen in Equation 1.1, where $M_{\rm SMBH}$ is the mass of the supermassive black hole, v is a measure of the velocity of the clouds, $R_{\rm BLR}$ is the radius of the BLR, G is the gravitational constant, and f is a factor that depends on the geometry and kinematics of the BLR. The two main techniques for measuring the size of the BLR are reverberation mapping and the use of a relationship noted between the BLR size and optical luminosity, which relies on the former technique for calibration. For reverberation mapping, changes in the continuum flux of an object are compared to changes in broad line fluxes. The time lag between these events gives a reliable estimate of the size of the BLR (Peterson 1993). Using these reverberation mapping estimates, it was noted that BLR size appears to correlate with the optical flux of

AGN, allowing for another, slightly weaker relationship between the optical luminosity of an AGN and the size of the BLR (Kaspi et al. 1996, 2000). While reverberation mapping and the optical luminosity relationship provide by far the best estimates of SMBH mass, they still produce a scatter in mass estimates of up to one order of magnitude (Woo & Urry 2002).

The second set of mass estimates are derived from kinematics in the bulge of the host galaxy of AGN. For many nearby galaxies, there appears to be a tight correlation between the stellar velocity dispersion of the bulge and the SMBH mass (Ferrarese & Merritt 2000; Gebhardt et al. 2000; Tremaine et al. 2002). Assuming that AGN host galaxies are similar (if not identical) to normal galaxies, this relationship should also hold for AGN. For many AGN, the host galaxy is easily resolved and direct measurements of the stellar velocity dispersion can be made. For more distant and fainter objects, the stellar velocity dispersion can be inferred through the use of the fundamental plane relation of velocity dispersion, effective radius, and mean surface brightness (O'Dowd et al. 2002; Jorgensen et al. 1996). Effective radius and surface brightness are easily measurable for many distant AGN with the use of Hubble Space Telescope (HST), although the use of the fundamental plane technique does introduce additional scatter into the mass estimate.

1.6 The Relationship Between Break Frequency and Black Hole Mass

With a growing number of black hole mass estimates of AGN in the past decade, it has become possible to search for a link between a characteristic timescale of variability and the mass of the object. Such a quest is not new in concept (Elliot & Shapiro 1974), but only in the past few years have both the measurement of mass and the method of determination of timescales become reliable. Many investigations (e.g., Liang & Liu 2003; Xie et al. 2001) have argued that the shortest timescales of variability in an object should be a good indicator of the black hole mass, because the fastest timescale for variability cannot be less than the light crossing time of the SMBH. However this picture becomes unclear when dealing with blazars and other beamed objects. For example, with microvariability, it is not known whether the rapid changes on very short timescales are due to bulk motion in the jet or some other property more fundamentally related to the black hole itself.

The frequency at which the break in the slope of the PDS occurs in accreting systems is an indicator for a characteristic timescale of variability. However, an understanding of how this timescale relates to the variability mechanism is unclear. A strong correlation between break timescale and black hole mass has been observed for a wide range of accreting systems. The relationship between break frequency and black hole mass appears to be a common property for both the stellar mass black holes in galactic x-ray binary (GXRB) systems and the much larger black holes of

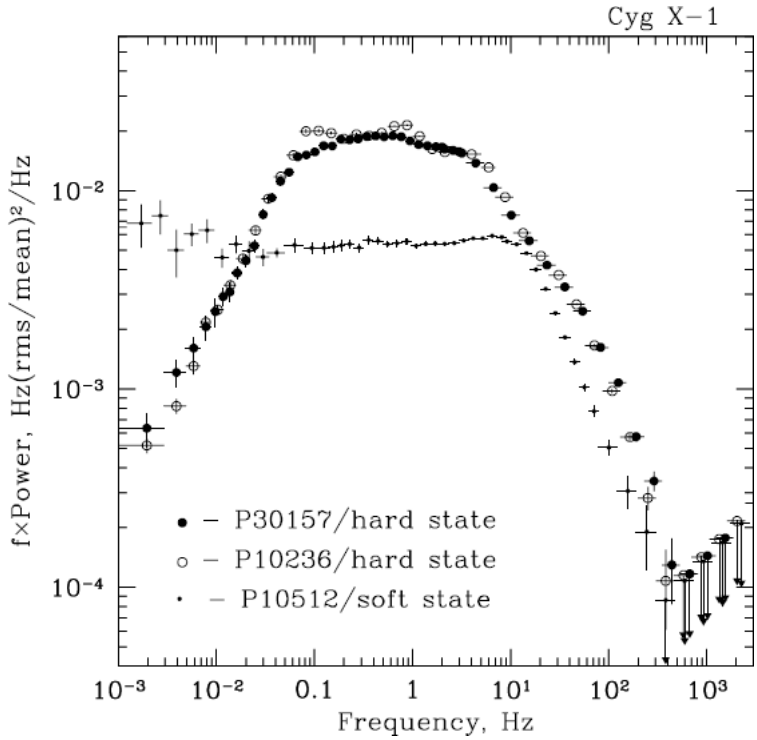

Figure. 1.10: The PDS shape of Cyg X-1 in both low/hard and high/soft states. Note that this representation of the PDS is in frequency multiplied by power versus frequency (Revnivtsev et al. 2000).

AGN.

The break in the PDS slope itself was first noted in GXRB systems, most notably, Cyg X-1. The shape of the PDS in Cyg X-1 and other similar systems is dependent on the state of the object, as seen in Figure 3.6. These data from Revnivtsev et al. (2000) show that in the low/hard state, to be describe shortly, the PDS slope displays two breaks, changing in slope from -2 at high frequencies, to -1 at midrange frequencies, and dropping off to zero slope at lower frequencies. Keep in mind that the PDS shown in Figure 3.6 is in terms of power multiplied by frequency, as is the common form for GXRB systems. In the high/soft state, Cyg X-1 displays a single break, changing in

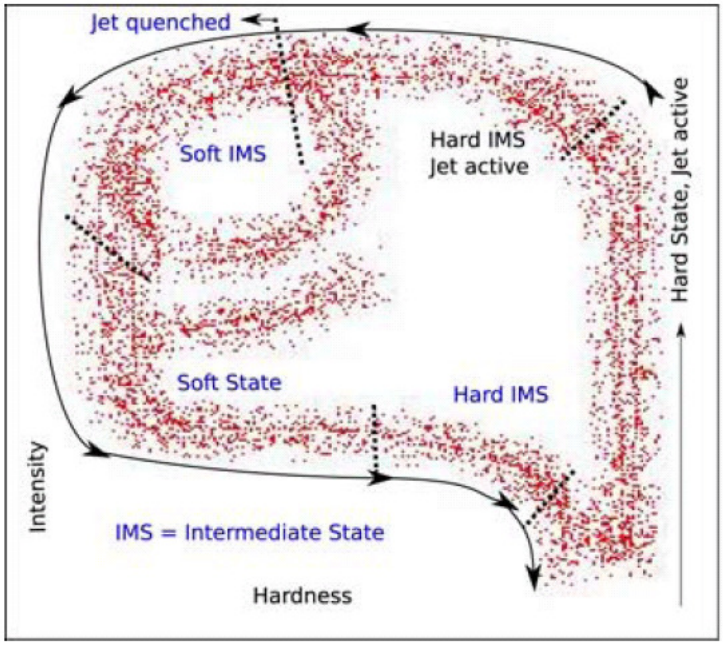

Figure. 1.11: A general diagram showing the transition between accretion states in GXRB systems. The abscissa corresponds to the hardness of the x-ray spectrum, with the ordinate representing x-ray intensity or flux (Körding et al. 2006).

slope from -2 at high frequencies to -1 at low frequencies.

The low/hard state is characterized by a hard x-ray spectrum and a steady jet at radio wavelengths. The accretion flow is diminished in this state, with much of the x-ray flux originating in the hot corona, although the jet may also contribute. Intermediate states have also been observed where the object appears to transition from a hard to soft x-ray spectrum in conjunction with decreasing radio emission. In the high/soft state, the x-ray spectrum is characterized by a thermal component from the accretion disk, the jet is quenched, and radio emission is at a minimum. Figure 1.11 displays the overall cycle that is thought to occur in GXRB systems (Körding et al. 2006).

The extension of these studies to AGN systems in the x-ray regime was greatly aided by the launch of the Rossi X-ray Timing Explore (RXTE). The possibility that the characteristic break frequency scales with black hole mass had been proposed even before the launch of RXTE (McHardy 1988). However, it was only after more than a decade worth of observations that we amassed sufficient data and are truly beginning to see the applications of time series analysis to AGN.

If the relationship between break frequency and black hole mass truly holds from GXRB systems to AGN, it is expected that AGN break timescales would be on the order of days to weeks, if not months for some higher mass objects. Therefore, it was necessary to have well sampled light curves for a time significantly longer than these timescales in order to reliably determine the break timescale.

Figure 1.12 displays a comparison between the PDS shape of a galactic x-ray binary system, Cyg X-1, and two Seyfert galaxies. In the case of each Seyfert, the shape clearly resembles the high/soft state of Cyg X-1 with a single break. As expected, the break has been shifted to much longer timescales. The detection of a break in the PDS for Seyfert galaxies is a very intriguing clue to the nature of the AGN central engine. In essence, as far as the variability mechanism is concerned, AGN appear to be nothing more than large scale models of GXRB systems (McHardy et al. 2006).

This relationship is further supported by measurements of the PDS of other Seyfert galaxies and even some broad line radio galaxies. In Figure 1.13, we see that the linear scale (in log-log space) of the break timescale with black hole mass extends over an

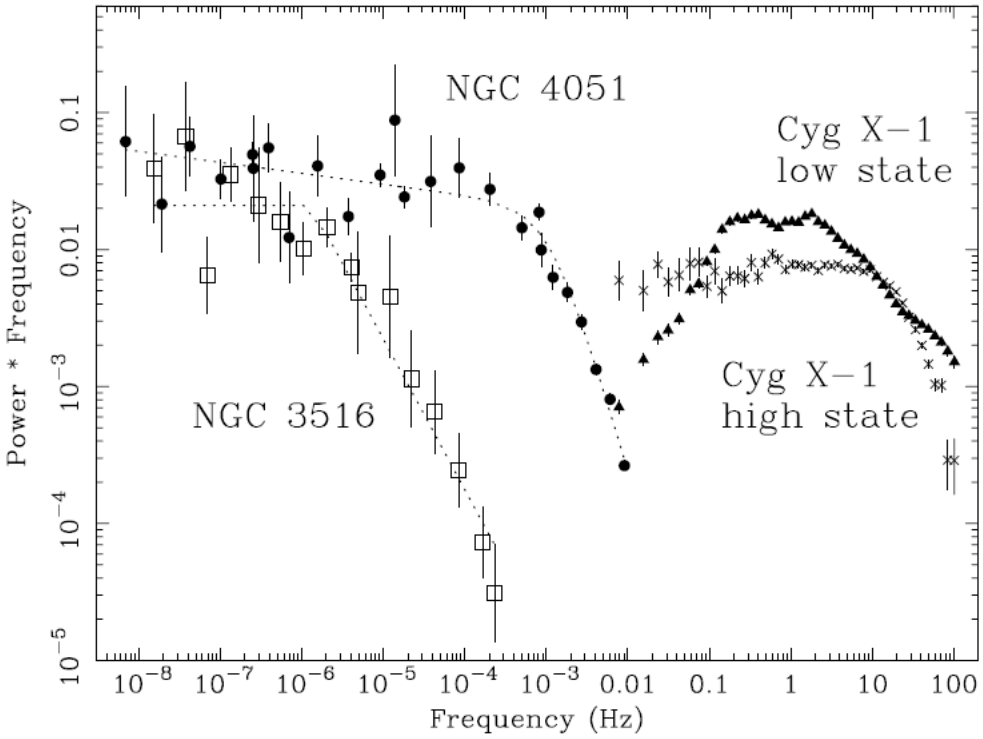

Figure. 1.12: A comparison of the PDS shape between two Seyfert galaxies and Cyg X-1 in the low and high states (McHardy et al. 2004).

extraordinary range in mass.

Recent studies have also shown that the scatter in the break frequency versus black hole mass relationship can be reduced if one includes another parameter, mass accretion rate (McHardy et al. 2006). In GXRB systems, it is clear that the characteristic break timescale shifts based on the state of the object. Changes in state for these objects are believed to be a direct consequence of changes in mass accretion rate. Bolometric luminosity is used as a proxy for accretion rate because the two quantities should scale equally based on the Eddington ratio for the object. A cross section of this fundamental plane can be seen in Figure 1.14 from Fender et al. (2007).

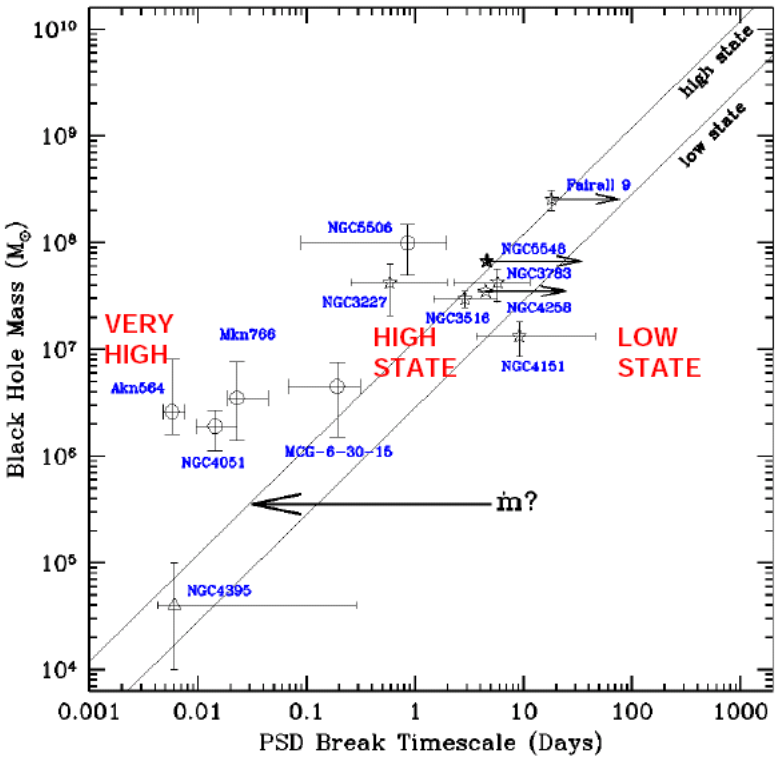

Figure. 1.13: Scaling of black hole mass with break timescale for various AGN. Solid lines represent an extrapolation from the low and high states of Cyg X-1 (McHardy et al. 2004).

Finally, another surprising result from the time series analysis of AGN is that the optical linewidths for many objects appear to closely correlate with the break timescale for x-ray variability. In a sense, this relationship, displayed in Figure 1.15, supersedes the relationship between break timescale and black hole mass because it removes the dependence on accretion rate seen above. Models which attempt to explain the relationships presented here are discussed in the next section.

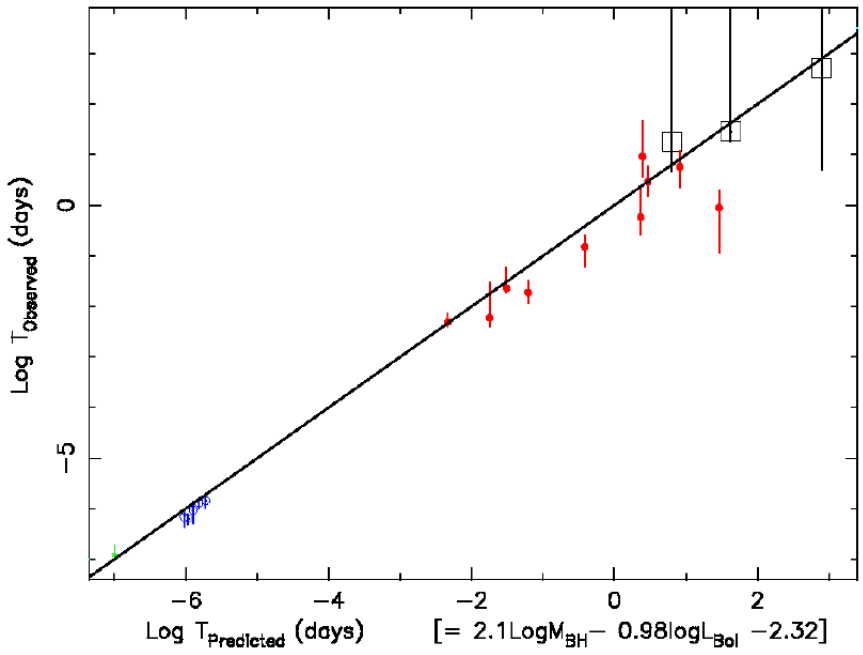

Figure. 1.14: A fundamental plane relationship between black hole mass, break timescale, and luminosity. Luminosity is used as a proxy for accretion rate (McHardy et al. 2006; Fender et al. 2007).

1.7 Blazar Models and Implications

The final discussion of background material that must be presented are the models which attempt to describe the properties of the radiation and variability observed. While the unification model presented earlier explains the differences between types of AGN, we have not yet addressed how the central engine is believed to produce variability over a wide range of wavelengths. In order to complete this picture, we must understand how the mechanics of the central engine, namely the accretion disk and relativistic jet, function together to produce the observed characteristics.

The broad synchrotron peak seen in a blazar SED is almost certainly due to the spiraling of electrons along the strong magnetic field lines of the jet. In some cases, the

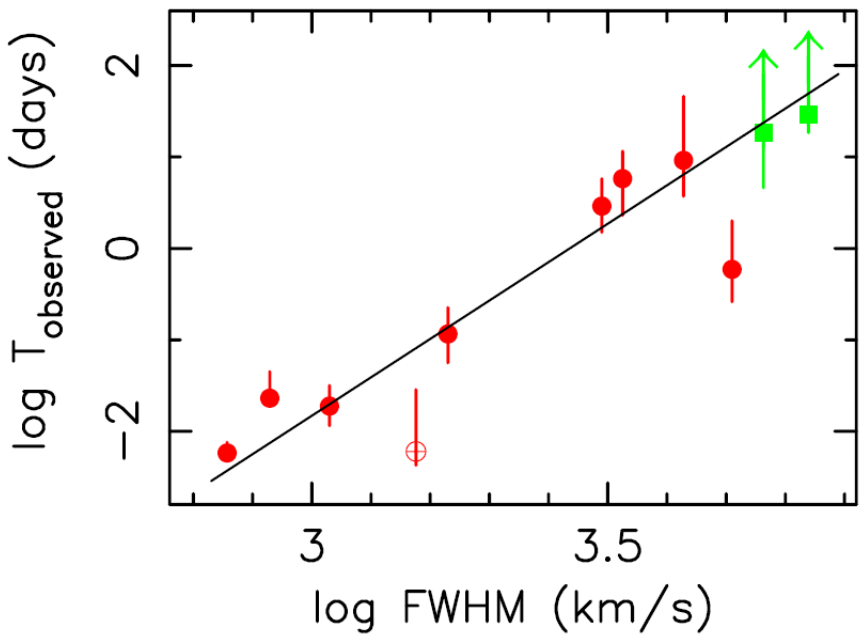

Figure. 1.15: Relationship between optical line width and break timescale for AGN (McHardy et al. 2006).

radio portion of the spectrum is broadened to the point where it becomes flat. It is believed that in these situations, there are multiple synchrotron components distributed along the jet and therefore also spread out in energy (Robson 1996; Marscher 1988). Identification of an object as a flat spectrum radio quasar (FSRQ) can be interpreted as the signature of a relativistic jet emitted by the object.

The second, higher energy peak seen in the SED is most likely due to an inverse Compton process, where the high energy electrons are 'cooled' by scattering with photons. The source of the seed photons for this process has been a matter of much debate. The first possibility is that the synchrotron emission itself provides the input photons which are upscattered to higher energies (e.g., Marscher & Travis 1996). In a situation where the electron and photon densities are high enough, as in a relativistic

jet, this synchrotron self-Compton (SSC) model is a viable way to lower electron energy while increasing the photon energy. The other option for seed photons is some external source, such as the accretion disk, accretion corona, or perhaps even the broad line clouds (Hartman et al. 1996).

While synchrotron and inverse Compton models explain how the emission is created, they still do not describe the manner in which the marked variability of blazars is produced. There have been many theoretical scenarios suggested in the literature, but the most widely accepted view is a shock propagating down a relativistic jet. We will discuss one very recent model which attempts to describe the process of variability production beginning at the accretion disk and propagating out the jet.

In many GXRB systems with jets, sometimes referred to as 'microquasars', there is a distinct drop in x-ray flux immediately preceeding the emission of a radio blob in the jet (Mirabel & Rodríguez 1998). It is believed that most of the x-ray emission in these objects occurs in the accretion disk very near to the compact object, which is either a neutron star or black hole. According to Belloni (2001), the dip in x-ray flux is thought to be caused be a sudden disruption and consumption of the inner edge of the accretion disk. Some of the material from the inner accretion disk is expelled along the relativistic jet, fueling the emission of a radio blob.

The galaxy 3C 120 was chosen for an intense multiwavelength campaign due to its similarities with GXRB systems, albeit at a much higher mass. The x-ray spectral properties of 3C 120 resemble that of a Seyfert galaxy, with the soft x-rays believed

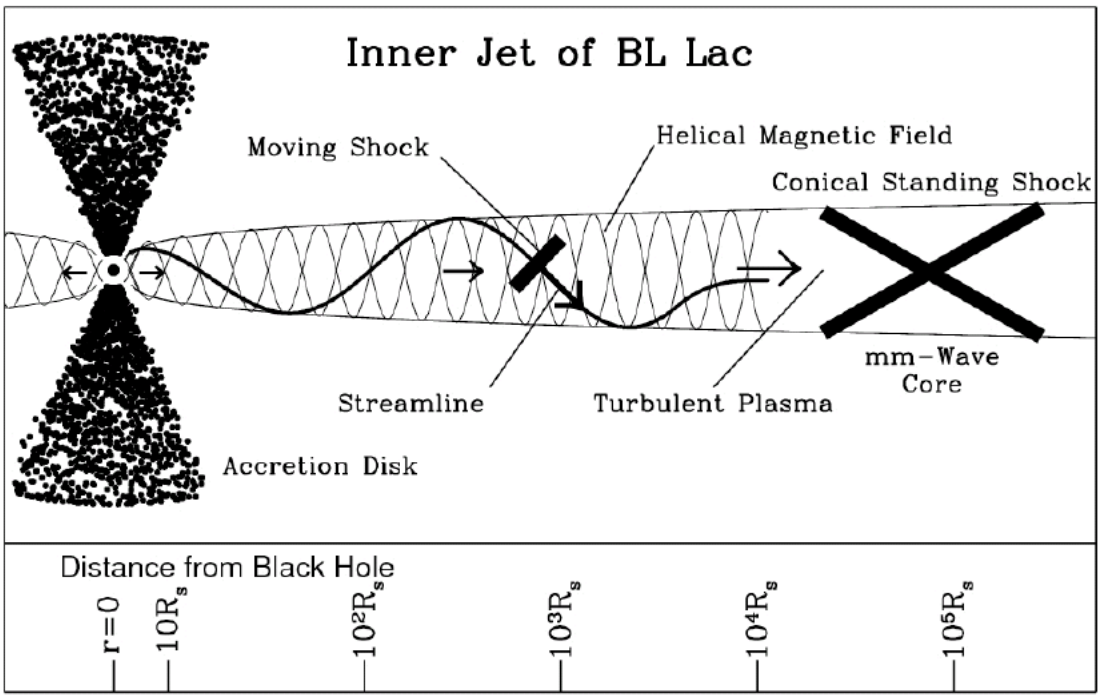

Figure. 1.16: A detailed model of the inner jet of BL Lac (Marscher et al. 2008).

to originate at the inner accretion disk and harder x-rays produced through the re-processing of disk photons by a hot corona. Unlike most Seyfert galaxies, however, 3C 120 has a pronounced radio jet. Using long baseline radio interferometry and RXTE monitoring, Marscher et al. (2002) showed that over a three year period, the same characteristic x-ray dip preceded the emission of blobs in the radio jet of 3C 120. Assuming a simple scaling with respect to black hole mass, this study provided a hard link between the accretion disk and the relativistic jet in AGN.

Another recent study by Marscher et al. (2008) gives a detailed example of how variability is generated deep in the jet for blazars. In this paper, multiwavelength studies of BL Lacertae show how a single event in the accretion disk/jet system can

create multiple flares in the observed light curve. In their model, there are two distinct zones to the relativistic jet. The first zone begins near the black hole and extends outward toward the location of the radio core of the jet. In this segment, the magnetic fields lines are in a tight helical coil due to their origins in the rotating accretion disk. The helical structure of the magnetic field acts as a nozzle for material streaming down the jet, both accelerating and collimating the motion. This inner portion of the jet is terminated when it encounters a standing shock wave located at the core of the interferometrically observed radio jet. The helical structure of the jet is mainly destroyed at this boundary and the flow appears much more chaotic. A representation of this model can be seen in Figure 1.16.

In order to explain the variability characteristics produced in such a model, we must begin with an instability in the inner accretion disk. This instability causes a collapse of the inner accretion disk, with some of the material crossing the event horizon of the SMBH and some material being fueled into the relativistic jet. This material accelerates down the jet as a shock, following the spiral path of the helical magnetic field. When the shock is at a position along the path which approaches the observer's line of sight, the broadband emission increases due to beaming, then fades as the shock propagates out of the line of sight, as first described by Rosen (1990). Eventually, the traveling shock encounters the standing shock at the radio core, producing a second outburst of emission before dispersing and propagating further down the radio jet.

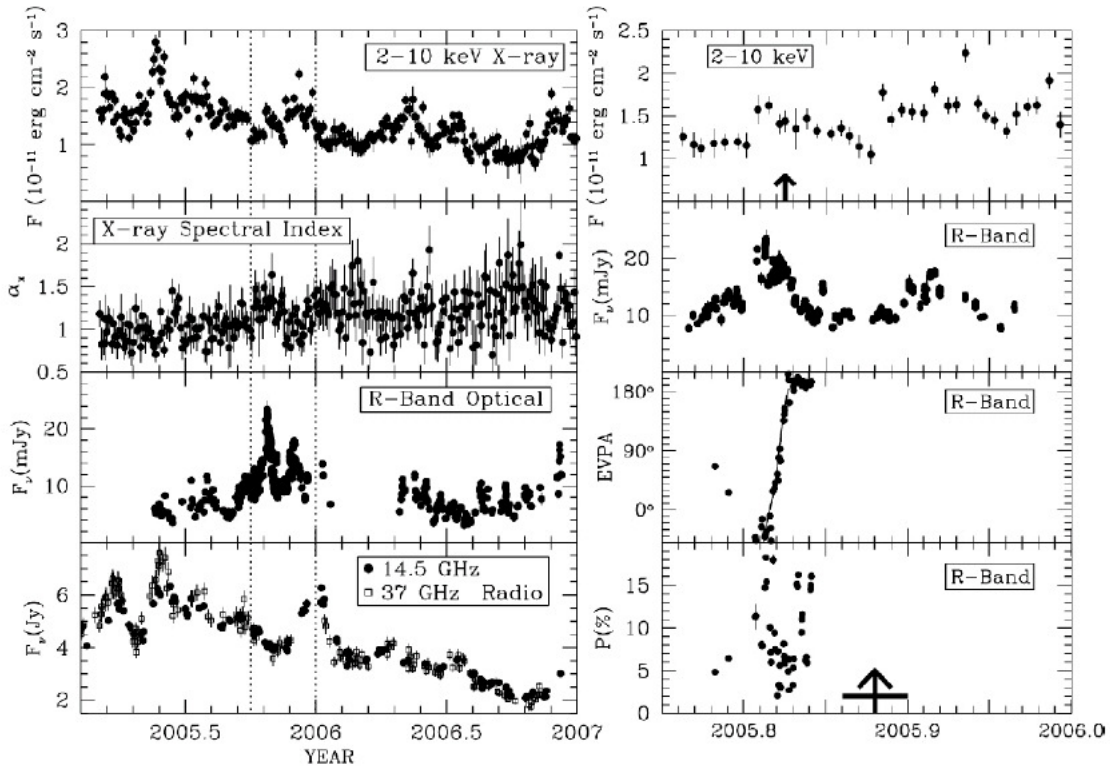

Figure. 1.17: Multiwavelength and polarization data used to support the model seen in Figure 1.16 (Marscher et al. 2008).

The detailed anatomy of the variability process is supported by observations taken by Marscher et al. (2008), shown in Figure 1.17. Two distinct flares can be seen in the optical data, corresponding first to the shock aligning with the observer's line of sight in the inner jet, followed by a burst of emission associated with passage through the standing shock at the radio core. Only the second flare, slightly delayed, is seen in the radio because the inner portion of the jet is opaque at radio wavelengths. Also, a clear change in polarization angle of the optical data is seen during the first flare, demonstrating the motion of the shock along the spiral path of the inner jet (e.g., Gopal-Krishna & Wiita 1992).

1.8 Synopsis of Thesis

This dissertation demonstrates the use of many decades of accumulated optical observations of blazars toward the determination of critical timescales of variability. The majority, if not all, of the optical emission in blazars is believed to originate from shocks traveling down a relativistic jet directed closely to our line of sight. Through the mechanisms described above, it is possible that the timescales of variability associated with the jet should also correspond to those produced by the accretion disk. If this link is true, then the observed breaks in the PDS of GXRB systems and Seyfert galaxies, believed to be caused by fluctuations in the accretion disk, should also be derivable from the optical light curves of blazars.

Chapter 2 discusses the origins and methods of data reduction for all photometric light curves presented in this thesis. Chapter 3 discusses the methods of analysis used on these light curves, including the structure function and the power density spectrum. Also included in Chapter 3 is a detailed description of our implementation of the Power Spectral Response (PSRESP) method presented by Uttley et al. (2002) for the use of determining a goodness of fit for various PDS models. Chapter 4 discusses the observations, variability, and light curves for each object in the sample. Chapter 5 details the results from the analysis and possible timescales derived for each object. The interpretation of these results and how they can be incorporated into current models for blazar variability are discussed in Chapter 6.

The Universe is like a safe to which there is a combination, but the combination is locked up in the safe.

—— *Peter de Vries*

– 2 –

Data Reduction and Photometry

In order to compile optical light curves that span decades in time, it is impossible to avoid piecing together data from different telescopes, instruments, and observers. This situation is most certainly the case for the material presented in this dissertation. The majority of recent observations (later than 1992) by the PEGA group were conducted at Lowell Observatory. There are, however, many other sources of data mixed in, including but not limited to, Cerro Tololo Interamerican Observatory (CTIO), Kitt Peak National Observatory (KPNO), and observations carried out by amateur astronomers. Also, for older data, these sources become even more varied and the data were obtained mainly through literature searches. While great care must be taken, data from a wide variety of sources can be combined to produce reliable information about an object's long-term behavior.

2.1 Data Reduction

For the purposes of this dissertation, data reduction will refer to the processing of raw image frames into clean, usable frames from which photometric measurements can be taken. The majority of the reduction processes were carried out by the author or other members of the PEGA group. In some cases, such as queued service observations or amateur astronomer data, the frames are already reduced. For archival data, usually

presented in tabular format, it must be assumed that the data reduction processes were carried out in an acceptable manner.

2.1.1 Data from Lowell Observatory

The PEGA group has been fortunate enough to receive time for blazar monitoring at Lowell Observatory for many years. Observations are usually carried out on one of two telescopes; the majority are performed with the 72"(1.8m) Perkins telescope and the remainder on the 42"(1.04m) Hall telescope. Due to the length of time these telescopes have been used by the PEGA group, we have had access to multiple instrument packages and configurations. A list of these instruments and some of their pertinent characteristics can be found in Table 2.1. Most of the data acquired after 2004 were obtained by the author.

Table. 2.1: Telescope and CCD Characteristics.

Telescope	Detector	Field of View	Platescale	Binning
Hall - 1.04m	SITe 2048x2048	$19.4' \times 19.4'$	$1.136''$/pix	2×2
Perkins - 1.08m	PRISM 2048x2048	$13.6' \times 13.6'$	$0.786''$/pix	2×2
...	Loral 2048x2048	$3.2' \times 3.2'$	$0.191''$/pix	2×2
...	SITe 2048x2048	$5.2' \times 5.2'$	$0.306''$/pix	2×2
SMARTS - 1.3m	ANDICAM 1024x1024	$6.0' \times 6.0'$	$0.369''$/pix	2×2
SMARTS - 0.9m	CCD 2048x2046	$13.5' \times 13.5'$	$0.396''$/pix	1×1

In all cases, the instruments were charge-coupled devices (CCD), and reductions were carried out in a fashion consistent with techniques used by almost all modern astronomers. In addition to standard object frames, bias and flat field calibration

frames were taken for each observing run. On average, an observing run would last 5-6 nights. Bias frames, typically a set of ten, were taken at the beginning of each night. Flat field frames, also a set of ten, were usually taken once per run in each filter used. In almost all cases, a dome flat field screen was used as opposed to sky flats. All instruments used were cooled with liquid nitrogen and most exposure times were relatively short (less than 5 minutes), therefore no dark frames were needed.

Bias or zero frames are needed in order assess the readout noise of a CCD chip. An exposure of zero length in time is taken with CCD shutter closed and the chip is simply read out. The bias level contains noise from a variety of mostly electronic sources including the design of the CCD itself, wiring, contacts, etc. The average bias level across the chip is ideally constant, with small pixel to pixel, column to column, or even row to row variations, depending on how the chip is read. In order to sample these variations evenly and to take account for other possible events, such as cosmic rays, it is necessary to take multiple bias images and then combine them into a single, master bias frame.

A flat field frame is multi-purposed, accounting for irregularities in chip illumination and primarily differences in pixel responses. The goal of a flat field image is to create a high signal to noise readout of the chip that displays the response of the chip to light in a given filter. Depending on the light path to the chip and deformities in the chip itself, there may be slightly different responses to incoming radiation. Flat fields will also help remove the possible effect of fringing and contamination of

the field by dust or debris in the light path. As with bias frames, it is necessary to combine multiple flat images into a single master flat in order to account for any anomalies which may occur in individual frames.

The software employed for data reduction was the Image Reduction and Analysis Facility (IRAF) suite of routines. In most cases, it was possible to use a script written by former PEGA member John McFarland that streamlined the reduction of data by calling various IRAF routines in sequence. In other cases, depending on the CCD, it was necessary to perform the reduction 'by hand' using the individual IRAF routines. Using either method, the process is relatively simple. A master bias is created from the set of individual bias frames, then the master bias is subtracted from all other frames for a given night. The flat field frames are combined into a master flat for each filter, and the corresponding observation frames are divided by the master flat. The end results are object frames which have been properly calibrated for imperfections in the CCD chip and the light path of the telescope.

2.1.2 Data from the SMARTS Consortium

Another major source of data for the PEGA group is queued service observing from the 1.3m telescope at CTIO via the Small and Moderate Aperture Research Telescope System (SMARTS). Since 2003, the 1.3m has been used to carry out daily to weekly observations of many southern sky AGN for the PEGA group. Typically, observations for a given object are spaced 3-4 days apart, though for some cases of intense flaring or other interesting activity, an object is observed on a near nightly basis. Each object

is usually monitored for at least 3 months of the observing season, if not longer.

Unlike the data obtained from Lowell Observatory, the queued SMARTS observations are received already reduced using a pipeline for the 1.3m telescope. The reduction procedures are essentially identical to that described above, with IRAF procedures used to create a master bias and master flat, and then apply the calibration frames to the object frames. Flat field frames are taken every night, using dome flats for the V,R, and I filters and sky flats for the B filter due to undesirable artifacts found in the B dome flats.

The instrument on the SMARTS 1.3m telescope is called ANDICAM, built by the Ohio State University. Specifications for the optical imager on the ANDICAM instrument are also displayed in Table 2.1. It is a valuable instrument due to the fact that it can obtain simultaneous images in the optical (BVRI) and IR (YJHK) bands. The PEGA group has obtained a huge database of IR frames for southern sky AGN, though these data are not included in this dissertation due to a lack of time to master the IR reduction procedures. The reduction and photometry of these data would be an excellent future project for the PEGA group.

2.1.3 Other Data Sources

A small portion of the data used in this dissertation were obtained by amateur astronomer Paul Boltwood, specifically for 3C 454.3 during the flare of 2005. Observations were obtained from private facilities located in Ontario, Canada. A 40cm Newtonian reflector was used with a 2.4X Barlow lens. The instrument was an Apogee

AP7p camera with standard filters and exposure times of 120 seconds. Boltwood reduced all images in the standard fashion including bias, dark, and flat calibrations, cosmic ray filtering, and standard aperture photometry.

Many of the objects in the sample have been monitored since their discovery as blazars in the 1960's. Due to their identification as highly variable objects, a wide variety of monitoring campaigns were set up, especially in the radio and optical. This dissertation benefits greatly from observations taken at the Rosemary Hill Observatory (RHO), operated by the University of Florida (Webb et al. 1988; Pica et al. 1988). These observations were taken mainly in with the B filter over an average time period of 1968-1982. Additionally, a compilation of blazar light curves from a variety of sources is presented in Fan & Lin (2000).

In some rare cases, it was also possible to go through archival photographic plates after the sources were identified as blazars (Miller 1975). While these measurements usually have a higher uncertainty and must be transformed to modern filter measurements, they provide valuable insight into the long-term behavior of these objects. In some cases, the full historical light curve can be extended to nearly a century.

2.2 Photometry

Traditionally, optical measurements for blazars have been carried out using differential aperture photometry. This technique has the benefit of providing reliable results while still allowing for small time resolution measurements and more efficient use of

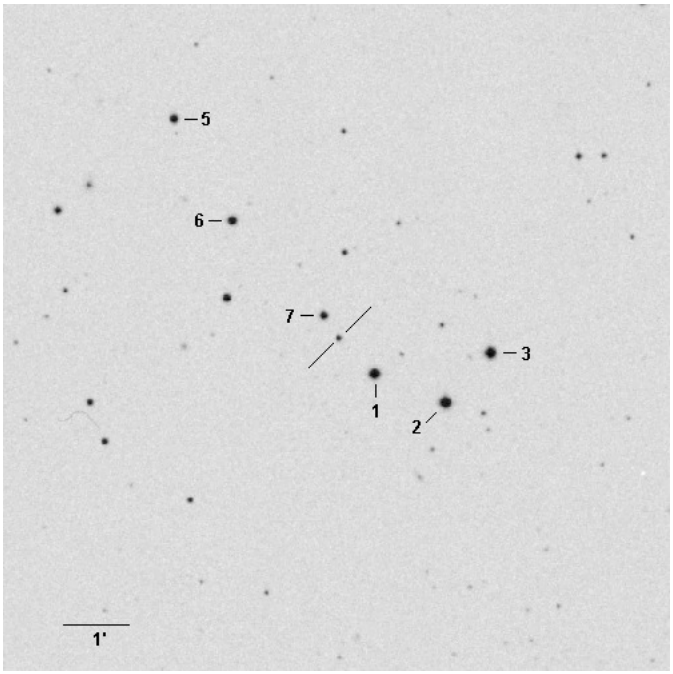

Figure. 2.1: Finder chart for the object AO 0235+16. The blazar is indicated by the lines, the checks stars by number.

observing time. A set of check stars are chosen within the blazar field of view, usually covered by a 15′x15′square or smaller. It is assumed and usually tested that these check stars are stable and do not vary significantly over short or long timescales. The instrumental magnitudes of the target and check stars can then be compared directly without concern for seeing, color, or airmass changes over the course of a night. If the photometrically calibrated magnitudes of the check stars are known, the apparent magnitude of the object can be estimated.

The PEGA group uses the CCDPhot program, written in Interactive Data Language (IDL) by Marc Buie. Artificial apertures are placed around the target and as many checks stars as needed. A common aperture radius is used for both targets

and check stars and the total counts located within the aperture are summed. For almost all data obtained, a 7″aperture was used for photometry to assure consistency between data sets. The background level for each aperture is determined from an annulus centered on the aperture. Once the background level has been subtracted, the instrumental magnitudes for the target and the checks are calculated and the output is written to a file.

Comparisons can then be made between the target of interest and the check stars, as well as between the check stars themselves. Ideally, the relative differences between check stars should remain constant because these objects are not intrinsically variable. Any changes in brightness due to seeing, clouds, airmass, or other factors will affect the check stars equally. However, if the target is intrinsically variable, brightness changes should be revealed when compared to the check stars.

In many cases, there have been concentrated efforts to obtain accurate apparent magnitudes of blazar check stars using all-sky photometry (Smith et al. 1985). Using these magnitudes, it is possible to transform the differential magnitude of the target blazar into an apparent magnitude. It should be noted that this transformation increases the uncertainty of the measurement compared to the results of the differential photometry. The error in the apparent magnitude of the target must take into account the root mean square (RMS) spread of the check star comparisons, the error in the apparent magnitude of the check stars, and the photon statistics of the faintest object (usually the target). The transformation to apparent magnitudes is

necessary, however, in order to compare the brightness level of the target with data from different telescopes, instruments, and epochs.

The majority of the recent data (since 1992) were taken in the Johnson R filter. Archival data mainly used the Johnson B filter with some of the much older data coming from photographic plates. In each case, a color correction is necessary in order to create a consistent long-term light curve. All data in this dissertation were converted to R magnitudes, using published zero-point color corrections. As before, this additional correction will add additional uncertainty in the apparent magnitude of the object of interest. There is no clear evidence of a measurable lag between observations taken in different filters at optical wavelengths (e.g., Osterman et al. 2007) and therefore the color corrections should not have a significant effect on the time series analysis.

2.3 Flux Calibration

The final calibration of the light curves before analysis is a transformation between apparent magnitude and flux. In this manner, the observed variability is measured in its true linear form. The form of this conversion can be seen in Equation 2.1, in terms of flux density F_ν, zero-point flux density F_{ν_0}, and apparent magnitude m. The zero-point flux density used in this dissertation for the R filter is $F_{\nu_0} = 2941$Jy.

$$F_\nu = F_{\nu_0} 10^{-0.4m} \tag{2.1}$$

The flux conversion utilized is not meant to be an absolute determination of the flux of the object at a given wavelength, but instead an internally consistent method of transforming the variability into flux space.

Self-education is, I firmly believe, the only kind of education there is.

—— *Isaac Asimov*

– 3 –

Time Series Analysis

All techniques employed in time series analysis seek to define the temporal character of a process. This may include the detection of a characteristic timescale, such as a periodic signal or the break timescales already discussed. It also includes the confirmation of the nature of the process, such as white, pink, or red noise. Each technique has both advantages and disadvantages, but there is a common thread throughout. The two techniques used in this dissertation and discussed below are the structure function (SF) and the power density spectrum (PDS).

3.1 Structure Function

The structure function provides more detailed information about the physical processes responsible for the variability observed (Simonetti et al. 1985). The SF of a perfect, evenly sampled time series, as seen in Equation 3.1, taken from Paltani et al. (1997), is constructed by summing the difference in flux at successive time lags, where f is the flux level at time t and τ is the time lag. Unevenly sampled data require the form seen in Equation 3.2, where we introduce a bin size δ in which the observed lags must be contained. For AGN, this usually results in larger values of the SF at longer timescales because the light curves display large amplitude variability only over long times scales. The SF has been used in many studies of AGN light curves in the radio,

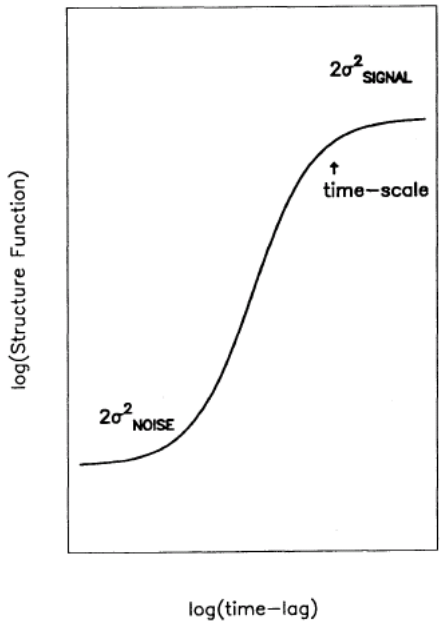

Figure. 3.1: A theoretical ideal form of the structure function (Hughes et al. 1992).

optical, and x-ray regimes (Hughes et al. 1992; Smith et al. 1993; Brinkmann et al. 2000).

$$SF_f(\tau) = \langle [f(t+\tau) - f(t)]^2 \rangle \tag{3.1}$$

$$SF_f(\tau, \delta) = \frac{1}{N(\tau, \delta)} \sum_{(i,j)|\tau-\delta/2<t_j-t_i<\tau+\delta/2} [f(t_j) - f(t_i)]^2 \tag{3.2}$$

The main advantage of SF analysis is that it remains in the time domain and does not involve a Fourier transform. This fortunately means that the data need not be evenly sampled. An ideal form of the SF is seen in Figure 3.1. The lower, flat portion of the structure function corresponds to the level of measurement uncertainty

in the input light curve. The higher plateau is thought to correspond to an intrinsic timescale associated with the object in question. The analysis of astronomical data never produces such a clean form in the SF, due in large part to long gaps in the data and an incomplete range of timescales sampled. However, if the proper portion of the SF is sampled, it may be possible to detect a turnover or break at certain timescales. The slope of the SF can also be related to the slope of the PDS, such that if the PDS has the form $P(\nu) = \nu^{-\alpha}$ and the SF the form $S(t) = t^{\beta}$ then $\alpha = 1 + \beta$ (Paltani et al. 1997).

While providing a means of analysis for the unaltered temporal data in the light curve, care must be taken in the interpretation of the SF. For most light curves, the sampling of the SF at long timescales will be much lower than that at shorter timescales. For this reason, the behavior of the SF at long timescales has a tendency to become erratic and unpredictable (Markowitz 2006). One can compensate for this behavior through the use of many simulations of fake data based on an input variability model. A discussion of these Monte Carlo simulations is given in detail in the next section.

3.2 Power Density Spectra

The second and more robust time series analysis technique used in this dissertation is the power density spectrum. In many ways, the PDS is the closest approximation to the true variability nature of the object, assuming that the variability of AGN can

be described as a noise process. The PDS in its basic form is the square modulus of the Fourier transform of a time series. Like the SF, the PDS displays the amount of variability power at a given frequency. As mentioned earlier, most AGN and other accreting systems display a red noise character, with stronger, large amplitude variability at low frequencies.

The PDS is an important tool because it provides the most direct method for comparing the observed nature of variability to a model. The observed power spectra for accreting systems have all shown a power law form, whether it be a broken or unbroken power law. A log-log representation of power versus frequency displays a linear trend, with a slope equal to the index of the power law. Unfortunately, the PDS is also the most data sensitive analysis tool of the two and great care must be taken to account for problems of sampling, windowing, and aliasing. A description of a successful method for modeling and testing the PDS of AGN data follows.

3.2.1 Power Spectral Response Method (PSRESP)

The PSRESP method, developed and explained fully in Uttley et al. (2002), is a procedure which produces a power spectra from observed data, compares that power spectrum to simulated power spectrum from an input model, then determines a goodness of fit. The models and goodness of fit are centered upon the use of Monte Carlo simulations. Power spectra are inherently noisy, so the use of multiple simulations is necessary in order to obtain a reasonable assessment of the uncertainty in any measurement.

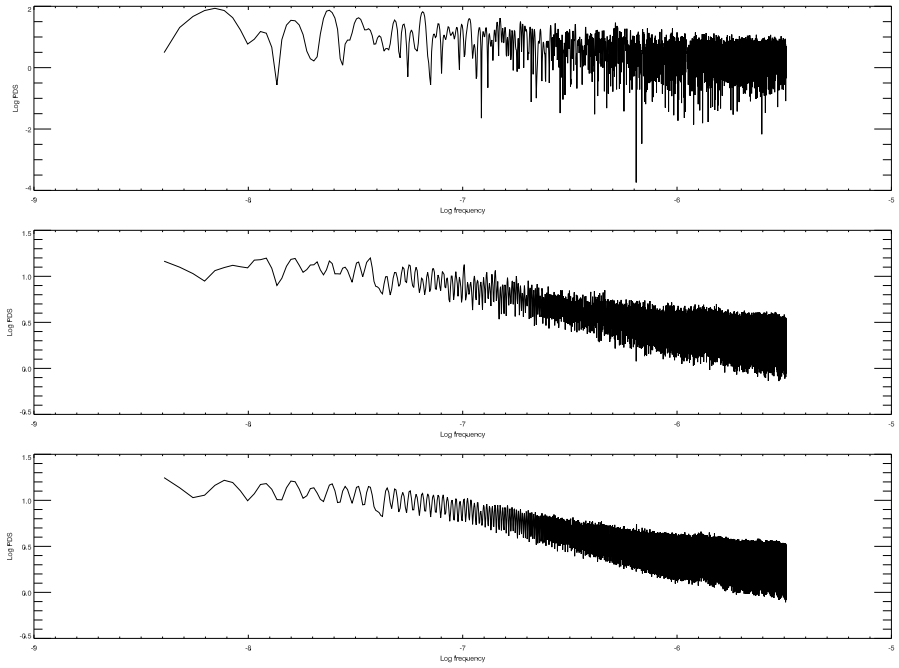

Figure. 3.2: The top panel shows the PDS calculated from a single light curve simulated based on a knee model with a low frequency slope of zero, high frequency slope of -1.5 and break at $10^{-7.0}$ Hz. The middle and bottom panels show the mean power spectra calculated from 100 and 1000 simulated light curves respectively.

An example of the benefits of the Monte Carlo simulations is demonstrated in Figure 3.2. In this scenario, light curves are simulated based on an input model PDS. In this case, the model is a broken power law, with a slope of -1.5 at high frequencies, a slope of zero at low frequencies, and a break located at $10^{-7.0}$ Hz. The top panel displays the the result of a single measurement of the PDS from the simulated light curve. Note that even though the light curve is simulated based on a known input model, the results of a single measurement of the PDS do not clearly return the shape of the original model. In order to regain the original model, it is necessary to simulate many light curves, calculate the PDS, then take an average of all simulated power

spectra. The middle and bottom panels of Figure 3.2 show the result of averaging 100 and 1000 of the simulated PDS, respectively. It is clear that the original shape of the input PDS becomes apparent through the averaging of multiple simulations.

The software used to calculate the PDS and execute the Monte Carlo simulations were written by the author in IDL. The programs are based on the description of the method in Uttley et al. (2002) and portions of the code from Marshall (2006). Hard copies of the programs used in this dissertation are available in the appendices. A more qualitative description is given below.

3.2.1.1 Computation of the Observed PDS

In order to sample the PDS over a wide range of frequency, it is necessary to break up the original light curve into sections and bin each section. For example, for the low frequency PDS, the entire historical light curve can be used, spanning decades of observations, but must be binned coarsely (50 days to yearly) in order to maintain an even sampling rate. On the high frequency end, a single night of microvariability observations may be used in order to sample timescales from one minute up to approximately six hours. One benefit of optical data over x-ray data is that the optical data are much more plentiful, allowing for PDS measurements at many different epochs. The representative PDS for a given frequency range is created by averaging the individual PDS from various epochs.

$$|F_N(\nu)|^2 = \left(\sum_{i=1}^{N} f(t_i)\cos(2\pi\nu t_i)\right)^2 + \left(\sum_{i=1}^{N} f(t_i)\sin(2\pi\nu t_i)\right)^2 \tag{3.3}$$

The square modulus of the Fourier transform is calculated for each input light curve, as given by Equation 3.3. The calculations are performed at evenly spaced intervals, from the minimum frequency observed, $\nu_{\rm min}$, through the Nyquist frequency, $\nu_{\rm Nyq}$, in steps of $\nu_{\rm min}$, where $\nu_{\rm min} = T^{-1}$, $\nu_{\rm Nyq} = (2T/N)^{-1}$, T is the duration of the light curve, and N is the number of data points. The Nyquist frequency respresents the highest measurable frequency for the time series which can be used to recover the true variability of the input light curve.

A normalization is also applied to arrive at the final value of power, given by Equation 3.4, with μ the mean flux of the light curve. This normalization allows for the PDS from different epochs, flux levels, and frequency ranges to be compared in a broadband fashion. Once the PDS is calculated for each section, they are joined to form a single broadband PDS that can span more than five orders of magnitude in frequency.

$$P(\nu) = \frac{2T}{\mu^2 N^2}|F_N(\nu)|^2 \tag{3.4}$$

The inherent noise in the calculation of the single observed PDS can be decreased through a logarithmic binning of the PDS (Papadakis & Lawrence 1993). The logarithm of power is binned by a constant factor in frequency, producing a smooth

representation of the observed PDS.

3.2.1.2 Simulation of Model Light Curves and PDS

In order to test the legitimacy of the observed PDS, it is necessary to carry out multiple simulations of fake data based on an input model and sampled in exactly the same manner as the original data. Great care is taken to ensure that the simulated light curves and their PDS are an accurate representation of real world data. The true underlying PDS shape is distorted by the effects of the sampling window. In this manner, the Fourier transform is a convolution of the true variability process and a window function. The form of this window function cannot be expressed analytically and must be accounted for using Monte Carlo simulations. The main consequence of the window function is an addition of power from frequencies above and below those observed, namely red noise leak and aliasing. However, a proper accounting of these factors, described below, can provide a useful means of comparing observed variability behavior to that of a model.

The simulated light curves are created using an IDL program following the method of Timmer & Koenig (1995). This program uses an input model PDS, which can be of any form the user supplies, to create a synthetic light curve of specified length, sampling rate, mean, and variance. It is at this initial step that corrections are made in order to account for some amounts of red noise leak and aliasing.

Red noise leak is caused by the fact that there may be significant power at frequencies lower than the minimum frequency sampled in the observed light curve and

this extra power is mirrored into the observed frequency range. In order to account for this extra power, instead of simulating N individual light curves of length T, a single light curve of length NT is created and then divided up into N segments.

Similar to red noise leak, aliasing is caused by the fact that the PDS is not sampled at frequencies higher than the Nyquist frequency. The variability above the Nyquist frequency is not resolved, and the power from this variability is shifted into the observed frequency range. For red noise-like processes like those found in accreting systems, power drops off rapidly at higher frequencies, so the effect of this aliasing is relatively small. However, because the amount of aliased power will increase for a model PDS with a shallower slope compared to one with a steeper slope, it is necessary to take this aliasing into account when calculating the simulated PDS. The amount of power transfered into the observed frequency range can be approximated by adding a constant value to the simulated PDS, given by Equation 3.5, where $T_{\rm sim}$ is the sampling rate of the simulated light curve and $T_{\rm bin}$ is the sampling rate of the binned observed light curve.

$$P_{\rm alias} = \frac{1}{f_{\rm Nyq} - f_{\rm min}} \int_{(2\Delta T_{\rm sim})^{-1}}^{(2\Delta T_{\rm bin})^{-1}} P(f) df \tag{3.5}$$

The simulated light curve is created at a frequency resolution ten times that of the observed light curve in order to account for additional aliasing at higher frequencies. The simulated light curve is divided into N segments, resampled, and binned in exactly the same fashion as the observed light curve. The PDS for each simulated light

curve is calculated and logarithmically binned in the same manner as the observed light curve.

$$P_{\rm noise} = \frac{\sum_{i=1}^{N}(\sigma(i))^2}{N(\nu_{\rm Nyq} - \nu_{\rm min})} \tag{3.6}$$

A final correction to the simulated PDS is the addition of a constant level of power due to the Poisson noise of the input light curve. In essence, this is the level at which the measurement error in the flux overcomes the variability power. The power from Poisson noise, $P_{\rm noise}$, is given in Equation 3.6, where $\sigma(i)$ are the observational uncertainties for each measurement in the input light curve.

3.2.1.3 Determining Goodness of Fit

An average model PDS, $\overline{P_{\rm sim}}(\nu)$, is calculated from the N simulated PDS for each input model. The error in the model PDS, $\Delta\overline{P_{\rm sim}}(\nu)$, is defined as the RMS spread of the value of power at a given frequency for the N simulations. When making comparisons to the observed PDS, the use of the traditional χ^2 statistic is not appropriate because the PDS error is not strictly Gaussian in nature. The alternative statistic used in this method, $\chi^2_{\rm dist}$, is defined in Equation 3.7.

$$\chi^2_{\rm dist} = \sum_{\nu=\nu_{\rm min}}^{\nu_{\rm max}} \frac{(\overline{P_{\rm sim}}(\nu) - P_{\rm obs}(\nu))^2}{\Delta\overline{P_{\rm sim}}(\nu)^2} \tag{3.7}$$

An arbitrary normalization is found by minimizing the value of $\chi^2_{\rm dist}$ over a range of multiplicative factors in order to best match the observed PDS. This normalization

only affects the relative amplitude of the PDS, but does not alter the shape. This is acceptable because it is only the shape of the PDS that reveals the underlying variability processes.

A goodness of fit can be determined by comparing the $\chi^2_{\rm dist}$ value of the observed PDS to the $\chi^2_{\rm dist}$ values created from random combinations of individual simulated power spectra from each time segment. Ideally, the number of random combinations, M, must be ≥ 1000. The probability of acceptance for the given model is then given by the percentile of random simulated power spectra for which the measurement of $\chi^2_{\rm dist}$ is less than that for the observed PDS. This process can be repeated for a range of models (single power law, broken power law, etc.) and over a range of model parameters (slope, break, etc.) in order to determine the model that best fits the data. This goodness of fit estimate is adapted from Uttley et al. (2002) and explained thoroughly in Press et al. (1992).

3.3 Test Models

The computation of the power density spectrum or the structure function for an input light curve, as outlined earlier in this Chapter, is a straightforward process. The interpretation of the result, however, is very sensitive to observational factors such as an uneven sampling rate or large gaps in the data. Visual examination of the SF or PDS of an object's variability may suggest the presence of a break in slope, but these conclusions must be tested in a statistically relevant manner.

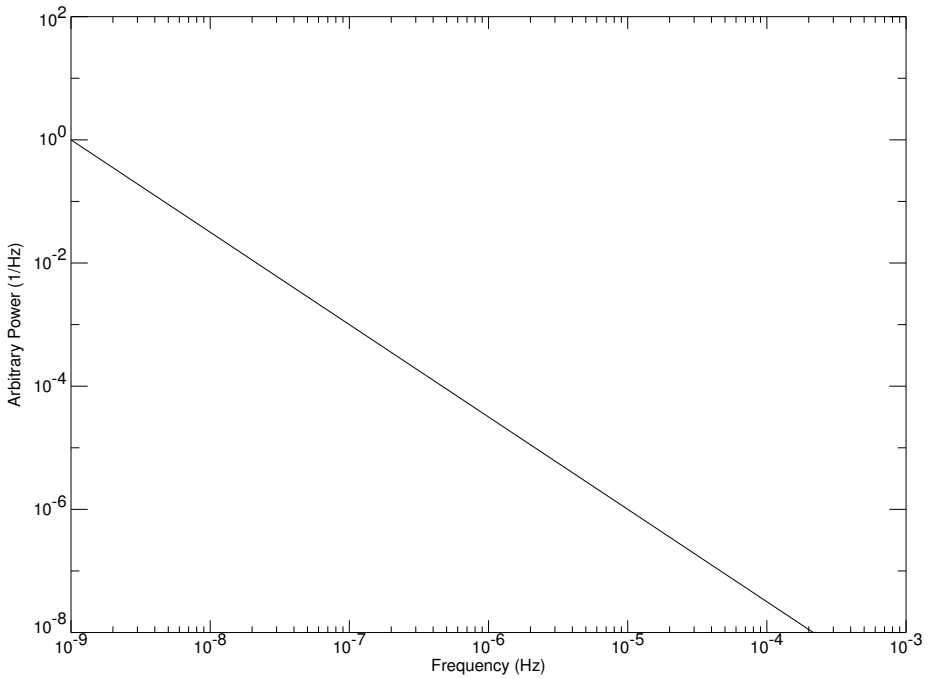

Figure. 3.3: Model form of an unbroken power law with slope $\alpha = -1.5$.

For these reasons, we employ the use of Monte Carlo simulations of fake data, described above, in order to test an input model of variability. The form of the test model is chosen to reflect processes already observed in nature. In the case of accreting systems, observations of GXRB systems provide an excellent source for test model parameters. The three test models used in this dissertation all have the form of a power law, such that the variability power is proportional to frequency raised to a power, $P(\nu) \propto \nu^{\alpha}$. In a log-log representation of power versus frequency, this relationship takes a linear form with slope equal to the value of α. The delimiter between models is the presence, location, and sharpness of a break frequency, f_b, where the slope, α, changes value.

The simplest test model is that of an unbroken power law. Almost all of the

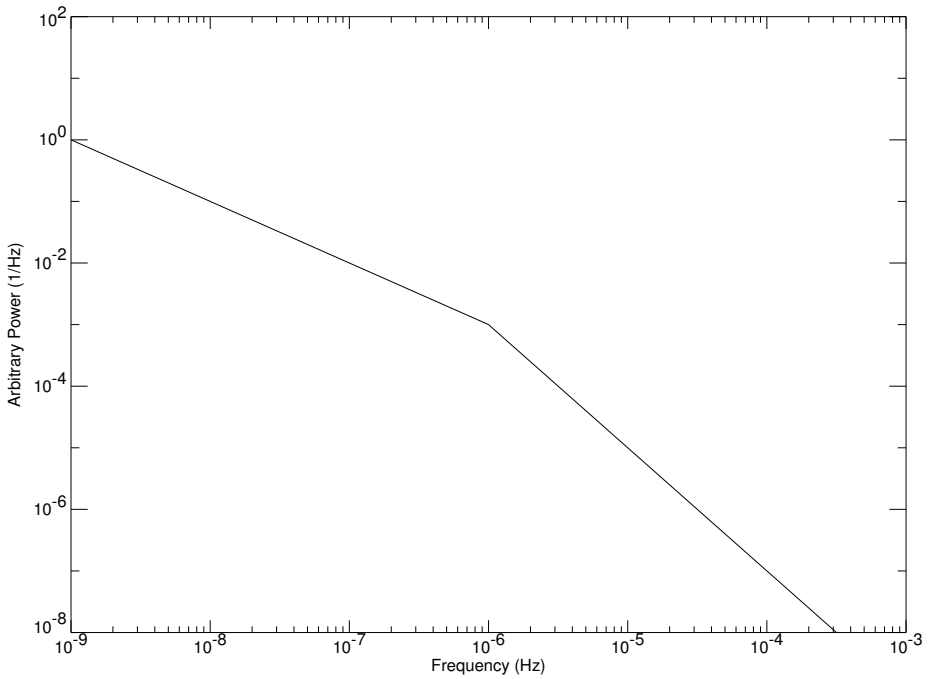

Figure. 3.4: Model form of an broken power law with break frequency $f_b = 10^{-6.0}$Hz, changing from slope $\alpha = -1.0$ to $\alpha = -2.0$.

power spectra measured for GXRB systems show a change in slope of some form. This model can therefore be thought of as a control, determining whether there need be a change in slope in order to describe the observed data.

$$P(\nu) = A\left(\frac{\nu}{\nu_0}\right)^{\alpha} \tag{3.8}$$

The form of this model can be seen in Equation 3.8, with A the amplitude of the power spectrum at the frequency ν_0. The amplitude for the test model, A, is arbitrary because it is only the shape of the model power spectrum that is tested. Figure 3.3 displays the form of the unbroken power law model. The only free parameter in this model is the slope, α, making this model the easiest to test computationally.

The next test model is that of a power law with a single, sharp break in slope. This model is based on observations of the power spectrum of Cyg X-1 (Nowak et al. 1999) and many other GXRB systems (Belloni & Hasinger 1990). The power spectra of GXRB in a low/hard state tend to display a high frequency break from a slope of $\alpha = -1.0$ to a steeper slope of $\alpha \approx -2.0$. The form of this model can be seen in Equation 3.9 and in Figure 3.4, with A the power amplitude at break frequency $\nu_{\rm b}$ and high frequency slope α.

$$P(\nu) = \begin{cases} A\left(\frac{\nu}{\nu_{\rm b}}\right)^{-1.0} & \nu \leq \nu_{\rm b} \\ A\left(\frac{\nu}{\nu_{\rm b}}\right)^{\alpha} & \nu > \nu_{\rm b} \end{cases} \tag{3.9}$$

In this model, the low frequency slope is locked at a value of negative one while the high frequency slope is a free parameter. Allowing the low frequency slope to vary would undoubtedly produce a better fit to the observed data, but we refrain from taking this step for two reasons. First, having two free parameters, α and $\nu_{\rm b}$, already leads to very extensive computation time in order to explore a sufficient range in parameter space. Also, we are reluctant to expand the number of free parameters because this is an initial attempt to test the PSRESP technique on optical data. In keeping the low frequency slope fixed, we are comparing the behavior of blazars at optical wavelengths directly to the observed behavior of GXRB systems in the low/hard state.

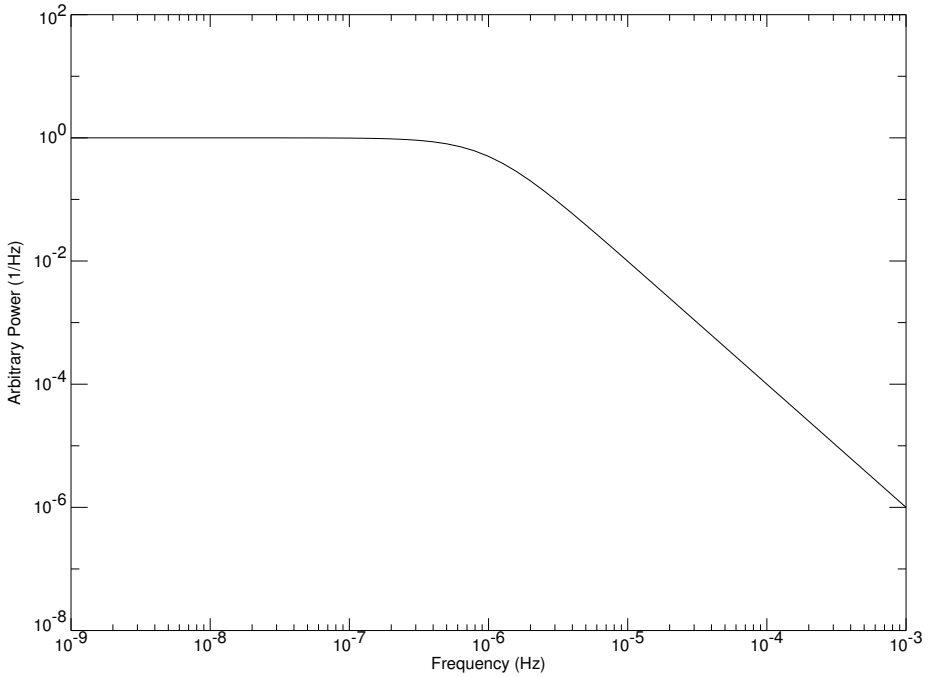

Figure. 3.5: Model form of a knee power law with break frequency $f_b = 10^{-6.0}$Hz, changing from slope $\alpha = 0.0$ to $\alpha = -1.0$.

$$P(\nu) = A\left(1 + \left(\frac{\nu}{\nu_{\rm b}}\right)^2\right)^{\alpha/2} \tag{3.10}$$

The knee power law model used in this analysis is also based on the low/hard state of GXRB systems. In this case, the low frequency slope is locked at zero and the high frequency slope allowed to vary as a free parameter. This shape, seen in Figure 3.5, mimics the power spectra of GXRB systems at the low frequency break in the low/hard state. The form of the knee model is shown in Equation 3.10.

It is important to note that the broken power law (BPL) and knee models test two different regions of the power spectrum observed in GXRB systems. The power spectral shape of Cyg X-1 is shown again in Figure 3.6 for reference. The knee model

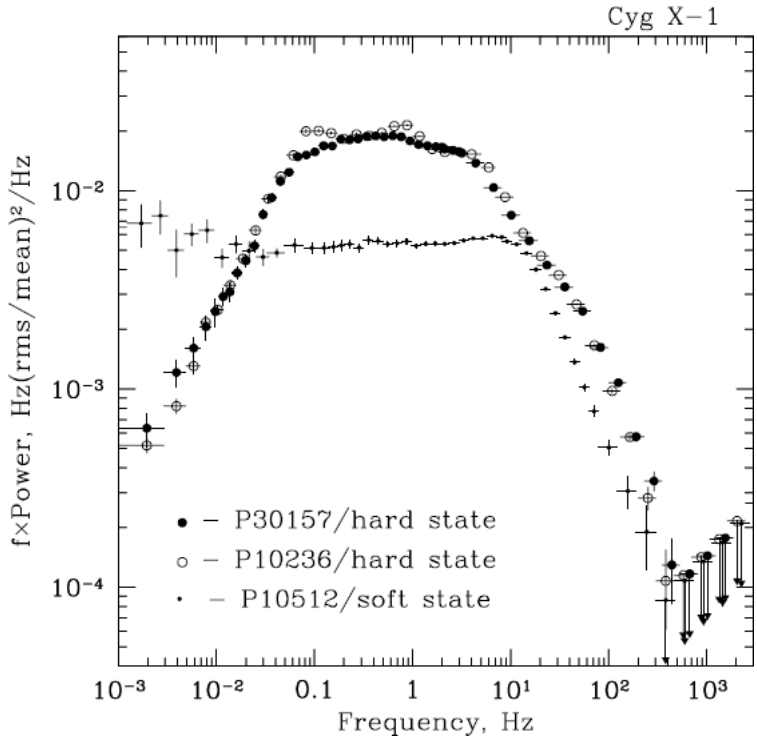

Figure. 3.6: The PDS shape of Cyg X-1 in both low/hard and high/soft states. Note that this representation of the PDS is in frequency multiplied by power versus frequency (Revnivtsev et al. 2000).

is a test for the first break seen in the hard state at low frequencies while the broken power law tests for the second break seen at higher frequencies. Any breaks detected in the power spectra of blazars are assumed to be scaled versions of the breaks seen in the PDS of Cyg X-1. However, it is not initially known whether the observed breaks in the blazar PDS will correspond to the hard or soft state of Cyg X-1, nor is it known whether the observed breaks will correspond to the low or high frequency break. The use of these two models provides a diagnostic to determine which region of the PDS is sampled and follows the methodology presented in Uttley et al. (2002).

When I, sitting, heard the astronomer, where he lectured with such applause in the lecture room, how soon, unaccountable, I became tired and sick; Till rising and gliding out, I wandered off by myself, in the mystical moist night air, and from time to time, looked up in perfect silence at the stars.

—— Walt Whitman

– 4 –

Observations and Variability

This chapter provides a brief overview of background information on each object and a presentation of the data used in the time series analysis. Although all objects belong to the blazar class, each possesses characteristics that make it an unique candidate for study. The light curves presented below provide insight into the interesting behavior displayed by blazars over more than 40 years.

4.1 0235+164 (AO 0235+16)

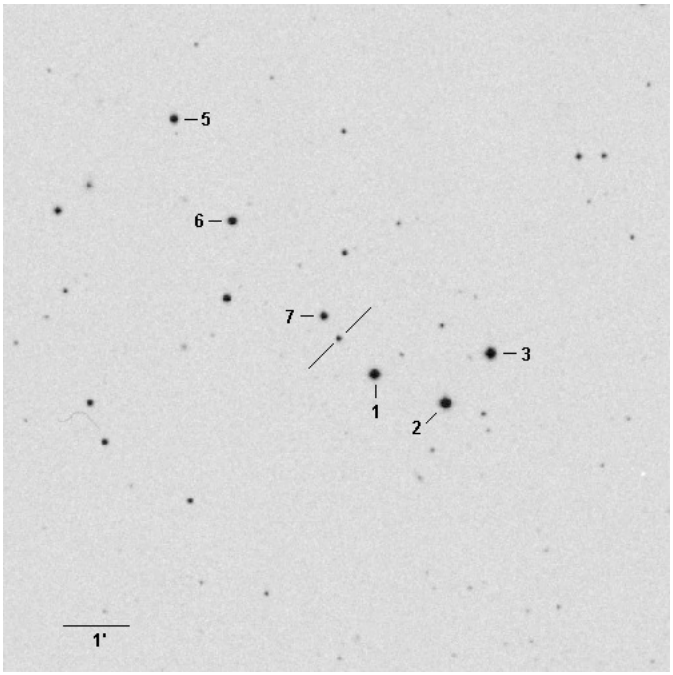

Figure. 4.1: Field of view of AO 0235+16 (target marked by lines, check stars by letter or number, north is up, east if left).

4.1.1 Background

The radio source AO 0235+16 was identified with a red, stellar-like object in the optical by Argue et al. (1973). The finder chart for AO 0235+16 is displayed in Figure 4.1. Shortly after the optical identification, spectra revealed that the object belonged to the BL Lac class, with no measurable optical emission lines and a very red continuum (Spinrad & Smith 1975). The object has exhibited one of the largest ranges in variability at radio, infrared, and optical wavelengths. In its lowest state, it is the faintest object in the sample (R$\sim$19), but has reached significantly brighter levels (R$<$13) during outbursts.

Many outbursts have been detected in this object, including ones in 1975, 1997, and most recently during the 2006-2007 observing season. Simultaneous observations in the radio and optical show a strong correlation between flux at these wavelength regimes during strong outbursts (Balonek & Dent 1980; Balonek 1982). In the IR, outbursts in flux are also correlated with large variations in linear polarization. Impey et al. (1982) recorded a strong IR outburst that produced a simultaneous peak in polarization of 28.7% at 2.2μm. Simultaneous optical polarization observations detected a polarized flux as high as 44%.

The size and rapidity of the outbursts in AO 0235+16 have led many to seek alternative explanations for variability. In order to explain the rapid, large amplitude changes in flux, some models require Doppler factors of $\sim$100. AO 0235+16 has been suggested as a favored candidate for microlensing events as one possible explanation

for the observed rapid variability. Investigations of the regions around AO 0235+16 have revealed the presence of multiple absorption line systems in its spectrum (Webb et al. 2000). The results from these studies have been inconclusive, but it appears that while microlensing may contribute to variations in the light curve, it cannot account for all observed variability (Raiteri et al. 2007).

4.1.2 Observations

The large range in observed variability of AO 0235+16 is apparent in Figure 4.2. Changes in brightness are very rapid, with multiple outbursts occurring in both older archival data and the more recent data obtained by the PEGA group. The historical maximum for the object is near R=13, while at low flux levels the object can be as faint as R≈19.

Figure 4.3 displays the archival data for AO 0235+16 obtained through a literature search. Over more than a decade, there are no linear trends apparent in the mean brightness of the object. However, numerous rapid outbursts and dips occur on year-like timescales, such as those detected near 1975, 1979, and 1987.

Recent data obtained by the PEGA group (Figure 4.4) do not provide light curves which are as well sampled as those produced by the archival data, but they still display behavior similar to that seen in earlier decades. As an example, a large amplitude flare captured during 2006-2007 is visible toward the end of the light curve. During this flare, the object brightened from R∼19 to R∼14.5 over approximately 6 months.

The leading rise of the 2006-2007 flare is seen in detail in Figure 4.5. The rise

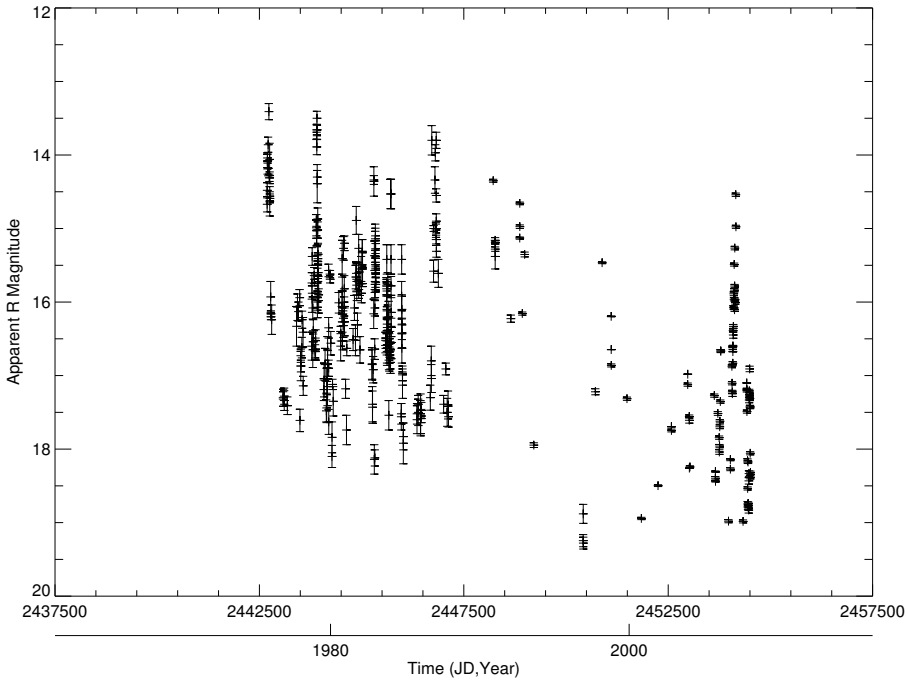

Figure. 4.2: Complete light curve for 0235+164 (AO 0235+16) binned at 1 day intervals.

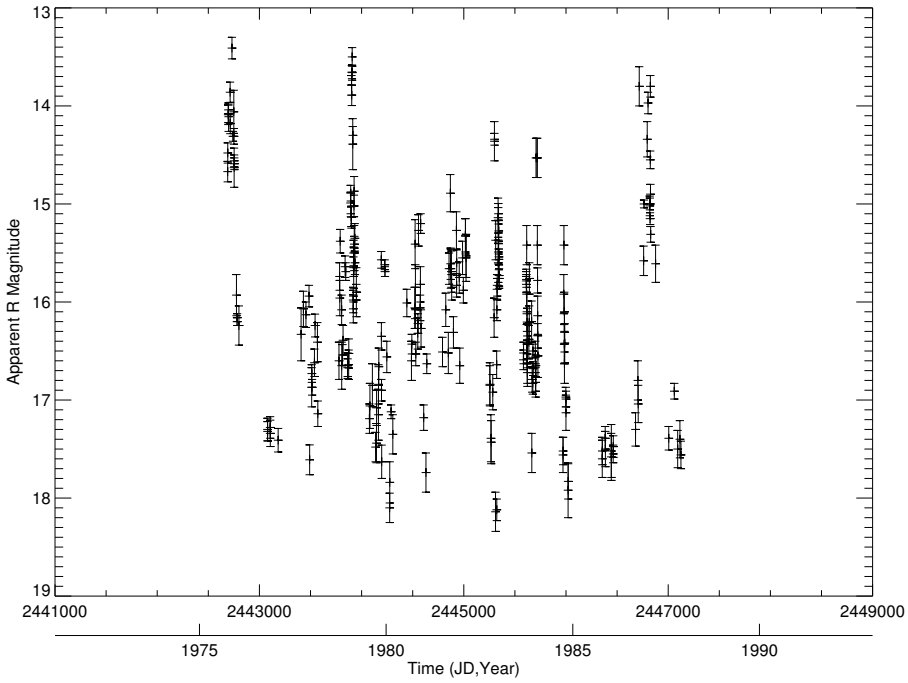

Figure. 4.3: Long term light curve for 0235+164 (AO 0235+16) binned at 1 day intervals.

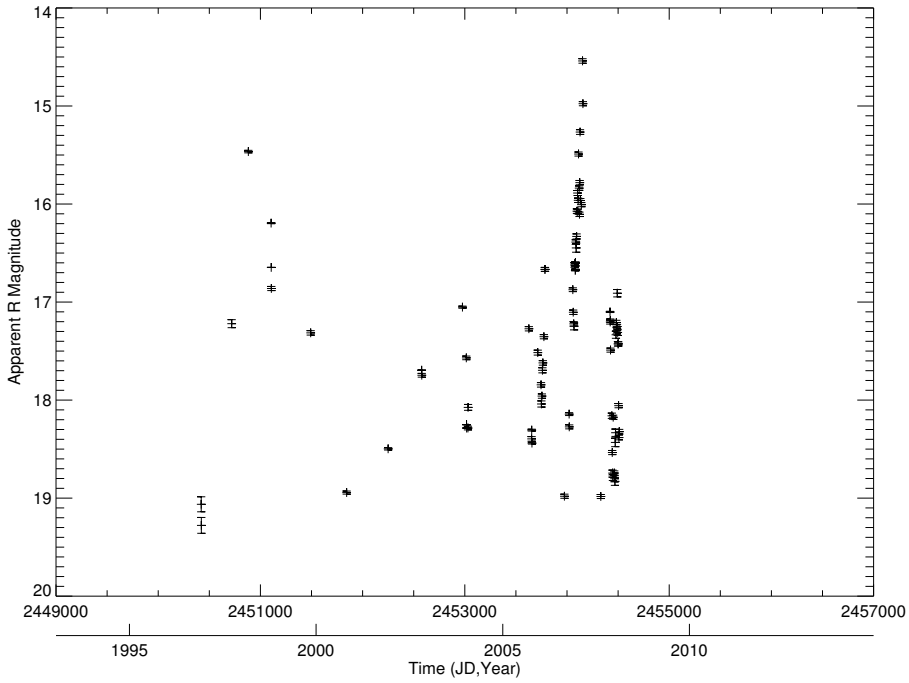

Figure. 4.4: Long term light curve for 0235+164 (AO 0235+16) binned at 1 day intervals.

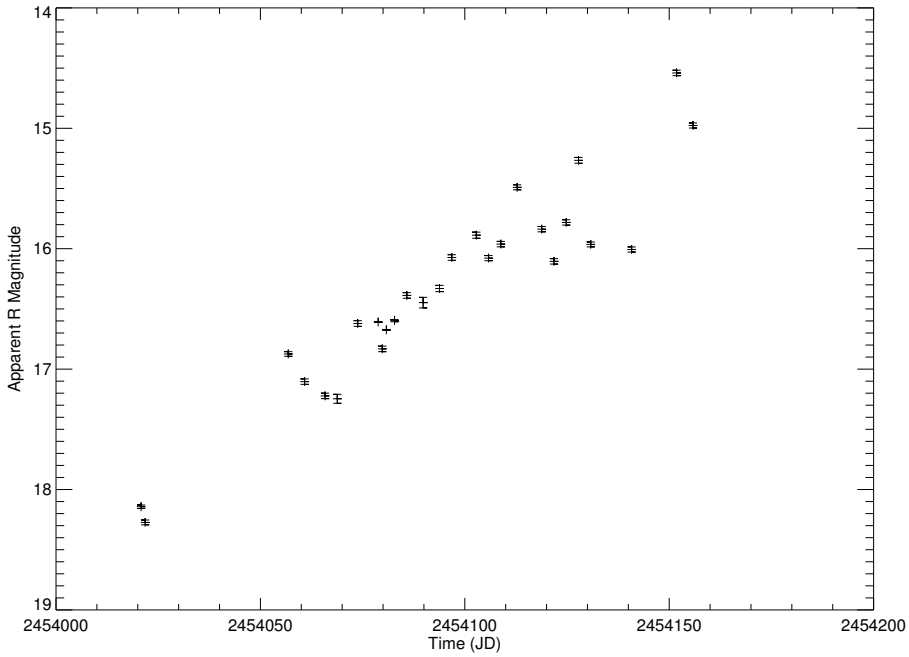

Figure. 4.5: Medium term light curve for 0235+164 (AO 0235+16) binned at 1 day intervals.

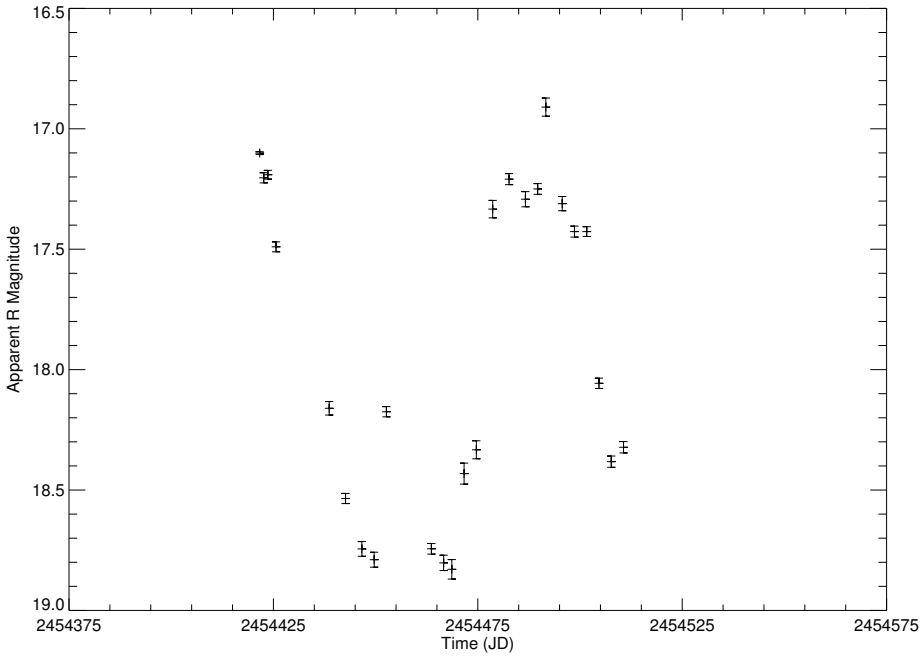

Figure. 4.6: Medium term light curve for 0235+164 (AO 0235+16) binned at 1 day intervals.

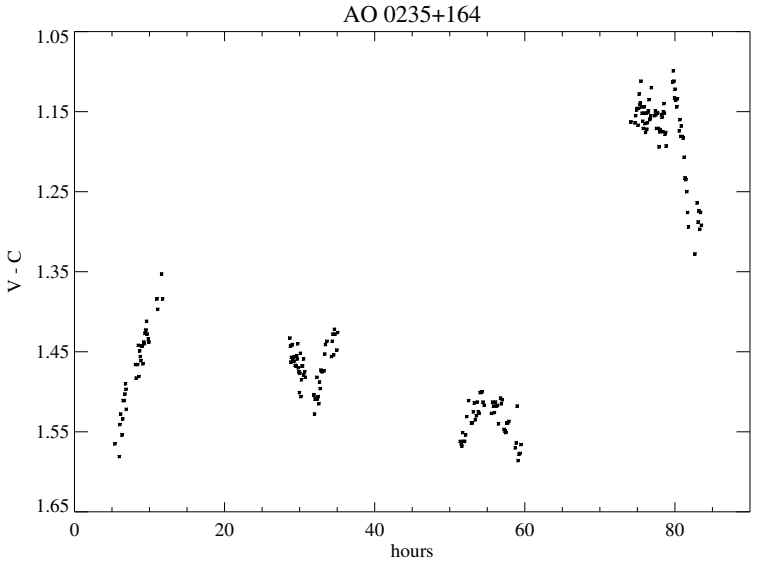

Figure. 4.7: Short term light curve for 0235+164 (AO 0235+16) binned at ∼7 minute intervals (Noble 1995).

is generally smooth and approximately linear (in magnitude), though there is some evidence of smaller amplitude variability near JD2454060 and JD2454115.

Figure 4.6 displays the SMARTS light curve from the 2007-2008 observing season. AO 0235+16 returned to a relatively low state during this time period, but remained highly variable. After an initial dip from R$\sim$17 to R$\sim$19, a large symmetric flare occurs with equal amplitude to the preceding dip. The timescale for the two magnitude flare is on the order of 50 days.

AO 0235+16 has displayed large amplitude microvariability on occasions, as shown in Figure 4.7 from Noble (1995). Over four nights of observation, the object varied by $\sim$0.4 magnitudes, including a rapid rise during the first night and sharp decline on the final night. Microvariability observations of AO 0235+16 over the past decade have not shown variability near the amplitude of those observations.

4.2 0430+052 (3C 120)

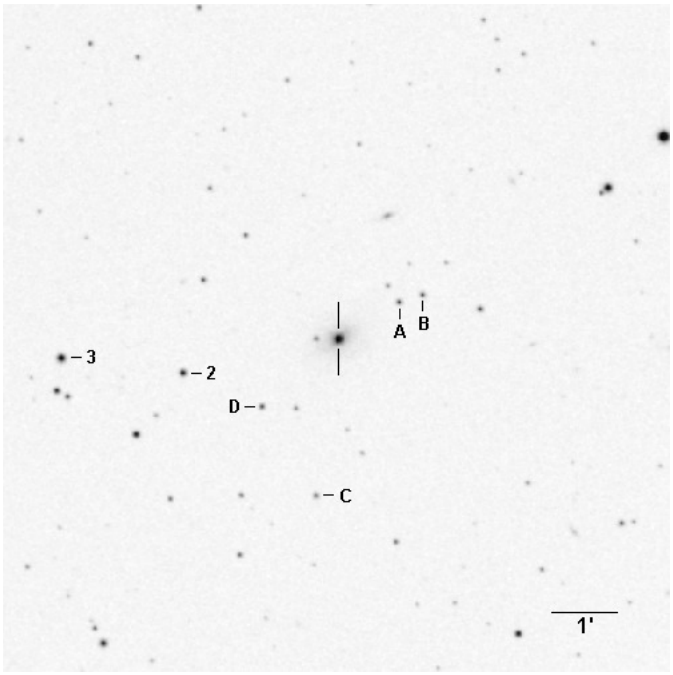

Figure. 4.8: Field of view of 3C 120 (target marked by lines, check stars by number or letter).

4.2.1 Background

The object 3C 120 is one of the most interesting objects included in the sample, due mainly to the characteristics that it shares with different types of AGN. It is nearby (z=0.033), relatively bright (R∼14), and the host galaxy is prominently visible, as seen in Figure 4.8. The host galaxy is not well organized, but exhibits some evidence of a weak spiral structure (Moles et al. 1988). The presence of strong emission lines places 3C 120 in the category of broad line radio galaxies, with many of the features in the spectrum, seen in Figure 4.9, appearing similar to that of a Seyfert 1 galaxy

(Burbidge 1967). A superluminal jet was observed at radio wavelengths for 3C 120 (Harris et al. 2004), with many ejections detected, similar to the behavior seen in blazars.

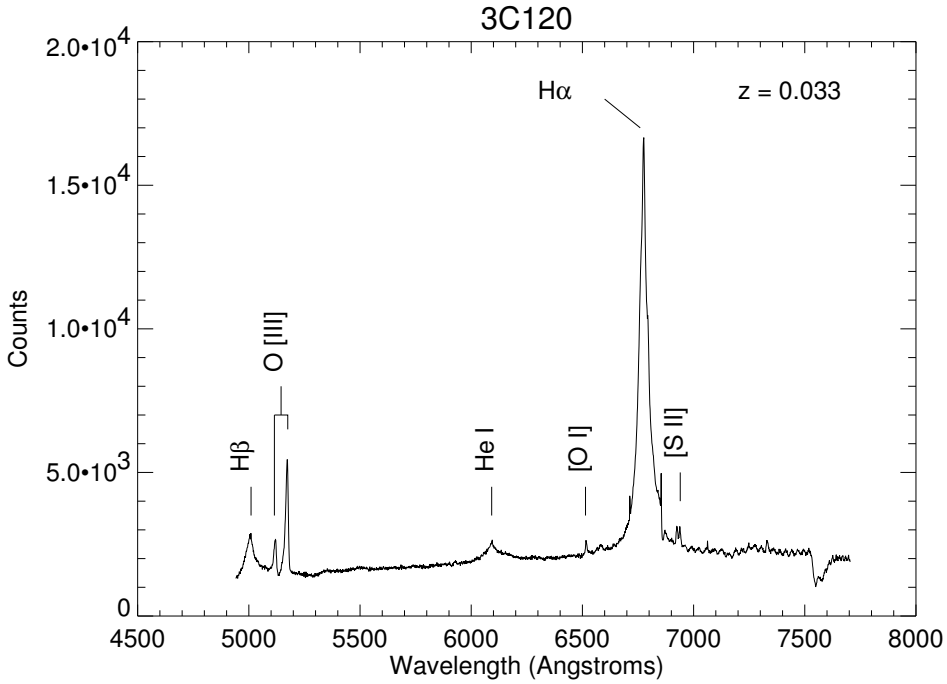

Figure. 4.9: Optical spectrum of 3C 120 obtained with the grism spectrograph at the Perkins Telescope with the PRISM instrument.

3C 120 is also bright and variable in x-rays (Maraschi et al. 1991), and has been the focus of several multiwavelength AGN campaigns. One of these studies monitored the ejection of new blobs of material in the well-studied radio jet and their observed correlations with dips in the x-ray light curve (Marscher et al. 2002). As described in Marscher et al. (2002), these studies suggest a connection between processes probably related to the accretion disk (x-ray emission), and the relativistic jet in 3C 120. The wide range of observed characteristics make 3C 120 an ideal testbed for investigating

these types of phenomena.

4.2.2 Observations

The complete light curve for 3C 120 can be seen in Figure 4.10. The variability seen in the first half of this plot led many researchers to search for possible periodicities. However, optical variations of the object since that time do not confirm the presence of any stable periodicity. Despite being embedded in a bright host galaxy, 3C 120 still exhibits relatively large optical variations, varying by $\sim$1.5 magnitudes over a 40 year period.

Figure 4.11 displays the variations observed by Webb et al. (1988) from the early 1970's to mid 1980's. Although the overall shape of the light curve appears quasi-sinusoidal, with a symmetric trough surrounded by two peaks, this pattern is not repeated in other archival data or the data obtained in the past 20 years.

The most recent 20 years of data obtained by the PEGA group, shown in Figure 4.12, do not display the same large, distinct peaks as the archival data. In general, the variations are smaller in amplitude and shorter in timescale. The overall variability does not exceed one magnitude.

On timescales of months, 3C 120 displays modest variability with amplitudes of a few tenths of a magnitude. Figure 4.13 displays an initial gradual decline followed by a small event with an amplitude of 0.2 magnitudes over a one year period. In a single observing season (Figure 4.14), a rise and decline of $\sim$0.3 magnitudes is followed by another gradual rise to R$<$14.2.

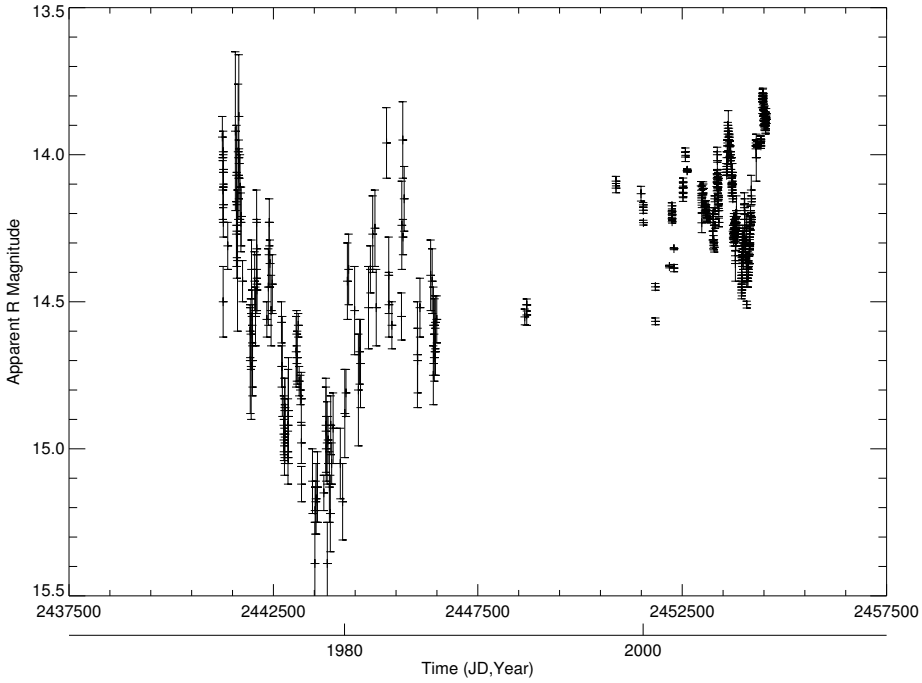

Figure. 4.10: Complete light curve for 0430+052 (3C 120) binned at 1 day intervals.

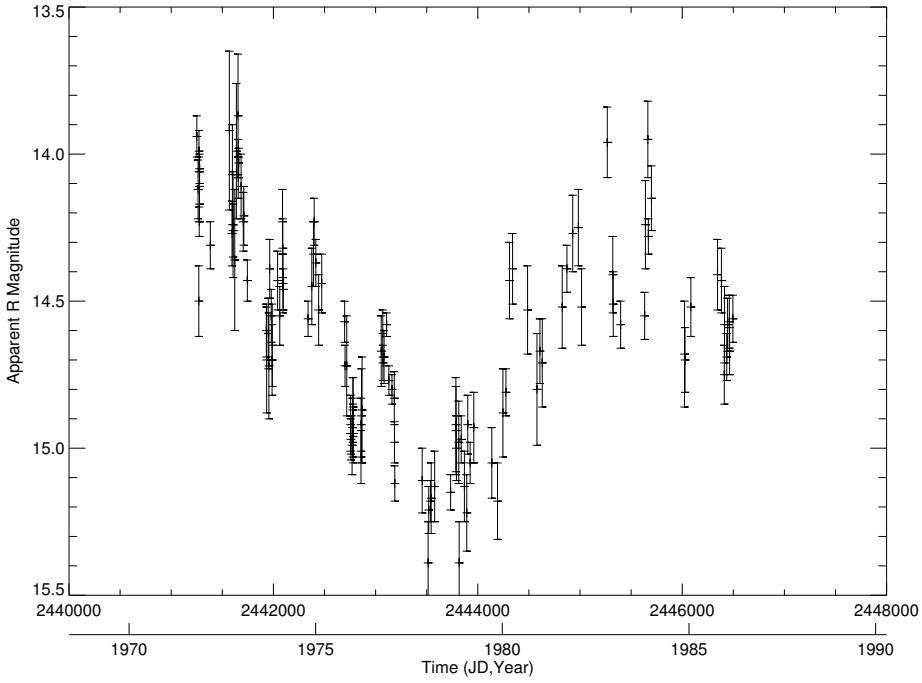

Figure. 4.11: Long term light curve for 0430+052 (3C 120) binned at 1 day intervals.

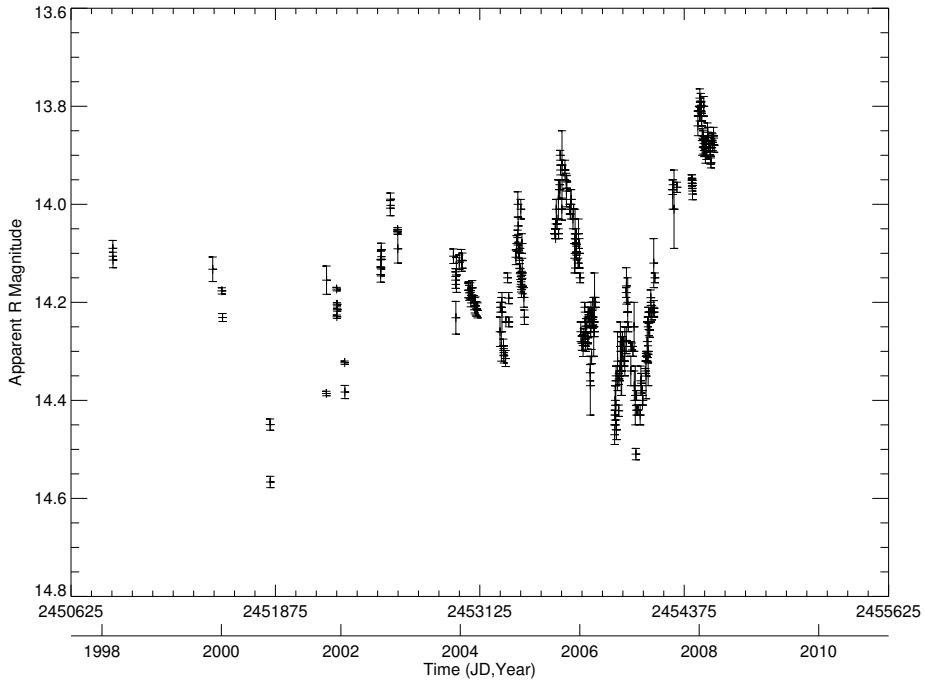

Figure. 4.12: Long term light curve for 0430+052 (3C 120) binned at 1 day intervals.

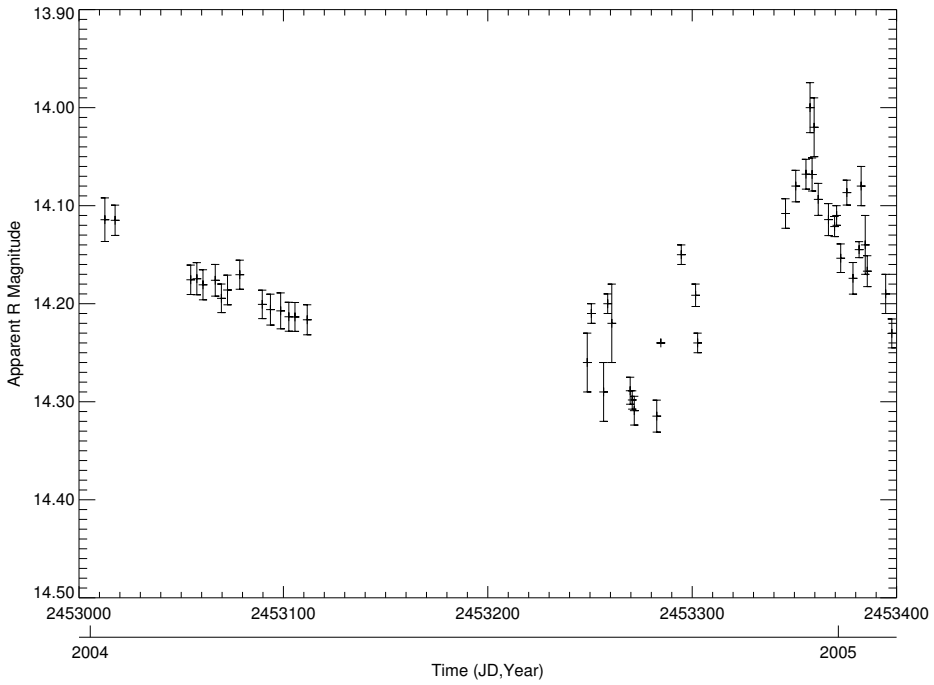

Figure. 4.13: Medium term light curve for 0430+052 (3C 120) binned at 1 day intervals.

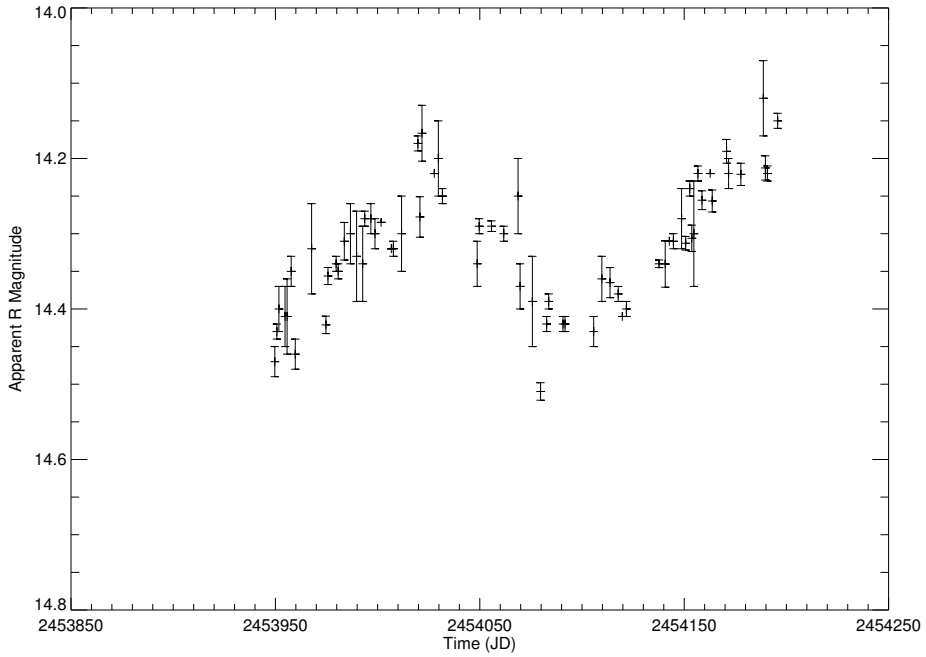

Figure. 4.14: Medium term light curve for 0430+052 (3C 120) binned at 1 day intervals.

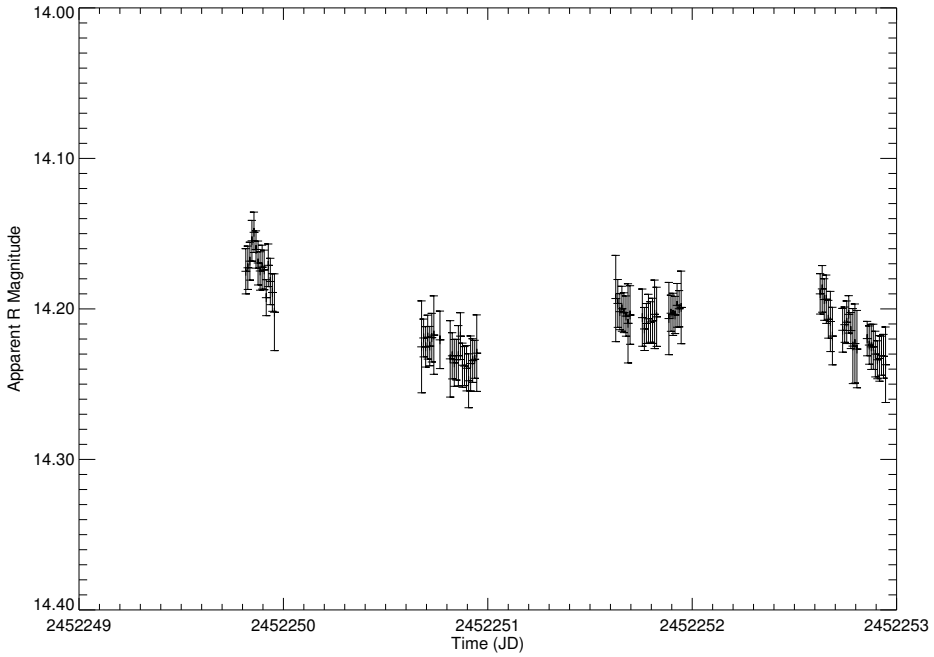

Figure. 4.15: Short term light curve for 0430+052 (3C 120) binned at ∼15 minute intervals.

In terms of microvariability, 3C 120 has exhibited some rapid changes in the course of a single night. Figure 4.15 displays the light curve of 3C 120 over 4 nights. Variations on the order of one tenth of a magnitude are detected over the entire time span, with some evidence of smaller amplitude variability on shorter timescales.

4.3 0735+178 (PKS 0735+178)

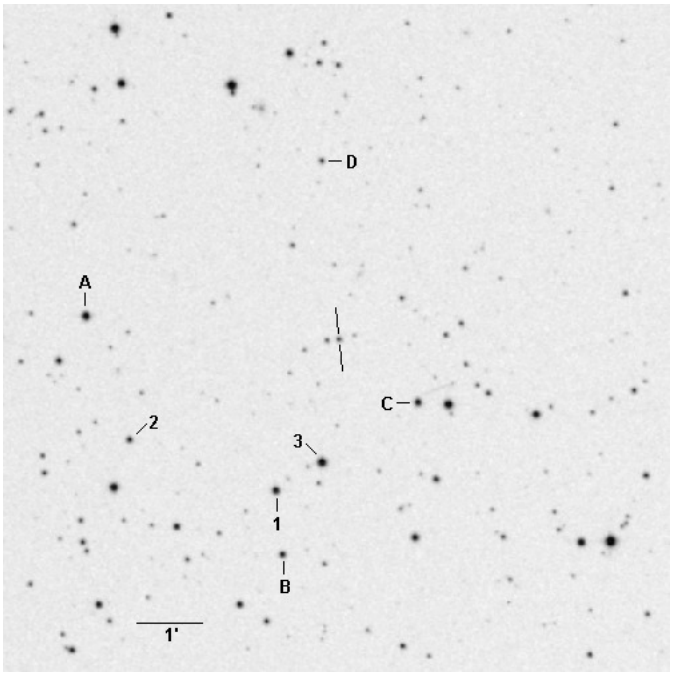

Figure. 4.16: Field of view of PKS 0735+178 (target marked by lines, check stars by number or letter).

4.3.1 Background

The field of view for PKS 0735+178 can be seen in Figure 4.16. The optical counterpart to the radio source was discovered by Blake (1970) and found to be variable by Wing (1973). Carswell et al. (1974) first identified PKS 0735+178 as a BL Lac object based on the absence of discrete features in its spectrum and the presence of a high degree of polarization. As one of the earliest identified BL Lac objects, PKS 0735+178 has been monitored consistently in the radio and optical since the 1960's. It is variable at radio (Teräsranta et al. 2004), optical (Ciprini et al. 2007), and x-

ray (Lamer et al. 1996) wavelengths, but shows little evidence of radio to optical correlation (Clements et al. 1995).

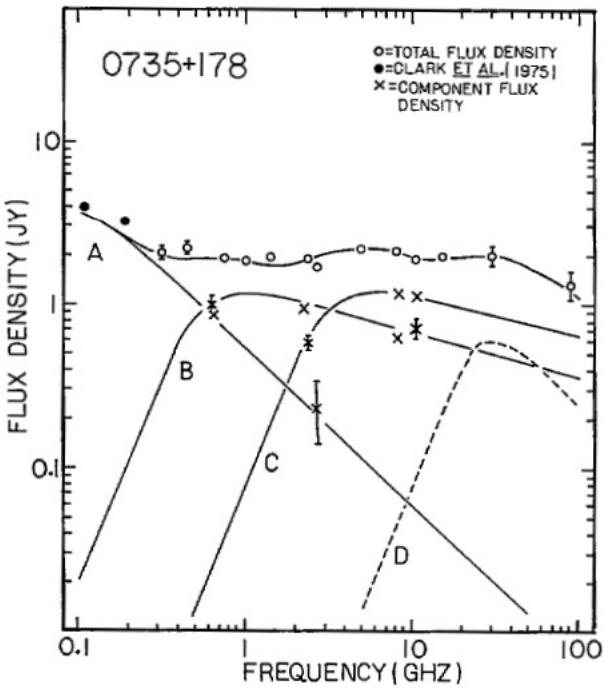

Figure. 4.17: Model fit of multiple synchrotron components in PKS 0735+178 used to explain the extremely flat radio spectrum (Cotton et al. 1980).

The VLBI jet of PKS 0735+178 displays emission of components over time, similar to many other BL Lac objects, and there is evidence that the direction of the jet nozzle has changed significantly over time (Baath 1984). PKS 0735+178 has an exceptionally flat radio spectrum leading to debate over the physical interpretation. Cotton et al. (1980) used VLBI imaging to show that the flatness is most likely attributable to the superposition of multiple synchrotron components in the jet (Figure 4.17) as opposed to a single broad synchrotron peak. These observations are in agreement with the models proposed in Marscher (1977).

4.3.2 Observations

The long term light curve of PKS 0735+178 is displayed in Figure 4.18. The mean magnitude over this ∼20 year period is slightly fainter than R=15. Multiple outbursts have reached R∼14 over the past 20 years. In the past five years, the object has been undergoing a steady decline with rapid, smaller amplitude variability superposed on that decline.

The amplitude of variability on monthly timescales is modest for PKS 0735+178. Figure 4.19 displays the light curve of the object over a 4 month period. Activity includes a decline from R∼14.0 to R∼14.5, followed by a small peak near JD2445410.

PKS 0735+178 also displays modest variability on timescales of approximately one week. An overall change in brightness of more than 0.2 magnitudes is seen in Figure 4.20.

Despite numerous observing runs devoted to microvariability observations of PKS 0735+178, the object rarely displayed variations of more than a tenth of a magnitude in a single night. An example of its steady brightness during a two hour period during a single night is shown in Figure 4.21.

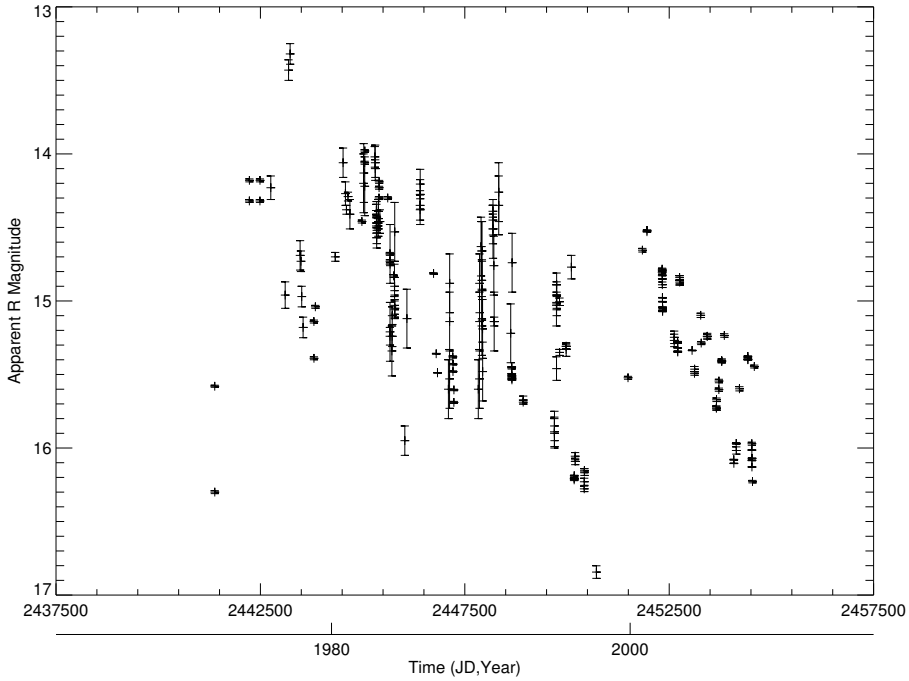

Figure. 4.18: Complete light curve for 0735+178 (PKS 0735+178) binned at 1 day intervals.

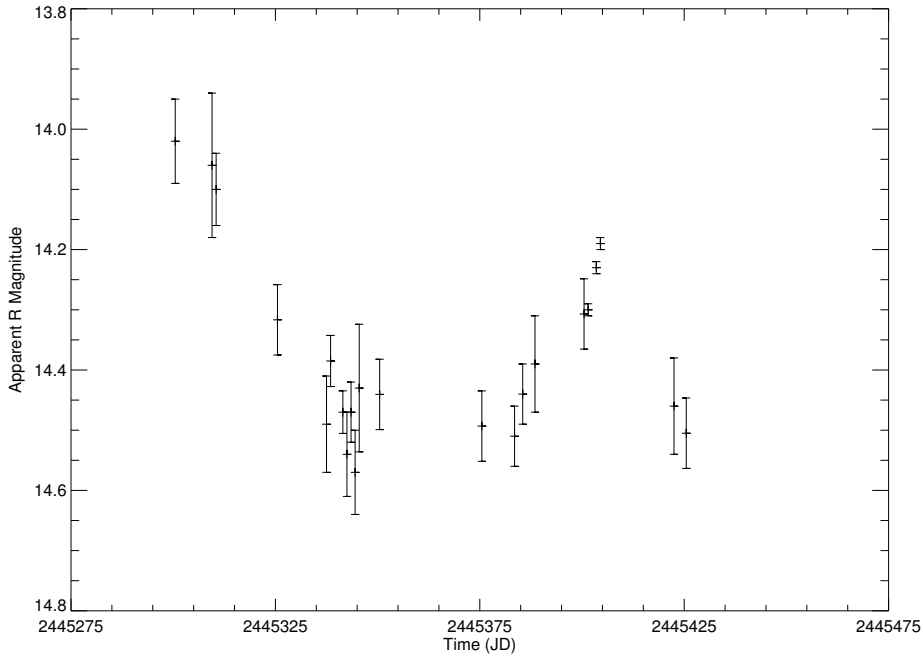

Figure. 4.19: Medium term light curve for 0735+178 (PKS 0735+178) binned at 1 day intervals.

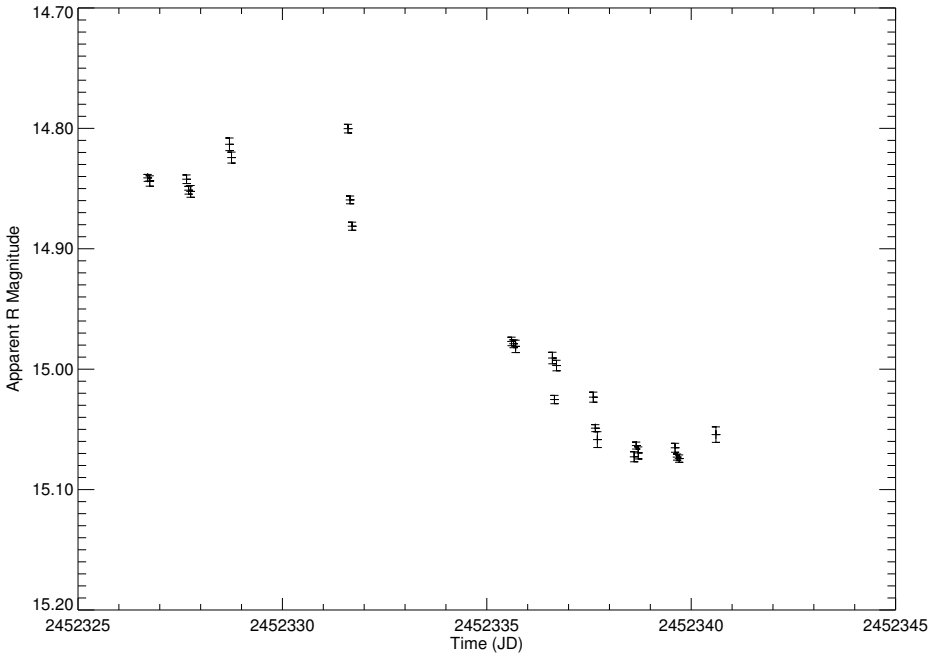

Figure. 4.20: Short term light curve for 0735+178 (PKS 0735+178) binned at 1 hour intervals.

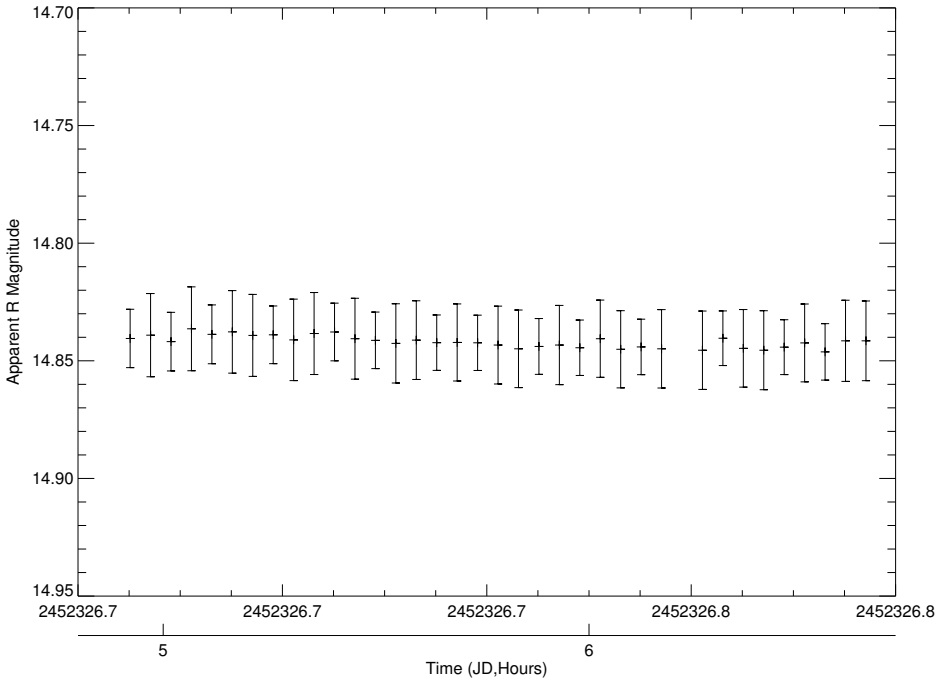

Figure. 4.21: Microvariability light curve for 0735+178 (PKS 0735+178) binned at 3 minute intervals.

4.4 0851+203 (OJ 287)

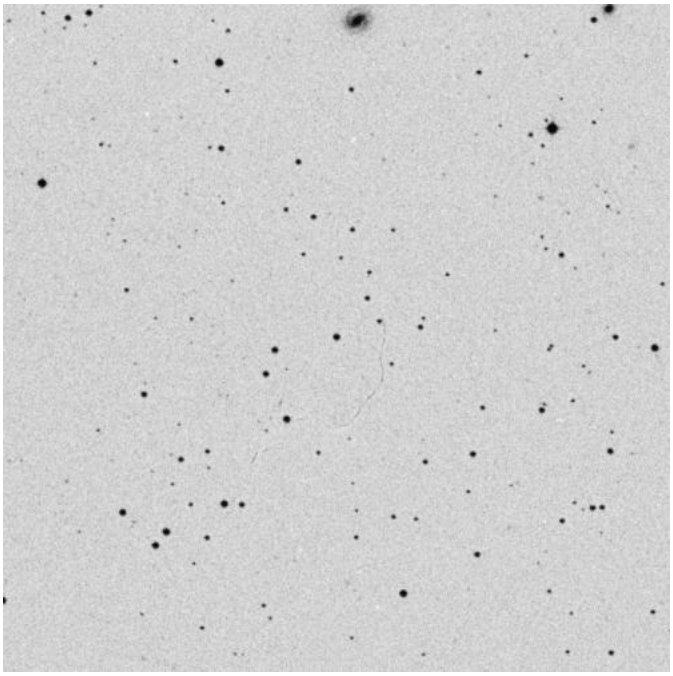

Figure. 4.22: Field of view of OJ 287. Taken from http://www.lsw.uni-heidelberg.de/projects/extragalactic/charts/.

4.4.1 Background

OJ 287 (finder chart shown in Figure 4.22) is historically one of the best observed blazars. Archival photographic plate searches have supplied data on this object dating to before 1900. Figure 4.23 displays one such compilation from Sillanpää et al. (1988). The object was discovered as part of the Ohio radio survey (Kraus et al. 1968), with its optical counterpart found shortly thereafter (Thompson et al. 1968).

OJ 287, like most blazars, is seen to possess a relativistic jet when observed at radio wavelengths (Jorstad et al. 2005). Multiple studies have shown a well defined

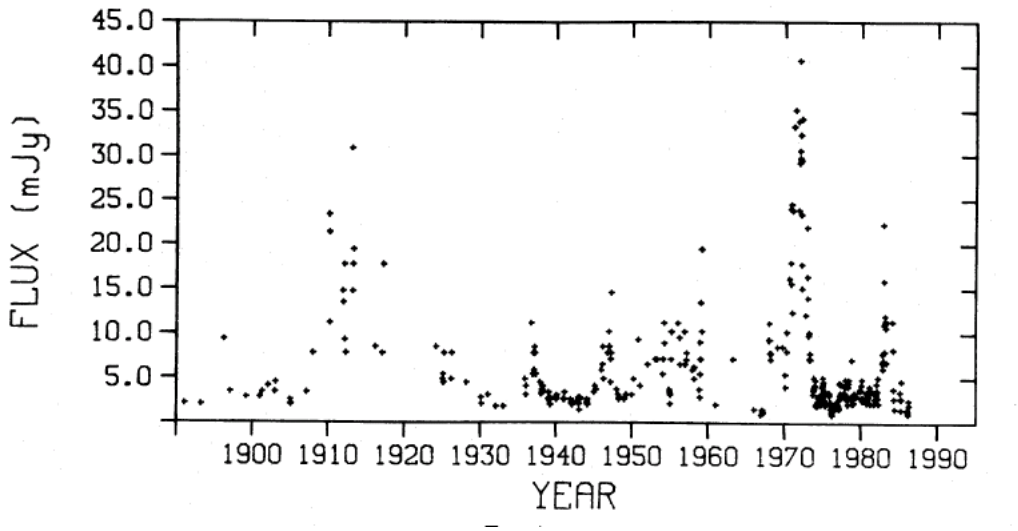

Figure. 4.23: Archival light curve of OJ 287 taken from a variety of sources (Sillanpää et al. 1988).

correlation between radio and optical events on timescales of a month or longer (Pomphrey et al. 1976; Balonek 1982). The object is prone to multiple distinct outbursts, on the order of a decade, that allow for distinct events to be compared at different wavelengths (Usher 1979).

The primary interest for many studies, however, is the possible periodicity of the long term light curve. As seen in Figure 4.23, the repeated outbursts of OJ 287 appear to occur at regularly spaced intervals. One possible explanation is the presence of a binary pair of supermassive black holes at the center of OJ 287 (Sillanpää et al. 1988). The argument for a binary supermassive black hole system is strengthened by observations of interaction between normal galaxies. Assuming AGN activity can be fueled by mergers of normal galaxies, there should be a small fraction of AGN that possess a binary supermassive black hole at their core.

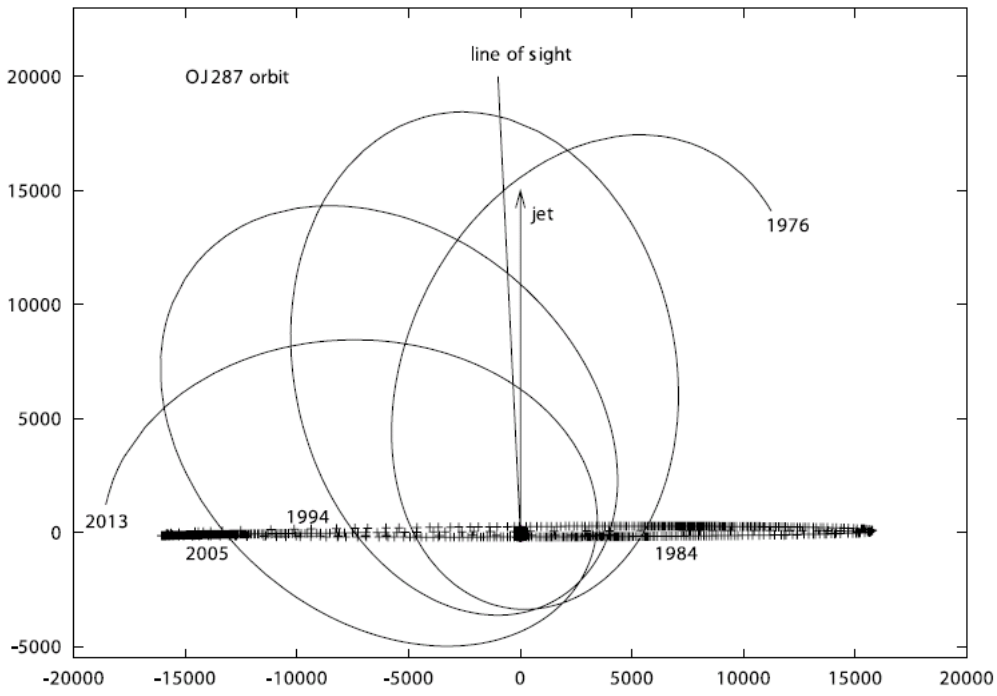

Figure. 4.24: A model for a binary black hole system in OJ 287. The primary is located at the origin with the secondary following the elliptical path of the solid line. Dates of passage through the accretion disk of the primary (crosses) are marked (Valtonen 2007).

The proposed binary model explains the large outbursts in OJ 287 through the smaller, secondary black hole's interaction with the accretion disk of the larger primary (Valtonen 2007). As shown in Figure 4.24, the orbit of the secondary is such that it passes through the accretion disk of the primary at regular intervals of roughly $\sim$11 years. These models provide a surprisingly accurate fit to the data and have even been used to test the effects of energy loss through gravitation radiation in the system (Valtonen et al. 2008).

4.4.2 Observations

The complete light curve of OJ 287, seen in Figure 4.25, is the longest in this sample. Unfortunately, due to extremely poor sampling, only the latter half of this light curve is used for time series analysis. The average magnitude of OJ 287 over the last century is near R=14.8, with large deviations both above (R$\sim$12) and below (R$\sim$17) the mean value. Multiple sharp outbursts are also visible at regular intervals in support of the 11-12 year periodicity.

Figure 4.26 provides a better assessment of the well sampled data from the past 30 years. The two large outbursts at the beginning of this light curve show a double peaked structure, with a secondary peak at a slightly smaller amplitude. The two outbursts in the second half of the light curve do not reach the same magnitude as those earlier, but there is some indication of a double peak structure in the latest flare of 2007-2008.

The outburst of 2007-2008 can be seen in detail in Figure 4.27. This flare was anticipated via the 11-12 year periodicity and predictions of the binary SMBH models. During the 2007 season, a steady rise from R$\sim$15.5 to R$\sim$14.0 marks the beginning of the flare. It is impossible to know the peak value of this flare as observations were interrupted when OJ 287 was too close to the sun. It is possible that the peak seen during the 2008 season is the secondary peak of a much larger, unobserved flare.

Figure 4.28 shows a close inspection of the rise during the 2007 season. While the overall trend is a gradual increase in brightness, it is evident that smaller events take

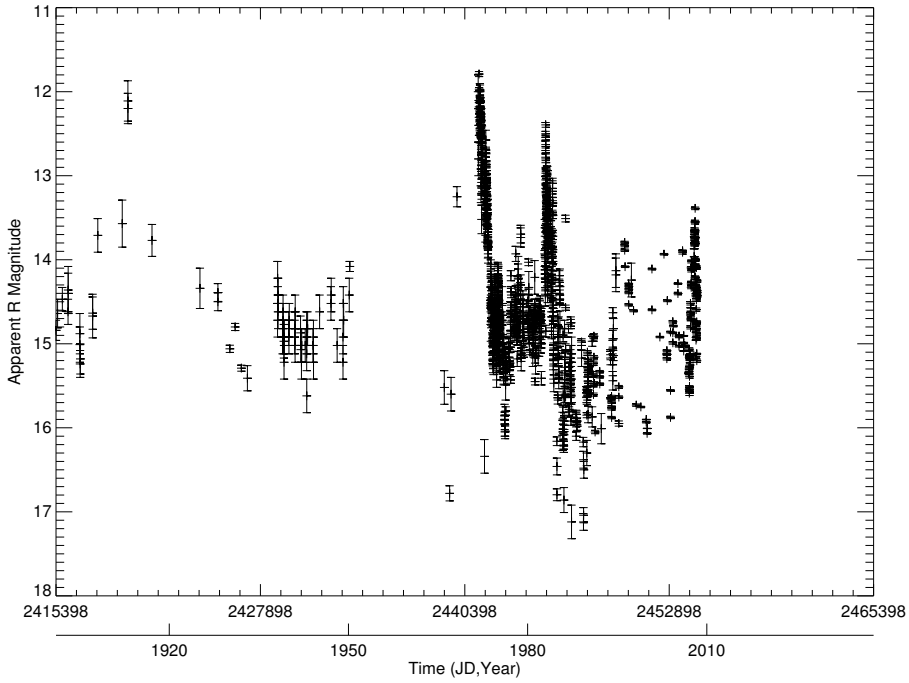

Figure. 4.25: Complete light curve for 0851+203 (OJ 287) binned at 1 day intervals.

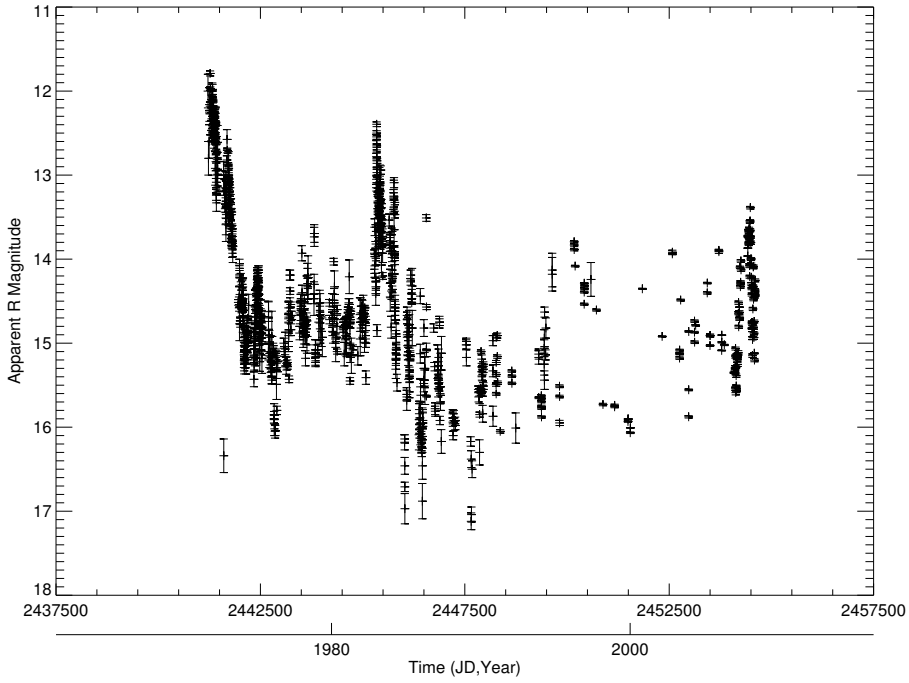

Figure. 4.26: Long term light curve for 0851+203 (OJ 287) binned at 1 day intervals.

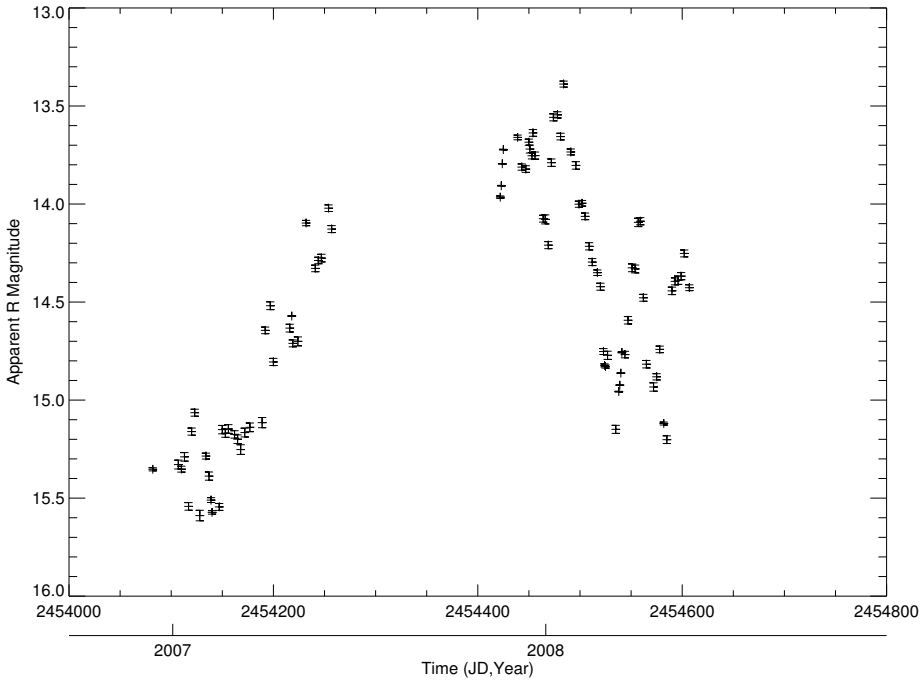

Figure. 4.27: Medium term light curve for 0851+203 (OJ 287) binned at 1 day intervals.

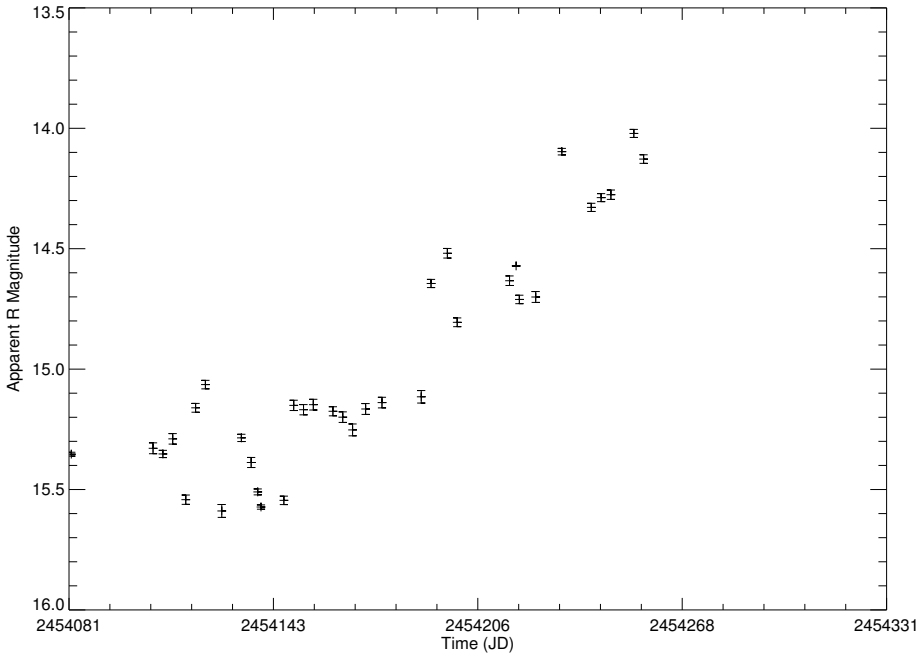

Figure. 4.28: Medium term light curve for 0851+203 (OJ 287) binned at 1 day intervals.

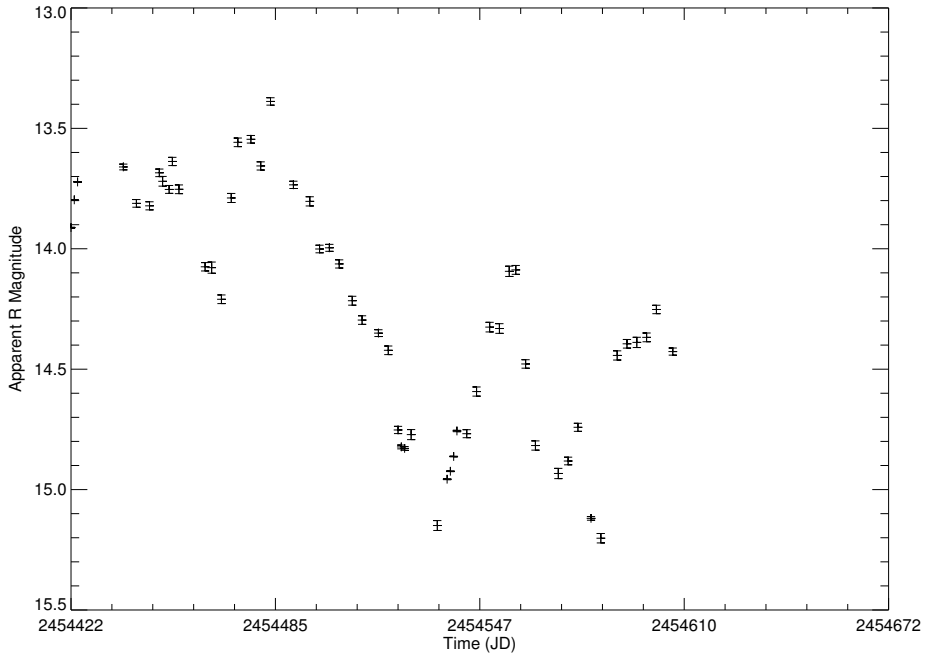

Figure. 4.29: Medium term light curve for 0851+203 (OJ 287) binned at 1 day intervals.

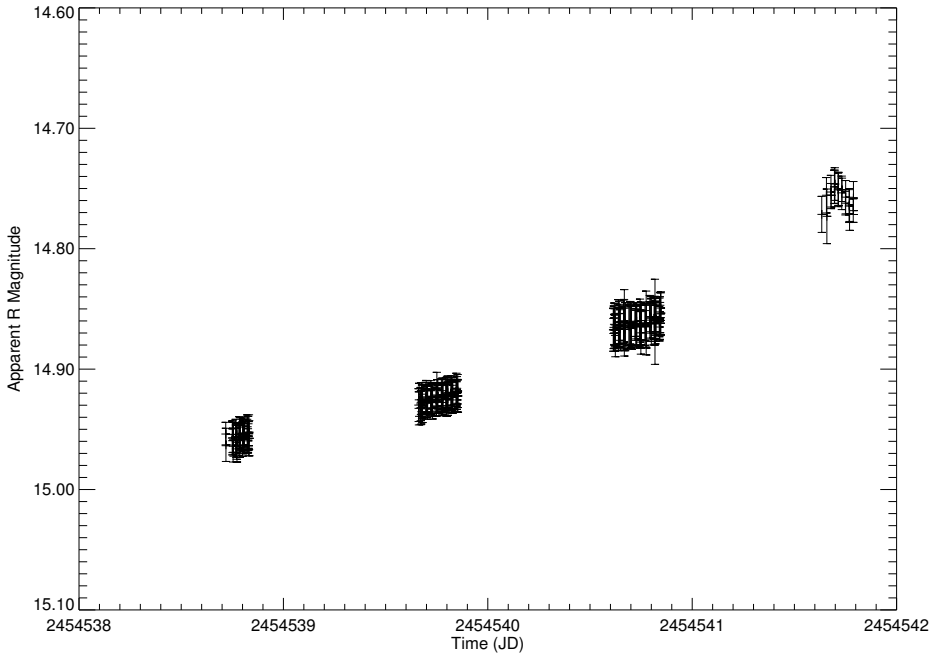

Figure. 4.30: Short term light curve for 0851+203 (OJ 287) binned at ∼15 minute intervals.

place at timescales less than the sampling interval of $\sim$3 days.

The overall decline in the recent outburst is seen in Figure 4.29. Smaller scale events are better defined in this light curve, including an early peak near JD2454485 and a later, symmetric peak near JD2454555.

On timescales of less than one day, OJ 287 is relatively devoid of distinct events like those seen in other BL Lac objects. Figure 4.30 displays the best example of the short term behavior of OJ 287 during a 4 night run. While a gradual increase in brightness is evident over the four nights, the variability within each night is weak. Only on the final night is there an indication of a small amplitude event.

4.5 1253−055 (3C 279)

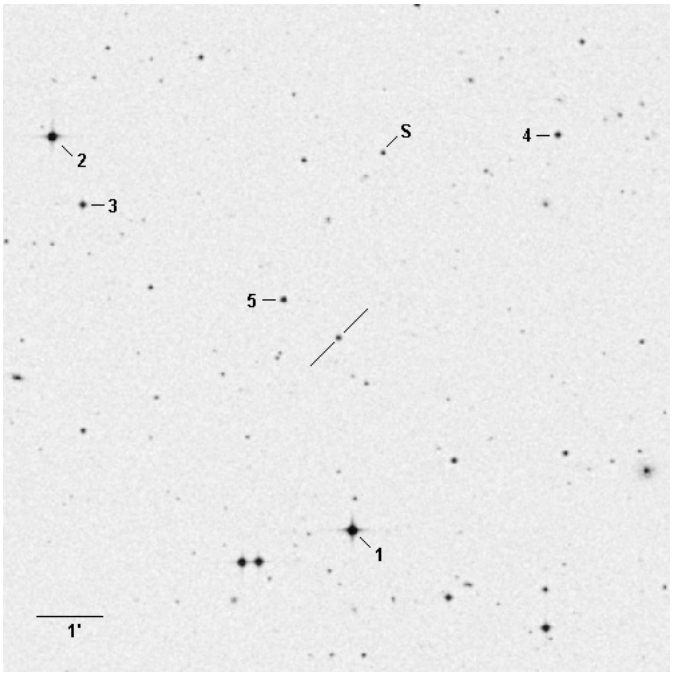

Figure. 4.31: Field of view of 3C 279 (target marked by lines, check stars by letter or number).

4.5.1 Background

The object 3C 279 is an OVV quasar and one of the brightest blazars in the optical sky. The field of view for 3C 279 can be seen in Figure 4.31. The object is highly variable from radio through gamma rays, making it a favored object of study for many multiwavelength campaigns (Netzer et al. 1994; Grandi et al. 1996; Wehrle et al. 1998). It is one of the brightest gamma ray objects in the sky and it was the first blazar to be discovered at gamma rays using the Energetic Gamma Ray Experiment Telescope (EGRET) (Hartman et al. 1992).

In the optical, 3C 279 has been through repeated high amplitude outbursts (Webb et al. 1990; Kartaltepe & Balonek 2007). The amplitude of these flares can be as great as five magnitudes and the flares were actually discovered from archival plates from the 1930's and 1940's, as seen in Figure 4.32 (Eachus & Liller 1975).

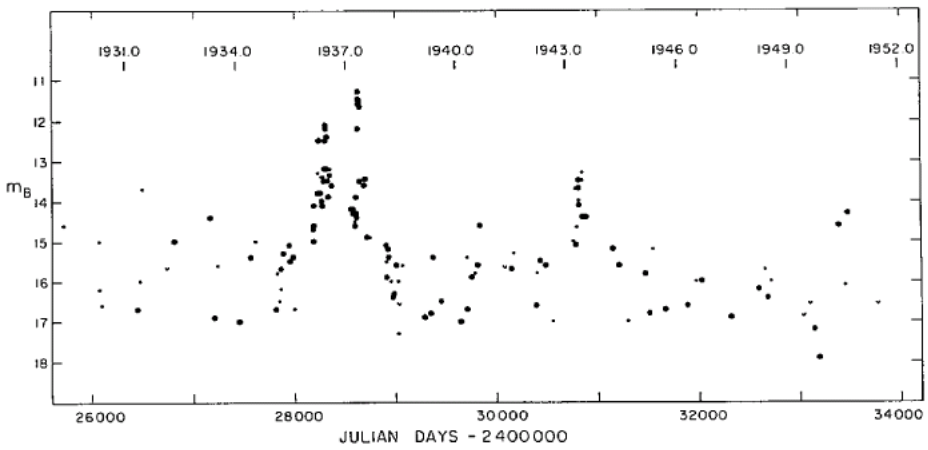

Figure. 4.32: Optical light curve of 3C 279 from archival plates displaying large amplitude flares (Eachus & Liller 1975).

3C 279 also possesses a relativistic jet seen clearly at radio wavelengths. It is the first object which was observed to display superluminal motion in the jet as seen from high resolution radio interferometry (Whitney et al. 1971; Cotton et al. 1979). Studies have shown that the optical emission is most likely produced through the synchrotron process within the relativistic jet (Marscher 1998).

4.5.2 Observations

The complete light curve for 3C 279, seen in Figure 4.33, is the shortest and most undersampled of all the light curves used in this dissertation. The early archival data

from Eachus & Liller (1975) cannot be integrated into the overall light curve without introducing very large gaps in sampling. There is also a surprising deficit of published optical data from the modern era for this object. 3C 279 is relatively bright, with an average magnitude of R$\sim$15. The object undergoes large variations in brightness. Following a large dip in 2003, 3C 279 exhibited a $\sim$5 year event with many smaller timescale, sharper flares present.

A detailed view of the 5 year event is displayed in Figure 4.34. The majority of these data were obtained through queued SMARTS observations with occasional contributions from Lowell Observatory. Ignoring the sharper flares on yearly timescales, the overall behavior of the light curve includes a gradual climb from R$\sim$17 to R$\sim$13.5, followed by a steep decline to R$\sim$16 in 2008.

The 2004 observing season, seen in Figure 4.35, displays a smoothly changing light curve with a sharp, symmetric peak near JD2453190. The variability appears smooth and continuous at the $\sim$ 3 day sampling rate.

In contrast, the 2005 observing season, seen in Figure 4.36, the variability has lost its structure and no longer appears resolved, despite being near the same flux level as during the 2004 season. It is surprising to see such a distinct change in behavior in an object on a yearly basis.

A similar, somewhat erratic pattern of variability was displayed during the first part of the 2006 observing season in Figure 4.37. The latter half of the light curve displays a consistent increase, finally flattening toward a constant level.

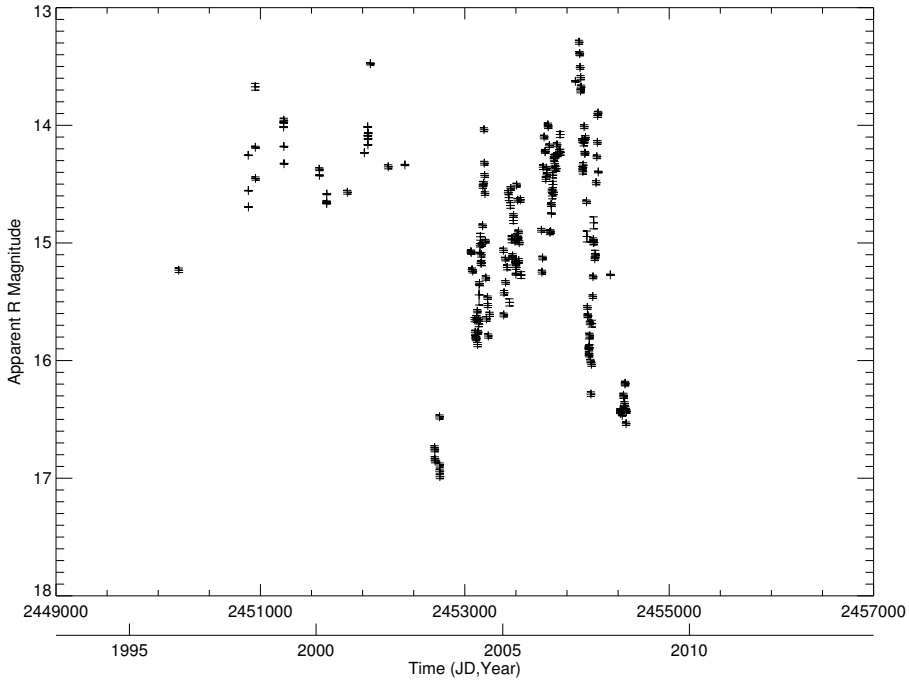

Figure. 4.33: Complete light curve for 1253−055 (3C 279) binned at 1 day intervals.

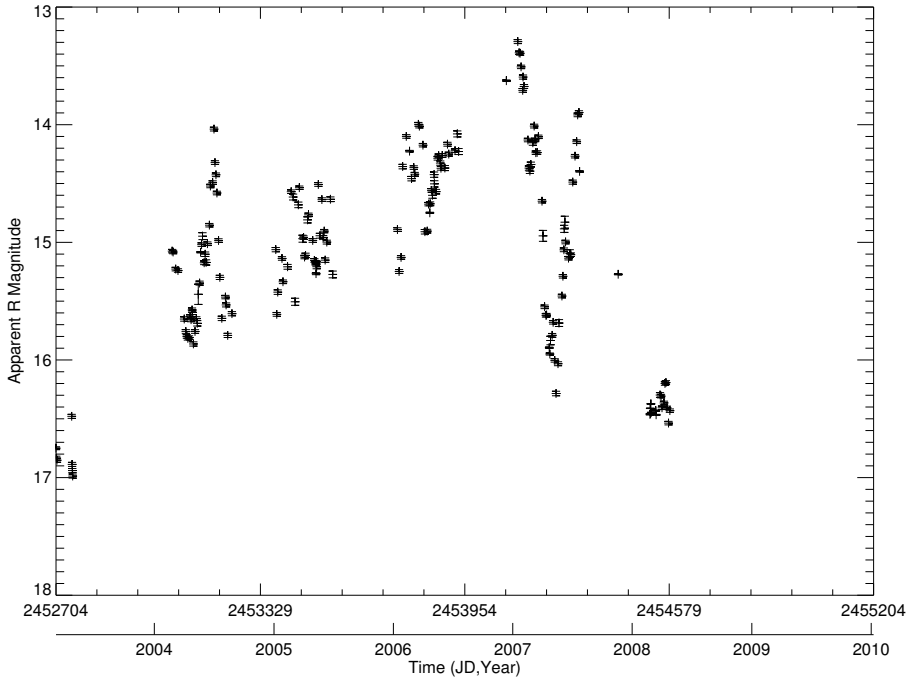

Figure. 4.34: Long term light curve for 1253−055 (3C 279) binned at 1 day intervals.

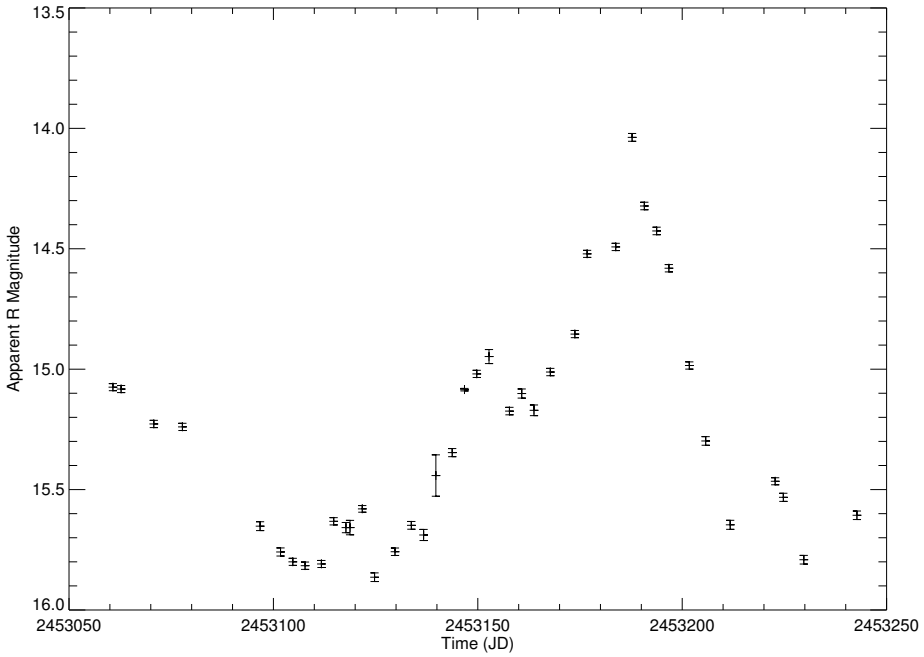

Figure. 4.35: Medium term light curve for 1253−055 (3C 279) binned at 1 day intervals.

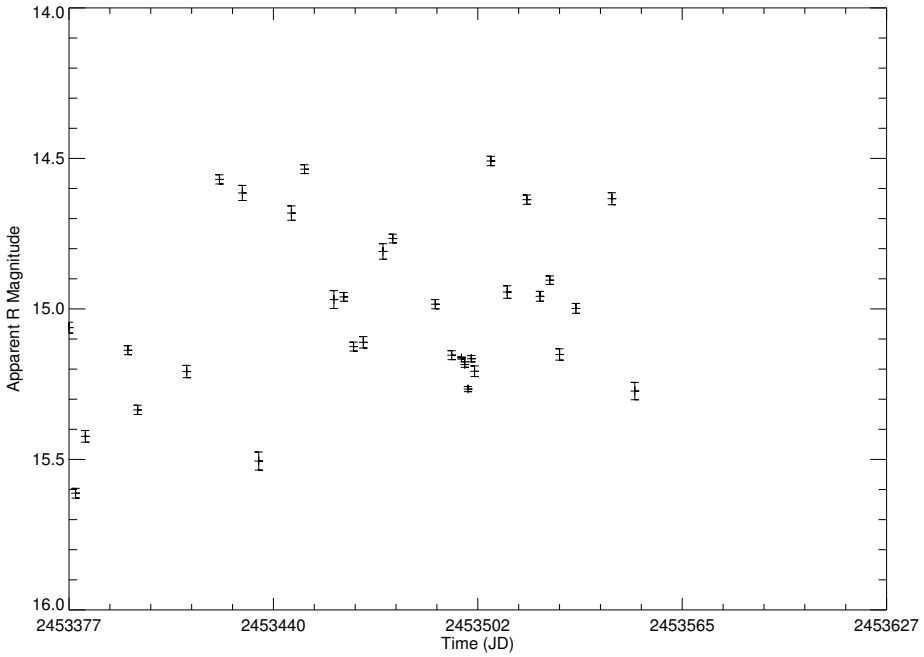

Figure. 4.36: Medium term light curve for 1253−055 (3C 279) binned at 1 day intervals.

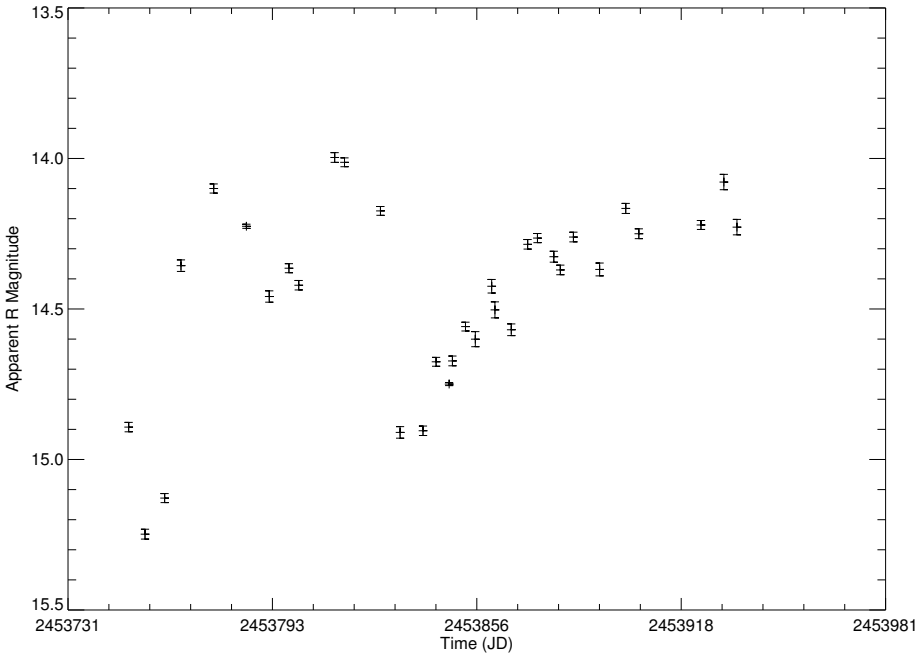

Figure. 4.37: Medium term light curve for 1253−055 (3C 279) binned at 1 day intervals.

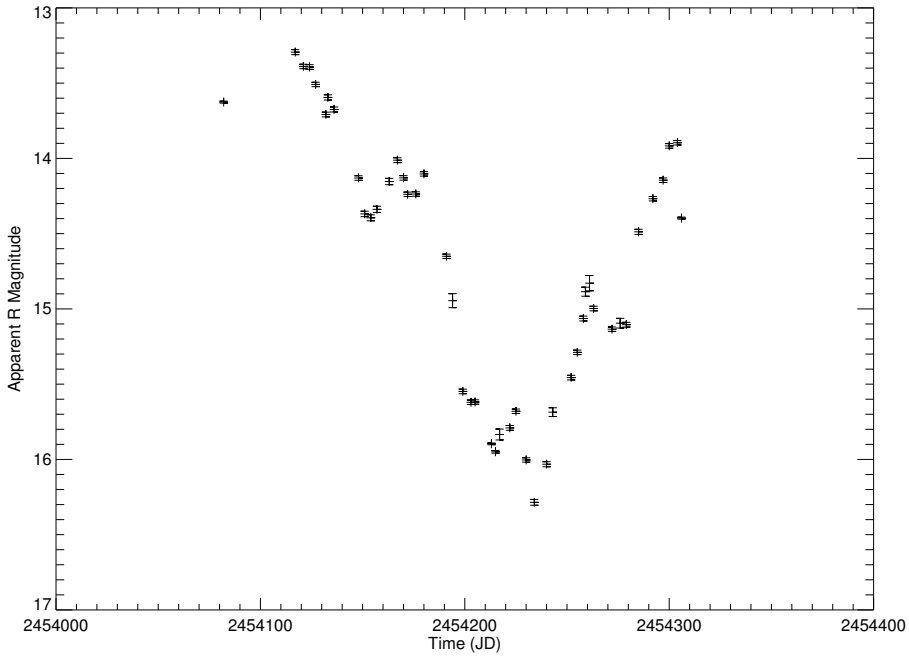

Figure. 4.38: Medium term light curve for 1253−055 (3C 279) binned at 1 day intervals.

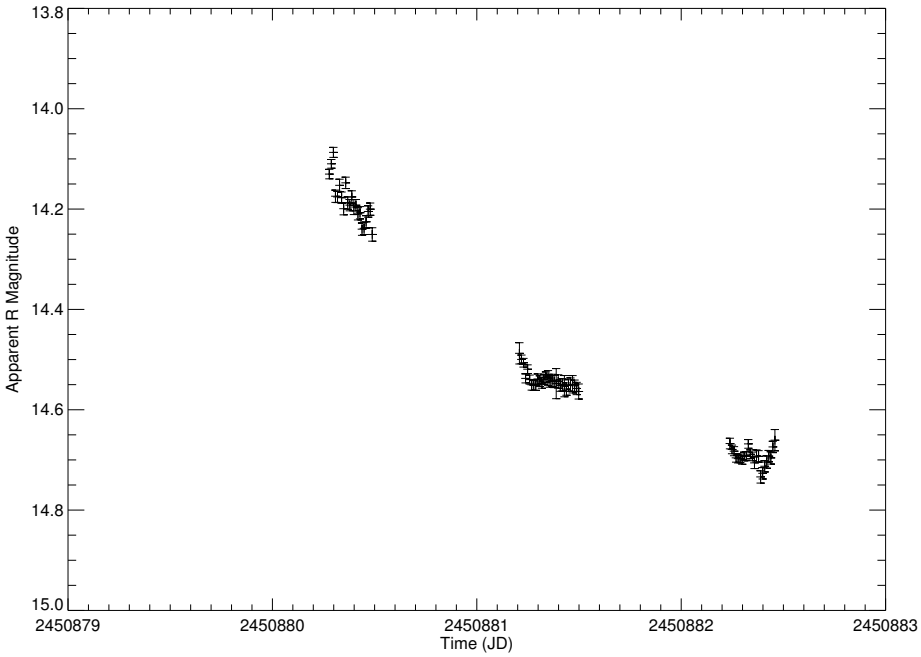

Figure. 4.39: Short term light curve for 1253−055 (3C 279) binned at $\sim$ 15 minute intervals.

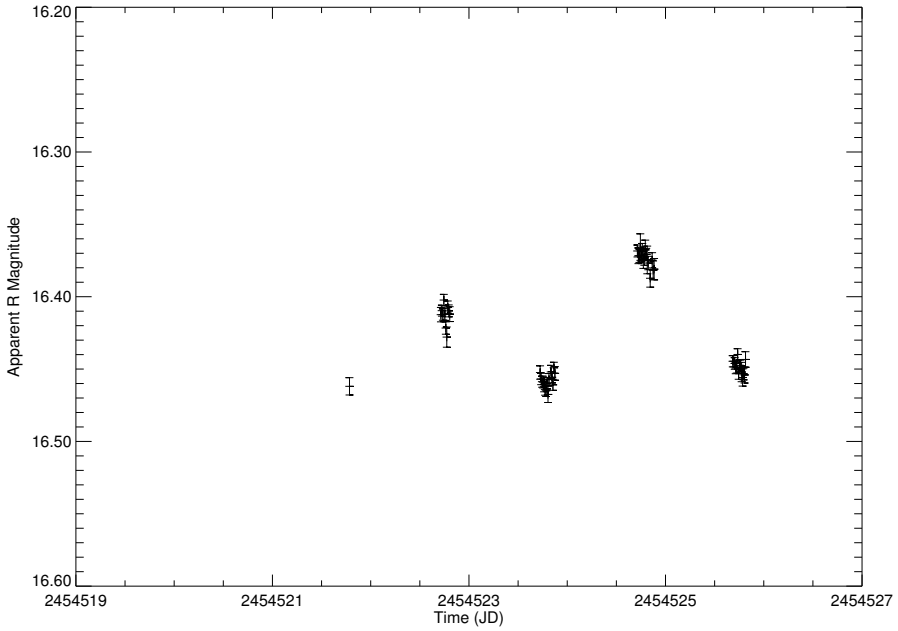

Figure. 4.40: Short term light curve for 1253−055 (3C 279) binned at $\sim$ 15 minute intervals.

The 2007 season, shown in Figure 4.38, displays similar variability to that seen in the 2004 observing season. In this case, 3C 279 was first observed at an elevated state near R$\sim$13.5, dropping quickly to R$>$16, then rising sharply again to R$<$14. Smaller events are superposed upon the longer timescale events, such as the small double flare seen around JD2454160.

On daily to intraday timescales, 3C 279 has displayed significant variability similar to that seen in BL Lac objects. Figure 4.39 shows an overall decline in brightness over three nights, during which it fell from R$\sim$14.1 to R$\sim$14.7. There is also evidence for smaller amplitude variability within each night of observation.

A four night observing run with observations of 3C 279 can be seen in Figure 4.40. While the duration of observations in a given night is not sufficient to see clear evidence of intranight variability, the object is changing in brightness significantly on daily timescales. Over the course of four nights, 3C 279 varied within a range of 0.1 magnitudes.

4.6 1510−089 (PKS 1510−089)

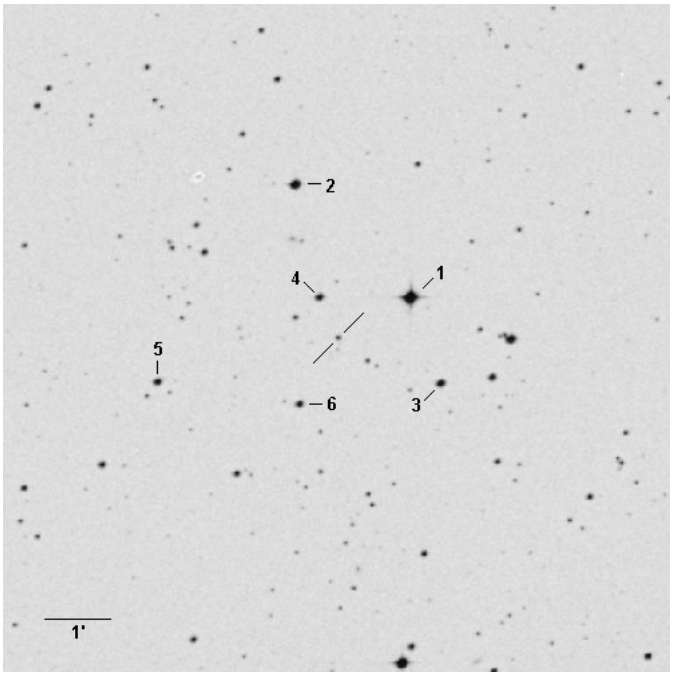

Figure. 4.41: Field of view of PKS 1510−089 (target marked by lines, check stars by letter).

4.6.1 Background

The field of view of PKS 1510−089 is shown in Figure 4.41. The redshift of PKS 1510−089 is moderate compared to other objects in the sample, at $z = 0.361$. The object is an OVV quasar, displaying the properties of a FSRQ and having a very high degree of optical polarization (Stockman et al. 1984; Hewitt & Burbidge 1993). PKS 1510−089 has a pronounced UV excess, flat x-ray spectrum, and steep gamma-ray spectrum (Hartman et al. 1999).

The parsec-scale jet of PKS 1510−089 is oriented very near to the line of sight

($\leq 3^{\circ}$) (Homan et al. 2002). The jet displays complex structure and superluminal speeds in excess of $20c$ (Homan et al. 2001).

Optical monitoring of PKS 1510−089 has shown periods of rapid activity both in rise and decline in brightness for the object (Villata et al. 1997; Xie et al. 2002). Historically, the object has gone through periods of quiescence with an occasional large outbursts. Archival plates measured by Liller & Liller (1975) show a large flare ($\Delta m_{\rm B} = 3$) during 1948.

4.6.2 Observations

The complete light curve for PKS 1510−089 is displayed in Figure 4.42. Over the past decade, the object has reached a brightness greater than R=15 and can typically be found at a brightness fainter than R=16. Multiple sharp outbursts of the object are present. A poorly sampled peak in the late 1990's reached R∼15.4, followed by better sampled outbursts over the last five years.

Figure 4.43 displays the light curve of PKS 1510−089 since 2001, the majority of which was obtained through queued SMARTS observations with the 1.3m telescope. A series of flares and troughs are superposed on a gradual linear increase over the ∼6 year period. Distinct peaks are seen in almost every observing season with very rapid rises and declines.

One of the outbursts, seen in Figure 4.44, shows a gradual rise in brightness from R∼16.7 to R∼16.4, punctuated by a rapid rise to R∼15.6 near JD2453220. Though the outburst itself is not well sampled, the overall variation is rapid and the shape is

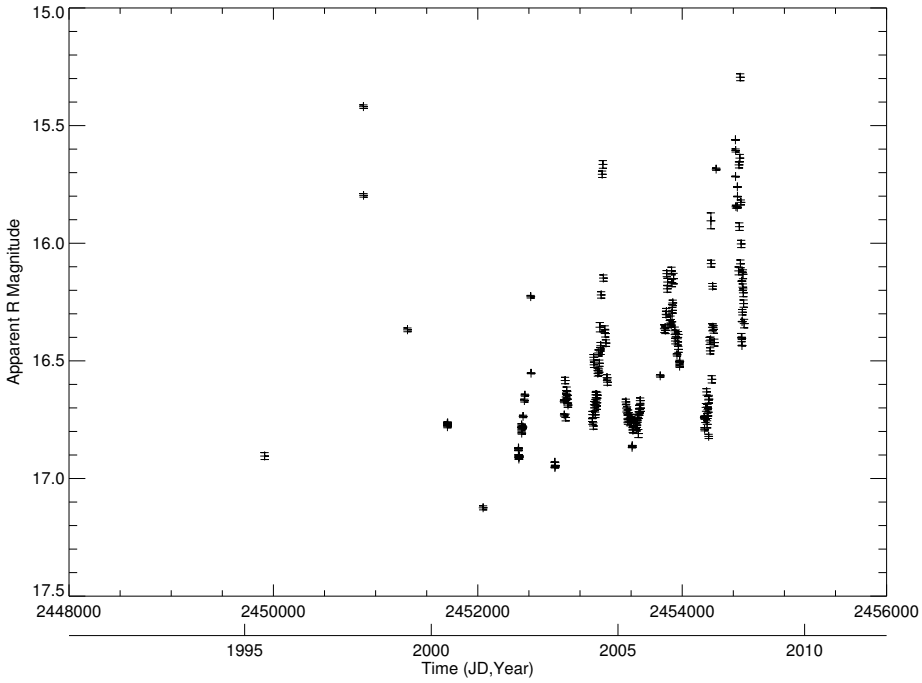

Figure. 4.42: Complete light curve for 1510−089 (PKS 1510−089) binned at 1 day intervals.

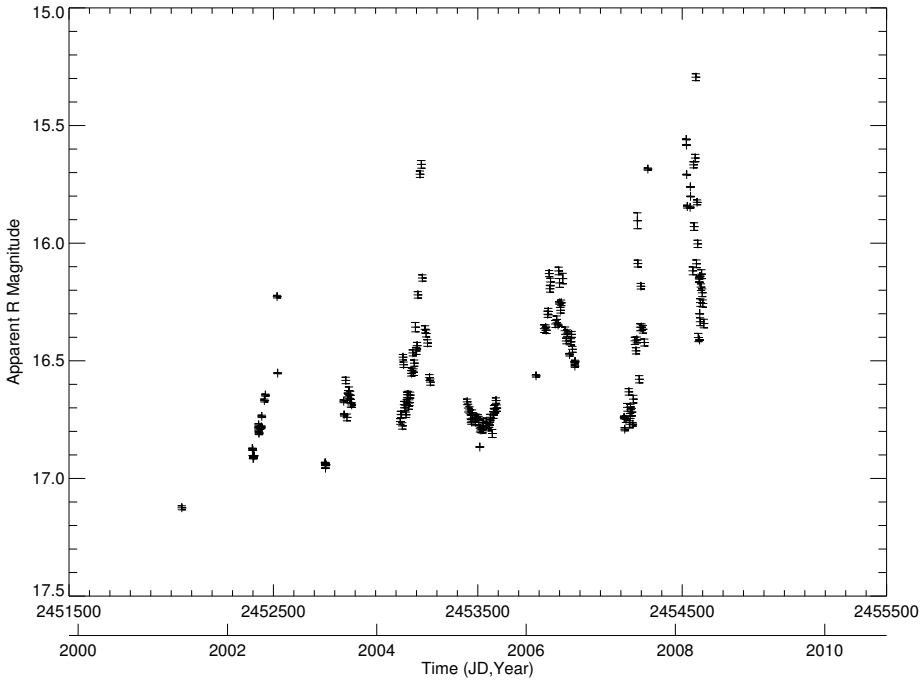

Figure. 4.43: Long term light curve for 1510−089 (PKS 1510−089) binned at 1 day intervals.

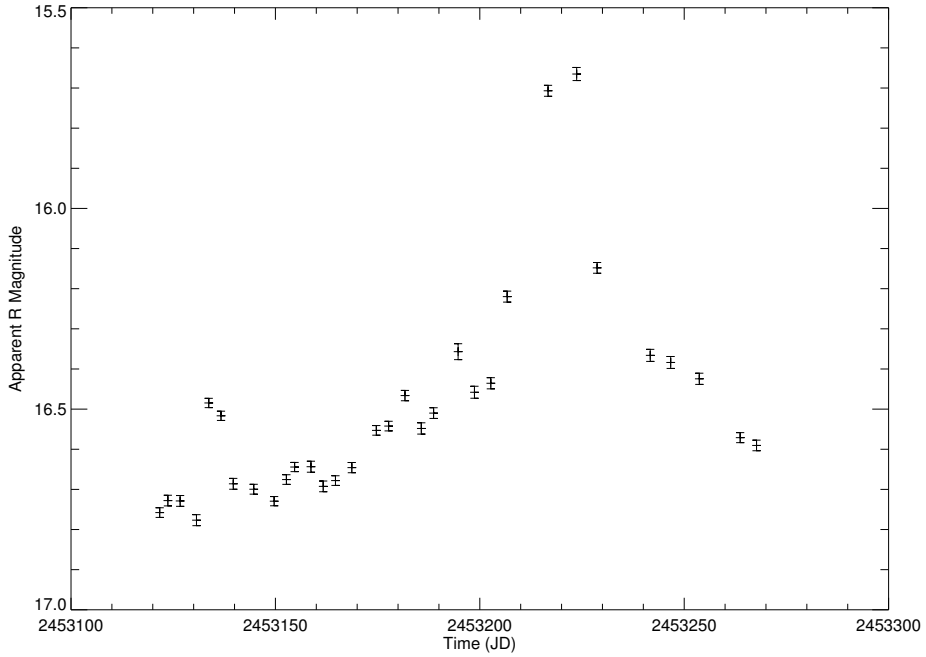

Figure. 4.44: Medium term light curve for 1510−089 (PKS 1510−089) binned at 1 day intervals.

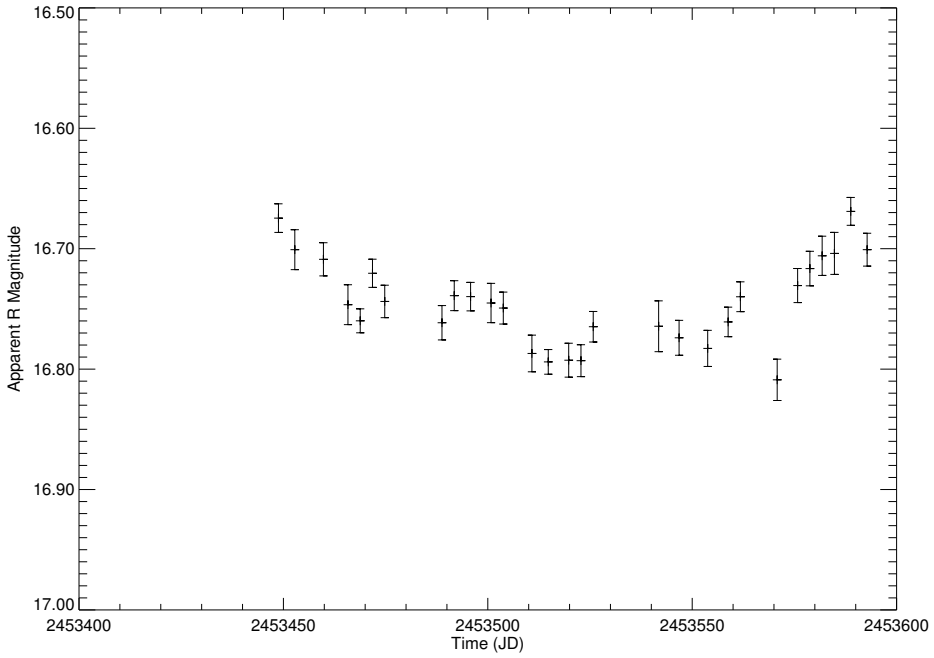

Figure. 4.45: Medium term light curve for 1510−089 (PKS 1510−089) binned at 1 day intervals.

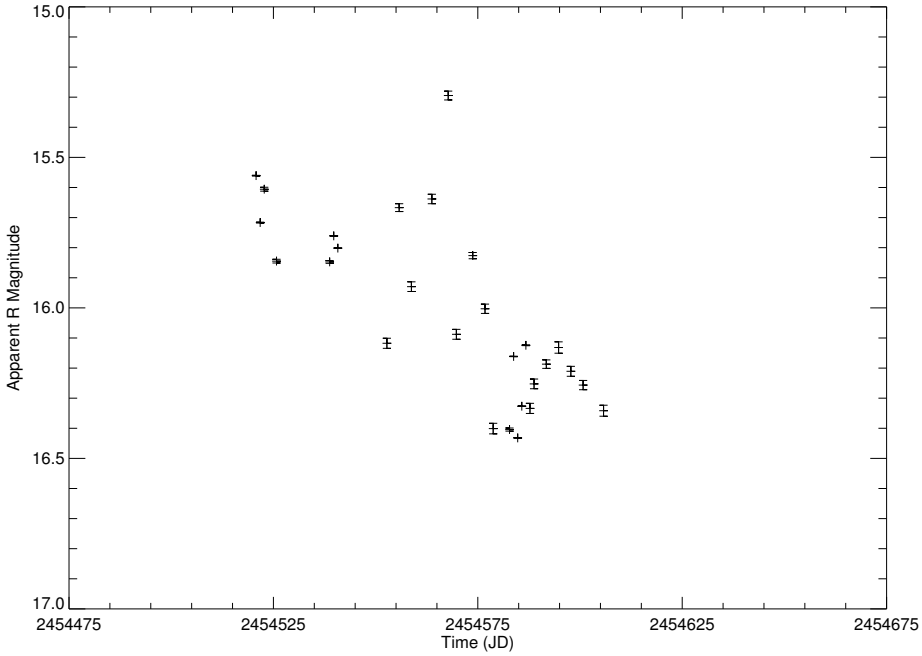

Figure. 4.46: Medium term light curve for 1510−089 (PKS 1510−089) binned at 1 day intervals.

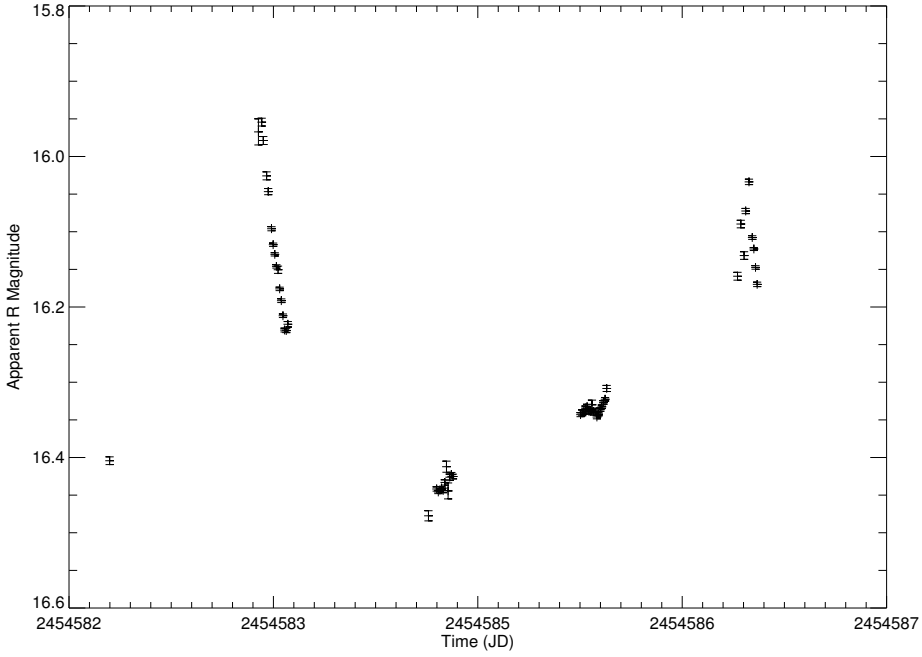

Figure. 4.47: Short term light curve for 1510−089 (PKS 1510−089) binned at ∼15 minute intervals.

roughly symmetric, with a total duration of approximately 20 days.

In contrast, a smooth trough in the light curve is displayed in Figure 4.45. Over this observing season, PKS 1510−089 does not appear to go through any major outburst and varies in magnitude by no more than $\Delta R = 0.2$.

Another medium term light curve can be seen in Figure 4.46. This light curve displays observations obtained during the 2008 observing season. A general linear decline is seen, with the object dropping from a relatively bright state (R$\sim$15.5) to a fainter state (R$\sim$16.4) over a period of 3 months. There is evidence of rapid variability on timescales smaller than those measured, with a possible flare near the middle of the observing period.

Figure 4.47 displays variability seen in PKS 1510−089 during a 5 night period. The object was initially measured at a brightness of R$\sim$16.4, but had elevated to R$<$16.0 by the following night. This night displays a dramatic, but steady drop in brightness. The final three nights show an overall gradual rise, with smaller amplitude events clearly visible within a single night.

4.7 2200+420 (BL Lac)

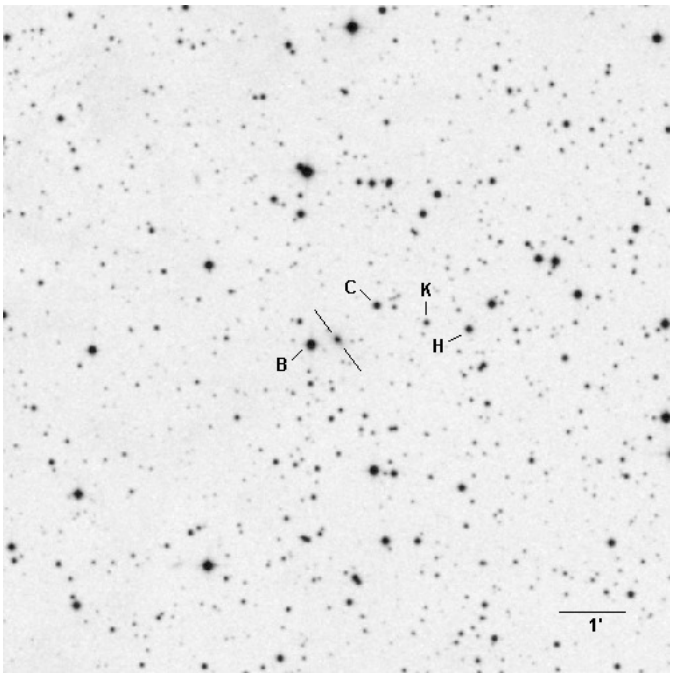

Figure. 4.48: Field of view of BL Lac (target marked by lines, check stars by letter).

4.7.1 Background

BL Lacertae is the prototype object of the BL Lac class. As mentioned earlier, it was initially mistaken as a variable star in the optical. Schmitt (1968) was the first to associate BL Lac with the radio source VRO 42.22.01. The field of view for BL Lac and its comparison stars can be seen in Figure 4.48. Deep optical images also clearly reveal the elliptical host galaxy of BL Lac, as well as the object's proximity to the galactic plane ($b = -10°$).

Many early spectroscopic studies failed to find any distinct features in the spectrum of BL Lac (DuPuy et al. 1969; Oke et al. 1969). With more refined mea-

surements, a weak and variable Hα line was detected with an equivalent width of $\sim$ 5Å (Miller et al. 1978; Vermeulen et al. 1995). The visibility of these lines coincides with a minimum in the continuum emission of the object.

The relativistic jet of BL Lac, seen using the Very Long Baseline Array (VLBA), is highly active and frequently emits blobs of material (Jorstad et al. 2005). The emission of these blobs, in conjunction with observations at x-ray and optical wavelengths, has given a detailed glimpse into the inner mechanics of blazar jets (Marscher et al. 2008).

Compared with other blazars, BL Lac is relatively nearby at $z = 0.069$ and relatively bright, with a mean brightness of R$\sim$14 in the optical. The object is known to vary up to 4 magnitudes in the optical (Shen & Usher 1970) and has regularly displayed rapid microvariability events in a matter of hours (Racine 1970; Miller et al. 1989).

4.7.2 Observations

The excellent optical coverage for BL Lac is evident in the complete light curve shown in Figure 4.49. The first $\sim$20 years of the light curve includes data from a variety of sources and is densely sampled due to the large level of initial interest in BL Lac. While the uncertainties on this initial data set are large, it is clear that BL Lac is very active on long timescales, with a full range of $\sim$3 magnitudes in R.

A closer inspection of the early BL Lac data can be seen in Figure 4.50. It is clear that BL Lac undergoes large changes in flux on year-like timescales, with slower

changes over decades. The brightness rises and declines with an amplitude of $\sim$1.5 magnitudes in a quasi-regular pattern.

The last 20 years of optical data for BL Lac (Figure 4.51) is undersampled compared to the initial 20 years. The majority of these data were obtained by the PEGA group at Lowell Observatory, whereas the previous data set represented a compilation from a large variety of sources. While there are certainly numerous observations from a wide variety of sources in the current era of astronomy, the level of cooperation and publishing of complete data sets has decreased with time. The literature searches used for this dissertation tend to produce a wealth of data from 1960-1985, but little afterward.

Even with a decrease in sampling rate, a similar behavior can be seen in this light curve as compared to the previous 20 years. On yearly timescales, BL Lac oscillates rapidly on a scale of over a magnitude. On decadal timescales, this time period shows a slightly elevated overall state.

On timescales equivalent to one observing season, BL Lac can be seen to vary by up to 2 magnitudes in R, as shown in Figure 4.52. The peaks and troughs in this light curve are sharp, including a distinct peak to R$<$12.5 near JD2440770 followed immediately by a sharp dip down to R$\sim$14.3. Isolated points appear scattered, but this is likely due to an undersampling of the variability at daily timescales.

Figure 4.53 displays the variability of BL Lac over the course of a single observing run. In this case, the majority of the observing time was devoted solely to BL Lac,

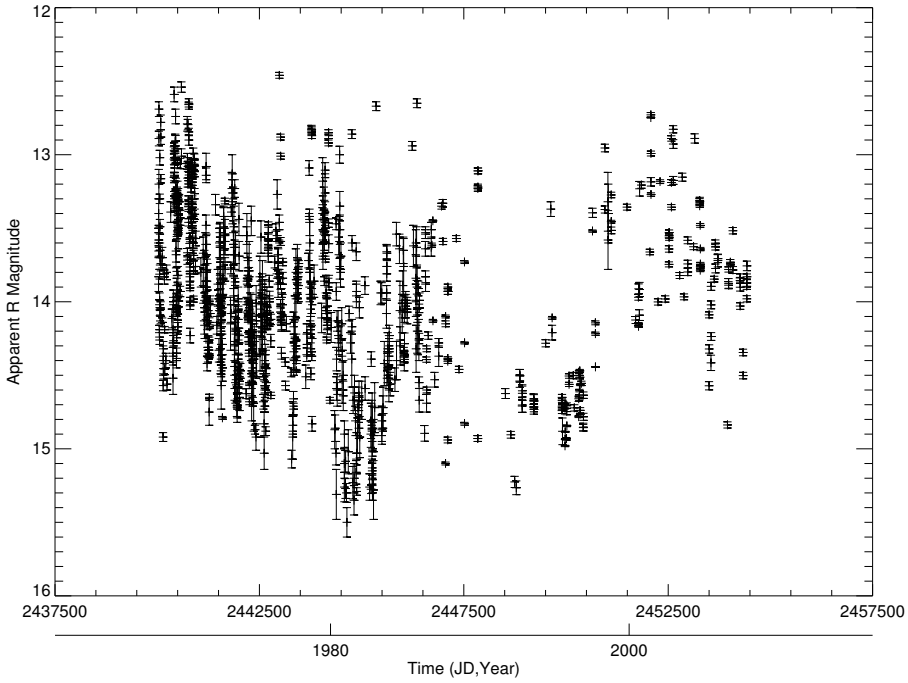

Figure. 4.49: Complete light curve for 2200+420 (BL Lac) binned at 1 day intervals.

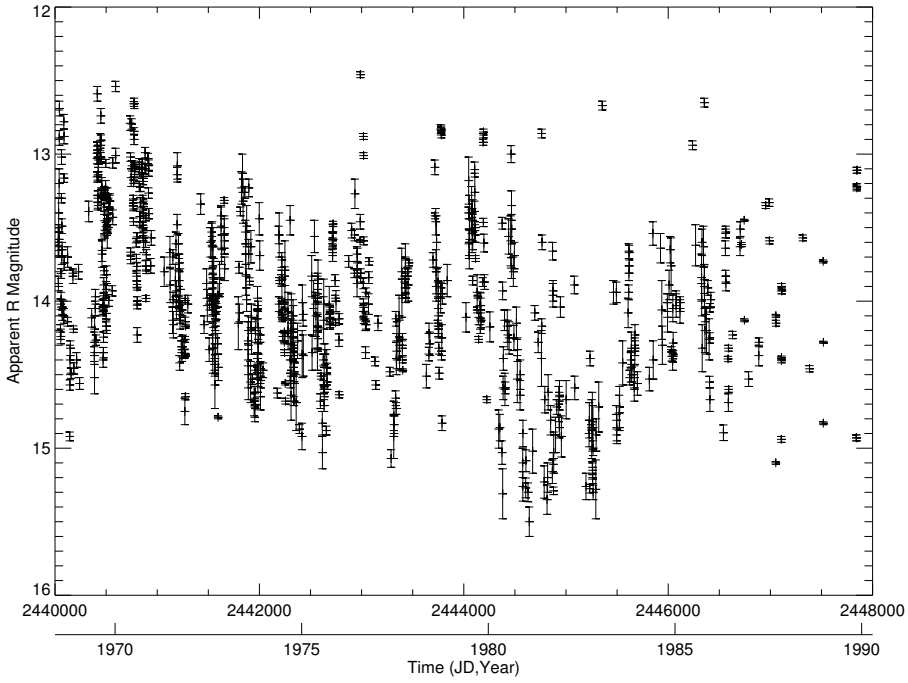

Figure. 4.50: Long term light curve for 2200+420 (BL Lac) binned at 1 day intervals.

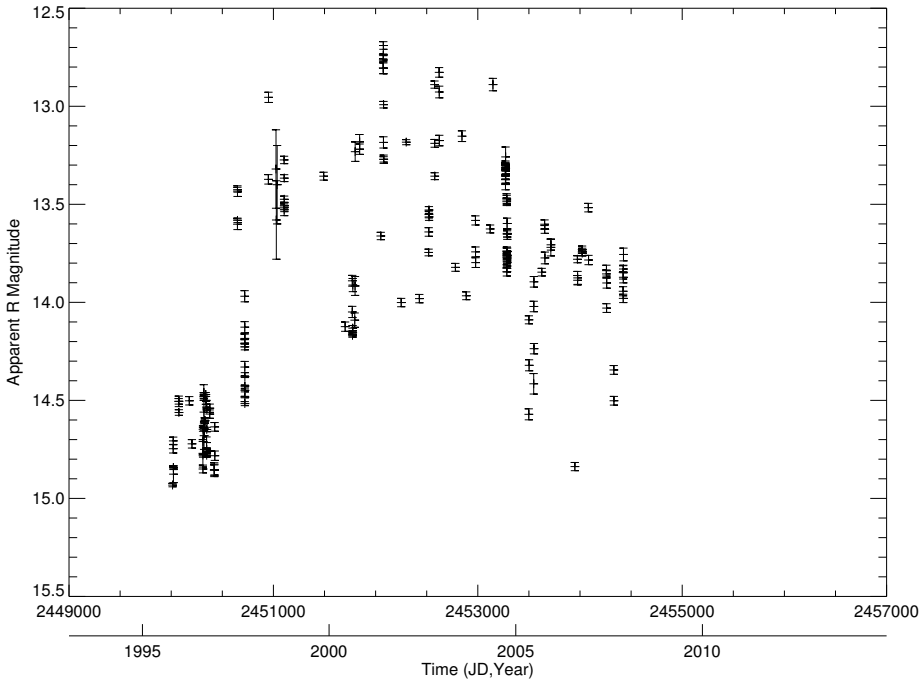

Figure. 4.51: Long term light curve for 2200+420 (BL Lac) binned at 1 day intervals.

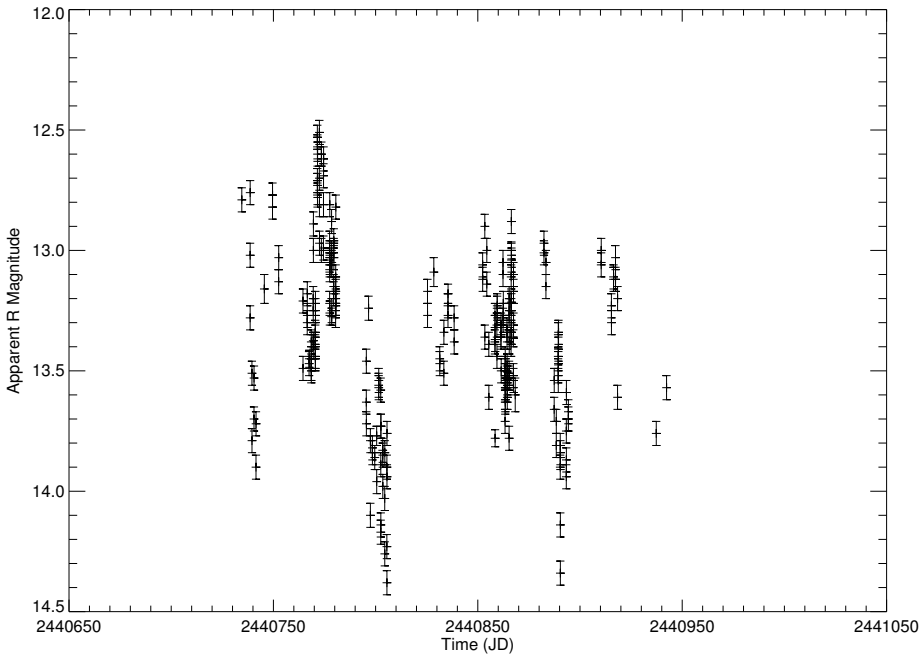

Figure. 4.52: Medium term light curve for 2200+420 (BL Lac) binned at 0.1 day intervals.

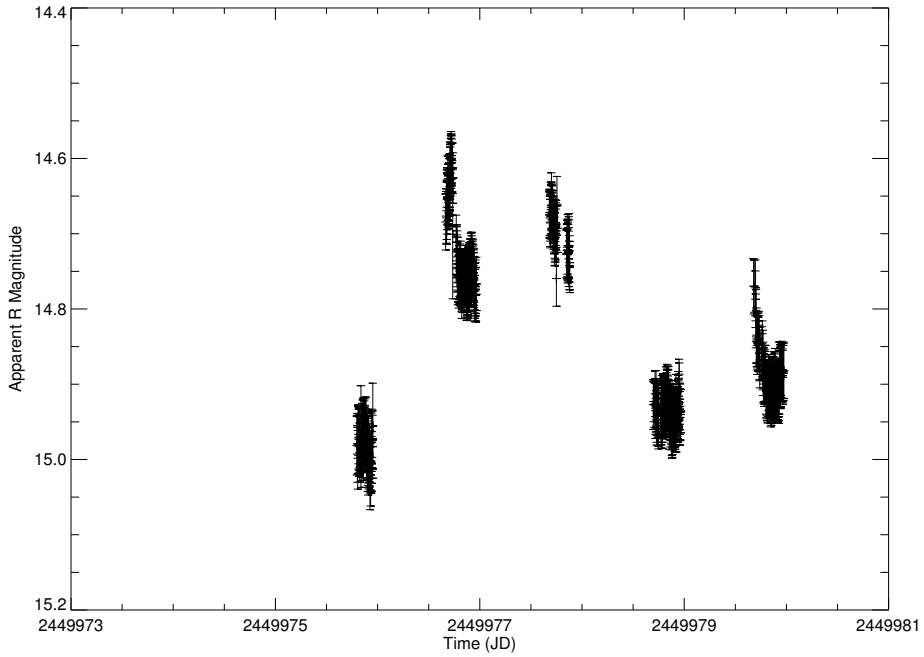

Figure. 4.53: Short term light curve for 2200+420 (BL Lac) binned at $\sim$ 15 minute intervals.

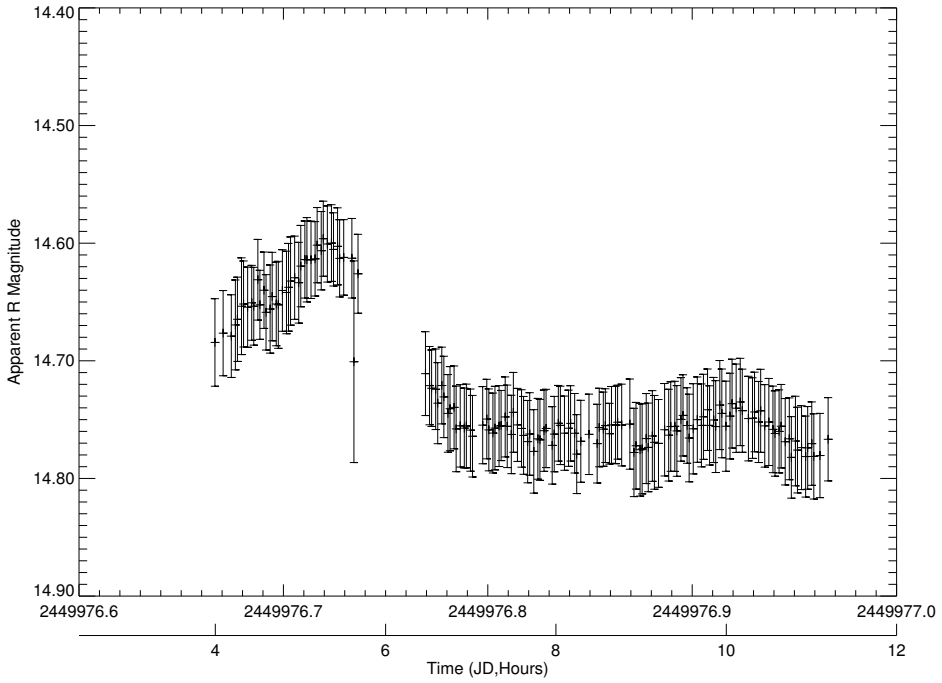

Figure. 4.54: Microvariability light curve for 2200+420 (BL Lac) binned at $\sim$ 1.5 minute intervals.

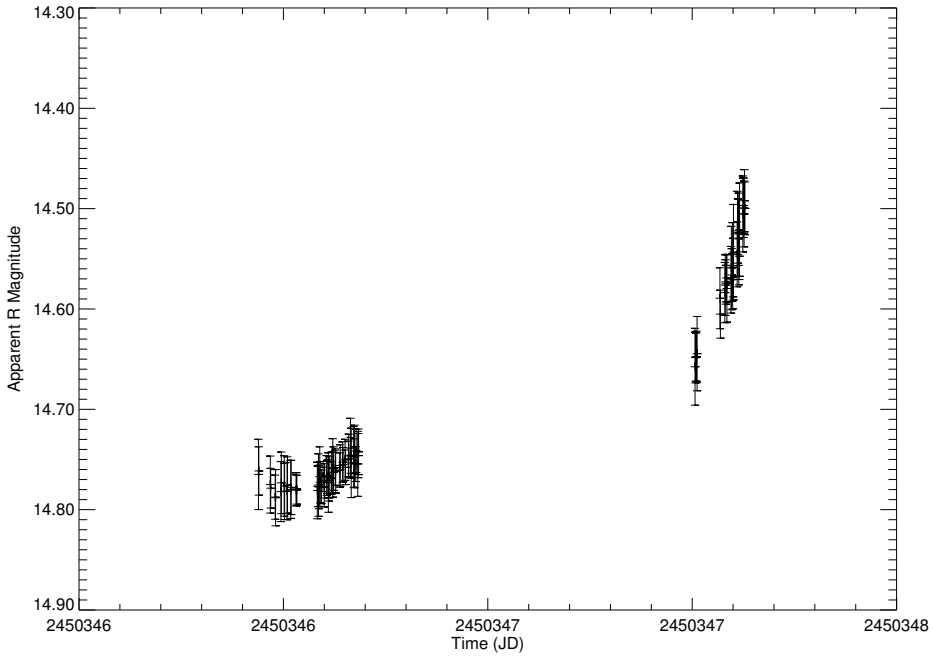

Figure. 4.55: Microvariability light curve for 2200+420 (BL Lac) binned at $\sim$ 1.5 minute intervals.

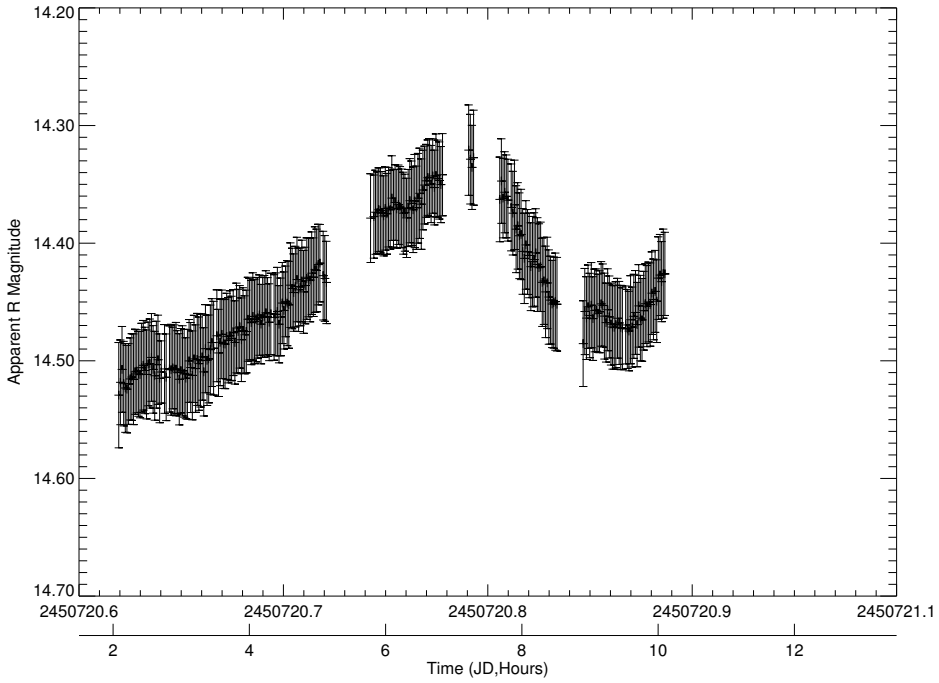

Figure. 4.56: Microvariability light curve for 2200+420 (BL Lac) binned at $\sim$ 1.5 minute intervals.

providing insight into the behavior of the object on timescales less than a day. Over the course of the 5 night run, the object is seen to change in brightness by up to $\sim$0.4 magnitudes. It is also clear that variations within a single night are significant.

The second night of the five night run is visible in Figure 4.54. A distinct, symmetric event occurs at the beginning of this night with an amplitude of one tenth of a magnitude. A smaller amplitude event can also be seen later in the night. Microvariability of this amplitude or greater is common for BL Lac.

Similar rapid microvariability can be seen in Figure 4.55 during a two night observing run. During the first night, BL Lac undergoes a modest increase in brightness, followed by a rapid increase of approximately 0.15 magnitudes on the second night.

Another set of intensive observations is shown is Figure 4.56. As before, a distinct event is captured over the course of just a few hours. The variability is smooth and continuous at short timescales on the order of the exposure time for the object (1.5 minutes).

4.8 2251+158 (3C 454.3)

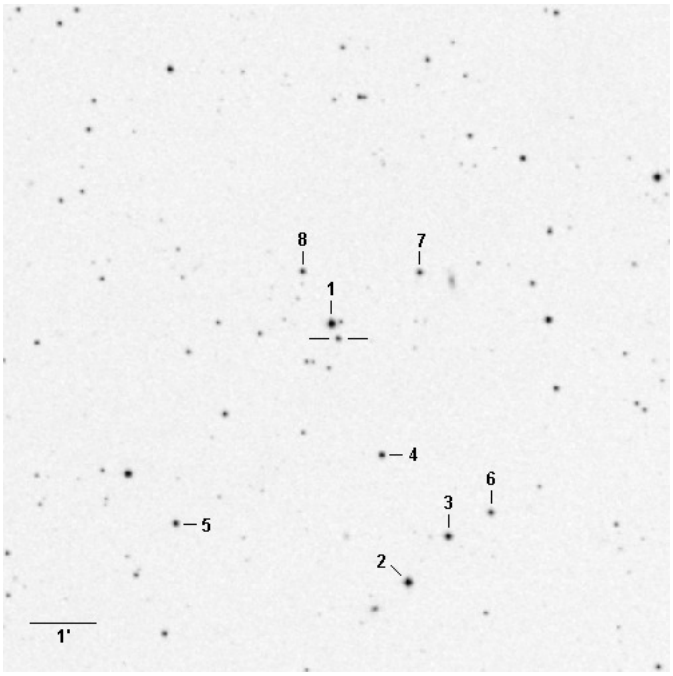

Figure. 4.57: Field of view of 3C 454.3 (target marked by lines, check stars by number).

4.8.1 Background

The OVV quasar 3C 454.3 has been regularly observed by the PEGA group over the past 30 years and was subject to an intense observing effort during the flare of 2005. It is a FSRQ at a relatively high redshift (z=0.859) and displays the high amplitude, rapid variability that is characteristic of this class.

VLBI studies reveal a one-sided relativistic jet with regular fluctuations in flux density over time (Aller et al. 1997). Multiple emissions are seen over the decades and

in many cases, a strong correlation with optical brightening is seen with the emission of new material.

3C 454.3 is highly variable across the entire electromagnetic spectrum. It has been observed in x-rays by numerous satellites and became one of the brightest sources in the x-ray sky during the 2005 flare. 3C 454.3 was also detected in gamma rays by both COMPTEL (Zhang et al. 2005) and EGRET (Hartman et al. 1993).

In the optical, the variability of 3C 454.3 can be traced back to 1900 (Angione 1968). It is variable on shorter timescales as well, displaying intranight variability (Angione 1971) and microvariability (Villata et al. 1997; Raiteri et al. 1998) on numerous occasions.

The flare of 2005 was first observed by the author on UT May 08. The object had brightened to R$\sim$11.8 compared to a typical faint state of R$\sim$16.0. Subsequent measurements by other observers triggered an alert to the blazar community and began an unprecedented concentration of observations at all available wavelengths. For the PEGA group, the 2005 flare of 3C 454.3 represents the most concentrated and numerous data set obtained for any blazar.

4.8.2 Observations

Figure 4.58 displays the complete compilation of optical data from a variety of different sources. It is clear from this plot that the flaring activity of the past decade represents somewhat of a change in state compared the light curve of the 1960's, 1970's and 1980's. Additional flares are visible both before and after the large flare of

2005, including a flare that peaked near R∼13 in 2007. It will be intriguing to learn if the very rapid and dramatic outbursts continue over the coming years.

The long term behavior of 3C 454.3 during the late 1960's, 1970's and early 1980's is displayed in Figure 4.59. The majority of these observations were taken from Webb et al. (1988) at Rosemary Hill Observatory. Though this period is relatively quiescent compared to the recent flaring activity, a few distinct events are still clearly visible. The object is rarely seen to dip below R∼16.5, with a range in magnitude of about 1.5 magnitudes.

The second long term light curve, Figure 4.60, focuses on the recent data, most of which was taken by amateur astronomer Paul Boltwood, with smaller contributions from the PEGA group at Lowell Observatory and the SMARTS 1.3m telescope. While the first five years in this plot are similar to earlier behavior, a distinct change can be seen beginning in 2002. Rapid and sharp flares can be seen in 2002, 2005, and 2007.

PEGA observations of the 2005 flare are shown in Figure 4.61, binned at 0.1 day intervals. The initial detection was made at Lowell Observatory on the Perkins 1.8m telescope. Subsequent observations were taken mainly through the SMARTS observing queue and amateur astronomer Paul Boltwood. Unfortunately, initial observations showed the object already in decline and the peak magnitude of this already extreme flare is not known. While there is a steady decline over the ∼220 day time period, there is clear evidence of smaller amplitude events superposed onto the large flare. By the end of the observing season, 3C 454.3 had returned to near its faintest level.

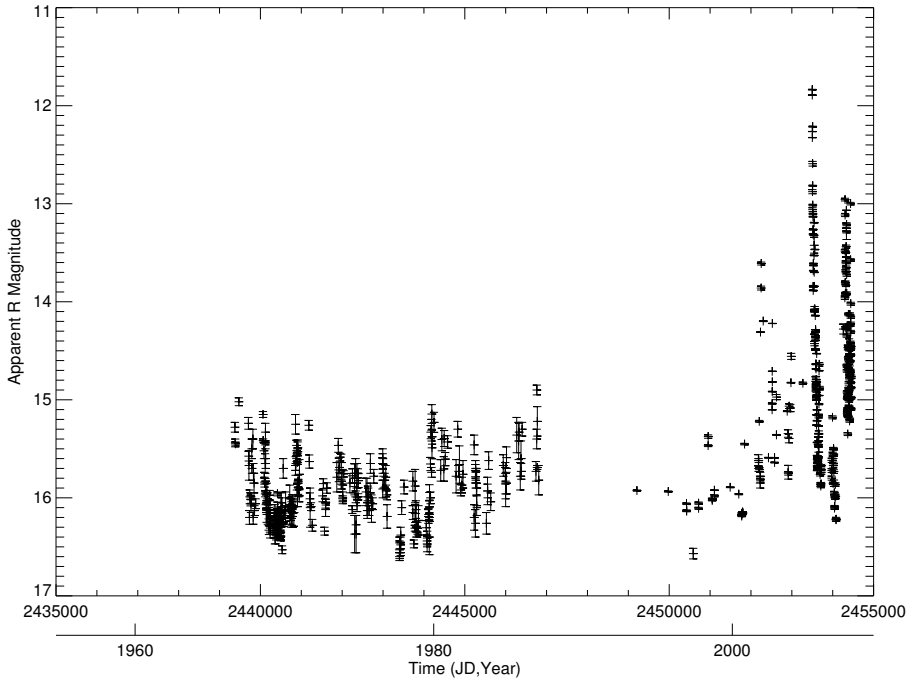

Figure. 4.58: Complete light curve for 2251+158 (3C 454.3) binned at 1 day intervals.

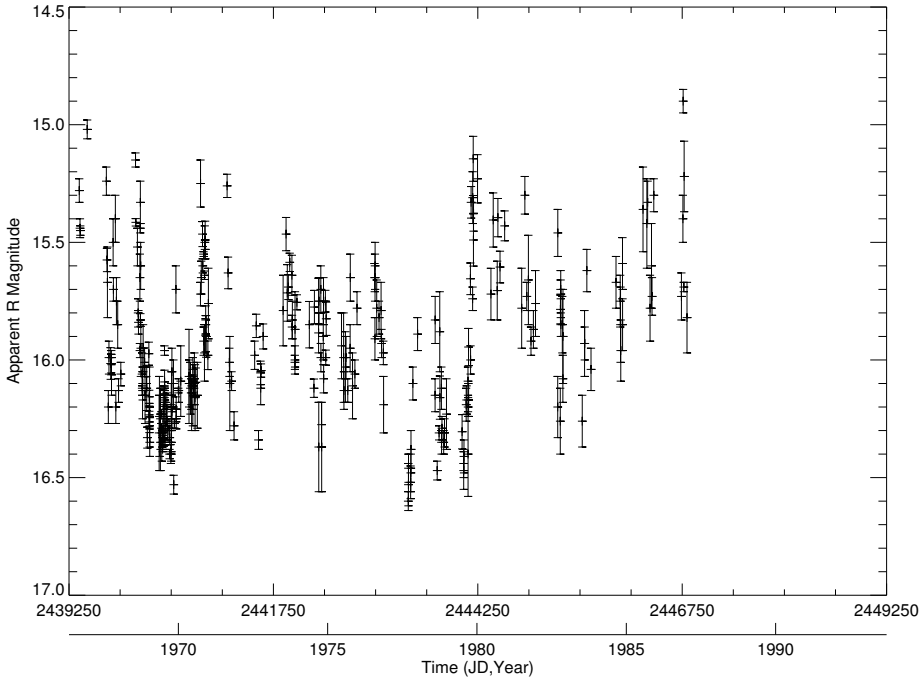

Figure. 4.59: Long term light curve for 2251+158 (3C 454.3) binned at 1 day intervals.

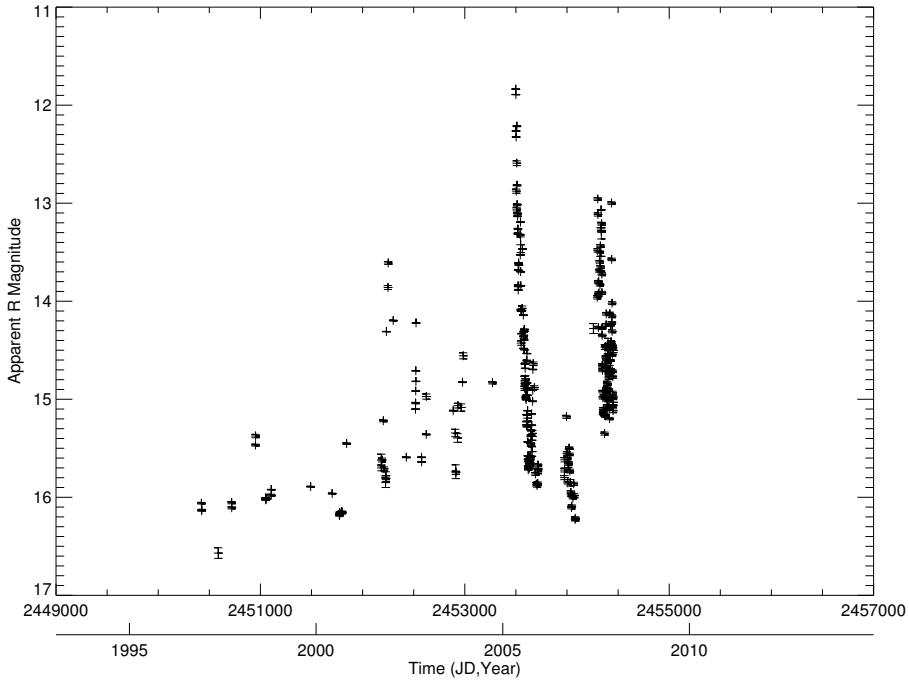

Figure. 4.60: Long term light curve for 2251+158 (3C 454.3) binned at 1 day intervals.

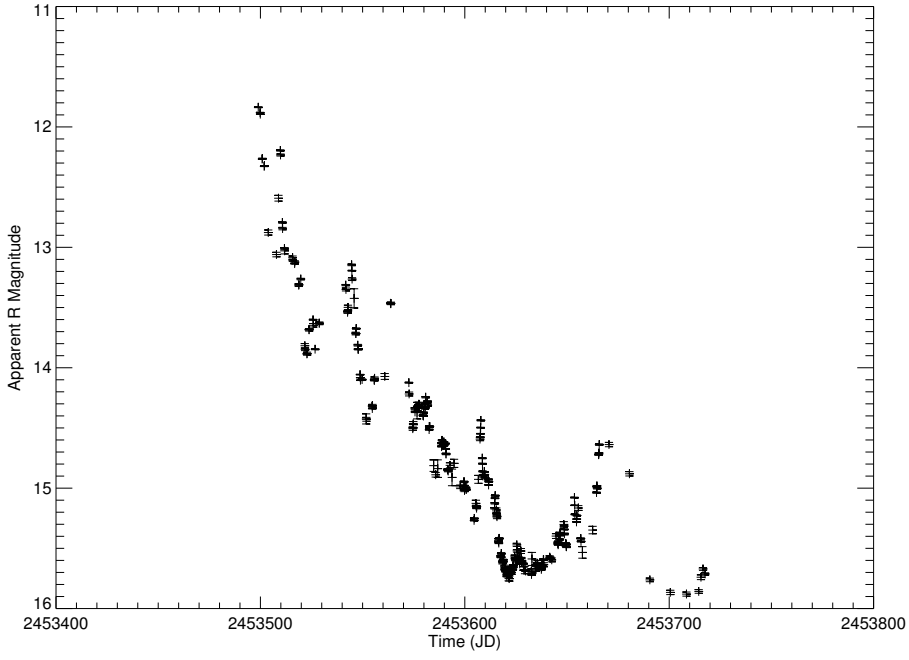

Figure. 4.61: Light curve of 2251+158 (3C 454.3) from the flare of 2005 binned at 0.1 day intervals.

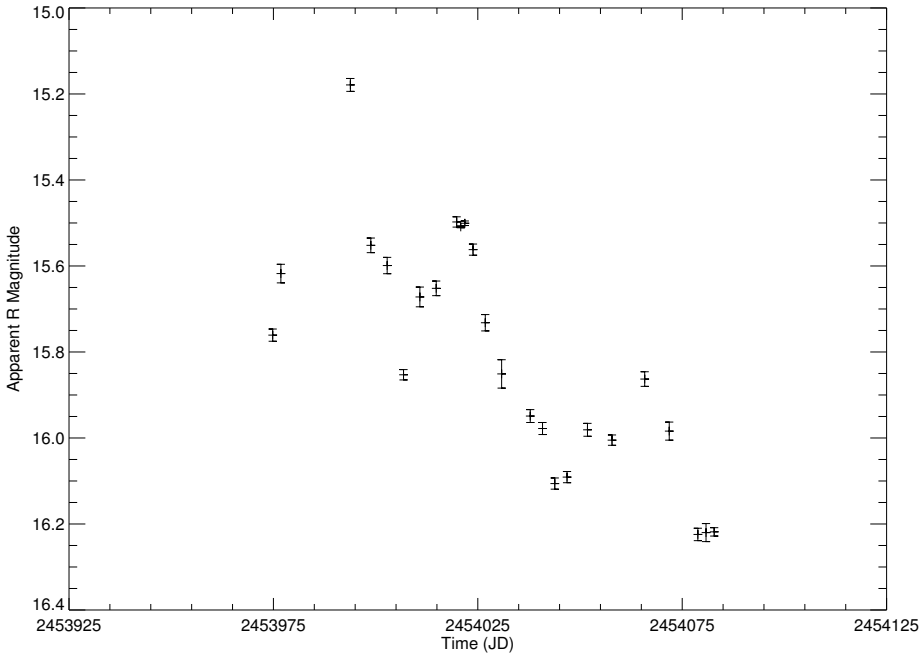

Figure. 4.62: Medium term light curve for 2251+158 (3C 454.3) binned at 1 day intervals.

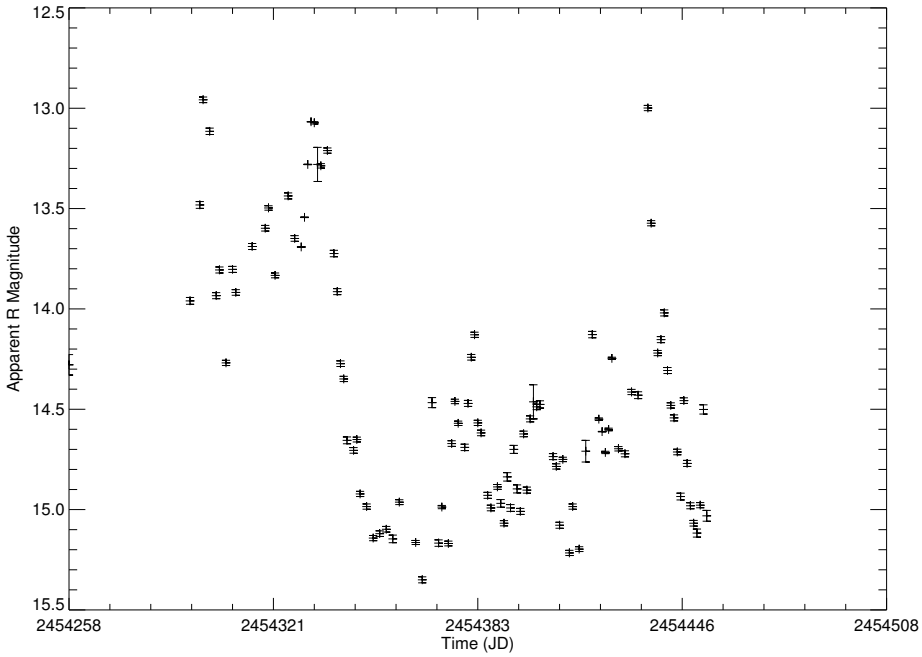

Figure. 4.63: Medium term light curve for 2251+158 (3C 454.3) binned at 1 day intervals.

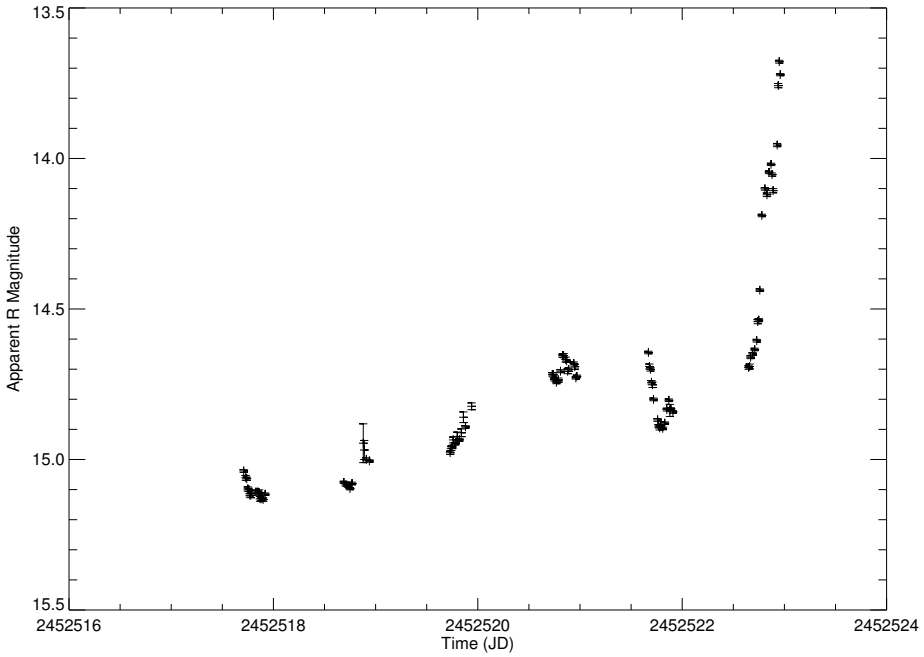

Figure. 4.64: Short term light curve for 2251+158 (3C 454.3) binned at $\sim$ 15 minute intervals.

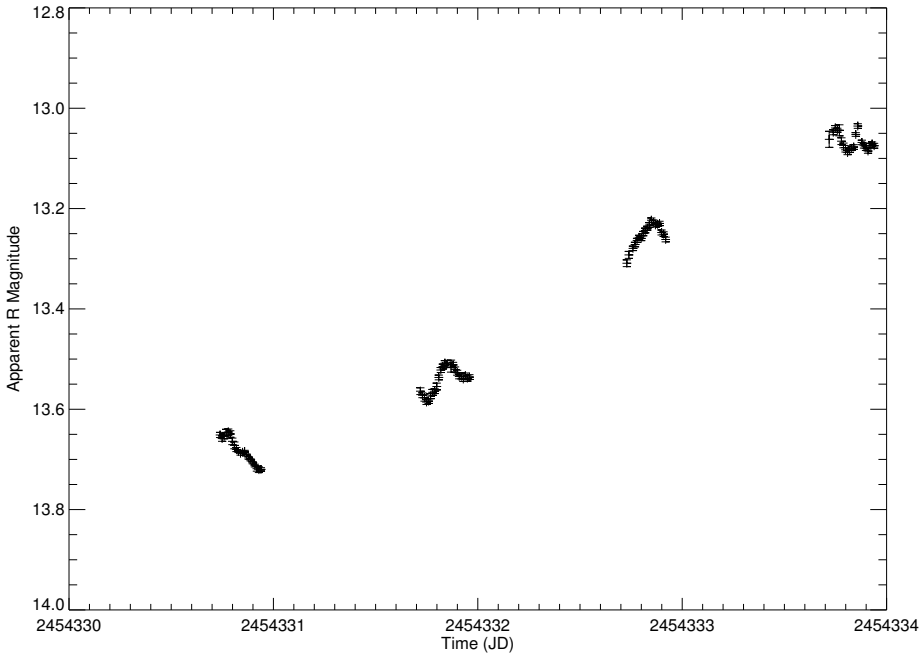

Figure. 4.65: Short term light curve for 2251+158 (3C 454.3) binned at $\sim$ 15 minute intervals.

In contrast to the extreme events of 2005, the relatively quiescent period of the 2006 season can be seen in Figure 4.62. During this time, 3C 454.3 never brightened over R=15.0 and again is seen to hover near its faintest level. Despite the poor sampling, it is clear that a modest level of variability is still present in the object.

Figure 4.63 shows a return to rapid and extreme variability during the 2007 season. Due to its elevated state, the PEGA group requested nightly observations from the SMARTS queue for the majority of observing season. The peaks (R$\sim$13) located near the beginning and end of this plot are extremely sharp, with a rise and decline greater than a magnitude occurring in just a few weeks. In contrast, a smoother, but no less dramatic decline can be seen in the first half of the light curve, which falls to a level of R$\sim$15.2.

The presence of marked variability of 3C 454.3 is still displayed on even smaller timescales. Figure 4.64 shows the results from observations obtained UT August 31 through September 5, 2002. A slow rise from R<15 is seen for the first few nights, marked with smaller amplitude rapid variations within each night. In the final third of the light curve, the variations become much more rapid, with a sharp drop off near the end of JD 2452521 followed by an extreme brightening by more than magnitude over the next day. This very steep rise is similar to the behavior seen in the 2007 light curve, although in this case, the microvariability is resolved.

A more recent microvariability study of 3C 454.3 is shown in Figure 4.65. As in the previous light curve, the improved temporal resolution of the microvariability

provides clarification to the less well-sampled data seen in earlier figures. In this case, the total range is a little less than a magnitude, with 3C 454.3 in a relatively bright state peaking near R=13.0. Within each night, smaller amplitude events on timescales of hours are clearly visible.

The most exciting phrase to hear in science, the one that heralds the most discvories, is not 'Eureka!', but 'That's funny...'.

—— *Isaac Asimov*

– 5 –

Results

The final results of the time series analysis for each object in the sample are presented below. For each object, simulations were carried out using the unbroken power law, sharply broken power law, and knee power law models described in Chapter 3.

In each case, the observed power spectrum is compared to the average simulated spectrum, producing a confidence value for each model with a specified set of parameters. For the unbroken power law, this produces a two-dimensional plot of confidence percentage versus model slope. For the broken and knee power law models, the result is a contour plot with slope and break frequencies as the x- and y-axes and confidence value as the z-axis.

The confidence values calculated for each model are an estimation of the goodness of fit based on the $\chi^2_{\rm dist}$ statistic. A model with a confidence level of $\leq 10\%$, corresponding to a rejection level of $\geq 90\%$, can be considered a poor fit to the data. Models with confidences $\geq 10\%$ are considered acceptable fits to the data, with higher values of confidence corresponding to stronger fits. Because the analysis is model dependent, more than one model may provide an acceptable fit to the data.

The peak value of each confidence contour is chosen as the best fit model to the observed power spectrum. A plot displaying the observed power spectrum overlaid with the simulated power spectrum is presented for many of these best fit models.

In order to determine the best fit value and errors for each model, a two-dimensional slice of the contour plot is made at the peak values of each parameter, which is then fit with a simple Gaussian. For the unbroken power law models, a Gaussian fit is made directly to the confidence versus slope parameter plot. The best fit value and error for model parameters are the peak value and 1σ width of the Gaussian fit, respectively.

In addition to the power density spectrum, the structure function is utilized to confirm the presence or absence of a break in the observed data. The Monte Carlo simulations are carried out in an identical manner to the PSRESP method, with the structure function replacing the power spectrum as the time series analysis tool. Fake light curves are simulated based on known input models and comparisons are made between the observed structure function and an average simulated structure function.

In this manner, the structure function can be used as a reliable confirmation of possible breaks observed in the power density spectrum. The structure function simulations are performed only for the broken power law models, except for objects where an unbroken power law is an acceptable fit. Comparisons between the structure function and power spectrum results will be discussed in Chapter 6.

5.1 0235+164

5.1.1 0235+164 - Power Density Spectrum

The first object presented, in order of right ascension, is the BL Lac object AO 0235+16. Compared to other objects in the sample, AO 0235+16 suffered from a

poor sampling rate on long timescales. The medium term and short term variability appear to be sufficiently sampled.

The observed PDS is fit with a modest level of acceptance by the broken power law model. Figure 5.1 shows the confidence contour for the broken power law model with a peak confidence value at 37.7%. The parameters for the best fit are a slope of $\alpha = -2.0$ and break frequency $f_{\rm b} = 10^{-7.13}$Hz.

Figure 5.2 shows the observed power spectrum of AO 0235+16 (lines) and the best fit simulated power spectrum (squares). The errors on the simulated power spectrum are the RMS spread of the 100 power spectra simulations. While the broken power law provides a good fit to the data at mid and high frequencies, the fit at low frequencies is poor.

The knee model provides a significantly better fit than the broken power law, with a peak confidence value of 59.1%. The maximum value in the confidence contour, seen in Figure 5.3, corresponds to a slope of $\alpha = -2.0$ and $f_{\rm b} = 10^{-7.30}$Hz.

The reason for the higher confidence value of the knee model is apparent in Figure 5.4. The fit above $\sim 10^{-7.0}$Hz is essentially identical to that of the broken power law, with the same slope value of $\alpha = -2.0$. At low frequencies, however, the knee model provides a better fit to the flat profile of the observed power spectra.

The unbroken power law provides the worst fit of the three test models at a confidence level of 5.1%. The best fit slope value for this model, $\alpha = -1.4$, is likely the result of a balance between a low frequency slope of $\alpha < -1.0$ and the high

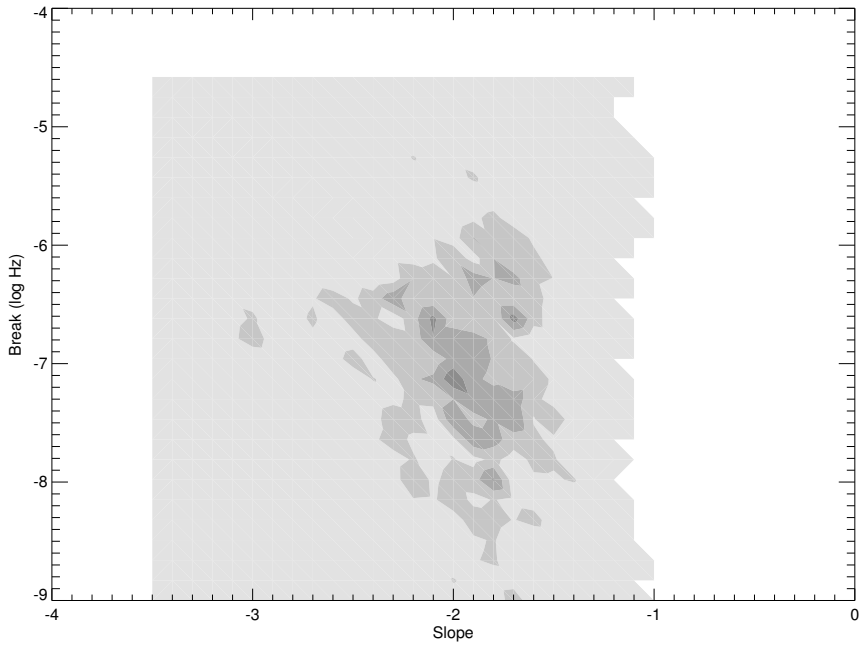

Figure. 5.1: Confidence contour for the broken power law model for AO 0235+16. Highest confidence is 37.7% at $\alpha = -2.0$ and $f_{\rm b} = 10^{-7.13}$Hz.

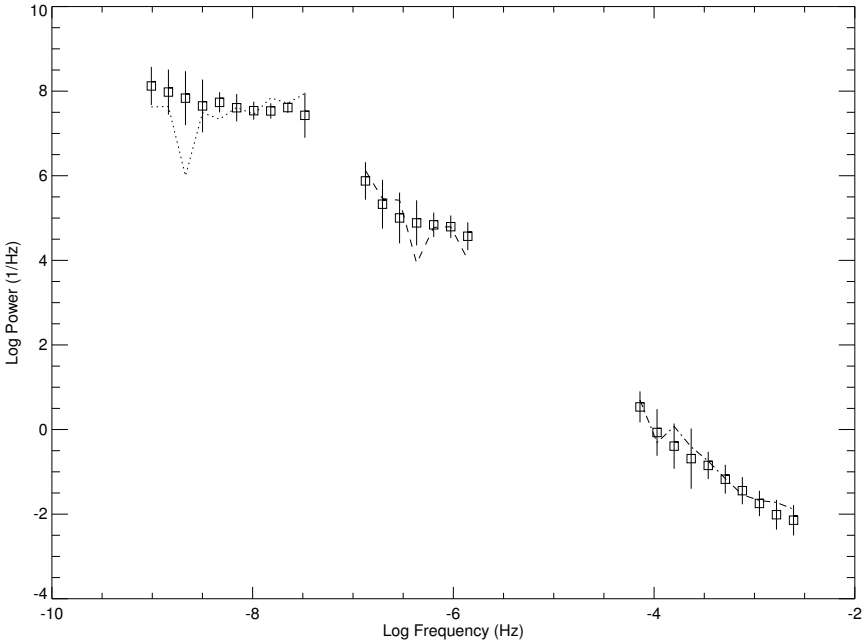

Figure. 5.2: Power density spectrum of AO 0235+164. Lines represent the observed power spectrum, points with error the power density spectrum of the best fit broken power law simulation. Best fit parameters are $\alpha = -2.0$ and $f_{\rm b} = 10^{-7.13}$Hz.

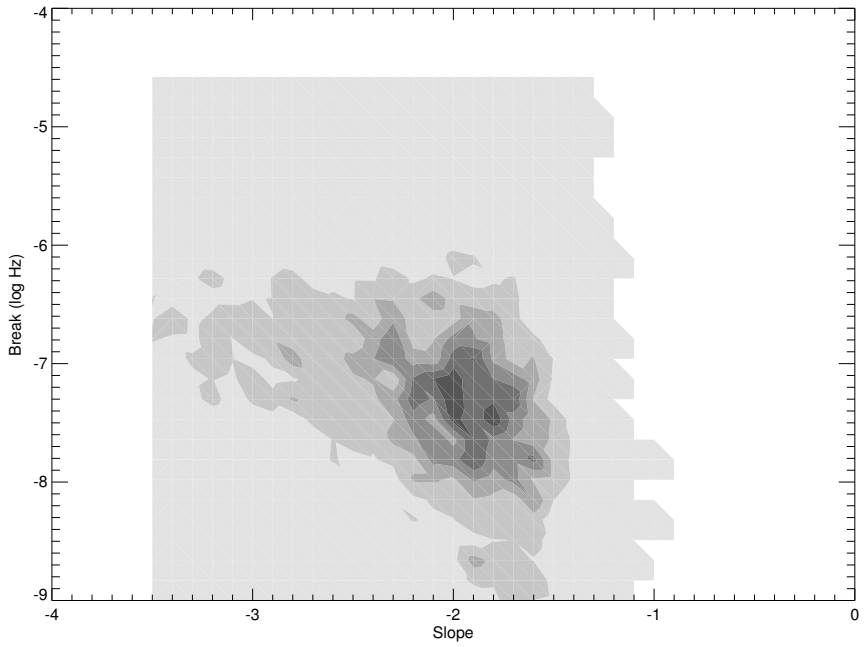

Figure. 5.3: Confidence contour for the knee power law model for AO 0235+16. Highest confidence is 59.1% at $\alpha = -2.0$ and $f_b = 10^{-7.30}$Hz.

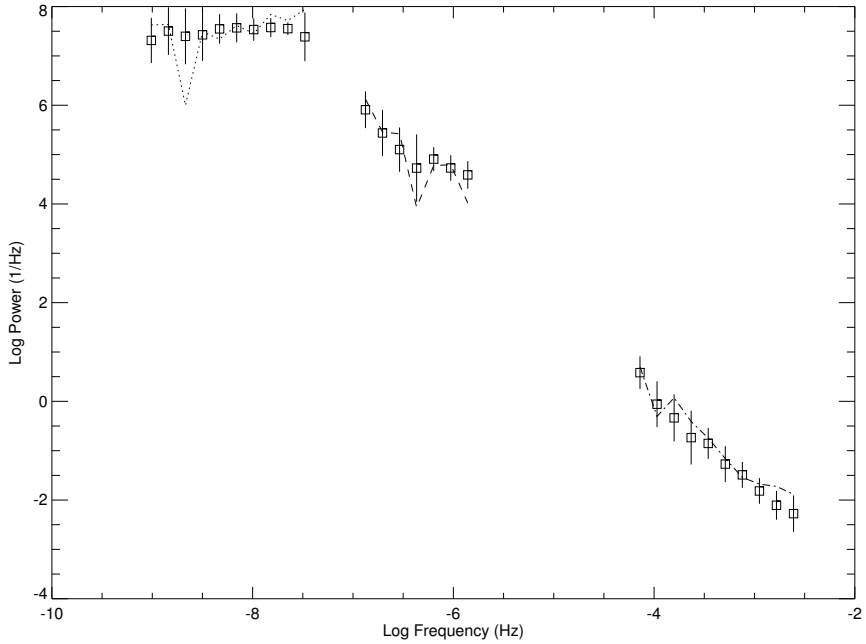

Figure. 5.4: Power density spectrum of AO 0235+164. Lines represent the observed power spectrum, points with error the power density spectrum of the best fit knee simulation. Best fit parameters are $\alpha = -2.0$ and $f_b = 10^{-7.30}$Hz.

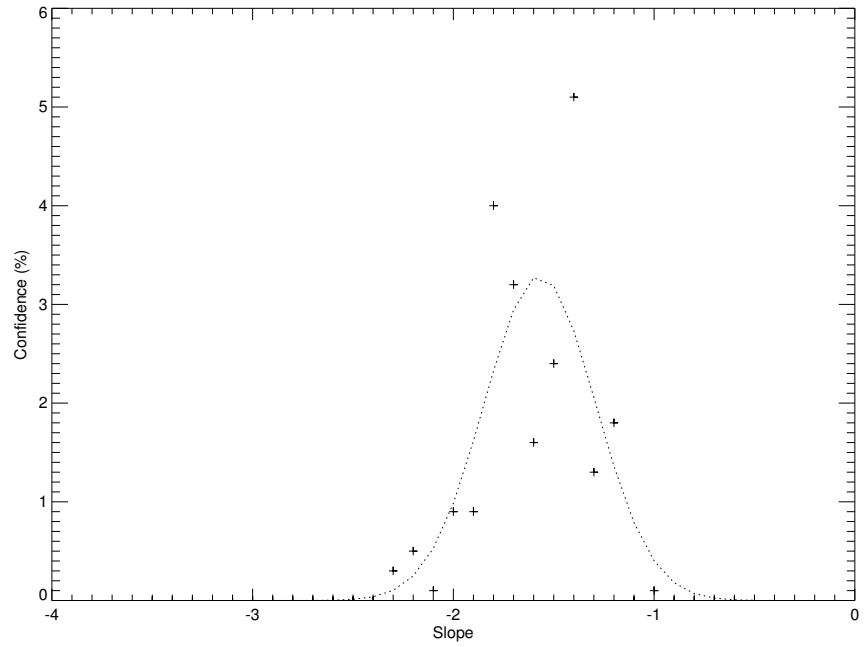

Figure. 5.5: Confidence contour for the unbroken power law model for AO 0235+16. Highest confidence is 5.1% at $\alpha = -1.4$.

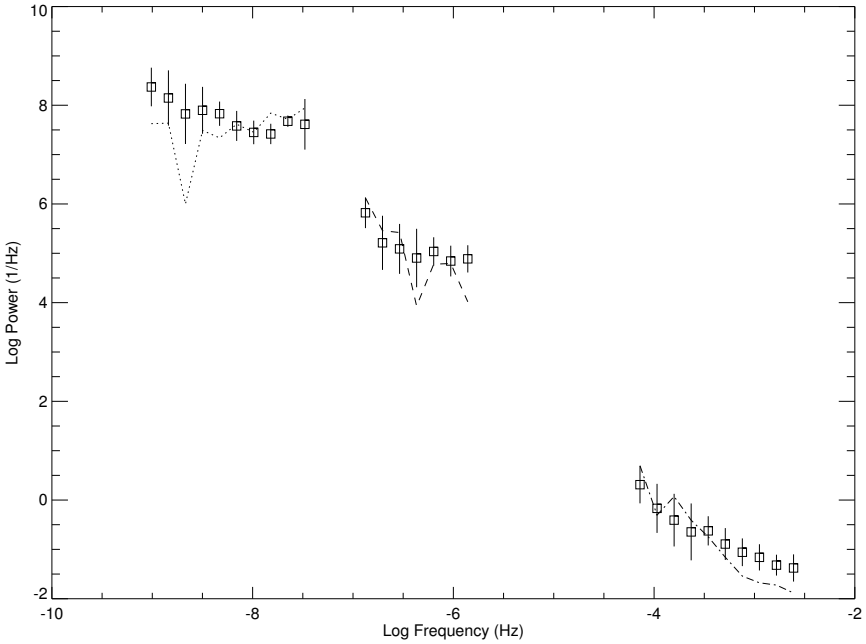

Figure. 5.6: Power density spectrum of AO 0235+164. Lines represent the observed power spectrum, points with error the power density spectrum of the best fit unbroken power law simulation. Best fit slope is $\alpha = -1.4$.

frequency slope of $\alpha = -2.0$. At a low level of confidence compared to the broken power law models, the unbroken power law does not provide an adequate fit to the observed PDS of AO 0235+16.

Table. 5.1: Summary of PDS results for AO 0235+164.

Model	Confidence(%)	Slope (α)	Break Timescale (Days)
PL	5.1	-1.57±0.12	...
BPL	37.7	-1.98±0.12	139^{+171}_{-77}
Knee	59.1	-2.01±0.15	214^{+138}_{-84}

Table 5.1 summarizes the results for the PDS simulations of AO 0235+16. The slope and break values and corresponding errors are calculated based on the Gaussian fit method described above. The slope above the break frequency in both the broken and knee power law models agree at a value near $\alpha \sim -2.0$. The break timescales for the broken and knee power laws are at values of 139 and 214 days respectively, which are consistent given the large error bars on each.

5.1.2 0235+164 - Structure Function

A structure function analysis for the broken power law model produces a very high confidence value for AO 0235+16. The peak in the confidence contour (Figure 5.7) is sharp and well constrained in terms of both slope and break. The best fit parameters are a slope of $\alpha = -2.1$ and $f_{\rm b} = 10^{-7.15}$Hz at a confidence of 96.5%.

A Gaussian fit to the confidence contour produces the peak values and errors quoted in Table 5.2. The break timescale of 117 days is in good agreement with the

Table. 5.2: Summary of SF results for AO 0235+164.

Model	Confidence(%)	Slope (α)	Break Timescale (Days)
BPL	96.5	-2.24±0.16	117^{+103}_{-55}

timescale of 139 days obtained using the PDS simulations. Figure 5.8 shows that the simulated average structure function for this model is an excellent fit to the observed structure function.

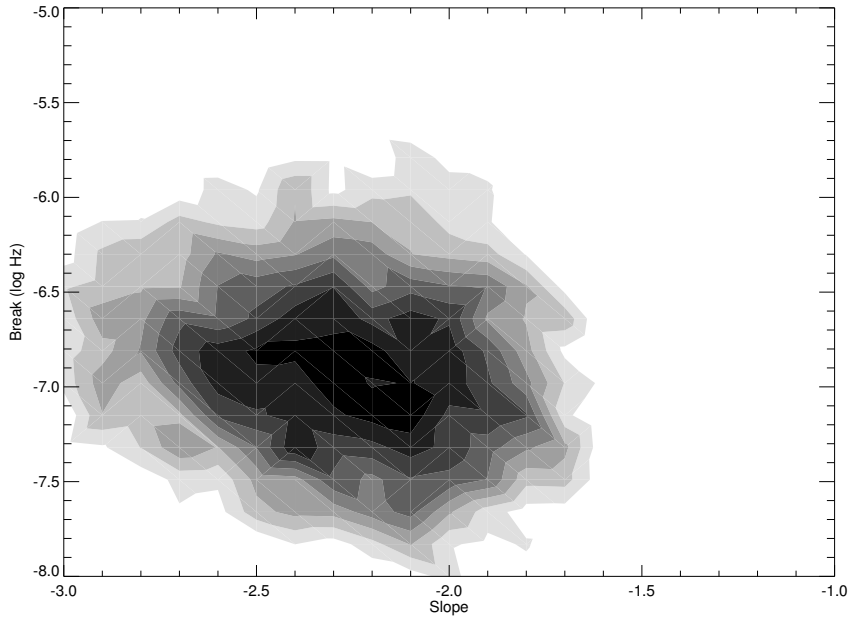

Figure. 5.7: Confidence contour for the broken power law model for AO 0235+16 using structure function simulations. Highest confidence is 96.5% at $\alpha = -2.1$ and $f_{\rm b} = 10^{-7.15}$Hz.

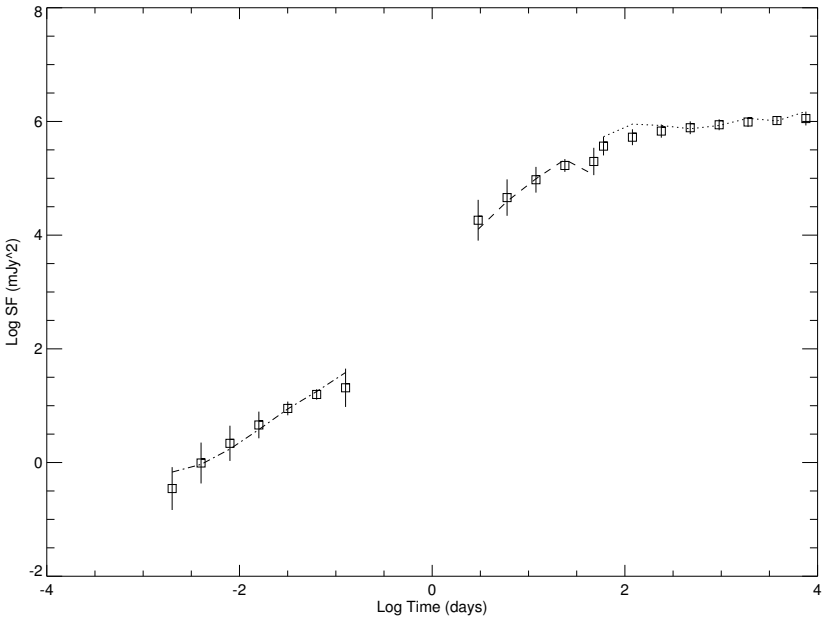

Figure. 5.8: Structure function of AO 0235+164. Lines represent the observed structure function, points with error the structure function of the best fit broken power law simulation. Best fit parameters are $\alpha = -2.1$ and $f_{\rm b} = 10^{-7.15}$Hz.

5.2 0430+052

5.2.1 0430+052 - Power Density Spectrum

Observations for 3C 120 were well-sampled for the long term light curve. The medium and short term light curves are also reasonably sampled, but suffer from large uncertainties in the apparent magnitude. These uncertainties are primarily caused by the large uncertainties for comparison stars in the field of 3C 120. Attempts are currently underway to obtain a better magnitude calibration for 3C 120 using absolute photometry.

Unlike that of AO 0235+16, the confidence contour for 3C 120 is not well defined. Figure 5.9 displays the confidence contour, peaked at a value of 75.9%, near the edge of the parameter grid space. The best fit parameters are a slope of $\alpha = -1.8$ and a break frequency of $f_{\rm b} = 10^{-8.66}$Hz. The low value for break frequency is beyond the lowest observed frequency for this object, transforming the model into an unbroken power law with a slope of -1.8 in the observed frequency range.

The results of the knee model simulations for 3C 120 are nearly identical to those of the broken power law model. The best confidence value is 67.0% at a slope of $\alpha = -1.8$ and $f_{\rm b} = 10^{-9.00}$Hz (Figure 5.10). Again, the best fit break frequency is well beyond the lowest observed frequency. Therefore, both models that include a break in slope appear to be poor fits to the observed data.

The unbroken power law, supported by the poor fits for the broken power law

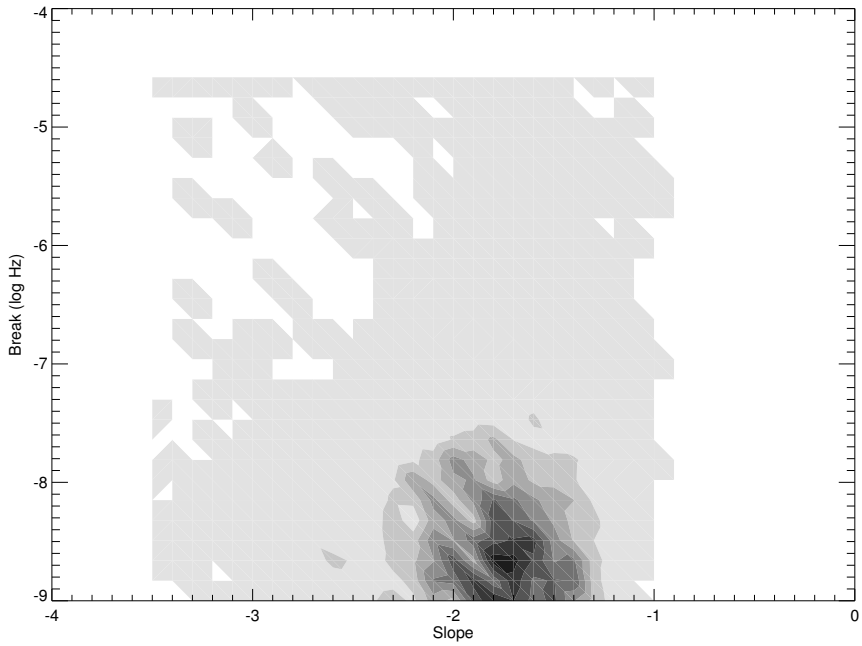

Figure. 5.9: Confidence contour for the broken power law model for 3C 120. Highest confidence is 75.9% at $\alpha = -1.8$ and $f_{\rm b} = 10^{-8.66}$Hz.

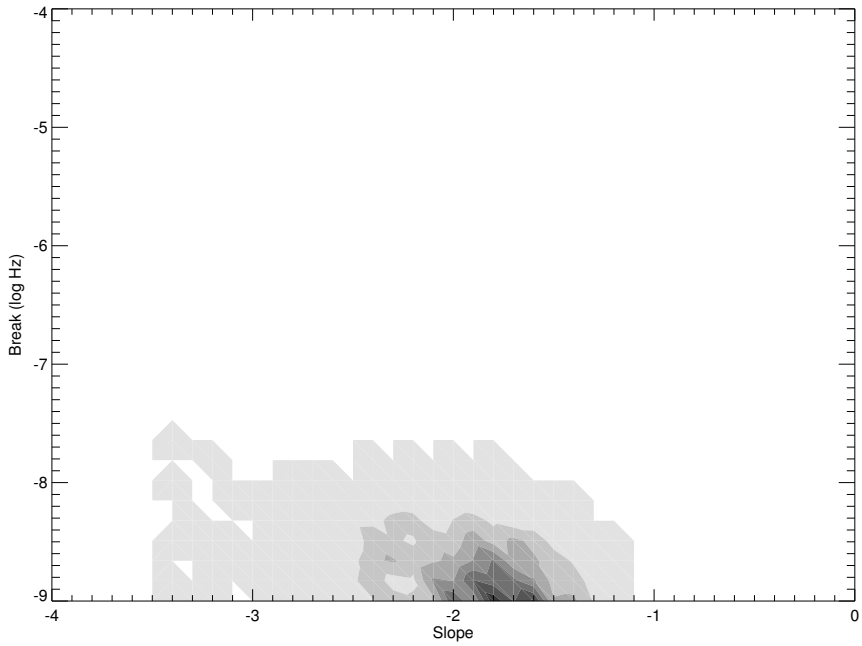

Figure. 5.10: Confidence contour for the knee power law model for 3C 120. Highest confidence is 67.0% at $\alpha = -1.8$ and $f_{\rm b} = 10^{-9.00}$Hz.

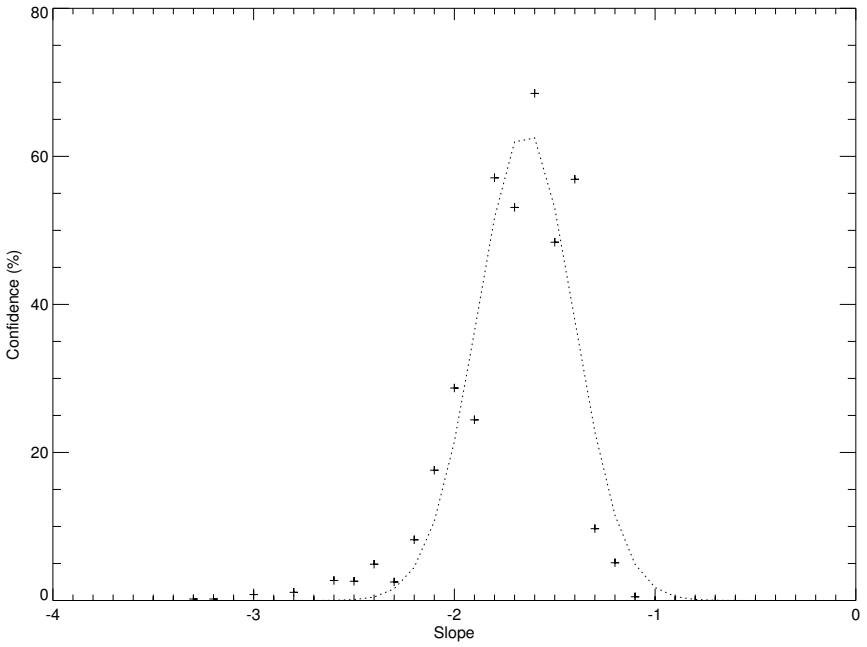

Figure. 5.11: Confidence contour for the unbroken power law model for 3C 120. Highest confidence is 68.5% at $\alpha = -1.6$.

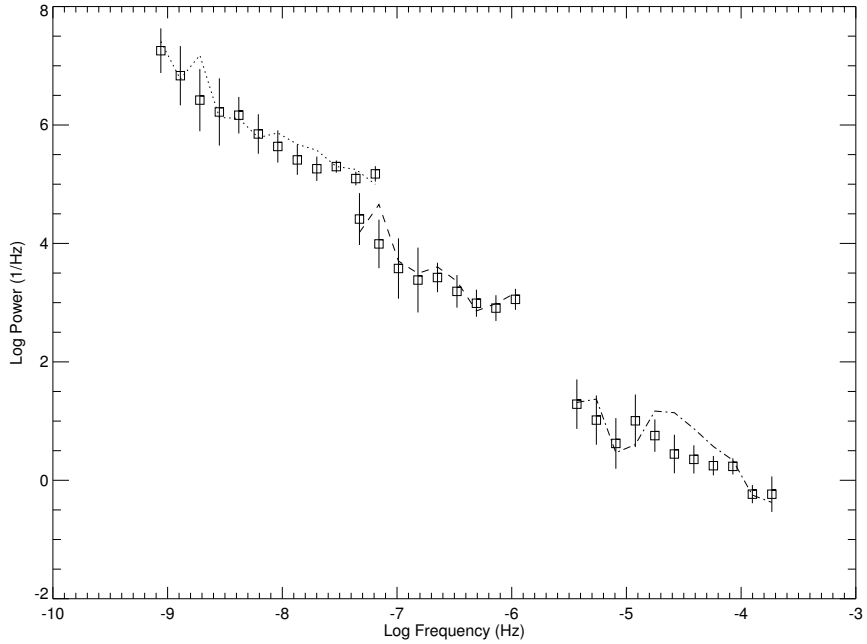

Figure. 5.12: Power density spectrum of 3C 120. Lines represent the observed power spectrum, points with error the power density spectrum of the best fit unbroken power law simulation. Best fit slope is $\alpha = -1.6$.

models, shows a similar confidence value of 68.5%. The confidence contour for the unbroken power law is displayed in Figure 5.11, indicating a slope value of $\alpha = -1.6$. The best fit simulated power spectrum and the observed power spectrum are also shown in Figure 5.12.

Every test model used on the 3C 120 data supports an unbroken power law in this object. If a break in slope does occur, it must be located outside of the observed frequency range. All models are in good agreement with a constant value of slope near $\alpha = -1.7$.

Table. 5.3: Summary of PDS results for 3C 120.

Model	Confidence(%)	Slope (α)	Break Timescale (Days)
PL	68.5	-1.65±0.10	...
BPL	75.9	-1.74±0.12	> 3500
Knee	67.0	-1.76±0.11	> 3500

The break timescales listed in Table 5.3 correspond to the lower limit in observed frequency, $\sim 10^{-8.5}$Hz. Under the assumption that the PDS of 3C 120 does possess a break at lower frequencies than those observed, this value can be thought of as an estimated lower limit of its break timescale.

5.2.2 0430+052 - Structure Function

Structure function simulations were carried out on the data for 3C 120 using the unbroken power law model. The structure function analysis supports the results

obtained through PDS analysis, with a slope of $\alpha = -1.6$ and confidence value of 69.5% (Table 5.4).

Table. 5.4: Summary of SF results for 3C 120.

Model	Confidence(%)	Slope (α)	Break Timescale (Days)
PL	69.5	-1.67±0.06	...

Figure 5.14 displays the best fit simulated structure function and the observed structure function of 3C 120 for the unbroken power law model. The simulated structure function is in good agreement with the observed structure function at all timescales.

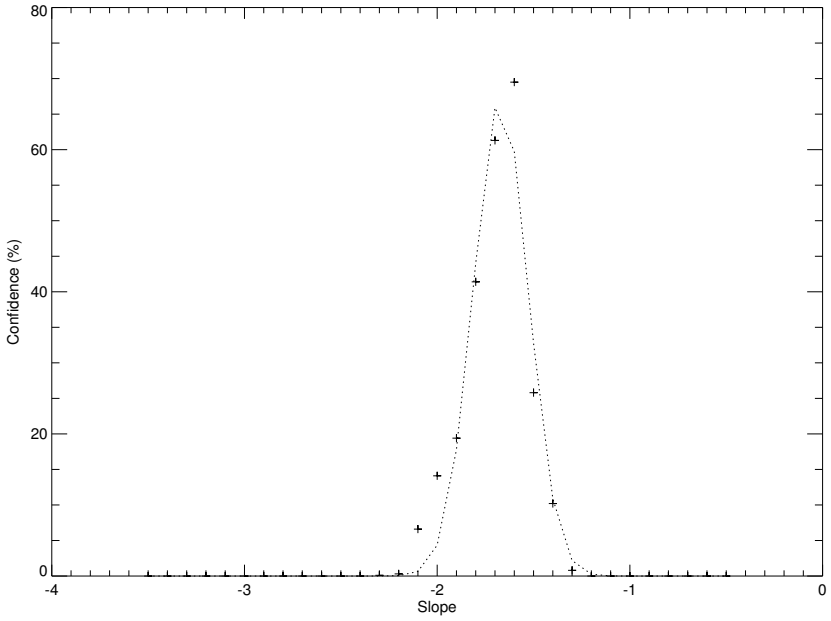

Figure. 5.13: Confidence contour for the unbroken power law model for 3C 120 using structure function simulations. Highest confidence is 69.5% at $\alpha = -1.6$.

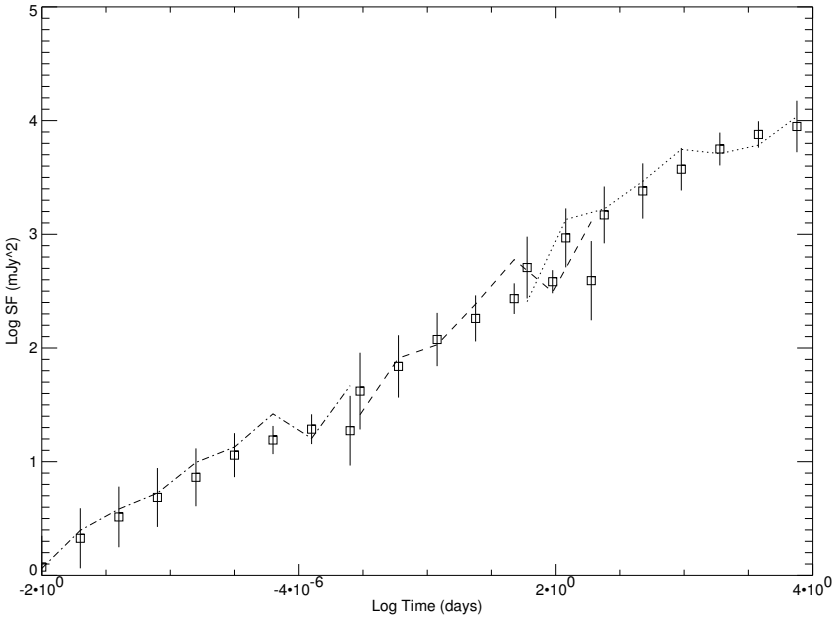

Figure. 5.14: Structure function of 3C 120. Lines represent the observed structure function, points with error the structure function of the best fit unbroken power law simulation. Best fit slope is $\alpha = -1.6$.

5.3 0735−178

5.3.1 0735−178 - Power Density Spectrum

The light curves for PKS 0735+178 are not sampled at an optimal rate. Medium timescale information is the most lacking, due to no regularly spaced monitoring over the course of one observing season. The low declination of PKS 0735+178 makes it an ideal candidate for future monitoring using SMARTS queued observations.

The confidence contour for the broken power law model is displayed in Figure 5.15. The best fit model is described by a slope of $\alpha = -2.3$ and $f_{\rm b} = 10^{-6.83}$Hz at a confidence level of 65.6%. The confidence contour is not as smooth as those seen for other blazars, with a broad plateau of high confidences and many smaller peaks.

The plot of the observed power spectrum and average simulated power spectrum for the broken power law model is shown in Figure 5.16. While the observed power spectrum at low frequencies flattens significantly, this behavior is likely not intrinsic to the variability of the object. Described in Chapter 3, the effects of Poisson noise and alias can add a constant level of power to the observed and simulated power spectra. The fact that the average simulated power spectrum matches the observed power spectrum well in the flat region, despite having a model slope of -1.0, indicates the the PSRESP routine accounts for these distortions properly.

Figure 5.17 displays the confidence contour for the knee power law model with the best fit confidence value of 60.6%. The knee model contour is also broad in shape,

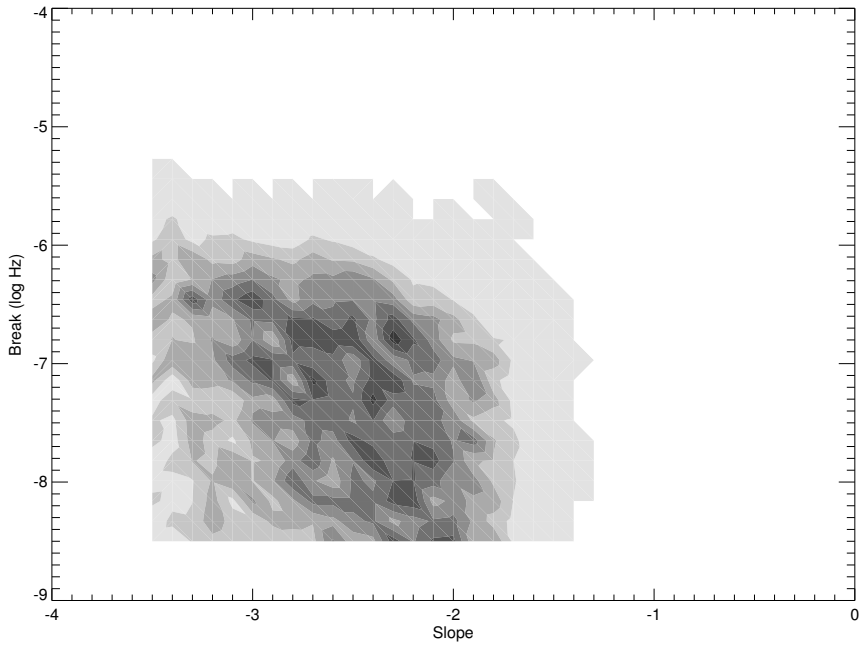

Figure. 5.15: Confidence contour for the broken power law model for PKS 0735+178. Highest confidence is 65.6% at $\alpha = -2.3$ and $f_{\rm b} = 10^{-6.83}$Hz.

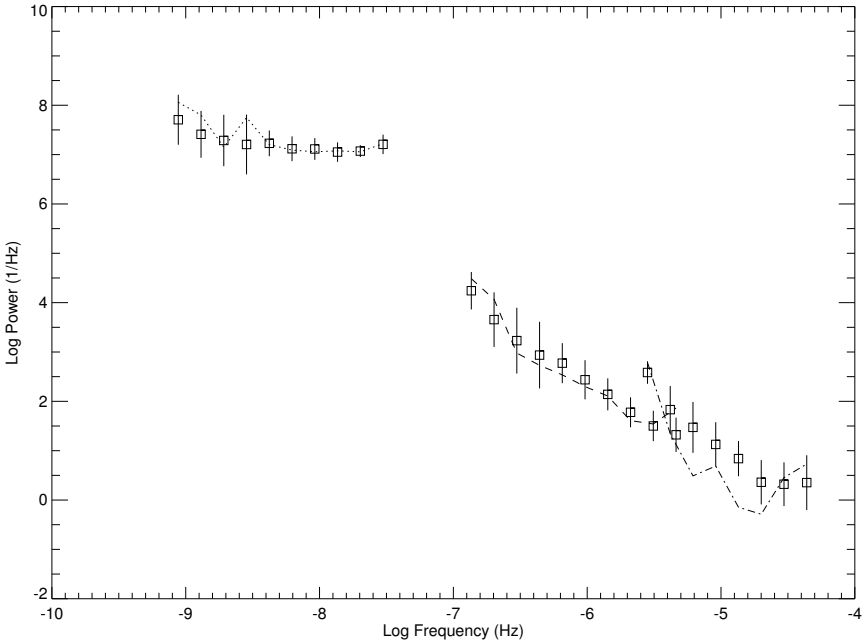

Figure. 5.16: Power density spectrum of PKS 0735+178. Lines represent the observed power spectrum, points with error the power density spectrum of the best fit simulation. Best fit parameters are $\alpha = -2.3$ and $f_{\rm b} = 10^{-6.83}$Hz.

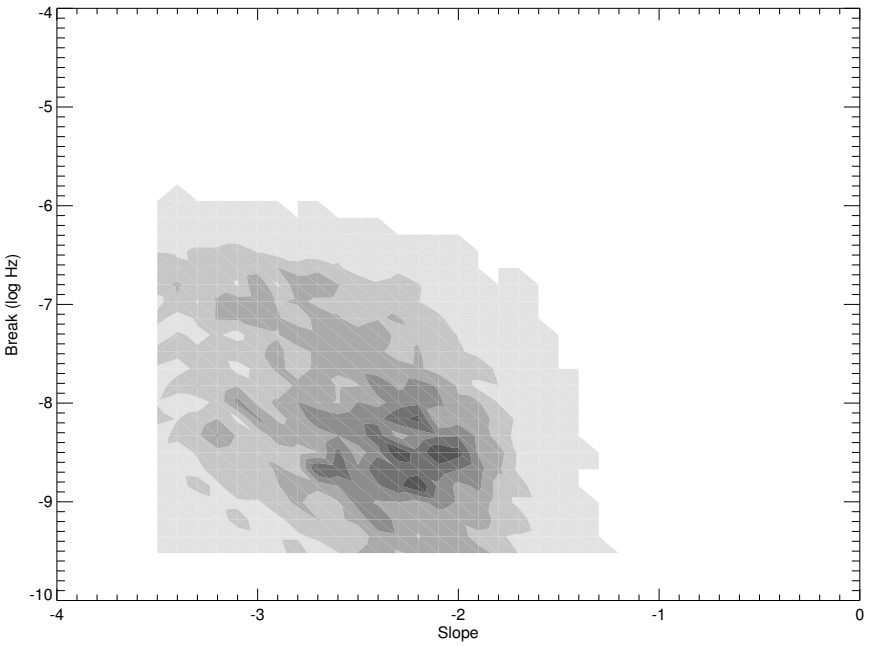

Figure. 5.17: Confidence contour for the knee power law model for PKS 0735+178. Highest confidence is 60.6% at $\alpha = -2.1$ and $f_{\rm b} = 10^{-8.50}$Hz.

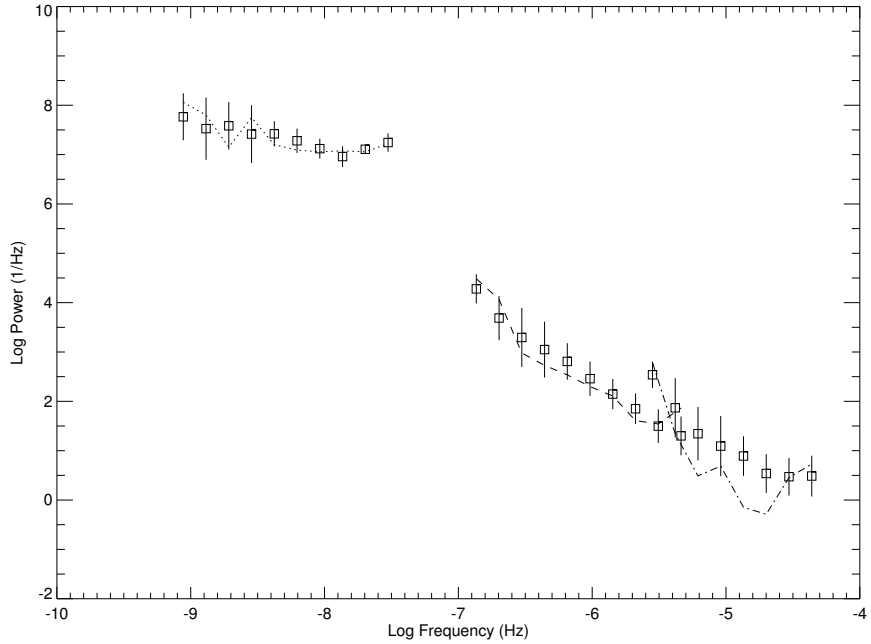

Figure. 5.18: Power density spectrum of PKS 0735+178. Lines represent the observed power spectrum, points with error the power density spectrum of the best fit knee simulation. Best fit parameters are $\alpha = -2.1$ and $f_{\rm b} = 10^{-8.50}$Hz.

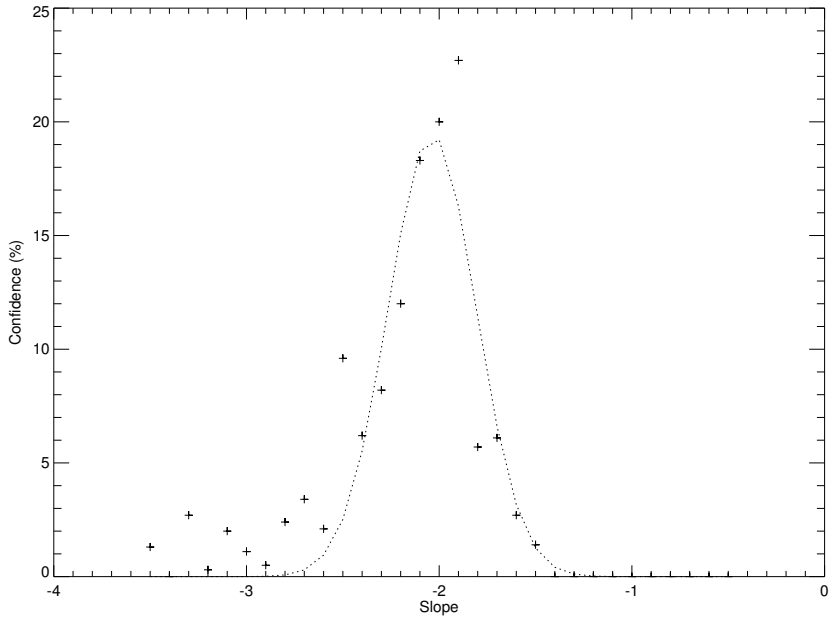

Figure. 5.19: Confidence contour for the unbroken power law model for PKS 0735+178. Highest confidence is 22.7% at $\alpha = -1.9$.

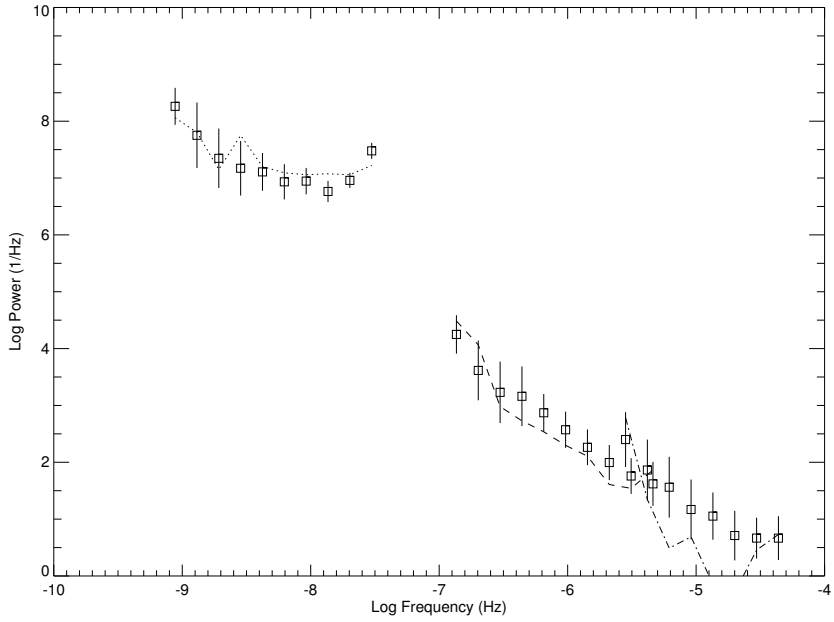

Figure. 5.20: Power density spectrum of PKS 0735+178. Lines represent the observed power spectrum, points with error the power density spectrum of the best fit unbroken power law simulation. Best fit slope is $\alpha = -1.9$.

indicating that the fit is not well defined. The best fit parameter values are a slope of $\alpha = -2.1$ and break frequency of $f_{\rm b} = 10^{-8.50}$Hz. This value of break frequency is significantly lower than that obtained through the broken power law model, but it still within the observed frequency range.

The fit to the observed power spectrum, seen in Figure 5.18, is very similar to that of the broken power law model. The coarseness of the contour plot, combined with the fact that the suggested break occurs in the distorted, low frequency segment of the PDS suggest that the confidence in this break may be overestimated. The analysis for PKS 0735+178 would benefit greatly from a more even sampling of data at all timescales.

The unbroken power law model provides a reasonable fit to the data with a slope of $\alpha = -1.9$ and peak confidence value of 22.7% (Figure 5.19). The observed power spectrum and average simulated power spectrum are shown in Figure 5.20. The peak in the simulated PDS near a frequency of $10^{-7.5}$Hz is caused by the yearly sampling pattern of the data. The peak is more prevalent in the unbroken power law model due to the higher amount of variability power at lower frequencies when compared to the broken power law models.

Table 5.5 displays the confidence and best fit parameter estimations for PKS 0735+178. While the values for the slope are relatively consistent, the break timescales found for the broken power law and knee power law models differ by an order of magnitude. Both values for break timescale also have large uncertainties, due to the broad

nature of the confidence contours described above.

Table. 5.5: Summary of PDS results for PKS 0735+178.

Model	Confidence(%)	Slope (α)	Break Timescale (Days)
PL	22.7	-2.04±0.10	...
BPL	65.6	-2.57±0.20	462^{+789}_{-291}
Knee	60.6	-2.25±0.16	4401^{+4977}_{-2336}

The results of the PDS analysis for PKS 0735+178 suggest the possibility of a broken power law form but with a degree of uncertainty in the exact location of the break frequency. Additional monitoring of PKS 0735+178 would be greatly beneficial toward determining a reliable break timescale for the object.

5.3.2 0735−178 - Structure Function

The confidence contour for the broken power law model using structure function analysis is displayed in Figure 5.21. The maximum confidence value of 66.4% corresponds to a slope of $\alpha = -2.6$ and break frequency of $f_{\rm b} = 10^{-7.49}$Hz.

Table. 5.6: Summary of SF results for PKS 0735+178.

Model	Confidence(%)	Slope (α)	Break Timescale (Days)
BPL	66.4	-2.53±0.17	281^{+197}_{-116}

Figure 5.22 shows the observed structure function and average simulated structure function for PKS 0735+178. The fit is in relatively good agreement with the observed data, with the largest deviations occurring at medium timescales. This is also the

window in which PKS 0735+178 sampling is the poorest. Estimations for slope and break timescale are displayed in Table 5.6. The break timescale of 280 days detected through the structure function analysis is slightly lower than the 462 days obtained through the power density spectrum.

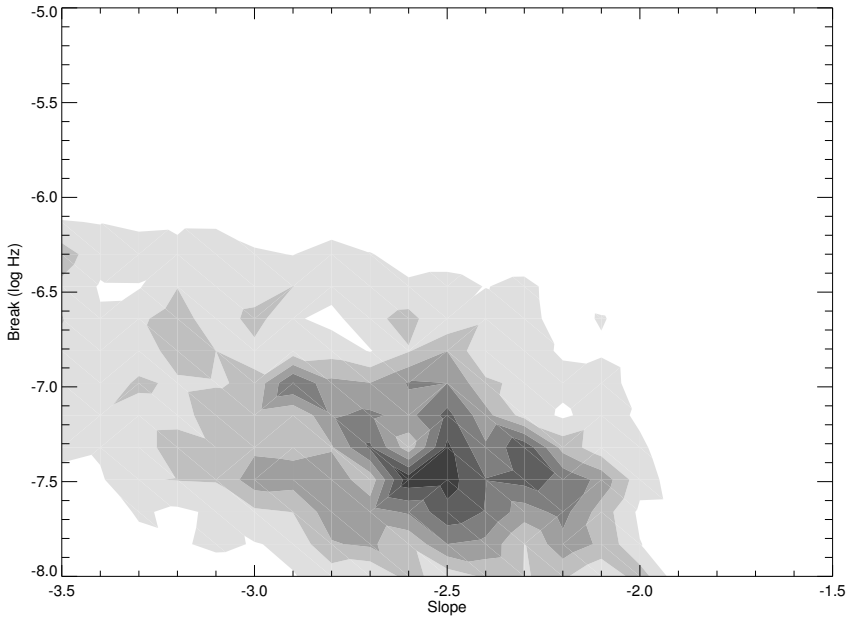

Figure. 5.21: Confidence contour for the broken power law model for PKS 0735+178 using structure function simulations. Highest confidence is 66.4% at $\alpha = -2.6$ and $f_{\rm b} = 10^{-7.49}$Hz.

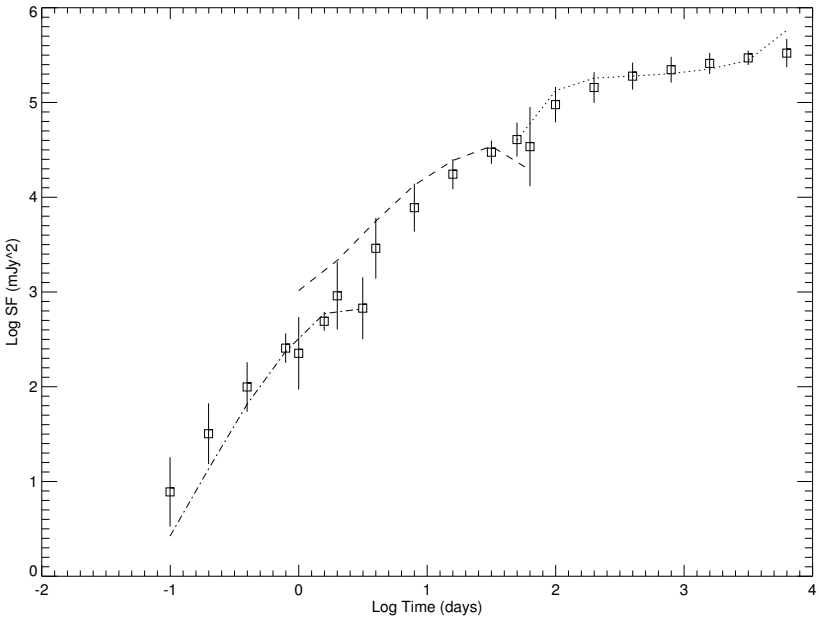

Figure. 5.22: Structure function of PKS 0735+178. Lines represent the observed structure function, points with error the structure function of the best fit broken power law simulation. Best fit parameters are $\alpha = -2.6$ and $f_{\rm b} = 10^{7.49}$Hz.

5.4 0851+203

5.4.1 0851+203 - Power Density Spectrum

OJ 287 has one of the most complete long term light curves in the sample. Medium timescales are also well measured through queued observations from the SMARTS 1.3m. The broadband PDS of OJ 287 spans of frequency range of $10^{-9.0} - 10^{-4.5}$Hz.

The confidence contour for the broken power law model is displayed in Figure 5.23. The contour is well constrained in terms of break frequency, with a wider spread in confidence for slope values. The best fit parameters are a slope of $\alpha = -2.2$ and a break frequency of $f_{\rm b} = 10^{-7.64}$Hz, at a confidence of 43.6%. The break frequency for OJ 287 is low compared to other blazars, but still well within the observed frequency range. In addition, the shape of the contour is clearly peaked, unlike the broken power law contours seen for 3C 120.

A comparison between the observed power spectrum and the simulated power spectrum is shown in Figure 5.24. The observed power spectrum is fit well at all but the lowest frequencies, where the simulated power appears offset to slightly lower values. For any time series data set, the variability power at the lowest frequencies is the least well sampled due to a lack of data points at very long time lags. Recognizing the size of the error in the simulated power spectrum at low frequencies, the fit is acceptable.

A similar fit to the observed power spectrum is obtained using the knee power

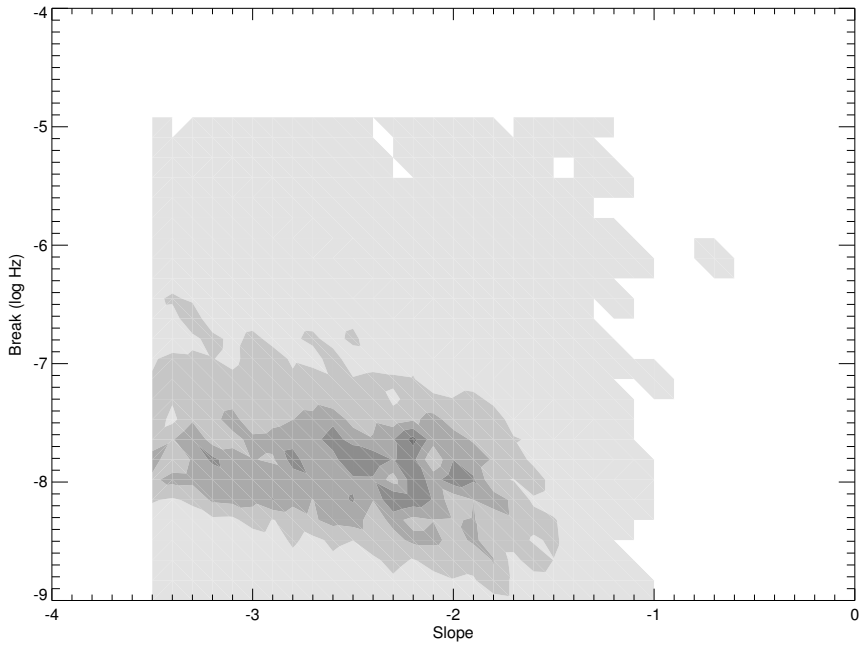

Figure. 5.23: Confidence contour for the broken power law model for OJ 287. Highest confidence is 43.6% at $\alpha = -2.2$ and $f_{\rm b} = 10^{-7.64}$Hz.

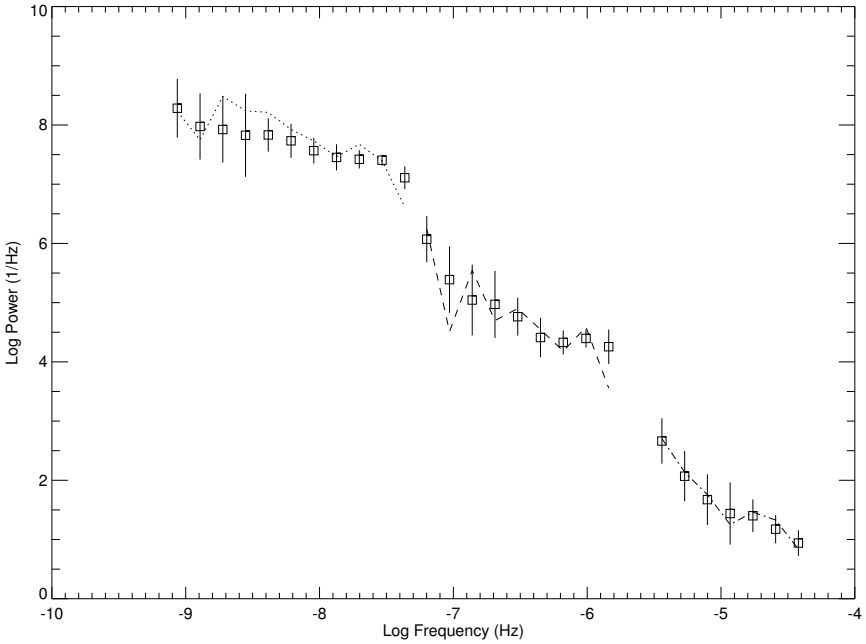

Figure. 5.24: Power density spectrum of OJ 287. Lines represent the observed power spectrum, points with error the power density spectrum of the best fit simulation. Best fit parameters are $\alpha = -2.2$ and $f_{\rm b} = 10^{-7.64}$Hz.

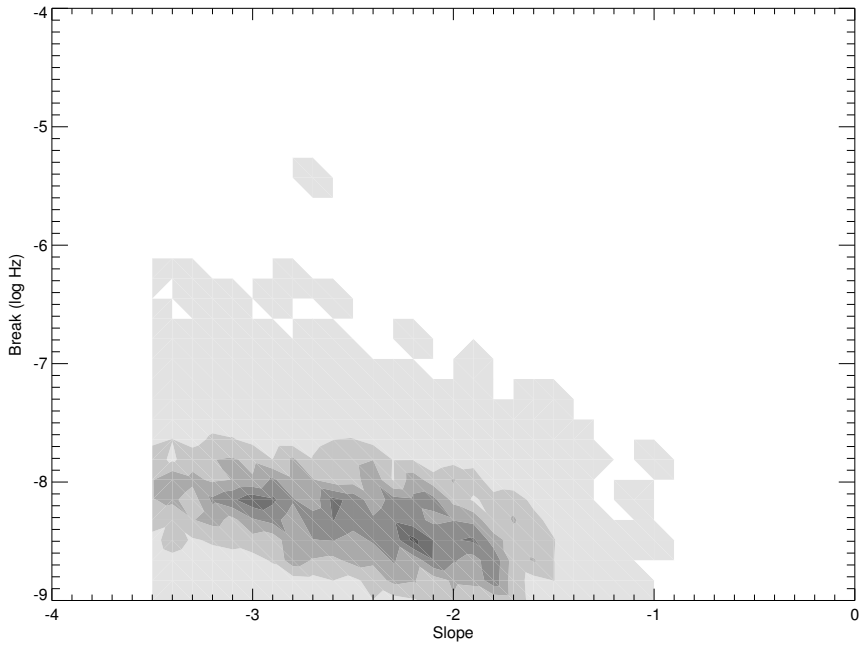

Figure. 5.25: Confidence contour for the knee power law model for OJ 287. Highest confidence is 53.3% at $\alpha = -2.2$ and $f_{\rm b} = 10^{-8.49}$Hz.

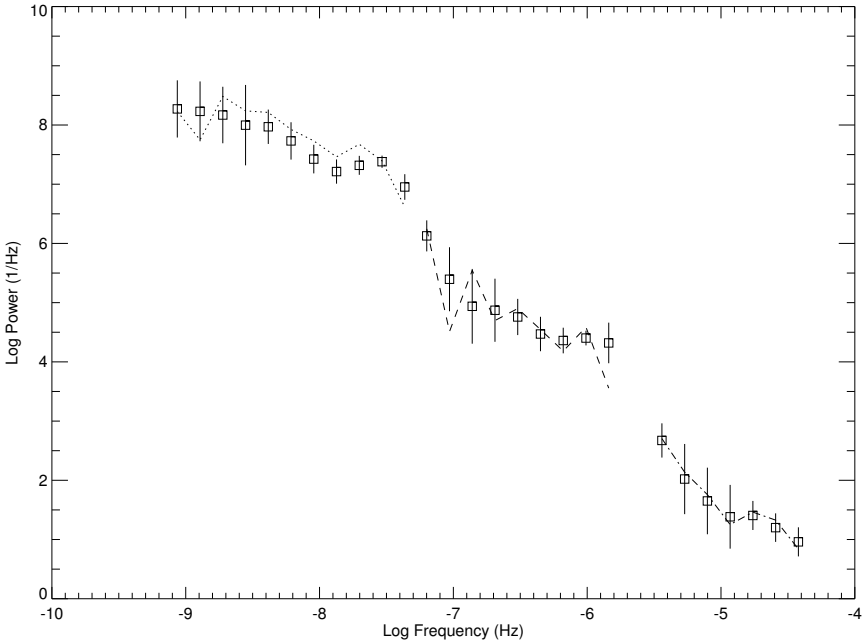

Figure. 5.26: Power density spectrum of OJ 287. Lines represent the observed power spectrum, points with error the power density spectrum of the best fit knee simulation. Best fit parameters are $\alpha = -2.2$ and $f_{\rm b} = 10^{-8.49}$Hz.

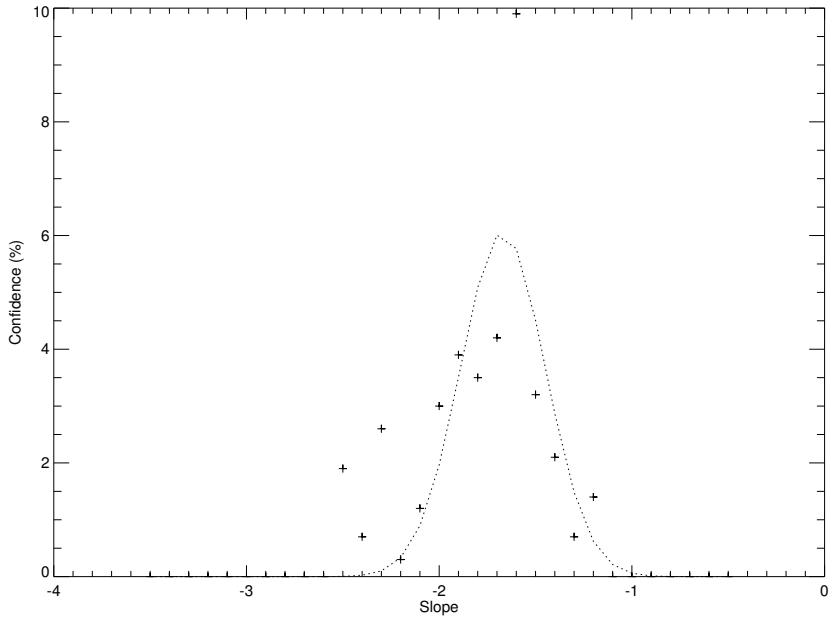

Figure. 5.27: Confidence contour for the unbroken power law model for OJ 287. Highest confidence is 9.9% at $\alpha = -1.6$.

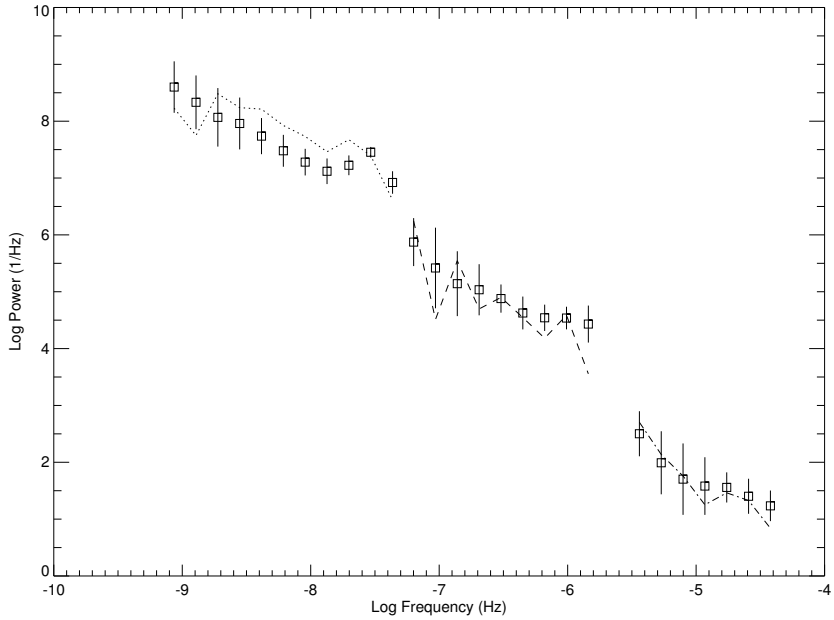

Figure. 5.28: Power density spectrum of OJ 287. Lines represent the observed power spectrum, points with error the power density spectrum of the best fit unbroken power law simulation. Best fit slope is $\alpha = -1.6$.

law model. Figure 5.25 displays the confidence contour using the knee power law for OJ 287. The best fit parameters are a slope of $\alpha = -2.2$ and a break frequency of $f_{\rm b} = 10^{-8.49}$Hz at a confidence of 53.3%. The break frequency is near the lowest observed frequency of $\sim 10^{-9.0}$Hz, but appears well defined.

The model fit to the observed data, displayed in Figure 5.25, shows a nearly identical form to the broken power law at medium and high frequencies. At low frequencies, the knee model provides a modestly improved fit over the sharply broken power law.

The unbroken power law model produces the worst confidence value of the three models at 9.9%. The confidence contour, with a best fit slope of $\alpha = -1.6$, is shown in Figure 5.27. Figure 5.28 clearly shows that the unbroken power law is not a good fit to all segments of the PDS. The slope appears too steep at low frequencies and too shallow at medium frequencies.

Table. 5.7: Summary of PDS results for OJ 287.

Model	Confidence(%)	Slope (α)	Break Timescale (Days)
PL	9.9	-1.67±0.09	...
BPL	43.6	-2.59±0.28	906^{+543}_{-340}
Knee	53.3	-2.28±0.21	2792^{+1170}_{-824}

The PDS analysis results for OJ 287 are displayed in Table 5.7. The results support a broken power law of some form in OJ 287, with both the knee and the broken power law models having significantly higher confidence values than the unbroken power law.

The break timescales are relatively large compared to the other blazars in the sample, but appear well constrained both broken power law models.

5.4.2 0851+203 - Structure Function

Structure function analysis on the light curves for OJ 287 result in a high confidence value (80.8%) for the broken power law model. The confidence contour, shown in Figure 5.29, is very narrow in break frequency profile but considerably broader in terms of slope. The best model parameters are a slope of $\alpha = -2.6$ and a break frequency of $f_{\rm b} = 10^{-7.98}$Hz.

Table. 5.8: Summary of SF results for OJ 287.

Model	Confidence(%)	Slope (α)	Break Timescale (Days)
BPL	80.8	-2.72±0.18	1042^{+286}_{-225}

The Gaussian estimates for slope and break timescale (Table 5.8) provide a reasonable fit to the observed structure function shape at all timescales, as demonstrated in Figure 5.30. The large value of break timescale, 1042 days, is consistent with the value of 906 days determined through PDS analysis.

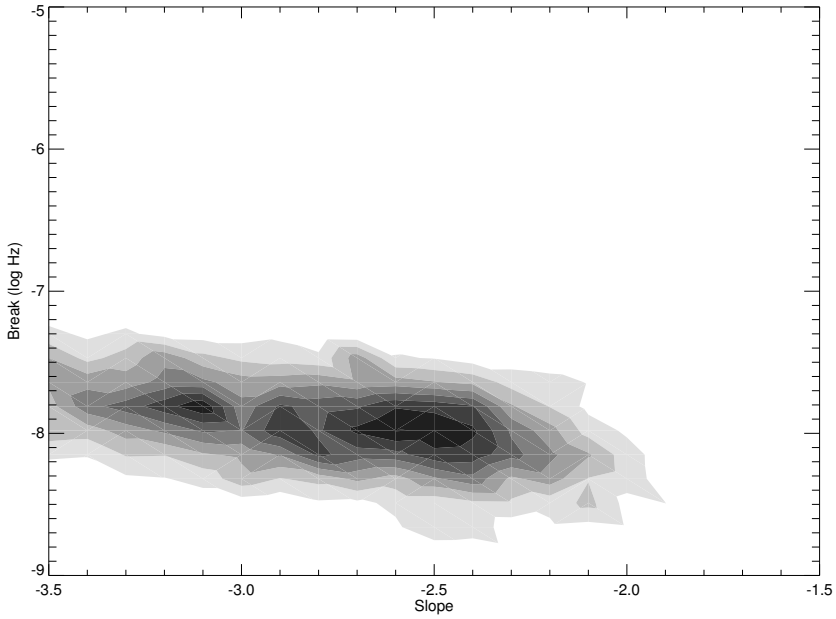

Figure. 5.29: Confidence contour for the broken power law model for OJ 287 using structure function simulations. Highest confidence is 80.8% at $\alpha = -2.6$ and $f_{\rm b} = 10^{-7.98}$Hz.

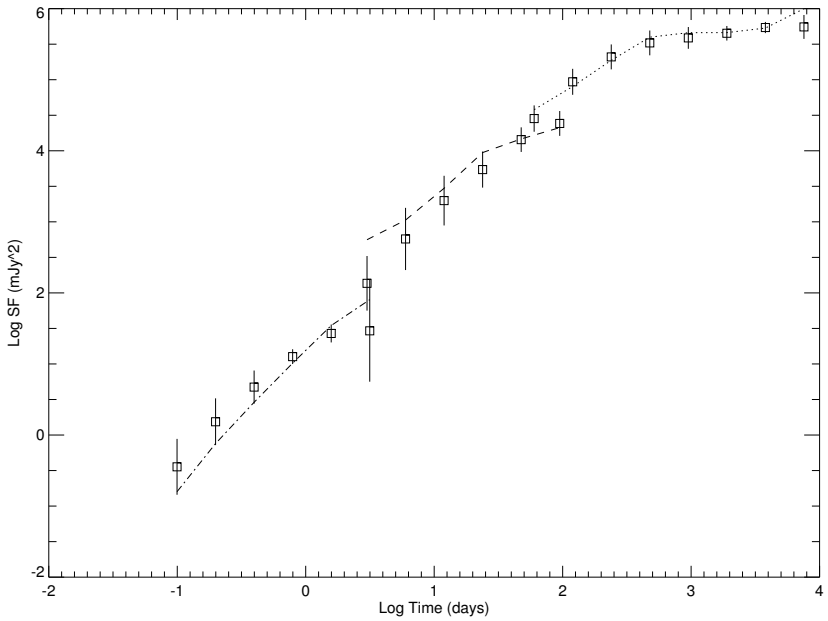

Figure. 5.30: Structure function of OJ 287. Lines represent the observed structure function, points with error the structure function of the best fit broken power law simulation. Best fit parameters are $\alpha = -2.6$ and $f_{\rm b} = 10^{-7.98}$Hz.

5.5 1253−055

5.5.1 1253−055 - Power Density Spectrum

3C 279 has been observed regularly through queued SMARTS observations for the past 5 years, leading to a very well-sampled light curve at medium timescales. On longer timescales, however, 3C 279 is drastically under-sampled. Literature searches for this object did not produce enough data in order to form a quality long term light curve. A PDS frequency range of $10^{-8.5} - 10^{-3.0}$Hz was obtained using the data obtained by the PEGA group over the past decade.

The results for the broken power law simulations for 3C 279 are similar to those seen for 3C 120. The highest confidence levels are located at the edge of the break parameter grid, with a peak value of 33.6% at a slope of $\alpha = -1.5$ and break frequency of $f_{\rm b} = 10^{-7.83}$Hz. As with the results of 3C 120, this is indicative of a better fit by an unbroken power law in the observed frequency range.

The observed power spectrum and simulated power spectrum are displayed in Figure 5.32. The simulated power is a good fit to the observed power at low and medium frequencies, but appears to underestimate the slope at high frequencies.

The confidence contour for the knee power law model is shown in Figure 5.33. The maximum confidence is 34.7% at a slope of $\alpha = -1.5$ and a break frequency of $f_{\rm b} = 10^{-8.65}$Hz. The best fit break frequency is above the lowest observed frequency for the knee model and therefore suggests an unbroken power law in this frequency

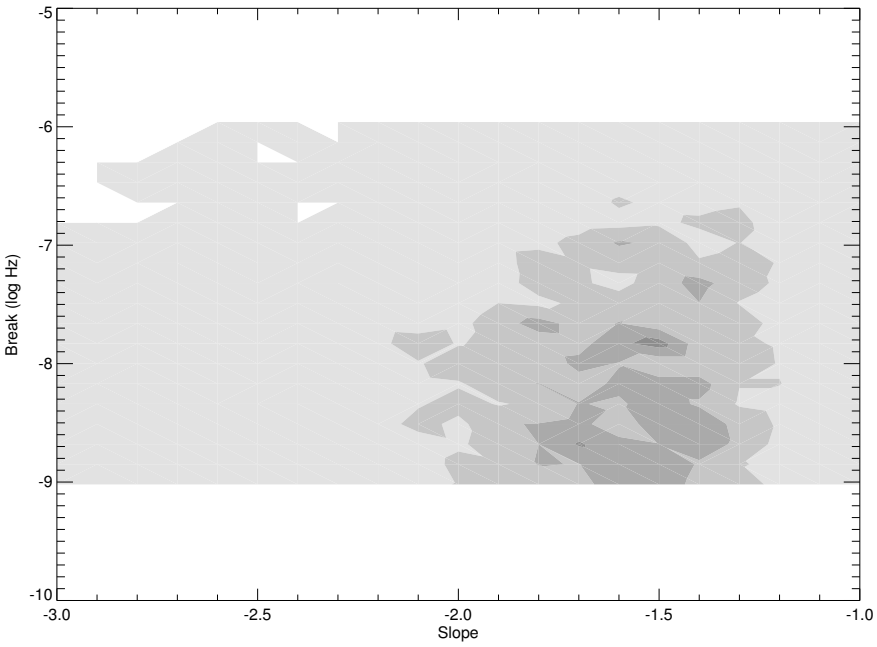

Figure. 5.31: Confidence contour for the broken power law model for 3C 279. Highest confidence is 33.6% at $\alpha = -1.5$ and $f_b = 10^{-7.83}$Hz.

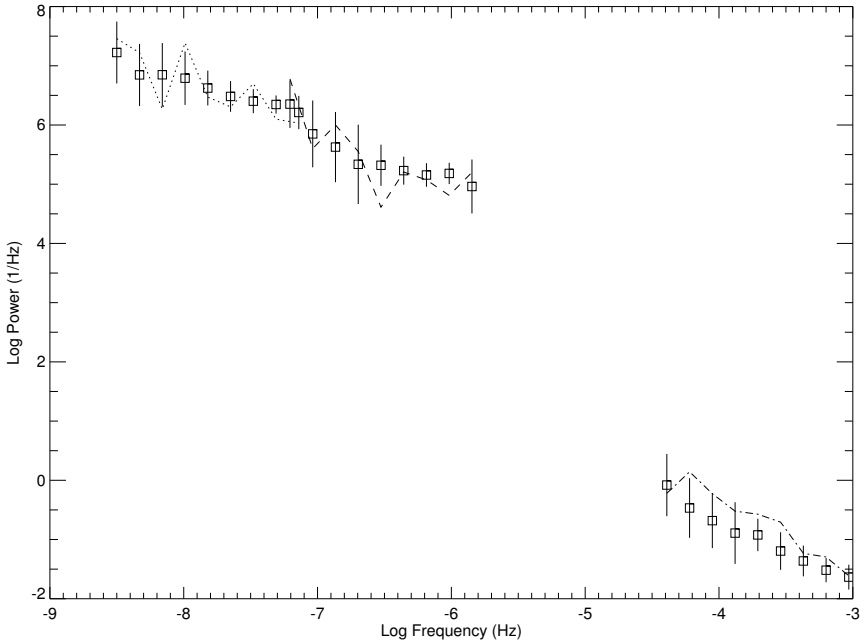

Figure. 5.32: Power density spectrum of 3C 279. Lines represent the observed power spectrum, points with error the power density spectrum of the best fit simulation. Best fit parameters are $\alpha = -1.5$ and $f_{\rm b} = 10^{-7.83}$Hz.

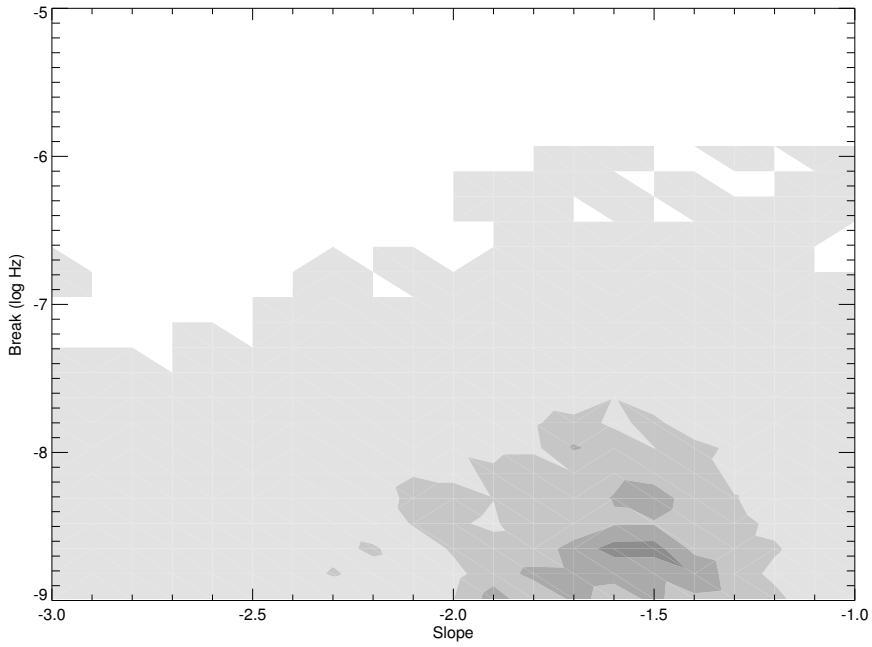

Figure. 5.33: Confidence contour for the knee power law model for 3C 279. Highest confidence is 34.7% at $\alpha = -1.5$ and $f_{\rm b} = 10^{-8.65}$Hz.

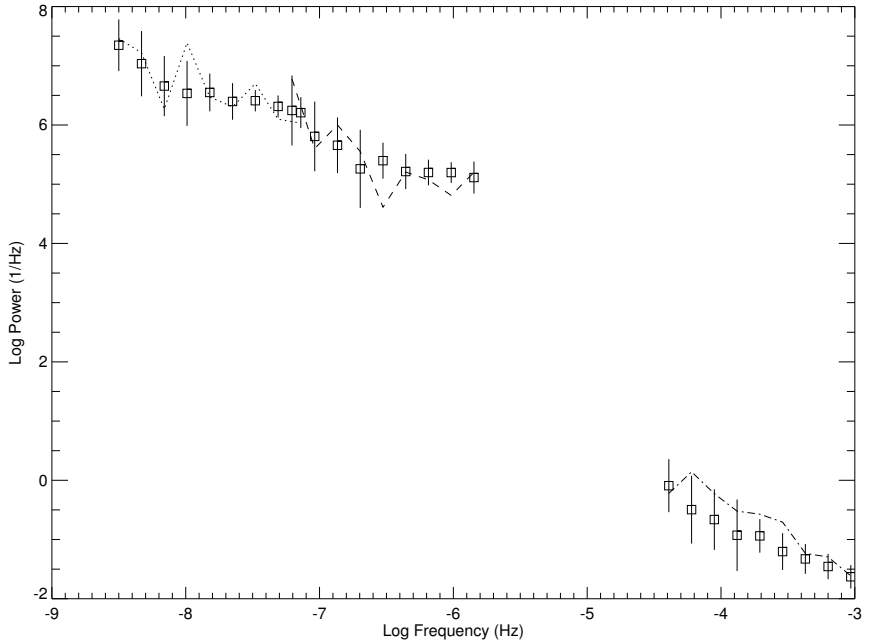

Figure. 5.34: Power density spectrum of 3C 279. Lines represent the observed power spectrum, points with error the power density spectrum of the best fit knee simulation. Best fit parameters are $\alpha = -1.5$ and $f_{\rm b} = 10^{-8.65}$Hz.

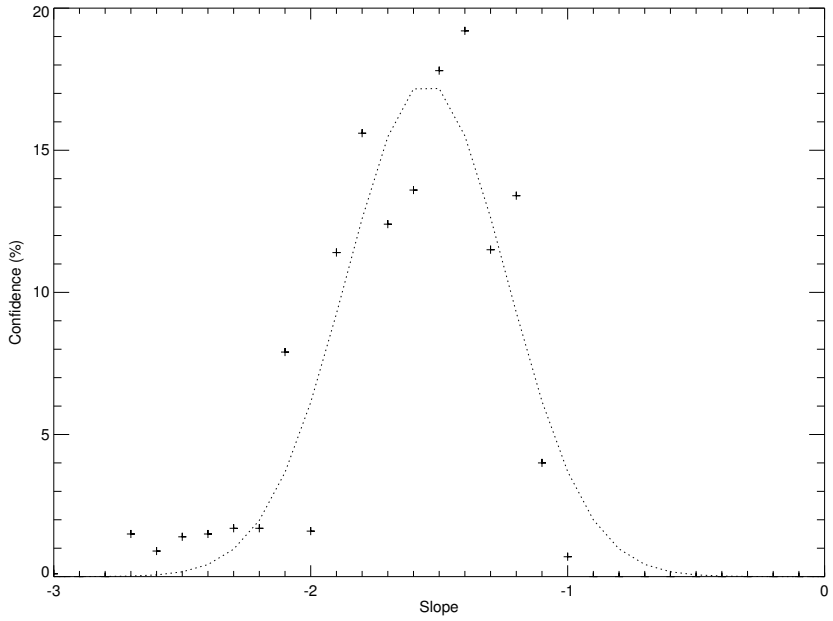

Figure. 5.35: Confidence contour for the unbroken power law model for 3C 279. Highest confidence is 19.2% at $\alpha = -1.4$.

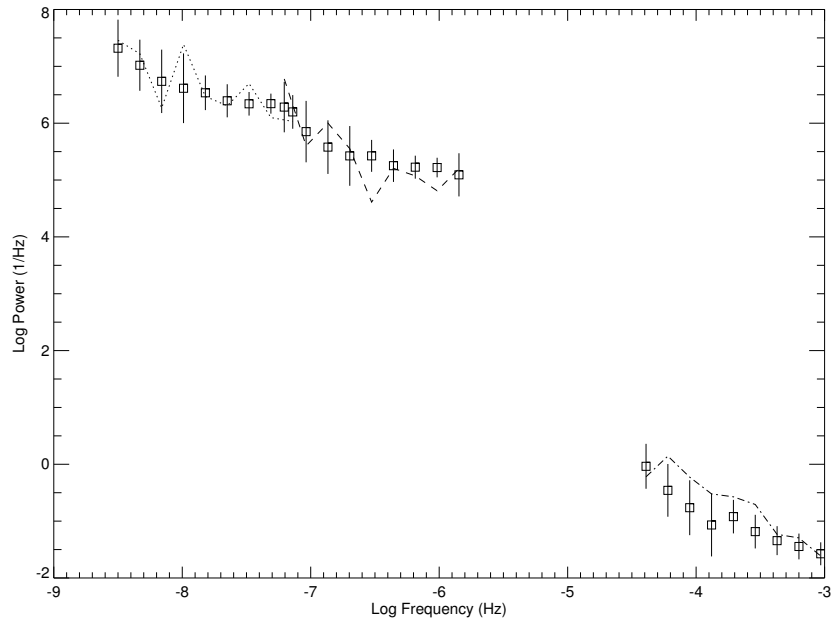

Figure. 5.36: Power density spectrum of 3C 279. Lines represent the observed power spectrum, points with error the power density spectrum of the best fit unbroken power law simulation. Best fit slope is $\alpha = -1.4$.

range. The power spectrum fit, displayed in Figure 5.34, shows an underestimation in the simulated power at high frequencies similar to that seen in the broken power law model.

The unbroken power law model provides a modest fit to the variability of 3C 279, with a confidence of 19.2% at a slope of $\alpha = -1.4$. The confidence contour for this model is shown in Figure 5.35. The slope appears to match the low frequency power well (Figure 5.36), but is too shallow for both the medium and high frequency data.

A summary of the PDS simulation results for 3C 279 are shown in Table 5.9. All three models support an unbroken power law within the observed frequency range. They share a common value of slope near $\alpha \sim -1.6$. Assuming the break frequency for 3C 279 is beyond the lowest observed frequency, a lower limit of 3500 days is estimated for the break timescale.

Table. 5.9: Summary of PDS results for 3C 279.

Model	Confidence(%)	Slope (α)	Break Timescale (Days)
PL	19.2	-1.55±0.13	...
BPL	33.6	-1.62±0.13	> 3500
Knee	34.7	-1.59±0.11	> 3500

The observed PDS of 3C 279 displays a large gap centered near a frequency of $10^{-5.0}$Hz. This gap is common in almost all of the data sets presented in this dissertation and represents a problem for any observations carried out with ground based, optical telescopes. This frequency gap corresponds to timescales near one day and

cannot be completely overcome due to the diurnal observing cycle. A prescription for optimum frequency coverage with optical telescopes will be discussed in Chapter 6.

5.5.2 1253−055 - Structure Function

The confidence contour for the broken power law model using structure function analysis is displayed in Figure 5.37. Similar to the results from the PDS analysis, the peak in the confidence contour (55.3%) is at the edge of the parameter space, beyond the lowest observed frequency. The best fit model values of slope ($\alpha = 2.1$) and break frequency ($f_{\rm b} = 10^{-8.50}$Hz) are an indication that an unbroken power law is supported by the structure function analysis as well.

Table. 5.10: Summary of SF results for 3C 279.

Model	Confidence(%)	Slope (α)	Break Timescale (Days)
PL	51.7	-2.00±0.10	...
BPL	55.3	-1.98±0.10	> 3500

Simulations were also carried out using the unbroken power law model and the structure function for 3C 279. The results of the model simulations can be seen in Figure 5.39 and Figure 5.40. The confidence contour for the unbroken power law is fit very well with a Gaussian and produces slope estimate of $\alpha = -1.98 \pm 0.10$, displayed in Table 5.10. The values of slope obtained through the structure function ($\alpha \sim -2.0$) are slightly steeper than those from the PDS ($\alpha \sim -1.6$).

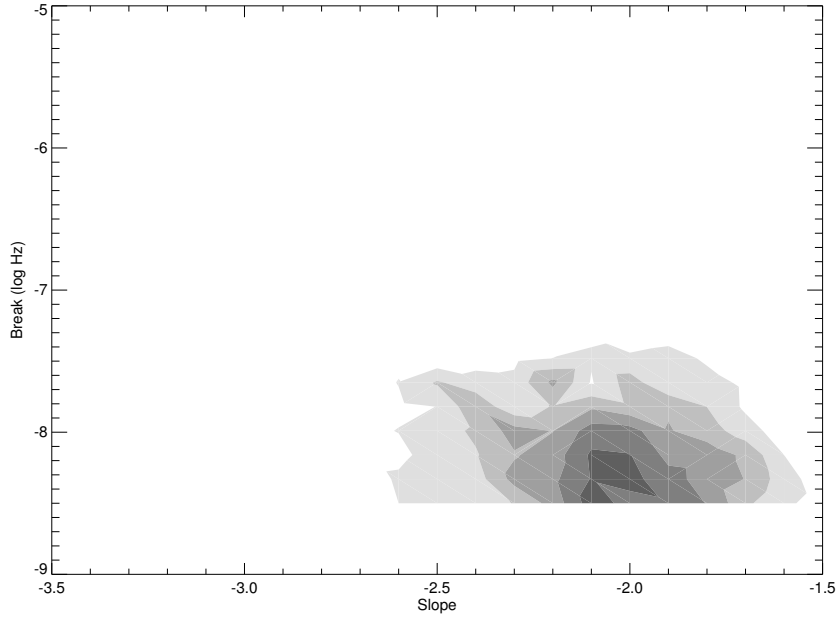

Figure. 5.37: Confidence contour for the broken power law model for 3C 279 using structure function simulations. Highest confidence is 55.3% at $\alpha = -2.1$ and $f_{/mathrmb} = 10^{-8.50}$Hz.

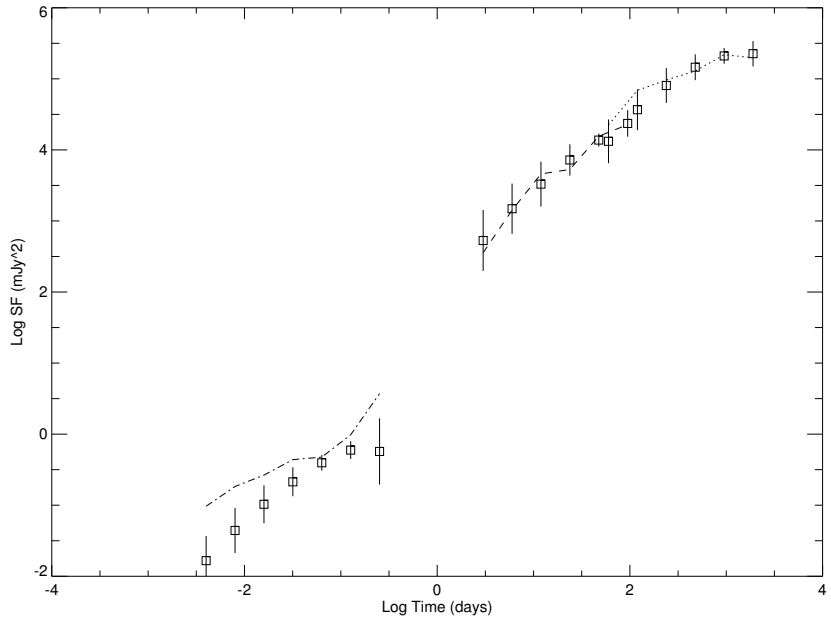

Figure. 5.38: Structure function of 3C 279. Lines represent the observed structure function, points with error the structure function of the best fit broken power law simulation. Best fit parameters are $\alpha = -2.1$ and $f_{\rm b} = 10^{-8.50}$Hz.

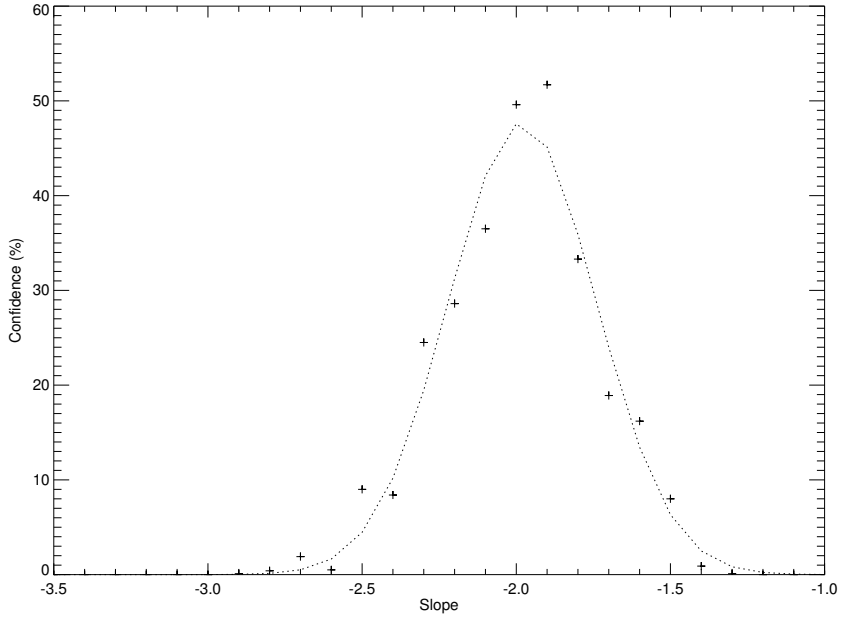

Figure. 5.39: Confidence contour for the unbroken power law model for 3C 279 using structure function simulations. Highest confidence is 51.7% at $\alpha = -1.9$.

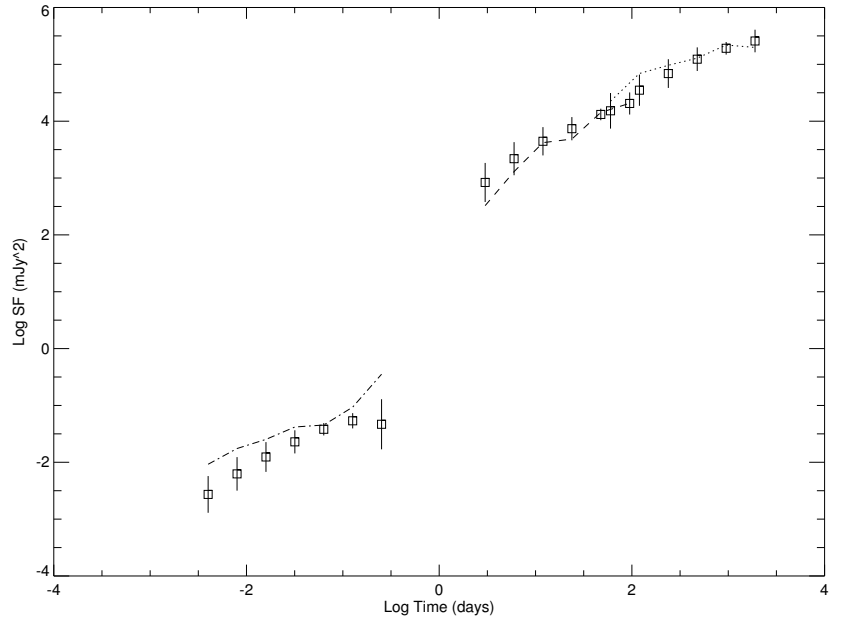

Figure. 5.40: Structure function of 3C 279. Lines represent the observed structure function, points with error the structure function of the best fit unbroken power law simulation. Best fit slope is $\alpha = -1.9$.

5.6 1510−089

5.6.1 1510−089 - Power Density Spectrum

Similar to 3C 279, PKS 1510−089 has been observed steadily with the SMARTS program over the past five years. The regular monitoring from queued observations has produced well-sampled light curves on medium timescales. At shorter timescales, multiple observing runs have been devoted to the monitoring of PKS 1510−089, leading to well-sampled light curves on short timescales. On longer timescales, data from the PEGA group are limited to the past decade and the amount of published data is minimal. The overall PDS for PKS 1510−089 constructed from these observations covers a range of $10^{-8.5}$-$10^{-3.0}$Hz.

The broken power law model (Figure 5.41) produces a peak confidence value of 63.5%, with a slope of $\alpha = -2.2$ and break frequency $f_{\rm b} = 10^{-7.48}$Hz. The shape of the contour is broad in terms of both slope and break frequency, indicating that the fit is not well constrained.

Figure 5.42 displays the observed power spectrum and the average simulated power spectrum for the broken power law model. The simulated power appears in good agreement at all frequencies, including the sharp break near $10^{-7.5}$Hz. The relatively large uncertainties on individual points may contribute to the broad shape of the confidence contour.

The confidence contours for the knee power law model are shown in Figure 5.43.

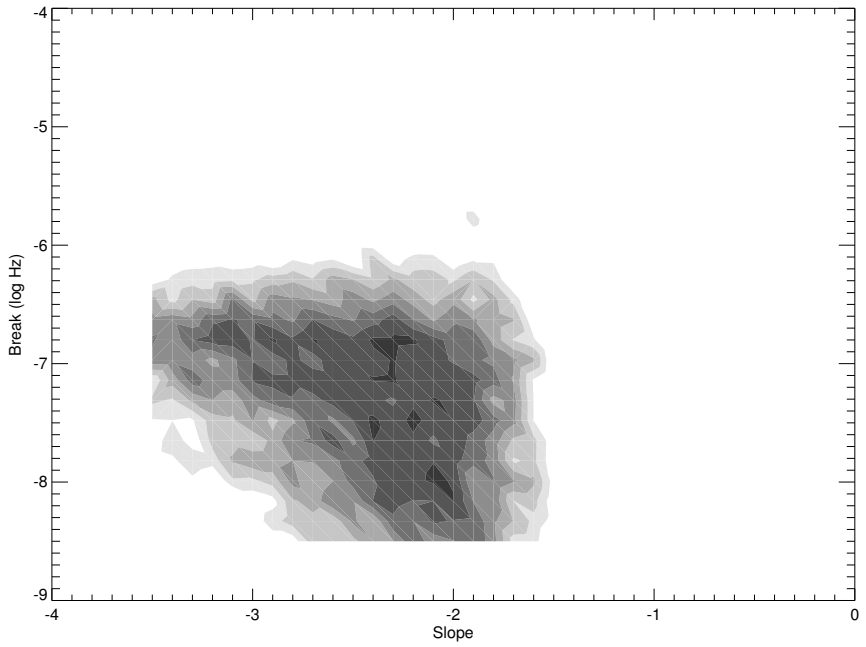

Figure. 5.41: Confidence contour for the broken power law model for PKS 1510−089. Highest confidence is 63.5% at $\alpha = -2.2$ and $f_{\rm b} = 10^{-7.48}$Hz.

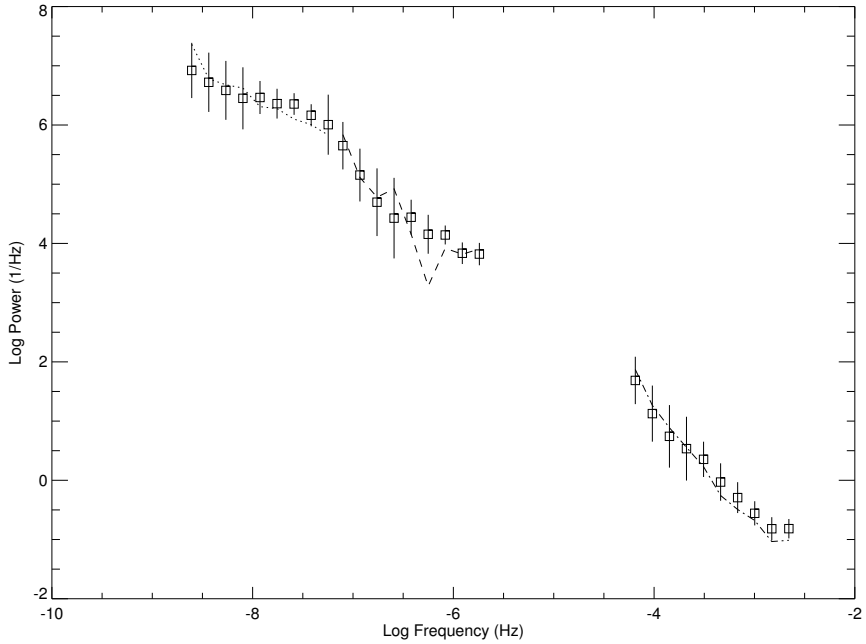

Figure. 5.42: Power density spectrum of PKS 1510−089. Lines represent the observed power spectrum, points with error the power density spectrum of the best fit simulation. Best fit parameters are $\alpha = -2.2$ and $f_{\rm b} = 10^{-7.48}$Hz.

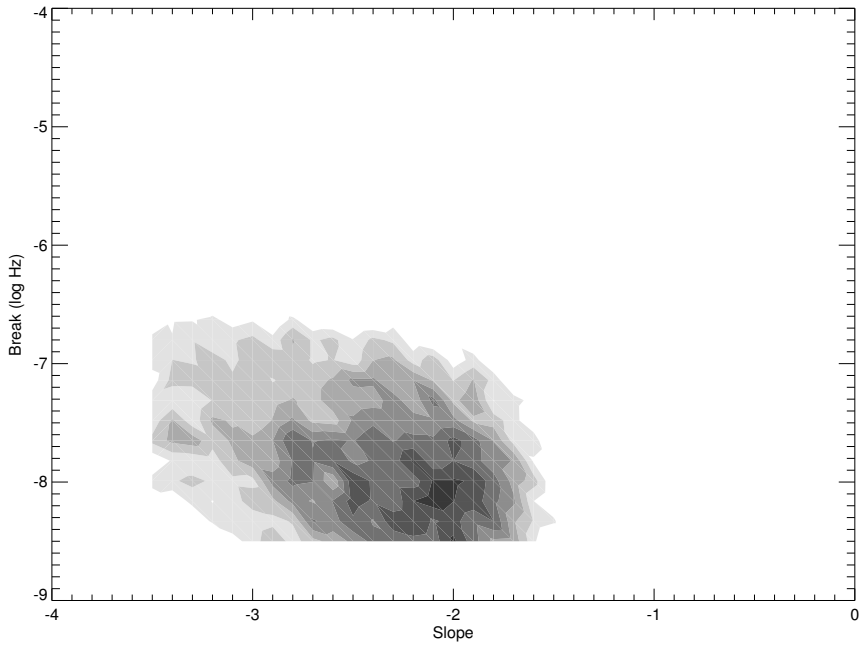

Figure. 5.43: Confidence contour for the knee power law model for PKS 1510−089. Highest confidence is 65.5% at $\alpha = -2.1$ and $f_{\rm b} = 10^{-8.16}$Hz.

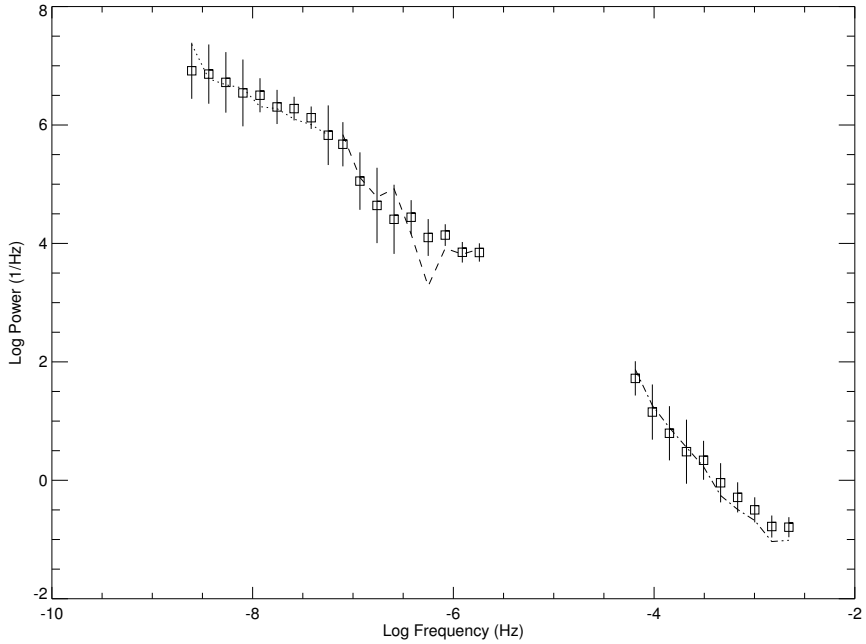

Figure. 5.44: Power density spectrum of PKS 1510−089. Lines represent the observed power spectrum, points with error the power density spectrum of the best fit simulation. Best fit parameters are $\alpha = -2.1$ and $f_{\rm b} = 10^{-8.16}$Hz.

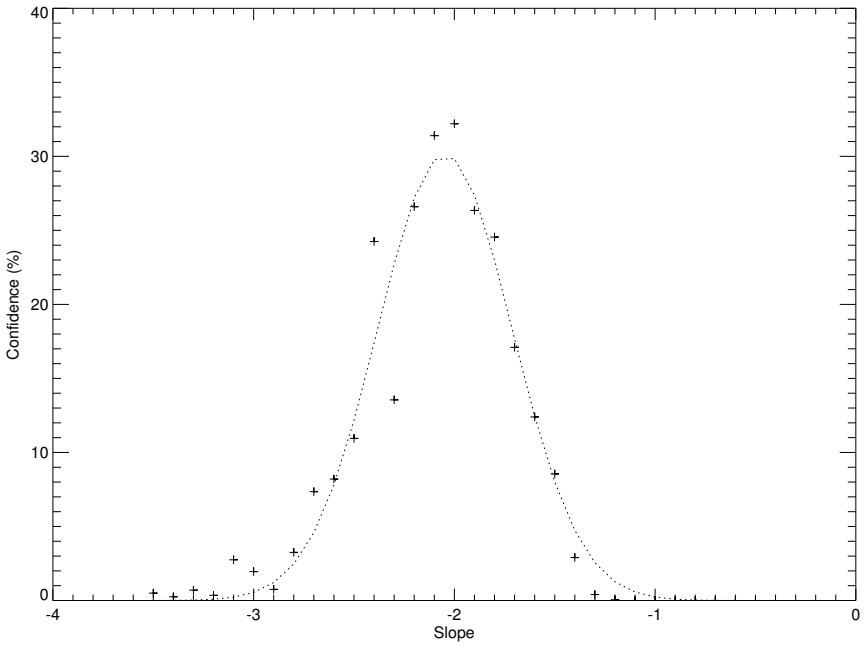

Figure. 5.45: Confidence contour for the unbroken power law model for PKS 1510−089. Highest confidence is 32.2% at $\alpha = -2.0$.

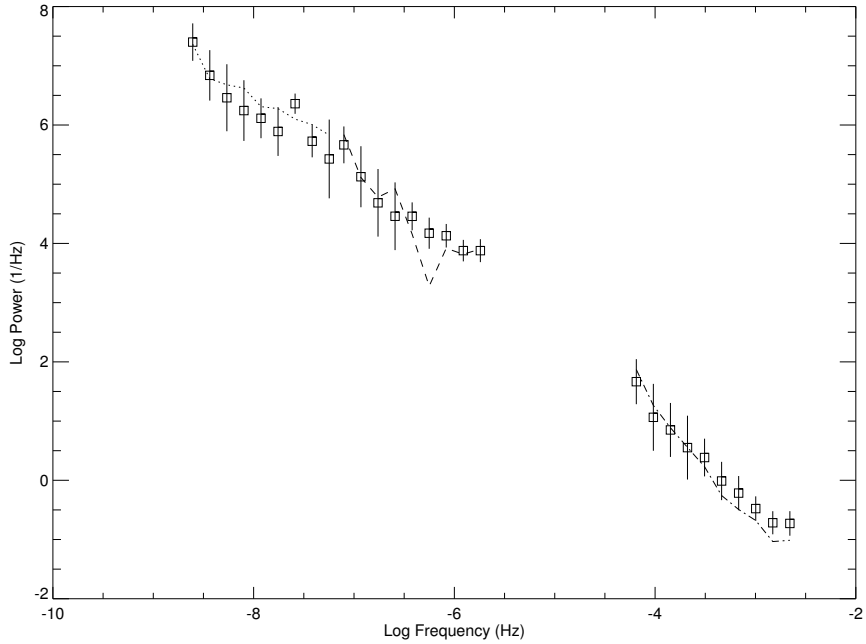

Figure. 5.46: Power density spectrum of PKS 1510−089. Lines represent the observed power spectrum, points with error the power density spectrum of the best fit simulation. Best fit slope is $\alpha = -2.0$.

The peak confidence value of 65.5% corresponds to a slope of $\alpha = -2.1$ and a break frequency of $f_{\rm b} = 10^{-8.16}$Hz. Although this break frequency is near the lowest observed frequency, the contour appears well defined. The confidence values for both the broken and knee power law models are almost equal, indicating that either model provides an acceptable fit to the data.

As with many other objects in the sample, the knee break frequency is lower than that of the broken power law. This behavior is most likely caused by the smoother transition between slopes inherent to the knee model. As seen in Figure 5.44, the simulated power matches the observed power at most frequencies. There is some evidence that the knee model is too shallow at the lowest measured frequencies.

The unbroken power law also provides a reasonable good fit to the data for PKS 1510−089, though at a significantly lower confidence than that of the models with a break in slope. The confidence contour, seen in Figure 5.45, has a peak value of 32.2% at a slope of $\alpha = -2.0$.

The unbroken power law fit to the observed power spectrum, displayed in Figure 5.46, is in good agreement at medium and high frequencies. At low frequencies, the slope of $\alpha = -2.0$ appears too steep. A longer and better sampled light curve on longer timescales would greatly improve the uncertainties in this frequency range.

A summary of the results from the PDS simulations for PKS 1510−089 is shown in Table 5.11. The break timescale for the broken power law model is ∼450 days, with large uncertainties due to the broad shape of the confidence contour. The timescale

Table. 5.11: Summary of PDS results for PKS 1510−089.

Model	Confidence(%)	Slope (α)	Break Timescale (Days)
PL	32.2	-2.05±0.14	...
BPL	63.5	-2.36±0.25	447^{+881}_{-297}
Knee	65.5	-2.31±0.24	1280^{+1550}_{-701}

from the knee power law model is much larger at ∼1280 days, although both agree on a high frequency slope of $\alpha \sim -2.3$ and the large error bars on the two break timescales indicate no significant difference between them. The unbroken power law also provides a reasonable fit, although at a reduced confidence level compared to the broken power law models. The fit is therefore improved by the addition of a break in slope of the PDS for PKS 1510-089.

5.6.2 1510−089 - Structure Function

The confidence contour for the broken power law model using structure function analysis is shown in Figure 5.47. The peak confidence value is low (22.0%) with best fit parameters of a slope $\alpha = -2.7$ and a break frequency $f_{\rm b} = 10^{-7.82}$Hz. Figure 5.48 displayed the observed structure function and the best fit simulated power spectrum for PKS 1510−089. The fit is not optimal, especially at short and medium timescales.

Table. 5.12: Summary of SF results for PKS 1510−089.

Model	Confidence(%)	Slope (α)	Break Timescale (Days)
BPL	22.0	-3.00±0.17	529^{+244}_{-167}

Despite the low confidence value, the best fit break frequency corresponds to a timescale that is in good agreement with that produced through the PDS analysis. Table 5.12 summarizes the results from the structure function analysis for PKS 1510−089. The break timescale of 529 days is close to the value of 447 days obtained through PDS analysis with the broken power law model.

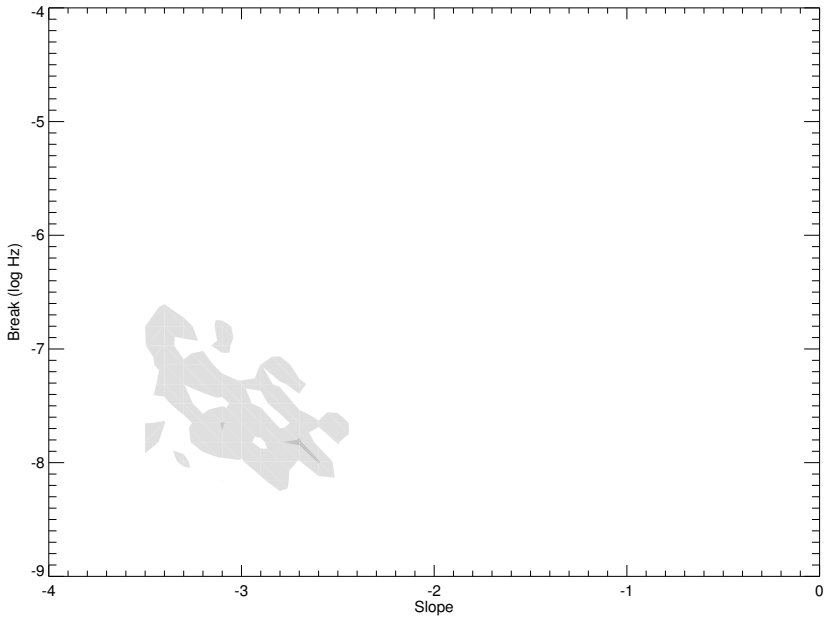

Figure. 5.47: Confidence contour for the broken power law model for PKS 1510−089 using structure function simulations. Highest confidence is 22.0% at $\alpha = -2.7$ and $f_{\rm b} = 10^{-7.82}$Hz.

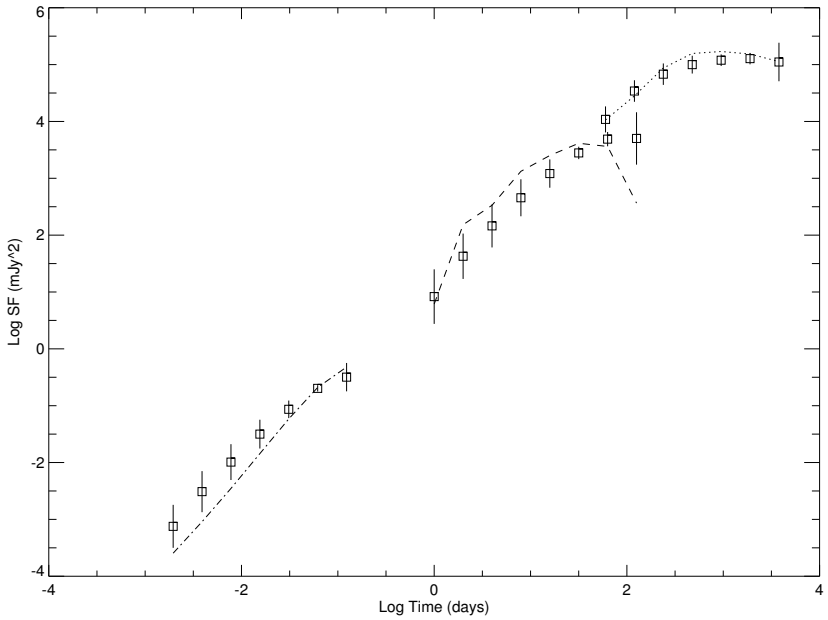

Figure. 5.48: Structure function of PKS 1510−089. Lines represent the observed structure function, points with error the structure function of the best fit broken power law simulation. Best fit parameters are $\alpha = -2.7$ and $f_{\rm b} = 10^{-7.82}$Hz.

5.7 2200+420

5.7.1 2200+420 - Power Density Spectrum

The data set for BL Lac is one of the most complete and well-sampled obtained by the PEGA group. A wealth of long term archival data, combined with intensive monitoring at smaller timescales by the PEGA group, create a complete broadband PDS for the object. The entire frequency range spanned by the data is $10^{-9.0} - 10^{-3.0}$Hz, interrupted only by a small gap near timescales of one day.

The confidence contour for the broken power law model is presented in Figure 5.49. The peak confidence value of 65.6% is located at a slope of $\alpha = -2.9$ and a break frequency of $f_{\rm b} = 10^{-6.13}$Hz. The contour plot is well constrained in terms of break frequency with a wider spread in high confidence slope values.

Figure 5.50 displays the observed power spectrum and the simulated power spectrum for the broken power law model. The simulated power spectrum is a good fit to the observed data at all frequency segments and supports a true break in slope for this object.

The confidence contour for the best fit knee model is shown in Figure 5.51. The confidence in the knee model is significantly lower than that of the sharply broken power law, with a peak confidence of 30.4%. The best fit parameter values for the knee model are a slope of $\alpha = -2.5$ and a break frequency of $f_{\rm b} = 10^{-6.81}$Hz.

The reason for the lower confidence in the knee model is evident in Figure 5.52.

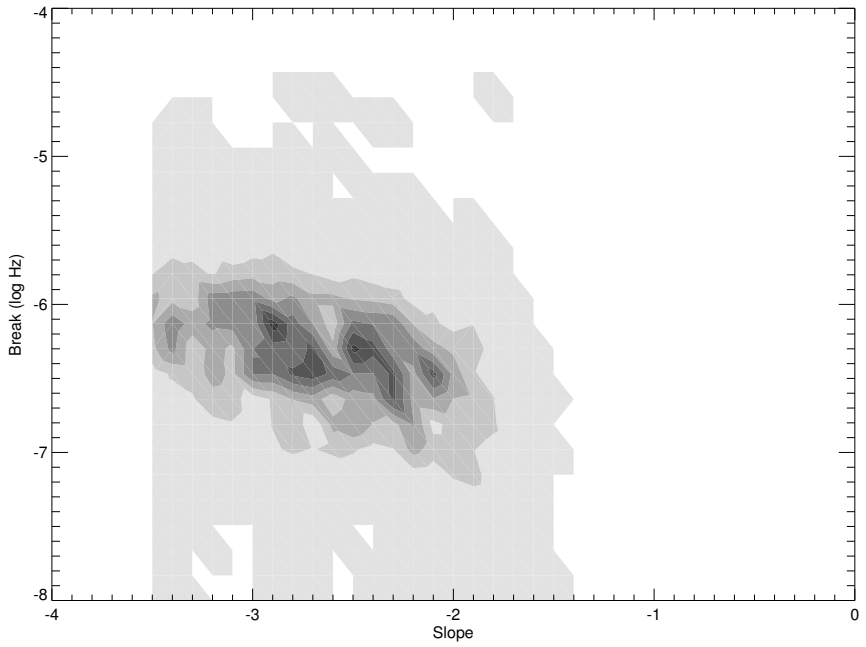

Figure. 5.49: Confidence contour for the broken power law model for BL Lac. Highest confidence is 65.6% at $\alpha = -2.9$ and $f_{\rm b} = 10^{-6.13}$Hz.

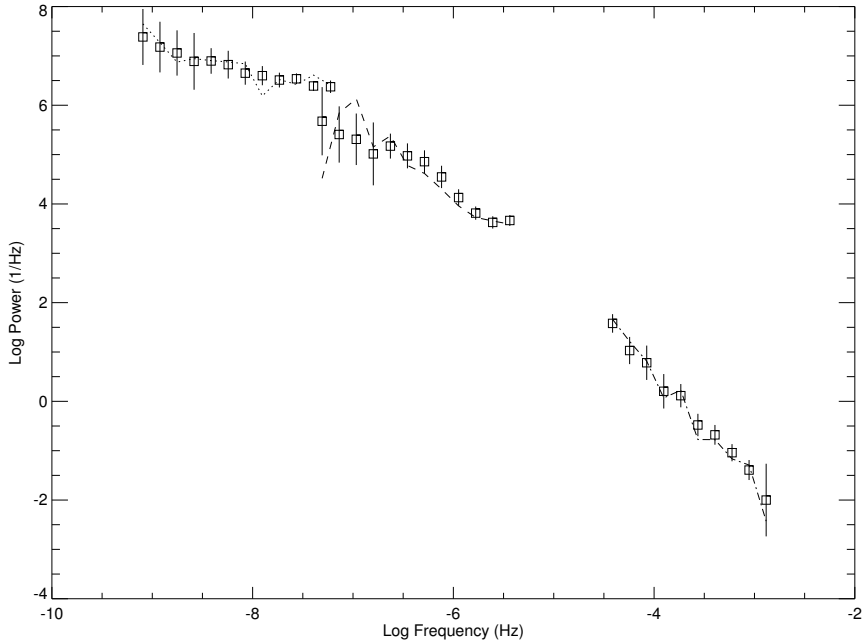

Figure. 5.50: Power density spectrum of BL Lac. Lines represent the observed power spectrum, points with error the power density spectrum of the best fit simulation. Best fit parameters are $\alpha = -2.9$ and $f_{\rm b} = 10^{-6.13}$Hz.

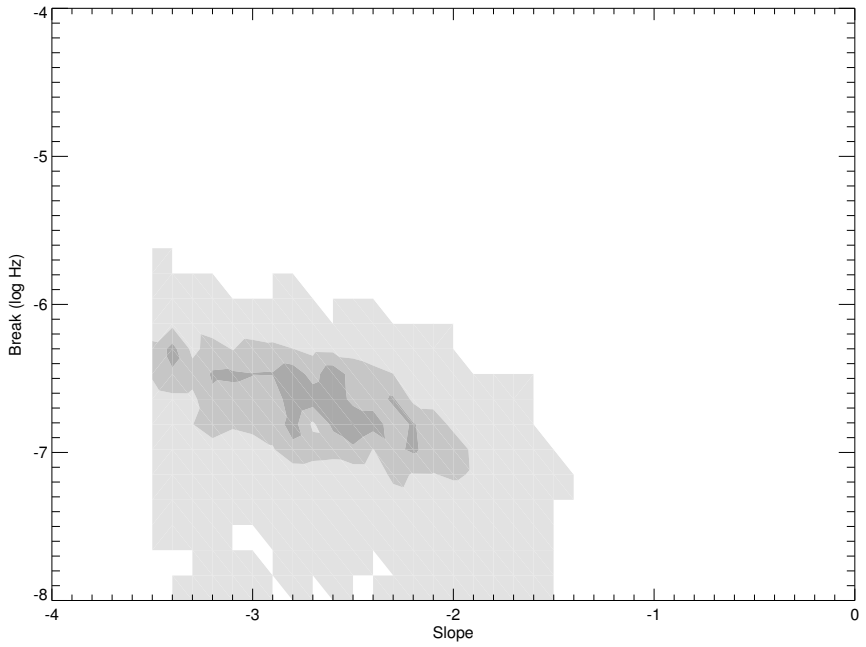

Figure. 5.51: Confidence contour for the knee power law model for BL Lac. Highest confidence is 30.4% at $\alpha = -2.5$ and $f_{\rm b} = 10^{-6.81}$Hz.

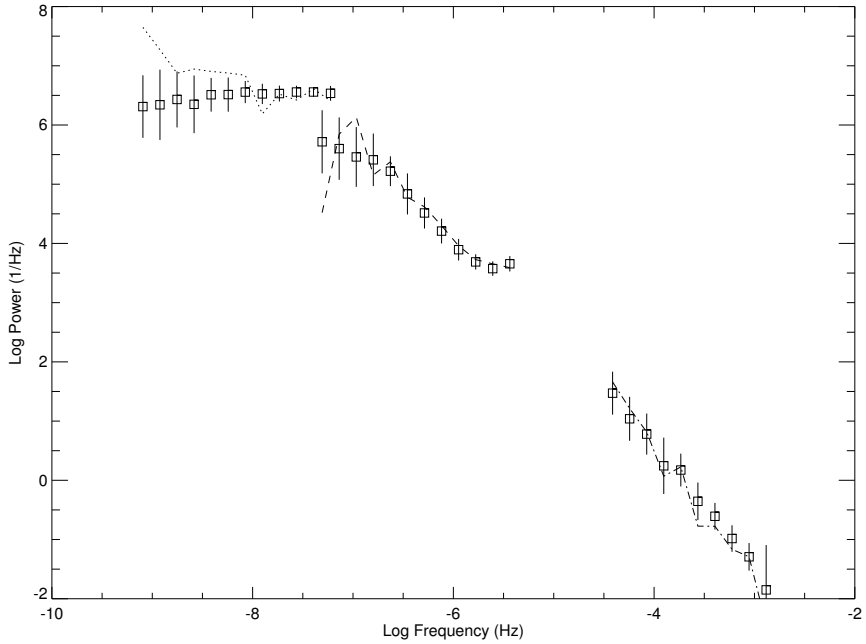

Figure. 5.52: Power density spectrum of BL Lac. Lines represent the observed power spectrum, points with error the power density spectrum of the best fit knee simulation. Best fit parameters are $\alpha = -2.5$ and $f_{\rm b} = 10^{-6.81}$Hz.

The simulated power spectrum provides a reasonable fit at medium and high frequencies, but is significantly shallower than the observed power spectrum at low frequencies.

The unbroken power law is an exceptionally poor fit to the observed power spectrum of BL Lac, with maximum confidence values of 0.2% at slopes of $\alpha = -2.4$ and $\alpha = -2.0$. This extremely low confidence value, corresponding to a rejection probability of 99.8%, is a clear indication that the underlaying PDS of BL Lac is not an unbroken power law.

Table. 5.13: Summary of PDS results for BL Lac.

Model	Confidence(%)	Slope (α)	Break Timescale (Days)
PL	0.2	-2.1	...
BPL	65.6	-2.87±0.23	19^{+6}_{-4}
Knee	30.4	-2.59±0.19	67^{+18}_{-14}

Table 5.13 displays a summary of the PDS results for BL Lac. The observed PDS for BL Lac is one of the best supported cases for a broken power law model. Both the knee and the broken power law model produced significantly higher confidence values compared to the unbroken power law. The break timescale for each model is on the order of tens of days, although there are nominally significant differences between the break timescales obtained from these two different types of broken power laws.

5.7.2 2200+420 - Structure Function

Structure function simulations for the variability of BL Lac result in a high confidence level (97.2%) for the broken power law model. The confidence contour (Figure 5.53) is steeply peaked at best fit model parameters of $\alpha = -2.5$ and $f_{\rm b} = 10^{-6.47}$Hz.

Table. 5.14: Summary of SF results for BL Lac.

Model	Confidence(%)	Slope (α)	Break Timescale (Days)
BPL	97.2	-2.62±0.17	45^{+21}_{-14}

The best fit break timescale and uncertainty, obtained through the Gaussian profile fit, is 45^{+21}_{-14} days. This break timescale agrees with the value of 19 days obtained through the PDS analysis and is the smallest value of break timescale in the sample.

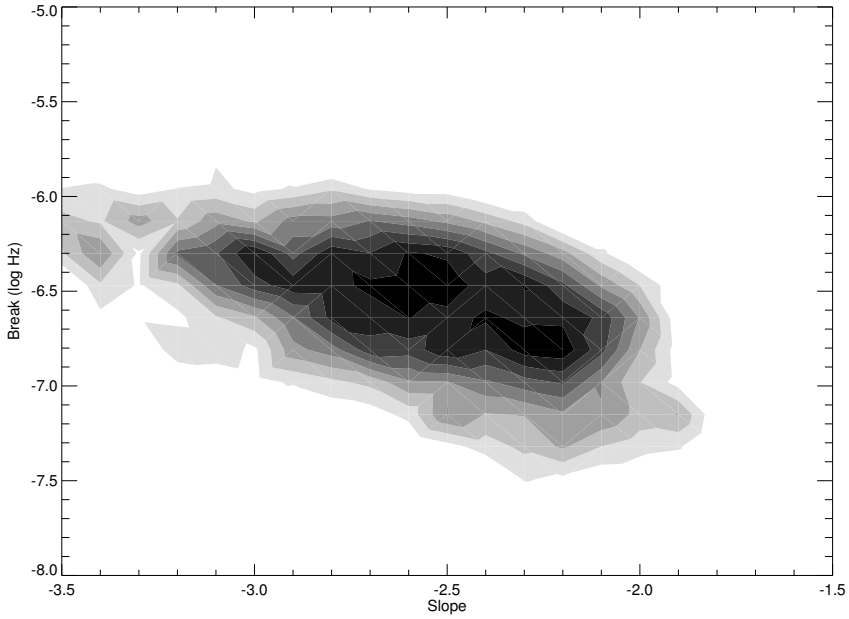

Figure. 5.53: Confidence contour for the broken power law model for BL Lac using structure function simulations. Highest confidence is 97.2% at $\alpha = -2.5$ and $f_{\rm b} = 10^{-6.47}$Hz.

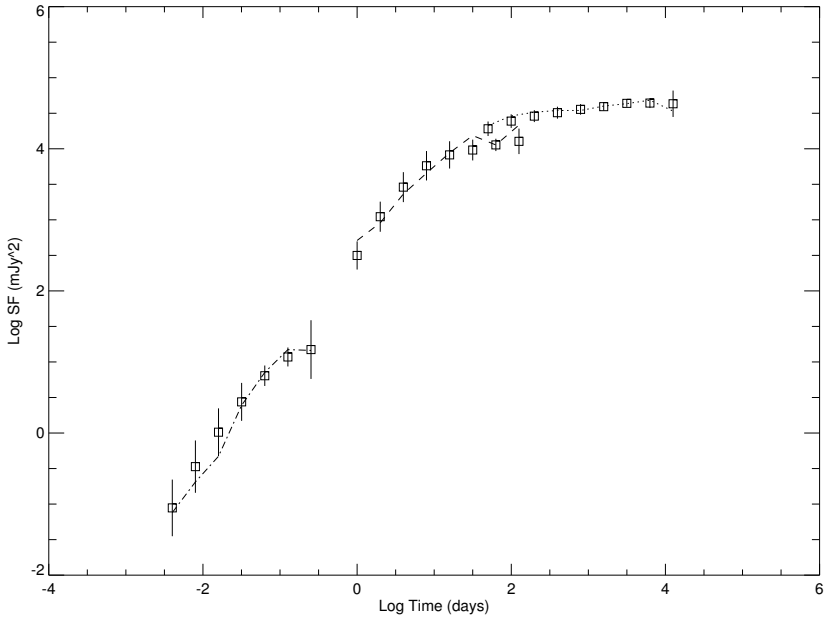

Figure. 5.54: Structure function of BL Lac. Lines represent the observed structure function, points with error the structure function of the best fit broken power law simulation. Best fit parameters are $\alpha = -2.5$ and $f_{\rm b} = 10^{-6.47}$Hz.

5.8 2251+158

5.8.1 2251+158 - Power Density Spectrum

3C 454.3 has been a favored object of study over the past three years. Long term monitoring, combined with an intense concentration of observations since the flare of 2005, have produced a clear picture of the variability at all timescales. The broadband PDS spans a range in frequency of $10^{-9.5} - 10^{-3.0}$Hz.

The broken power law model is the best fit to the observed power spectrum for 3C 454.3. The confidence contour, shown in Figure 5.55, is peaked at a value of 56.2% with a slope of $\alpha = -2.7$ and a break frequency of $f_{\rm b} = 10^{-6.12}$Hz. The break frequency is well defined along a rather broad range of acceptable slope values.

The observed power spectrum of 3C 454.3 and the best fit simulated power spectrum are displayed in Figure 5.56. The simulated power for the broken power law matches the behavior of the observed spectrum over the full six decades of frequency.

The knee power law model provides a worse fit to the observed data, with a confidence value of 51.2%. The best fit model parameters are a slope of $\alpha = -2.2$ and a break frequency of $f_{\rm b} = 10^{-6.63}$Hz. The overall appearance of the confidence contour is less constrained than the broken power law, but the break frequency is still approximately constant over a wide range of slope values.

The knee model underestimates the amount of power at the lowest frequencies, as seen in Figure 5.58. The behavior of the observed power spectrum at the lowest

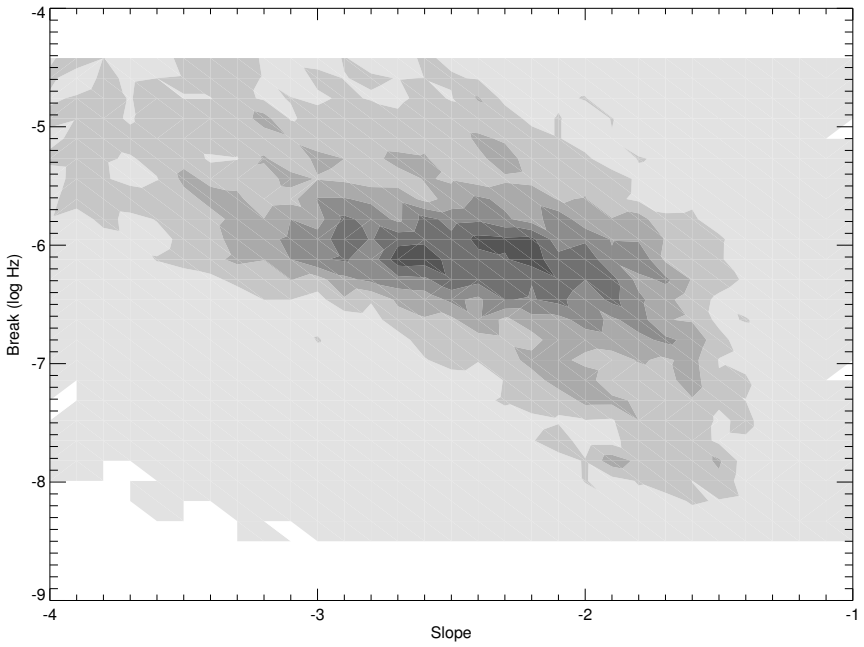

Figure. 5.55: Confidence contour for the broken power law model for 3C 454.3. Highest confidence is 56.2% at $\alpha = -2.7$ and $f_{\rm b} = 10^{-6.12}$Hz.

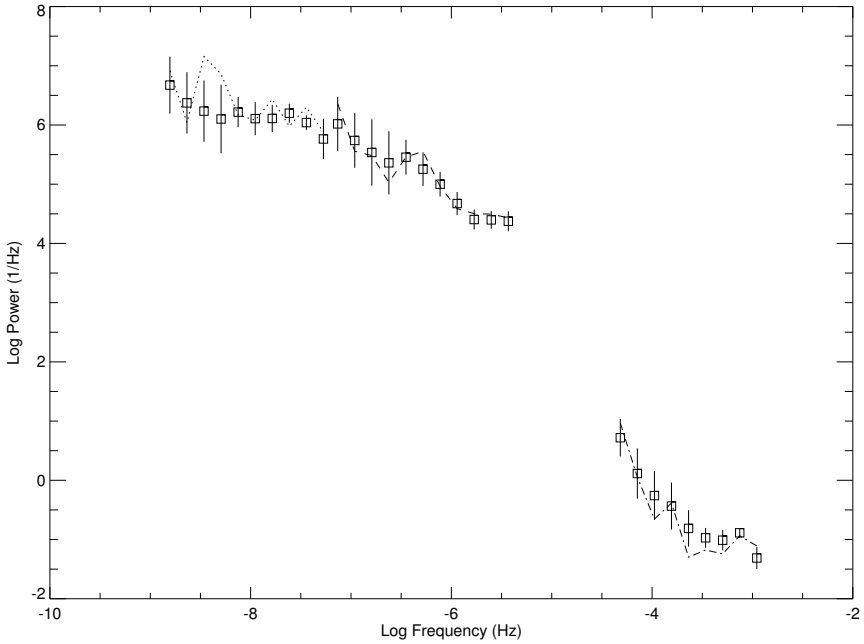

Figure. 5.56: Power density spectrum of 3C 454.3. Lines represent the observed power spectrum, points with error the power density spectrum of the best fit simulation. Best fit parameters are $\alpha = -2.7$ and $f_{\rm b} = 10^{-6.12}$Hz.

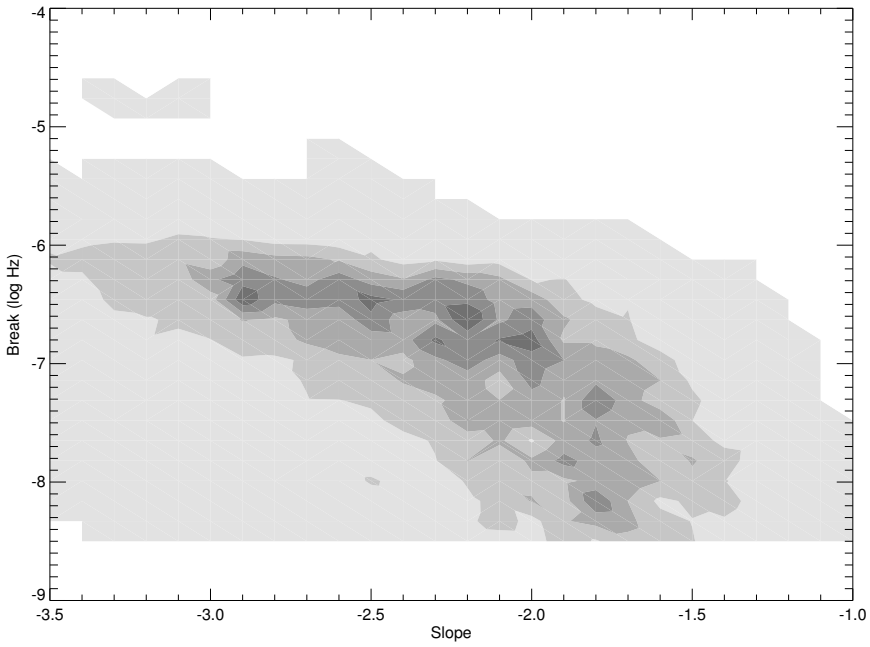

Figure. 5.57: Confidence contour for the knee power law model for 3C 454.3. Highest confidence is 51.2% at $\alpha = -2.2$ and $f_{\rm b} = 10^{-6.63}$Hz.

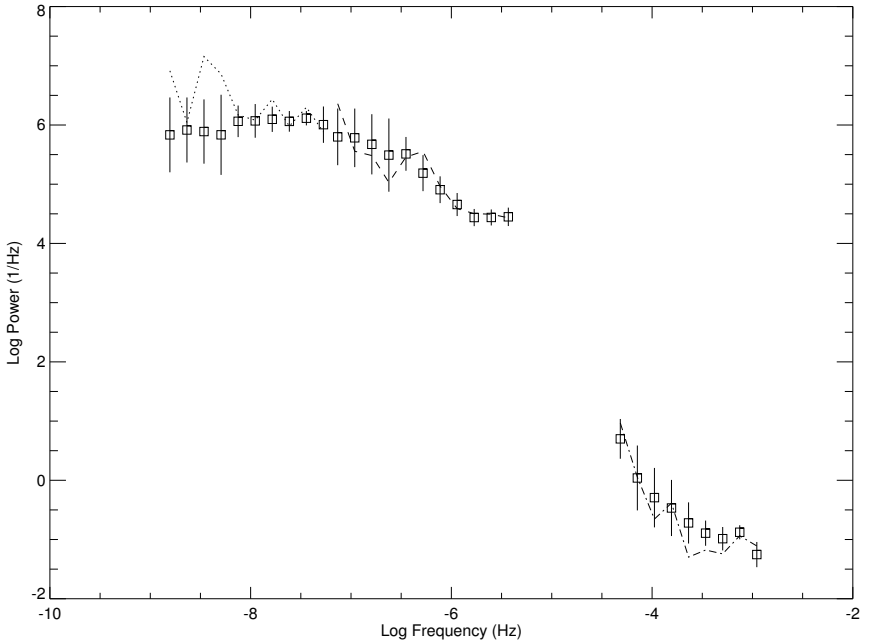

Figure. 5.58: Power density spectrum of 3C 454.3. Lines represent the observed power spectrum, points with error the power density spectrum of the best fit knee simulation. Best fit parameters are $\alpha = -2.2$ and $f_{\rm b} = 10^{-6.63}$Hz.

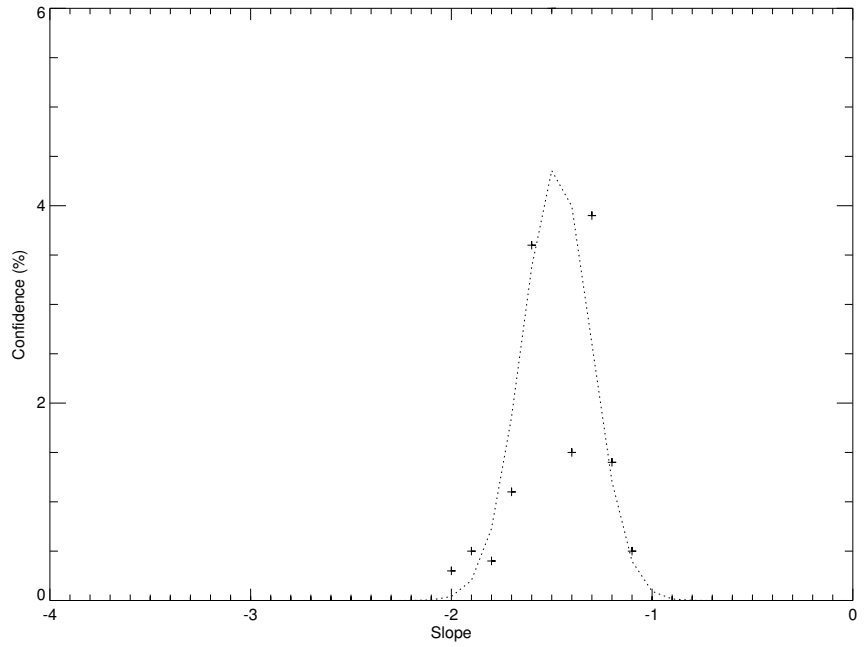

Figure. 5.59: Confidence contour for the unbroken power law model for 3C 454.3. Highest confidence is 6.0% at $\alpha = -1.5$.

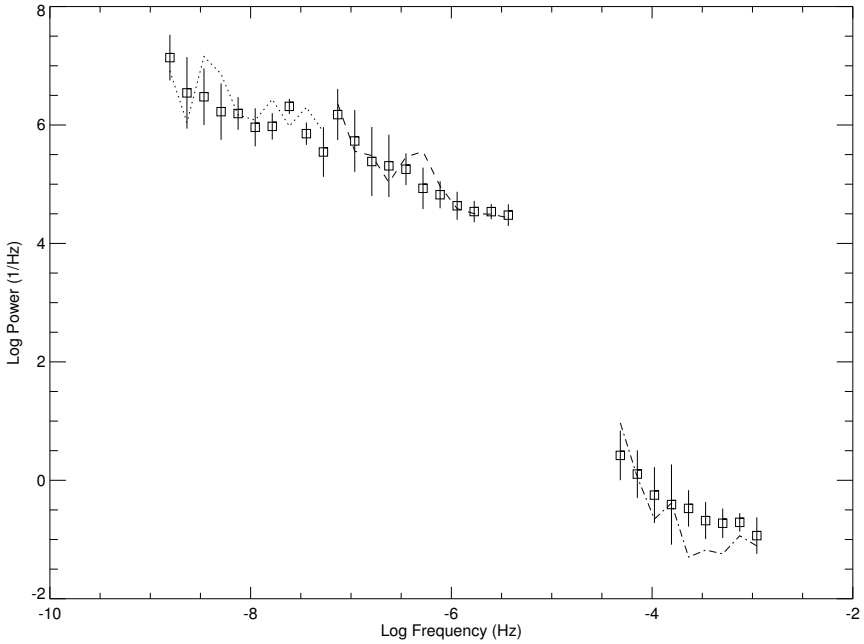

Figure. 5.60: Power density spectrum of 3C 454.3. Lines represent the observed power spectrum, points with error the power density spectrum of the best fit unbroken power law simulation. Best fit slope is $\alpha = -1.5$.

frequencies is somewhat erratic, but clearly not matched by the values of simulated power.

The unbroken power law model results in a poor fit to the observed power spectrum of 3C 454.3. A best fit slope of $\alpha = -1.5$ results in a confidence value of only 6.0%, shown in Figure 5.59. The simulated power spectrum provides a decent fit to the low and medium frequency data, but is too shallow compared to the observed power spectrum at the highest frequencies.

Table. 5.15: Summary of PDS results for 3C 454.3.

Model	Confidence(%)	Slope (α)	Break Timescale (Days)
PL	6.0	-1.48±0.07	...
BPL	56.2	-2.47±0.25	11^{+7}_{-4}
Knee	51.2	-2.34±0.20	93^{+72}_{-41}

The best fit parameters for each model are displayed in Table 5.15. The broken power law is the best fit with a break timescale of 11 days. The knee power law model has a slightly lower confidence, with a break timescale of approximately 100 days.

5.8.2 2251+158 - Structure Function

The confidence contour for the broken power law model of 3C 454.3 is displayed in Figure 5.61. The peak confidence value is high at 84.5%, supporting a broken power law form for the variability of 3C 454.3 The best fit model parameters are a slope of $\alpha = -2.3$ and a break frequency of $f_{\rm b} = 10^{-6.50}$Hz.

Table. 5.16: Summary of SF results for 3C 454.3.

Model	Confidence(%)	Slope (α)	Break Timescale (Days)
BPL	84.5	-2.38±0.16	84^{+77}_{-40}

The confidence contour shape is broad and not as well defined as that seen for BL Lac, leading to the slightly larger uncertainty values seen in Table 5.16. The simulated structure function is in good agreement with the observed structure function at all timescales (Figure 5.62). The estimated break timescale is 84 days, also in good agreement with the result of 11 days from PDS analysis.

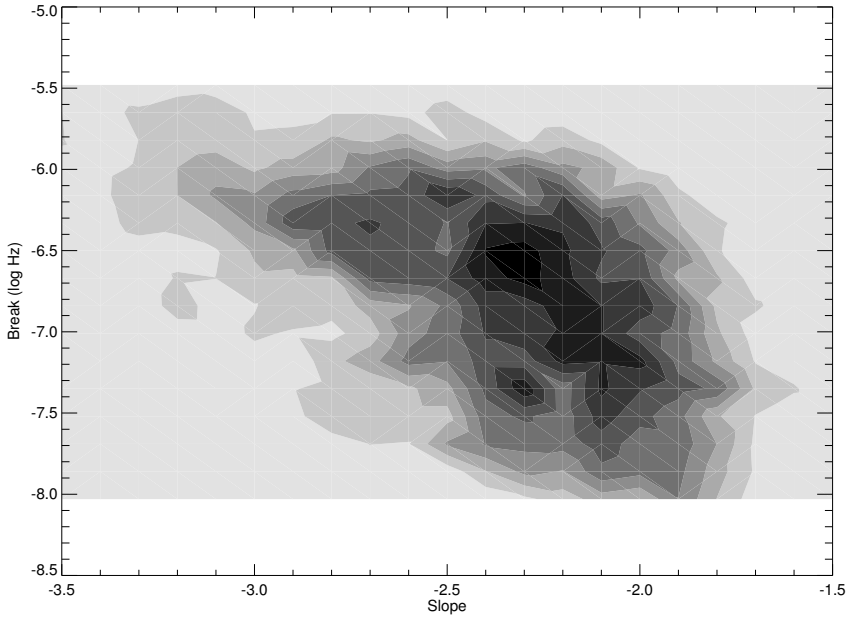

Figure. 5.61: Confidence contour for the broken power law model for 3C 454.3 using structure function simulations. Highest confidence is 84.5% at $\alpha = -2.3$ and $f_{\rm b} = 10^{-6.50}$Hz.

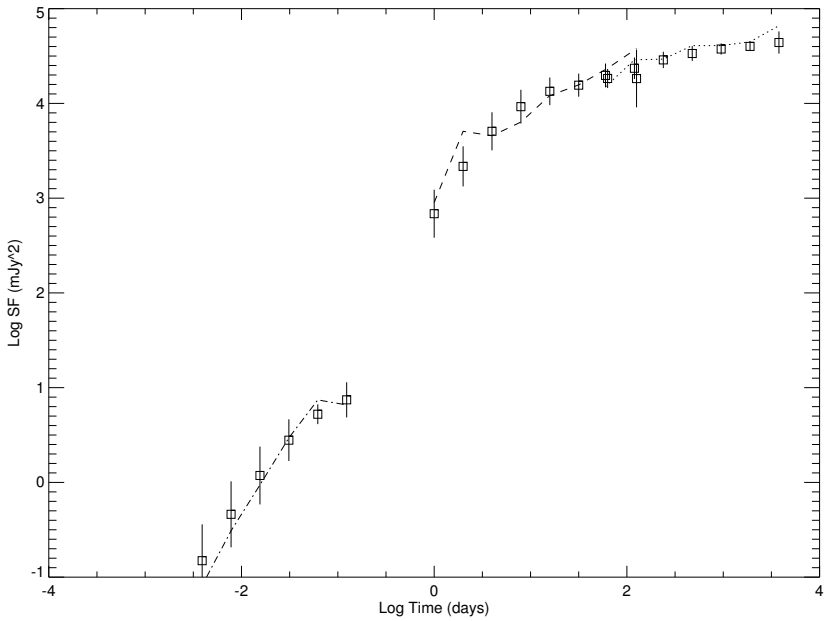

Figure. 5.62: Structure function of 3C 454.3. Lines represent the observed structure function, points with error the structure function of the best fit broken power law simulation. Best fit parameters are $\alpha = -2.3$ and $f_{\rm b} = 10^{-6.50}$Hz.

In questions of science, the authority of a thousand is not worth the humble reasoning of a single individual.

—— *Galileo Galilei*

– 6 –

Conclusions

The primary goal of this dissertation is to determine if time series analysis of optical light curves of blazars produces a characteristic timescale fundamentally related to the supermassive black hole mass. Power density spectra of x-ray light curves of both GXRB systems and Seyfert galaxies have shown a break frequency that appears to scale with mass over six orders of magnitude. The detection of break timescales in blazars extends this relationship an additional two orders of magnitude in mass and suggests a link between accretion disk phenomena and variability in the relativistic jet.

6.1 Detection of Breaks in the PDS of Blazars

Table 6.1 displays a summary of the break timescales found through the PDS analysis for all objects investigated in this study. The PDS of 1253−055 (3C 279) does not display a break in the observed frequency range. These results are supported by an independent analysis carried out by Chatterjee et al. (2008), using optical data with much better sampling than that used for this dissertation. According to Chatterjee et al. (2008), the optical PDS of 3C 279 was best fit by an unbroken power law with a slope of $\alpha = -1.2$ in a frequency range of $10^{-8.5}$-$10^{-5.5}$Hz.

The PDS of 0430+052 (3C 120) also appears to be an unbroken power law in the

Table. 6.1: Summary of Break Timescales for All Objects.

Object	BPL Break Timescale (days)	Knee Break Timescale (days)
0235+164	139^{+171}_{-77}	214^{+138}_{-84}
0430+052	> 3500	> 3500
0735+178	462^{+789}_{-291}	4401^{+4977}_{-2336}
0851+203	906^{+543}_{-340}	2792^{+1170}_{-824}
1253−055	> 3500	> 3500
1510−089	447^{+881}_{-297}	1284^{+1545}_{-701}
2200+420	19^{+6}_{-4}	67^{+18}_{-14}
2251+158	11^{+7}_{-4}	93^{+72}_{-41}

observed frequency range, with a slope of $\alpha \sim -1.7$. 3C 120 is the only object in the sample for which measurements of a break timescale have been carried out with x-ray data. The results of these analyses, shown in Figure 6.1 and Figure 6.2, support a break timescale of approximately 8 days.

The fact that no break is detected in the optical is somewhat perplexing, but may be explained by significant differences in 3C 120 compared to the other objects in the sample. 3C 120 is the only object that is embedded in a bright, extended host galaxy. Aperture photometry of a constant, extended source with a compact, variable core cannot be ideal. The constant level of brightness contributed by the host galaxy can act to dampen the variability observed in the core. Also, any seeing variations can induce variable contributions from the host to the nominal AGN light curve. Additionally, unlike blazars, the optical radiation from 3C 120 may be comprised of light from both the accretion disk and the relativistic jet. Thus, the true variability behavior, and therefore the break timescale, may be masked by contributions from

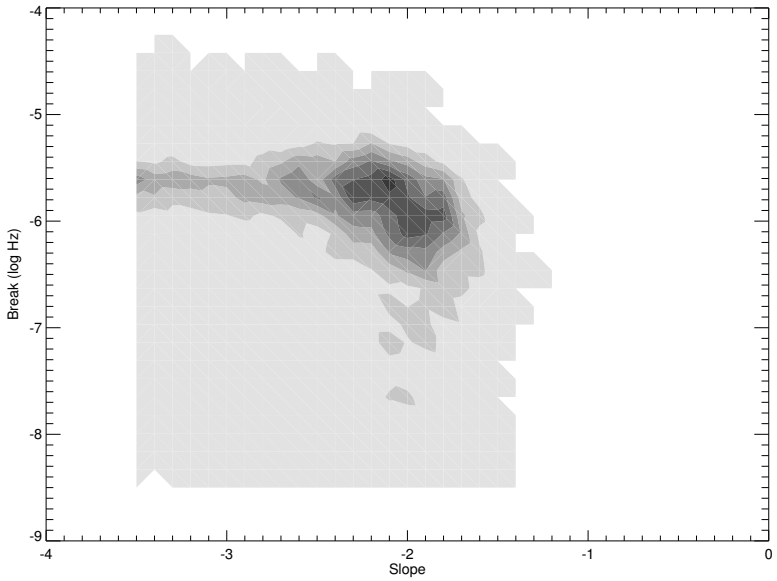

Figure. 6.1: Confidence contour for the broken power law model for 3C 120 using x-ray data. Highest confidence is 65.2% at $\alpha = -2.1$ and $f_{\rm b} = 10^{-5.61}$Hz.

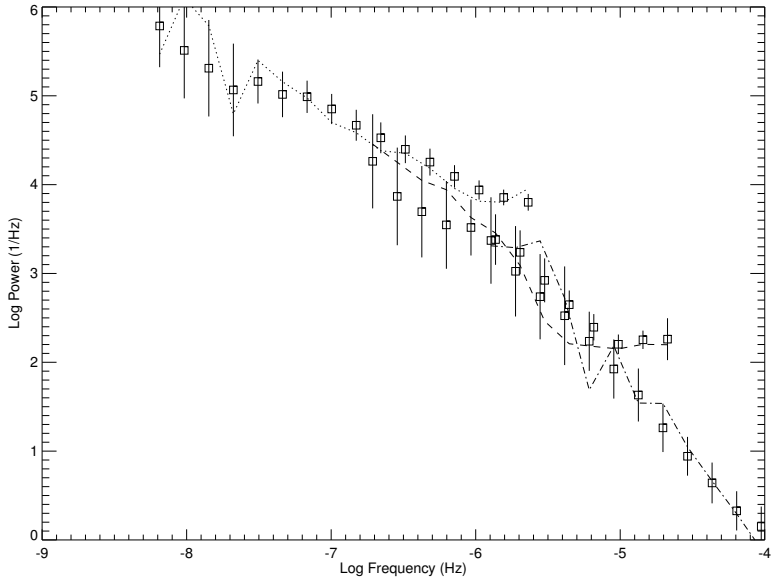

Figure. 6.2: Power density spectrum of 3C 120 from x-ray data. Lines represent the observed power spectrum, points with error the power density spectrum of the best fit broken power law simulation. Best fit parameters are $\alpha = -2.1$ and $f_{\rm b} = 10^{-5.61}$Hz.

the host galaxy at optical wavelengths.

For the remaining six objects, the presence of a break is supported with confidence levels greater than 30%. The broken power law and knee power law models both provide acceptable fits to the data. In all cases, the value for high frequency slope is steep ($\alpha \leq -2.0$). This indicates that the observed break is likely associated with the high frequency break seen in the PDS of GXRB systems. In all cases, the break timescale determined with the knee power law model is greater than that determined by the sharply broken power law model. This effect was also seen in Uttley et al. (2002), and is likely caused by the softer shape of the break in the knee model favoring slightly lower values of frequency. For consistency within the sample and with other quoted values in the literature, we henceforth adopt for our discussions the timescales obtained through the broken power law model.

The most robust results are seen in the objects 0851+203 (OJ 287), 2200+420 (BL Lac), and 2251+158 (3C 454.3). An examination of the light curves for these objects reveals that these objects are also the best sampled in terms of completeness in a given frequency range. This connection suggests that the level of confidence and the definition of the contour plot for the PDS analysis is greatly dependent on proper sampling. While the PSRESP method accounts for a modest level of distortion, there is undoubtedly a limit at which the sampling rate of the data becomes too poor. Further observations with even sampling for the objects 0235+164 (AO 0235+16), 0735+178 (PKS 0735+178) and 1510−089 (PKS 1510−089) would likely

lead to better defined break frequencies at improved confidence levels.

6.2 Comparison of PDS and SF Simulations

The structure function has been used to estimate timescales of variability in numerous studies of AGN with varied results. Most of these studies rely on a visual inspection of the shape of the structure function. Kataoka et al. (2001) performed structure function analysis on the x-ray light curves of three blazars, including simulations based on unbroken and broken power law models. Only two model cases, unbroken or broken, were tested and a full parameter space was not explored.

Table. 6.2: Comparison of PDS and SF Results.

Object	PDS Break Timescale (days)	SF Break Timescale (days)
0235+164	139^{+171}_{-77}	117^{+103}_{-55}
0430+052	> 3500	> 3500
0735+178	462^{+789}_{-291}	281^{+197}_{-116}
0851+203	906^{+543}_{-340}	1042^{+286}_{-225}
1253−055	> 3500	> 3500
1510−089	447^{+881}_{-297}	529^{+244}_{-167}
2200+420	19^{+6}_{-4}	45^{+21}_{-14}
2251+158	11^{+7}_{-4}	84^{+77}_{-40}

The use of structure function analysis in this dissertation provided a surprisingly strong confirmation of break timescales in all objects that display a break through PDS analysis. Figure 6.3 displays a comparison between the break timescales derived through PDS analysis and from structure function analysis. The results for structure function analysis are in good agreement with those derived from PDS analysis in

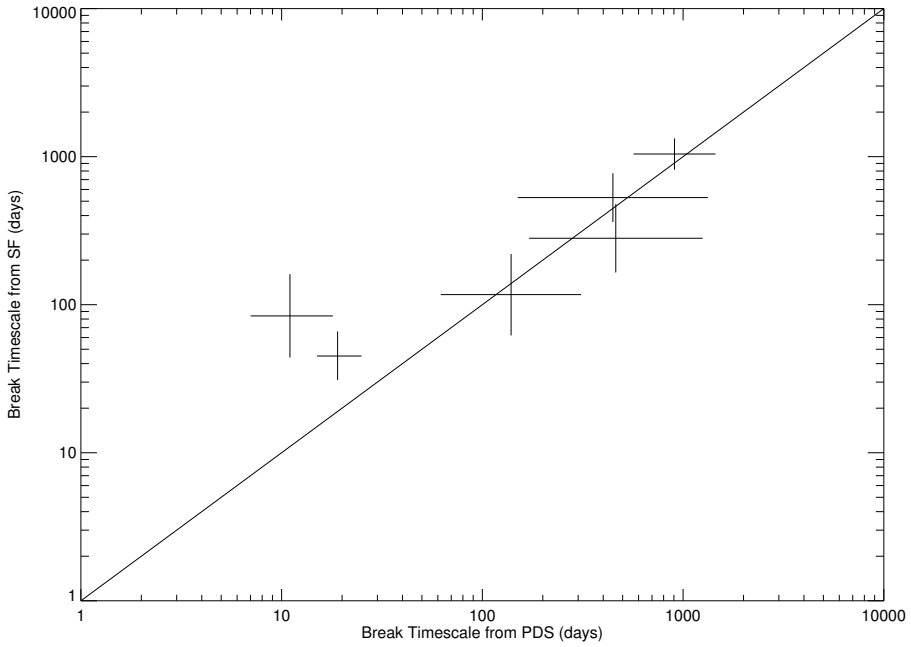

Figure. 6.3: Timescales obtained through PDS and SF analysis. Solid line represents a one-to-one correspondence.

most objects (Table 6.2). There is a possible deviation from this agreement at short timescales, but a larger sample is needed for confirmation. In addition, the confidence values obtained through the structure function analysis are significantly higher than those obtained through PDS analysis for a majority of the objects.

As a measurement tool for variability timescales, the PDS is the most robust technique because it is an attempt to directly relate a test model of variability to the true variability nature of the object. However, the requirement of a well sampled, long duration light curve is prohibitive for optical observations. The structure function is less dependent on an ideal sampling rate and appears to be a viable and successful method for detection of a break timescale from optical light curves. The utilization

of Monte Carlo simulations adds a level of statistical significance to the analysis that is absent in many previous studies.

6.3 Black Hole Mass and Break Timescale Relationship

Before direct comparison with the timescales of other objects, the break timescales for these objects must be corrected for redshift. This small correction, of the order $1+z$, is not of great importance for relatively nearby objects, such as GXRB systems and Seyfert galaxies. For the blazars in this sample, the correction is, at most, a factor of $\sim$2. A comparison of the observed and restframe break timescales from the broken power law PDS models for objects in this sample is displayed in Table 6.3.

Table. 6.3: Comparison of Observed and Restframe Timescales.

Object	Redshift (z)	Observed Timescale (days)	Restframe Timescale (days)
0235+164	0.940	139^{+171}_{-77}	72^{+88}_{-40}
0430+052	0.033	> 3500	> 3500
0735+178	0.424	462^{+789}_{-291}	324^{+554}_{-205}
0851+203	0.306	906^{+543}_{-340}	694^{+416}_{-260}
1253−055	0.536	> 3500	> 2400
1510−089	0.361	447^{+881}_{-297}	329^{+648}_{-218}
2200+420	0.069	19^{+6}_{-4}	18^{+5}_{-4}
2251+158	0.859	11^{+7}_{-4}	6^{+4}_{-2}

As discussed in Chapter 1, there is strong evidence for a relationship between break timescale and black hole mass that spans more than six orders of magnitude from GXRB systems to AGN. The time series analysis technique used for the optical

data in this dissertation is modeled after the technique used for other systems utilizing x-ray data. The results from those x-ray analyses, performed primarily on Seyfert galaxies, are presented in Table 6.4. Break frequencies have also been determined for both the low/hard (3.3Hz) and high/soft (14Hz) states of Cyg X-1. The mass of Cyg X-1 is $\sim 10 M_{\odot}$ (Nowak et al. 1999).

Table. 6.4: Previously Calculated Break Frequencies[a]

Name	PDS Break (days)	Ref[b]	$M_{BH}(10^6\ M_{\odot})$	Ref[b]
Akn 120	110	M06	150	P04
3C 390.3	74	M06	287	P04
Mkn 509	34.0	M06	143	P04
Fairall 9	28.9	M03	255	P04
NGC 5548	18.3	M03	67.1	P04
PG 0804+761	12	P03	693	P04
NGC 4151	9.2	M03	13.3	P04
3C 120	7.9	M06	55.5	P04
NGC 3516	5.8	M03	42.7	P04
NGC 3783	2.9	M03	29.8	P04
NGC 5506	0.89	U05	100	O99
MCG–6-30-15	0.15	M05	4.5	M05
NGC 3227	0.059	U05	42.2	P04
Mkn 766	0.023	V03	3.5	B05
NGC 4051	0.019	M04	1.91	P04
NGC 4395	0.006	V05	0.05	V05
Akn 564	0.005	P02	2.6	B04

[a] Adapted from Uttley & McHardy (2005); Marshall (2006).
[b] References used: M06 - Marshall (2006); M03 - Markowitz et al. (2003); P03 - Papadakis et al. (2003); U05 - Uttley & McHardy (2005); M05 - McHardy et al. (2005); V03 - Vaughan & Fabian (2003); M04 - McHardy et al. (2004); V05 - Vaughan et al. (2005); P02 - Papadakis et al. (2002); P04 - Peterson et al. (2004); O99 - Oliva et al. (1999); B05 - Botte et al. (2005); B04 - Botte et al. (2004)

Masses for blazars are harder to measure due to a variety of factors. For BL Lac objects, the featureless optical continuum provides no diagnostic lines for velocity

measurements. Stellar velocity dispersion measurements are also difficult to obtain because the host galaxies for many blazars are faint or undetected. Despite these limitations, mass determinations have been made for five of the objects in the sample, listed in Table 6.5.

Black hole mass estimates for AO 0235+16 and PKS 0735+178 have been published using minimum timescales of variability (Liang & Liu 2003), but we refrain from using these values. The use of minimum timescale of variability events is not a robust indicator of black hole mass and may, instead, be related to the light-crossing time of material in the relativistic jet of blazars. Mass determinations using this method ($M_{BH} = 10^{6.5} M_{\odot}$ for BL Lac (Liang & Liu 2003)) can be very discrepant with those determined from emission line or fundamental plane techniques ($M_{BH} = 10^{8.2} M_{\odot}$ for BL Lac (Urry et al. 2000)).

Table. 6.5: Mass Determinations for Sample Objects

Object	$M_{BH}(10^6\ M_{\odot})$	Ref[a]	$\log L_{bol}(\mathrm{erg\ s^{-1}})$	Ref[a]
0430+052	55.5	P04	45.34	W02
0851+203	18000	V07	...	...
1253−055	269	G01	46.10	W02
1510−089	447	G01	46.38	W02
2200+420	170	U00	...	...
2251+158	1480	G01	47.27	W02

[a] References used: G01 - Gu et al. (2001); P04 - Peterson et al. (2004); U00 - Urry et al. (2000); V07 - Valtonen (2007); W02 - Woo & Urry (2002)

Figure 6.4 displays the relationship between black hole mass and break timescale for objects including Cyg X-1, Seyfert galaxies, and the blazars studied in this disser-

tation. The relationship is linear over nine orders of magnitude in black hole mass, with only a modest amount of scatter. The solid and dashed lines represent an extrapolation of Cyg X-1 in the low/hard and high/soft state, respectively. The values for the four blazars with reliable mass estimates are in good agreement with this relationship and the behavior of other AGN in the larger sample. OJ 287, BL Lac, and 3C 454.3 all have relatively low timescales in comparison to the linear extrapolation, which may indicate that these objects are accreting at a fast rate. PKS 1510−089 may represent an object in a relatively low accretion state. However, substantial caution is required when using this relationship to determine accretion state due to the large amount of uncertainty in mass estimates for blazars.

It is interesting to note that the mass estimate used for the object OJ 287 ($M_{BH} = 1.8 \times 10^{10} M_{\odot}$), is obtained from the binary supermassive black hole model from Valtonen (2007). It appears that the large mass estimate is in good agreement with the long timescale associated with this object and strengthens the argument for the presence of a binary black hole.

The linear extrapolation from the low and high states of Cyg X-1 can be used to make naive estimates of black hole mass for the objects AO 0235+164 and PKS 0735+178. Assuming an extrapolation from the low state, the estimated black hole mass will follow the relation $M_6 = 2.85 T_b$, where M_6 is the black hole mass in units of $10^6 M_{\odot}$ and T_b is the break timescale in days. The high state extrapolation produces a mass a few times higher with the form $M_6 = 12.1 T_b$. Under these conditions, the

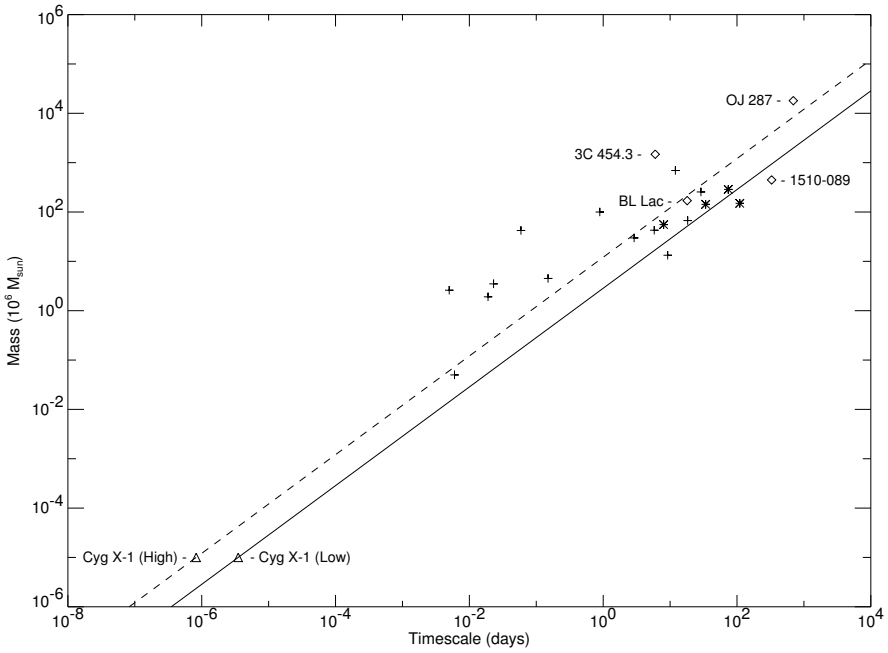

Figure. 6.4: Relationship between black hole mass and break timescale. The low/hard and high/soft states of Cyg X-1 are represented by triangles. Crosses represent Seyfert galaxies listed in Table 6.4. Asterisks represent the set of four galaxies presented in Marshall (2006). Diamonds represent the four blazars with reliable mass estimates from this work.

estimated mass for PKS 0735+178 is $M_{BH} = 900 \times 10^6 M_\odot$ for the low state and $M_{BH} = 3900 \times 10^6 M_\odot$ for the high state. The mass estimates for AO 0235+16 are $M_{BH} = 200 \times 10^6 M_\odot$ and $M_{BH} = 900 \times 10^6 M_\odot$ for the low and high states, respectively.

The break timescales measured in this dissertation can also be compared to those predicted by the more robust relationship between mass, luminosity, and break timescale proposed in McHardy et al. (2006). The relationship derived from a sample of objects, similar to those in Table 6.4, is shown in Equation 6.1, with T_b in days, M_{BH} in $10^6 M_\odot$, and L_{bol} in 10^{44}erg s^{-1}. In this relation, the bolometric luminosity, L_{bol}, of the object is used as a proxy for accretion rate.

$$\log T_{\rm b} = 2.1 \log M_{\rm BH} - 0.98 \log L_{\rm bol} - 2.32 \tag{6.1}$$

For the object 2251+158 (3C 454.3), the break timescale predicted from Equation 6.1 is ∼14 days. This value is in reasonably good agreement with the restframe break timescale of 6 days derived through the PDS analysis. The fact that 3C 454.3 comes into adequate agreement with this relation, combined with its location in Figure 6.4, is an indication that the object may be in an extremely high accretion state. This relation could be used to estimate the accretion states of other blazars assuming a reliable mass estimate and the detection of a break timescale.

6.4 The Disk-Jet Connection

The results presented above show that PDS analyses of optical data of blazars produce break timescales in a manner similar to that seen in Seyfert galaxies at x-ray wavelengths. Most of the radiation at optical wavelengths for blazars is assumed to originate in the relativistic jet. For Seyfert galaxies and GXRB systems, the x-ray variability used to estimate break timescales is believed to originate at or near the accretion disk. The good agreement between timescales derived through both techniques suggests a connection between the variability mechanism of the accretion disk and the variability observed in the jet.

The radiation from blazars is also highly beamed due to the relativistic speed of the jet and the orientation of the jet close to the line of sight. Due to large errors

on the break timescales for blazars, it is not clear if corrections for beaming should be applied. For some objects, this correction would reduce the break timescale by a factor of <10, but for others, such as AO 0235+164, the correction would be much larger. Though there may be a significant contribution to the variability of blazars from jet related phenomena, it appears that the general nature of the variability is similar to that produced by disturbances in the accretion disk. In this manner, the variability timescales associated with the accretion disk are thought to be modulating the variability produced in the jet.

This scenario is well described by the model presented in Marscher et al. (2002) and Marscher et al. (2008) for interaction between the accretion disk and the relativistic jet in blazars. Disturbances in the accretion disk lead to variations in accretion flow to the supermassive black hole. During times of increased accretion, additional material is fed into the relativistic jet. The pulses of radiation associated with the motion of the material along the jet are directly related to the feeding of the black hole through the accretion disk. The timescales of variability for the accretion disk and the relativistic jet are therefore linked through this interaction.

6.5 Future Work

The time series analysis techniques presented in this dissertation are capable of determining break timescales in the power spectra of optical blazar data. The greatest obstacle to the application of these techniques to additional objects is the lack

of large, well-sampled data sets. One method for obtaining sufficient data sets is through massive literature searches combined with large-scale collaborations between many observing institutions.

A sufficient data set could also be obtained through a dedicated observing regimen set in place over multiple observing seasons. A demonstration of one such regimen is given in Table 6.6, with T the total duration of observations, δT the ideal sampling rate, and $T_{\rm min}$ the minimum consistent sampling rate needed to avoid large data gaps.

Table. 6.6: Example of an Ideal Observing Regiment

Segment	Frequency(Hz)	T	δT	T_{min}
Long	$10^{-8.5} \leftrightarrow 10^{-6.4}$	10 yr	10 days	30 days
Medium	$10^{-7.2} \leftrightarrow 10^{-5.4}$	$\geq$6 months	1 day	3 days
Short	$10^{-5.9} \leftrightarrow 10^{-3.5}$	$\geq$10 days	30 minutes	1 hour
Micro	$10^{-4.3} \leftrightarrow 10^{-2.4}$	$\geq$6 hours	1 minute	5 minutes

In order to obtain adequate sampling and produce a full broadband PDS for optical data, the data must be collected in terms of observation segments. The long term segment requires a sampling rate from near one week to one month over the course of 10 years. Ideally, as is the case for the PEGA group, previously obtained observations or archival data are available. On medium timescales, daily observations over the course of an entire observing season are ideal. For the PEGA group, these observations can be obtained through the SMARTS observing queue for southerly objects. The most difficult time range to obtain sufficient observation is on short timescales. As seen in many of the PDS in this dissertation, the consequence of the

diurnal cycle for ground-based observing is a large gap near frequencies corresponding to one day. A dedicated campaign over the course of one week or longer with hourly observations would be sufficient, assuming observations could be taken and shared amongst observatories at greatly different longitudes. Finally, microvariability observations of a single object are required to measure the highest frequency portion of the PDS. Ideally, microvariability observations are made at larger aperture telescopes, allowing for a minimum exposure time.

There is promise for further analysis with blazar data already obtained by the PEGA group through the structure function simulations described above. The structure function appears to provide a higher degree of confidence in model comparisons than that of the PDS analysis for data that is unevenly sampled. There are many objects observed by PEGA over the past 30 years that would be ideal candidates for this analysis technique.

There are also a host of other relationships involving time series analysis of accreting systems that could be tested with optical blazar data. The connection between optical emission line width and break timescale presented by McHardy et al. (2006) could possibly be extended to include OVV objects. There is evidence that the RMS-flux relationship in GXRB systems (Uttley & McHardy 2001) and Seyfert galaxies (Vaughan & Fabian 2003) is also present in the x-ray data of blazars. Each of these relationships, if confirmed in the optical, would strengthen the argument for a scaling relationship between stellar mass black holes and the supermassive black holes of

AGN.

Gierliński et al. (2008) has proposed that the power amplitude of the high frequency tail of the PDS in GXRB systems may be a more direct estimator of black hole mass than the observed break frequency. As observed in Cyg X-1, the break timescale is a function of the state of the object, changing appreciably from the low to high accretion states. The high frequency tail, with slope $\alpha \approx -2$, is found to be independent of accretion state and the power amplitude inversely proportional to black hole mass.

For blazars, the high frequency tail corresponds to microvariability observations obtained during one night with a sampling rate on the order of minutes. If this property of accreting systems scales with mass, then higher mass supermassive black hole blazars should show a decreased level of microvariability when compared to low mass objects. A preliminary examination of the light curves presented in this dissertation supports this conclusion. Objects with long break timescales, such as OJ 287 and PKS 0735+178, have displayed little large amplitude microvariability over the past few decades. Objects with short break timescales, such as BL Lac and 3C 454.3, display large amplitude, rapid variability on numerous occasions. A detailed investigation into this behavior may support microvariability as a measurement tool for supermassive black hole mass in blazars.

References

Aller, H. D., Aller, M. F., & Hughes, P. A. 1996, in Astronomical Society of the Pacific Conference Series, Vol. 110, Blazar Continuum Variability, ed. H. R. Miller, J. R. Webb, & J. C. Noble, 208

Aller, M. F. et al. 1997, in American Institute of Physics Conference Series, Vol. 410, Proceedings of the Fourth Compton Symposium, ed. C. D. Dermer, M. S. Strickman, & J. D. Kurfess, 1423

Angione, R. J. 1968, PASP, 80, 339

——. 1971, AJ, 76, 25

Antonucci, R. R. J., & Miller, J. S. 1985, ApJ, 297, 621

Argue, A. N., Kenworthy, C. M., & Stewart, P. M. 1973, Astrophys. Lett., 14, 99

Baath, L. B. 1984, in IAU Symposium, Vol. 110, VLBI and Compact Radio Sources, ed. R. Fanti, K. I. Kellermann, & G. Setti, 127

Balonek, T. J. 1982, PhD thesis, (Massachusetts Univ., Amherst)

Balonek, T. J., & Dent, W. A. 1980, ApJ, 240, L3

Belloni, T. 2001, Astrophysics and Space Science Supplement, 276, 145

Belloni, T., & Hasinger, G. 1990, A&A, 230, 103

Blake, G. M. 1970, Astrophys. Lett., 6, 201

Botte, V., Ciroi, S., di Mille, F., Rafanelli, P., & Romano, A. 2005, MNRAS, 356, 789

Botte, V., Ciroi, S., Rafanelli, P., & Di Mille, F. 2004, AJ, 127, 3168

Brinkmann, W., Gliozzi, M., Urry, C. M., Maraschi, L., & Sambruna, R. 2000, A&A, 362, 105

Burbidge, E. M. 1967, ApJ, 149, L51

Carini, M. T. 1990, PhD thesis, (Georgia State Univ., Atlanta)

Carini, M. T., & Miller, H. R. 1992, ApJ, 385, 146

Carswell, R. F., Strittmatter, P. A., Williams, R. E., Kinman, T. D., & Serkowski, K. 1974, ApJ, 190, L101

Chatterjee, R. et al. 2008, ApJ, in press

Ciprini, S. et al. 2007, A&A, 467, 465

Clements, S. D., Smith, A. G., Aller, H. D., & Aller, M. F. 1995, AJ, 110, 529

Cotton, W. D. et al. 1979, ApJ, 229, L115

——. 1980, ApJ, 238, L123

DuPuy, D., Schmitt, J., McClure, R., van den Bergh, S., & Racine, R. 1969, ApJ, 156, L135

Eachus, L. J., & Liller, W. 1975, ApJ, 200, L61

Elliot, J. L., & Shapiro, S. L. 1974, ApJ, 192, L3

Fan, J. H., & Lin, R. G. 2000, ApJ, 537, 101

Fath, E. A. 1908, Lick Observatory Bulletin, 5, 71

Fender, R., Koerding, E., Belloni, T., Uttley, P., McHardy, I., & Tzioumis, T. 2007, ArXiv e-prints, 706

Ferrarese, L., & Merritt, D. 2000, ApJ, 539, L9

Gebhardt, K. et al. 2000, ApJ, 539, L13

Gierliński, M., Nikołajuk, M., & Czerny, B. 2008, MNRAS, 383, 741

Gopal-Krishna, & Wiita, P. J. 1992, A&A, 259, 109

Grandi, P. et al. 1996, ApJ, 459, 73

Gu, M., Cao, X., & Jiang, D. R. 2001, MNRAS, 327, 1111

Harris, D. E., Mossman, A. E., & Walker, R. C. 2004, ApJ, 615, 161

Hartman, R. C. et al. 1999, ApJS, 123, 79

——. 1993, ApJ, 407, L41

——. 1992, ApJ, 385, L1

——. 1996, ApJ, 461, 698

Hazard, C., Mackey, M. B., & Shimmins, A. J. 1963, Nature, 197, 1037

Hewitt, A., & Burbidge, G. 1993, ApJS, 87, 451

Homan, D. C., Ojha, R., Wardle, J. F. C., Roberts, D. H., Aller, M. F., Aller, H. D., & Hughes, P. A. 2001, ApJ, 549, 840

Homan, D. C., Wardle, J. F. C., Cheung, C. C., Roberts, D. H., & Attridge, J. M. 2002, ApJ, 580, 742

Hughes, P. A., Aller, H. D., & Aller, M. F. 1992, ApJ, 396, 469

Impey, C. D., Brand, P. W. J. L., & Tapia, S. 1982, MNRAS, 198, 1

Jorgensen, I., Franx, M., & Kjaergaard, P. 1996, MNRAS, 280, 167

Jorstad, S. G. et al. 2005, AJ, 130, 1418

Kartaltepe, J. S., & Balonek, T. J. 2007, AJ, 133, 2866

Kaspi, S., Smith, P. S., Maoz, D., Netzer, H., & Jannuzi, B. T. 1996, ApJ, 471, L75

Kaspi, S., Smith, P. S., Netzer, H., Maoz, D., Jannuzi, B. T., & Giveon, U. 2000, ApJ, 533, 631

Kataoka, J. et al. 2001, ApJ, 560, 659

Kembhavi, A. K., & Narlikar, J. V. 1999, Quasars and active galactic nuclei : an introduction (Cambridge University Press, Cambridge)

Kidger, M. R. 2000, AJ, 119, 2053

Körding, E. G., Jester, S., & Fender, R. 2006, MNRAS, 372, 1366

Kraus, J. D., Scheer, D. J., Dixon, R. S., Fitch, L. T., & Andrew, B. H. 1968, ApJ, 152, L35

Lamer, G., Brunner, H., & Staubert, R. 1996, A&A, 311, 384

Liang, E. W., & Liu, H. T. 2003, MNRAS, 340, 632

Liller, M. H., & Liller, W. 1975, ApJ, 199, L133

Maraschi, L., Chiappetti, L., Falomo, R., Garilli, B., Malkan, M., Tagliaferri, G., Tanzi, E. G., & Treves, A. 1991, ApJ, 368, 138

Markowitz, A. 2006, in Astronomical Society of the Pacific Conference Series, Vol. 350, Blazar Variability Workshop II: Entering the GLAST Era, ed. H. R. Miller, K. Marshall, J. R. Webb, & M. F. Aller, 51

Markowitz, A. et al. 2003, ApJ, 593, 96

Marscher, A. P. 1977, AJ, 82, 781

——. 1988, ApJ, 334, 552

Marscher, A. P. 1998, in Astronomical Society of the Pacific Conference Series, Vol. 144, IAU Colloq. 164: Radio Emission from Galactic and Extragalactic Compact Sources, ed. J. A. Zensus, G. B. Taylor, & J. M. Wrobel, 25

Marscher, A. P., Jorstad, S. G., Gómez, J.-L., Aller, M. F., Teräsranta, H., Lister, M. L., & Stirling, A. M. 2002, Nature, 417, 625

——. 2008, Nature, 452, 966

Marscher, A. P., & Travis, J. P. 1996, A&AS, 120, C537

Marshall, K. B. 2006, PhD thesis, (Georgia State Univ., Atlanta.)

Matthews, T. A., & Sandage, A. R. 1963, ApJ, 138, 30

McHardy, I. 1988, Memorie della Societa Astronomica Italiana, 59, 239

McHardy, I. M., Gunn, K. F., Uttley, P., & Goad, M. R. 2005, MNRAS, 359, 1469

McHardy, I. M., Koerding, E., Knigge, C., Uttley, P., & Fender, R. P. 2006, Nature, 444, 730

McHardy, I. M., Papadakis, I. E., Uttley, P., Page, M. J., & Mason, K. O. 2004, MNRAS, 348, 783

Miller, H. R. 1975, ApJ, 201, L109

——. 1981, ApJ, 244, 426

Miller, H. R. 1988, in Active Galactic Nuclei. Proceedings of a conference held at the

Georgia State University, Atlanta, Georgia, October 28-30, 1987., ed. H. R. Miller & P. J. Wiita, 146

Miller, H. R., Carini, M. T., & Goodrich, B. D. 1989, Nature, 337, 627

Miller, H. R., Clonts, S. L., & Folsom, G. H. 1974, AJ, 79, 1352

Miller, J. S., French, H. B., & Hawley, S. A. 1978, ApJ, 219, L85

Miller, J. S., Goodrich, R. W., & Mathews, W. G. 1991, ApJ, 378, 47

Mirabel, I. F., & Rodríguez, L. F. 1998, Nature, 392, 673

Moles, M., del Olmo, A., Masegosa, J., & Perea, J. D. 1988, A&A, 197, 1

Netzer, H. et al. 1994, ApJ, 430, 191

Noble, J. C. 1995, PhD thesis, (Georgia State Univ., Atlanta.)

Nowak, M. A., Vaughan, B. A., Wilms, J., Dove, J. B., & Begelman, M. C. 1999, ApJ, 510, 874

O'Dowd, M., Urry, C. M., & Scarpa, R. 2002, ApJ, 580, 96

Oke, J. B., Neugebauer, G., & Becklin, E. E. 1969, ApJ, 156, L41

Oliva, E., Origlia, L., Maiolino, R., & Moorwood, A. F. M. 1999, A&A, 350, 9

Osterman, M. A. 2006, PhD thesis, (Georgia State Univ., Atlanta.)

Osterman, M. A., Miller, H. R., Marshall, K., Ryle, W. T., Aller, H., Aller, M., & McFarland, J. P. 2007, ApJ, 671, 97

Paltani, S., Courvoisier, T. J.-L., Blecha, A., & Bratschi, P. 1997, A&A, 327, 539

Papadakis, I. E., Brinkmann, W., Negoro, H., & Gliozzi, M. 2002, A&A, 382, L1

Papadakis, I. E., & Lawrence, A. 1993, MNRAS, 261, 612

Papadakis, I. E., Reig, P., & Nandra, K. 2003, MNRAS, 344, 993

Peterson, B. M. 1993, PASP, 105, 247

——. 1997, An Introduction to Active Galactic Nuclei (Cambridge University Press, Cambridge)

Peterson, B. M. et al. 2004, ApJ, 613, 682

Pica, A. J., Smith, A. G., Webb, J. R., Leacock, R. J., Clements, S., & Gombola, P. P. 1988, AJ, 96, 1215

Pomphrey, R. B., Smith, A. G., Leacock, R. J., Olsson, C. N., Scott, R. L., Pollock, J. T., Edwards, P., & Dent, W. A. 1976, AJ, 81, 489

Press, W. H., Teukolsky, S. A., Vetterling, W. T., & Flannery, B. P. 1992, Numerical recipes in C. The art of scientific computing (Cambridge: University Press, —c1992, 2nd ed.)

Racine, R. 1970, ApJ, 159, L99

Raiteri, C. M., Ghisellini, G., Villata, M., de Francesco, G., Lanteri, L., Chiaberge, M., Peila, A., & Antico, G. 1998, A&AS, 127, 445

Raiteri, C. M. et al. 2001, A&A, 377, 396

Raiteri, C. M., Villata, M., Capetti, A., Heidt, J., Arnaboldi, M., & Magazzù, A. 2007, A&A, 464, 871

Revnivtsev, M., Gilfanov, M., & Churazov, E. 2000, A&A, 363, 1013

Robson, I. 1996, Active galactic nuclei (Wiley-Praxis Series in Astronomy and Astrophysics: Wiley, New York; Praxis Publishing, Chichester)

Rosen, A. 1990, ApJ, 359, 296

Schmidt, M. 1963, Nature, 197, 1040

Schmitt, J. L. 1968, Nature, 218, 663

Seyfert, C. K. 1943, ApJ, 97, 28

Shen, B. S. P., & Usher, P. D. 1970, Nature, 228, 1070

Sillanpää, A., Haarala, S., Valtonen, M. J., Sundelius, B., & Byrd, G. G. 1988, ApJ, 325, 628

Simonetti, J. H., Cordes, J. M., & Heeschen, D. S. 1985, ApJ, 296, 46

Smith, A. G. 1996, in Astronomical Society of the Pacific Conference Series, Vol. 110, Blazar Continuum Variability, ed. H. R. Miller, J. R. Webb, & J. C. Noble, 3

Smith, A. G., Nair, A. D., Leacock, R. J., & Clements, S. D. 1993, AJ, 105, 437

Smith, P. S., Balonek, T. J., Heckert, P. A., Elston, R., & Schmidt, G. D. 1985, AJ, 90, 1184

Spinrad, H., & Smith, H. E. 1975, ApJ, 201, 275

Stockman, H. S., Moore, R. L., & Angel, J. R. P. 1984, ApJ, 279, 485

Takalo, L. O. et al. 1998, A&AS, 129, 577

Teräsranta, H. et al. 2004, A&A, 427, 769

Thompson, J. R., Kraus, J. D., & Andrew, B. H. 1968, ApJ, 154, L1

Timmer, J., & Koenig, M. 1995, A&A, 300, 707

Tremaine, S. et al. 2002, ApJ, 574, 740

Urry, C. M., & Padovani, P. 1995, PASP, 107, 803

Urry, C. M., Scarpa, R., O'Dowd, M., Falomo, R., Pesce, J. E., & Treves, A. 2000, ApJ, 532, 816

Usher, P. D. 1979, AJ, 84, 1253

Uttley, P., & McHardy, I. M. 2001, MNRAS, 323, L26

——. 2005, MNRAS, 363, 586

Uttley, P., McHardy, I. M., & Papadakis, I. E. 2002, MNRAS, 332, 231

Valtaoja, E., Teräsranta, H., Tornikoski, M., Sillanpää, A., Aller, M. F., Aller, H. D., & Hughes, P. A. 2000, ApJ, 531, 744

Valtonen, M. J. 2007, ApJ, 659, 1074

Valtonen, M. J. et al. 2008, Nature, 452, 851

Vaughan, S., & Fabian, A. C. 2003, MNRAS, 341, 496

Vaughan, S., Iwasawa, K., Fabian, A. C., & Hayashida, K. 2005, MNRAS, 356, 524

Vermeulen, R. C., Ogle, P. M., Tran, H. D., Browne, I. W. A., Cohen, M. H., Readhead, A. C. S., Taylor, G. B., & Goodrich, R. W. 1995, ApJ, 452, L5

Villata, M. et al. 2000, A&A, 363, 108

——. 2006, A&A, 453, 817

——. 1997, A&AS, 121, 119

——. 2002, A&A, 390, 407

Webb, J. R., Carini, M. T., Clements, S., Fajardo, S., Gombola, P. P., Leacock, R. J., Sadun, A. C., & Smith, A. G. 1990, AJ, 100, 1452

Webb, J. R., Howard, E., Benítez, E., Balonek, T., McGrath, E., Shrader, C., Robson, I., & Jenkins, P. 2000, AJ, 120, 41

Webb, J. R., Smith, A. G., Leacock, R. J., Fitzgibbons, G. L., Gombola, P. P., & Shepherd, D. W. 1988, AJ, 95, 374

Wehrle, A. E. et al. 1998, ApJ, 497, 178

Whitney, A. R. et al. 1971, Science, 173, 225

Wing, R. F. 1973, AJ, 78, 684

Woo, J.-H., & Urry, C. M. 2002, ApJ, 579, 530

Xie, G. Z., Li, K. H., Bai, J. M., Dai, B. Z., Liu, W. W., Zhang, X., & Xing, S. Y. 2001, ApJ, 548, 200

Xie, G. Z., Liang, E. W., Zhou, S. B., Li, K. H., Dai, B. Z., & Ma, L. 2002, MNRAS, 334, 459

Zhang, S., Collmar, W., & Schönfelder, V. 2005, A&A, 444, 767

Appendices

– A –

Analysis Software

A.1 master.pro

```
PRO master,infile,bintime,segment,model

;This program is the front interface for the PDS calculation and
;Monte Carlo simulations.  It calls psresp.pro for each value of model
;parameters in the defined gridspace.

;Retain the onscreen plot
device,retain=2

;Define arrays for use by the transread program
time=0D
flux=0D
fluxerr=0D

;Read in values using C. Markwardt transread procedure
transread,UNIT,time,flux,fluxerr,filename=infile

;Prompt user for max/min break and slope for model
minbreak=0.0
maxbreak=0.0
read,minbreak,maxbreak,prompt='Minimum Break, Maximum Break: '

minslope=0.0
maxslope=0.0
read,minslope,maxslope,prompt='Minimum Slope, Maximum Slope: '

;Create a grid of slopes, stepsize of 0.1
slopes=fltarr(round((abs(maxslope-minslope)/0.1))+1)
for i=0,n_elements(slopes)-1 do slopes(i)=minslope + (0.1 * i)

;Create a grid of breaks, stepsize of 0.17
breaks=fltarr(round((abs(maxbreak-minbreak)/0.17))+1)
for i=0,n_elements(breaks)-1 do breaks(i)=minbreak + (0.17 * i)
```

```
;Call psresp.pro for each parameter grid space
for a=0,n_elements(slopes)-1 do begin
    for b=0,n_elements(breaks)-1 do begin
        print,'Slope=',slopes(a),'Break=',breaks(b)
psresp,time,flux,fluxerr,slopes(a),breaks(b),bintime,segment,model
    endfor
endfor

return
end

@powerlaw.fun
@hardbreak.fun
@knee.fun
@psresp.pro
```

A.2 psresp.pro

```
PRO psresp,date,rat,raterr,slopes,breaks,bin,segment,model

;This is the main program used to calculate the power density spectra
;(PDS) of the input lightcurve of length T.  The program then
;simulates one large lightcurve of length 100T, splits it into 100
;segments of length T, calculates the PDS for each lightcurve and
;averages.

;The input must be date(days), rate(flux or counts), rateerr(flux or
;counts), slope of the PDS model, break of the PDS model (log Hz), bin size,
;and name of the model segment (long,medium,short,etc.)

;This program is meant to be called by master.pro in order to run
;through a large grid of model parameters.

;*************************************************************************

;Initialization
date=date-date[0]  ;shift date to start at zero (easier to work with)
duration=MAX(date)-MIN(date)  ;lenght of lightcurve - used multipled times
daybreak=(10.^(breaks))*86400.   ;convert break from Hz to 1/day
npoints=long((duration)/bin)*1100. ; size of the large lightcurve
```

```
params=[slopes,daybreak]
lc_variance = variance(rat) - variance(raterr) ;variance of original LC
;create string for names of parameters
runname='s'+string(abs(slopes),format='(f4.2)')+'b'+string(abs(breaks)$
,format='(f4.2)')
file_mkdir,segment+'/'+runname  ;create directory for all output files

;*************************************************************************

;Observed PDS calculation
pdscalc,date,rat,obs_nu,obs_pds
obs_nu=alog10(obs_nu)

;Apply normalization from UMP02
obs_pds=(2.*(duration*86400.)) / ( (mean(rat)*mean(rat)*n_elements(rat)$
*n_elements(rat)) )*obs_pds

;Rebin observed PDS by step of 0.17 in log freq
rebinlc,obs_nu,obs_pds,obs_freqs,obs_power,dt=0.17

;Output observed PDS to file containing log freq, log power
outfile=filepath('observed',root_dir='/nfs/oke/data/ryle/mod/'+segment$
,subdir=runname)
openw,1,outfile
FOR i=0,n_elements(obs_freqs)-1 DO printf,1,obs_freqs[i],alog10(obs_power[i])
close,/all

;*************************************************************************

;Create fake lightcurve with length 100T, resolution 0.1*binsize of
;original lightcurve, and based off the test model PDS
timmerlc,faketime,fakerate,dt=(bin/10),seed=5.6415,nt=npoints$
,model=model,params=params

;Calculate level of Poisson noise based on original lightcurve
factor= ( (n_elements(raterr)/ (2.* (duration))) - (1./((duration))))
p_noise=TOTAL(raterr^2.) / ( (n_elements(raterr)) * factor)

;Calculate high frequency aliased power
uplim= 1./ (2.*bin)
lowlim= 1./ (2*(bin/10.))
intfreq=dblarr(((lowlim-uplim)/uplim)+2)
```

```
for i=0,n_elements(intfreq)-1 do intfreq(i)=uplim*(i+1)
intpds=call_function(model,intfreq,params)
int=int_tabulated(intfreq,intpds)
p_alias=int/factor

;Inside the following FOR loop, the long lightcurve is divided and
;resultant PDS are calculated

allpds=fltarr(100,n_elements(obs_freqs)) ;array of PDS for segments

FOR j=0,99 DO BEGIN
    print,'Computing PDS ',j+1

    ;Bintime and binrate will contain individual segments of long lightcurve
    bintime=dblarr(n_elements(date))
    binrate=dblarr(n_elements(date))

    ;Lobin and hibin are the indices for each segment
    lobin=long( (duration) *j/(bin/10.))
    hibin=long( (duration) *j/(bin/10.)) + long( (duration) /(bin/10.) -1 )

    ;Temptime, temprate are taken from appropriate section of long lighcurve
    temptime=faketime(lobin:hibin)
    temprate=fakerate(lobin:hibin)

    ;Shift start time to zero
    temptime=temptime-temptime(0)

    ;Set bintime equal to original lightcurve time
    ;Interpolate binrate to the original time steps
    bintime=date
    binrate=interpol(temprate,temptime,date)

    ;Rescale simulated LC to the mean and variance of the original
    tempvar=sqrt(variance(binrate))
    binrate=(binrate-mean(binrate))*( (sqrt(lc_variance)) / tempvar)+ mean(rat)

     ;Calculate PDS of simulated lightcurve
    pdscalc,bintime,binrate,sim_nu,sim_pds
    sim_nu=alog10(sim_nu)
    sim_pds=sim_pds+p_noise+p_alias
```

```
    ;Apply normalization from UMP02
    sim_pds=(2.*(max(bintime)-min(bintime))*86400.)/((mean(binrate)$
    *mean(binrate)*n_elements(binrate)*n_elements(binrate)))*sim_pds

    ;Rebin simulated PDS in same manner as observed
    rebinlc,sim_nu,sim_pds,logfreqs,power,dt=0.17
    logpower=alog10(power)

    ;Fill large array for later calculation of mean and rms error
    FOR k=0,n_elements(logpower)-1 DO allpds[j,k]=logpower[k]

    ;Output individual PDS to file for later use in error calc
    outfile=filepath(string(j,format='(I2.2)')+'.pds'$
    ,root_dir='/nfs/oke/data/ryle/mod/'+segment,subdir=runname)
    openw,1,outfile
    FOR i=0,n_elements(logfreqs)-1 DO printf,1,logfreqs[i],logpower[i]
    close,/all

ENDFOR

;*************************************************************************

;Calculate mean and rms error for all 100 simulations
avg_pds = dblarr(n_elements(obs_freqs))
pds_err = dblarr(n_elements(avg_pds))
FOR i=0,n_elements(avg_pds)-1 DO avg_pds[i]=mean(allpds[*,i])
FOR i=0,n_elements(pds_err)-1 DO pds_err[i]=sqrt(variance(allpds[*,i]))

;Output file with log freq, average PDS, and PDS error
outfile=filepath('average',root_dir='/nfs/oke/data/ryle/mod/'+segment$
,subdir=runname)
openw,2,outfile
FOR i=0,n_elements(logfreqs)-1 DO printf,2,logfreqs[i],avg_pds[i],pds_err[i]
close,/all

;*************************************************************************

;If desired, create plot of average and observed PDS
;set_plot,'ps'
;device,filename=filepath('plot.ps',root_dir='/nfs/oke/data/ryle/mod/'$
+segment,subdir=runname)
;plot,obs_freqs,alog10(obs_power),yrange=[MIN(alog10(obs_power))$
```

```
,MAX(alog10(obs_power))]
;oploterr,logfreqs,avg_psd,pds_err,6
;device,/close
;set_plot,'x'

;*****************************************************************************

RETURN
END
```

– B –

Optical Data - Nightly Averages

B.1 0235+164

Table. B.1: 0235+164 - Optical Data

JD	R Mag	Err
2448868	15.141	0.021
2448869	14.658	0.018
2448870	14.975	0.024
2448929	16.156	0.021
2448987	15.353	0.033
2449211	17.946	0.032
2450419	19.245	0.082
2450420	19.105	0.053
2450421	19.278	0.081
2450717	17.221	0.041
2450881	15.465	0.013
2451103	16.195	0.005
2451104	16.664	0.001
2451105	16.645	0.002
2451490	17.314	0.022
2451842	18.944	0.016
2452249	18.497	0.012
2452576	17.695	0.002
2452577	17.747	0.019
2452975	17.123	0.022
2452976	16.982	0.003
2453013	17.557	0.021
2453014	17.608	0.039
2453016	18.259	0.001
2453030	18.243	0.016
2453626	17.273	0.022

Continued on Next Page...

Table. B.1 – Continued

JD	R Mag	Err
2453652	18.396	0.023
2453653	18.307	0.009
2453655	18.439	0.010
2453713	17.516	0.025
2453745	17.844	0.023
2453749	18.040	0.031
2453754	17.959	0.022
2453759	17.696	0.026
2453763	17.621	0.023
2453773	17.354	0.022
2453783	16.667	0.020
2453784	16.668	0.020
2453974	18.981	0.021
2454019	18.143	0.015
2454020	18.273	0.020
2454056	16.874	0.019
2454060	17.104	0.023
2454065	17.223	0.023
2454068	17.246	0.037
2454073	16.621	0.024
2454078	16.609	0.003
2454079	16.832	0.023
2454080	16.622	0.001
2454082	16.597	0.009
2454085	16.388	0.023
2454089	16.448	0.044
2454093	16.331	0.026
2454096	16.073	0.023
2454102	15.888	0.026
2454105	16.078	0.021
2454108	15.962	0.023
2454112	15.490	0.021
2454118	15.838	0.022
2454121	16.105	0.023
2454124	15.782	0.022
2454127	15.266	0.024
2454130	15.964	0.020
2454140	16.006	0.021

Continued on Next Page...

Table. B.1 – Continued

JD	R Mag	Err
2454151	14.540	0.023
2454155	14.977	0.021
2454330	18.984	0.021
2454420	17.101	0.006
2454421	17.203	0.021
2454422	17.191	0.018
2454424	17.490	0.021
2454438	18.161	0.028
2454442	18.535	0.021
2454445	18.745	0.031
2454448	18.789	0.031
2454451	18.175	0.021
2454462	18.744	0.022
2454465	18.802	0.032
2454468	18.829	0.040
2454471	18.432	0.044
2454474	18.333	0.037
2454478	17.334	0.036
2454482	17.209	0.023
2454486	17.292	0.032
2454489	17.250	0.022
2454491	16.910	0.038
2454495	17.311	0.030
2454498	17.427	0.023
2454501	17.427	0.020
2454504	18.057	0.021
2454507	18.382	0.023
2454510	18.322	0.024

B.2 0430+052

Table. B.2: 0430+052 - Optical Data

JD	R Mag	Err
2448697	14.544	0.029
2448698	14.498	0.025
2450879	14.090	0.016
2450880	14.114	0.016
2451491	14.132	0.025
2451547	14.177	0.006
2451551	14.231	0.008
2451842	14.449	0.012
2451843	14.567	0.012
2452186	14.386	0.005
2452187	14.155	0.029
2452249	14.173	0.004
2452250	14.225	0.003
2452251	14.202	0.003
2452252	14.220	0.003
2452297	14.296	0.010
2452298	14.349	0.005
2452299	14.391	0.061
2452518	14.143	0.015
2452519	14.130	0.016
2452520	14.112	0.016
2452521	14.113	0.019
2452522	14.093	0.014
2452577	14.008	0.016
2452578	13.990	0.013
2452620	14.050	0.028
2452621	14.056	0.003
2452622	14.052	0.004
2452962	14.106	0.015
2452976	14.155	0.017
2452977	14.147	0.016
2452978	14.231	0.033
2452981	14.144	0.036
2452999	14.118	0.015
2453011	14.114	0.022
2453017	14.115	0.015

Continued on Next Page...

Table. B.2 – Continued

JD	R Mag	Err
2453054	14.176	0.015
2453057	14.175	0.016
2453060	14.181	0.015
2453066	14.176	0.016
2453069	14.194	0.015
2453072	14.186	0.015
2453078	14.170	0.015
2453089	14.201	0.015
2453093	14.206	0.016
2453098	14.207	0.018
2453102	14.213	0.015
2453105	14.213	0.015
2453111	14.216	0.015
2453269	14.289	0.014
2453270	14.298	0.009
2453271	14.309	0.015
2453282	14.315	0.016
2453301	14.203	0.021
2453345	14.108	0.015
2453350	14.080	0.016
2453355	14.068	0.015
2453358	14.068	0.017
2453361	14.094	0.016
2453366	14.114	0.016
2453369	14.153	0.018
2453372	14.154	0.015
2453375	14.163	0.016
2453378	14.174	0.016
2453381	14.180	0.016
2453385	14.167	0.016
2453397	14.230	0.015
2453626	14.010	0.022
2453653	13.952	0.015
2453654	13.973	0.032
2453656	13.954	0.013
2453714	14.083	0.004
2453715	14.101	0.003
2453716	14.097	0.016

Continued on Next Page...

Table. B.2 – Continued

JD	R Mag	Err
2453747	14.283	0.015
2453751	14.283	0.015
2453756	14.288	0.022
2453760	14.268	0.015
2453769	14.275	0.013
2453775	14.248	0.015
2453783	14.283	0.013
2453784	14.280	0.015
2453785	14.250	0.015
2453790	14.267	0.016
2453799	14.297	0.015
2453808	14.311	0.015
2453813	14.235	0.018
2453817	14.230	0.016
2453974	14.421	0.012
2453975	14.356	0.011
2454020	14.278	0.027
2454021	14.148	0.048
2454079	14.510	0.012
2454140	14.351	0.046
2454150	14.305	0.015
2454153	14.306	0.018
2454158	14.291	0.015
2454163	14.257	0.015
2454170	14.191	0.016
2454177	14.221	0.015
2454189	14.213	0.016
2454330	13.965	0.010
2454421	13.948	0.008
2454422	13.952	0.012
2454423	13.957	0.011
2454424	13.962	0.012
2454425	13.979	0.012
2454469	13.783	0.019
2454472	13.793	0.016
2454476	13.791	0.018
2454479	13.814	0.016
2454488	13.865	0.019

Continued on Next Page...

Table. B.2 – Continued

JD	R Mag	Err
2454491	13.883	0.015
2454494	13.876	0.015
2454497	13.882	0.021
2454500	13.886	0.016
2454504	13.902	0.015
2454507	13.877	0.017
2454510	13.886	0.022
2454517	13.853	0.019
2454520	13.860	0.017
2454523	13.878	0.015
2454532	13.884	0.015
2454535	13.902	0.017
2454538	13.915	0.010
2454544	13.869	0.015
2454547	13.873	0.017
2454554	13.861	0.018
2454557	13.879	0.014

B.3 0735+178

Table. B.3: 0735+178 - Optical Data

JD	R Mag	Err
2448646	15.450	0.003
2448647	15.492	0.003
2448648	15.521	0.005
2448649	15.521	0.017
2448650	15.511	0.004
2448651	15.521	0.002
2448652	15.537	0.002

Continued on Next Page...

Table. B.3 – Continued

JD	R Mag	Err
2448927	15.688	0.013
2448928	15.674	0.027
2449815	15.005	0.025
2449817	15.350	0.020
2449976	15.308	0.015
2449978	15.329	0.047
2449979	15.308	0.017
2450173	16.194	0.005
2450174	16.219	0.004
2450175	16.192	0.004
2450176	16.205	0.005
2450198	16.056	0.025
2450199	16.091	0.022
2450420	16.278	0.019
2450422	16.230	0.024
2450424	16.154	0.014
2450425	16.163	0.023
2450718	16.844	0.043
2451491	15.522	0.010
2451843	14.655	0.012
2451955	14.529	0.002
2451956	14.523	0.003
2452325	14.839	0.005
2452326	14.843	0.002
2452327	14.853	0.003
2452328	14.820	0.003
2452330	14.842	0.002
2452331	14.881	0.004
2452334	14.979	0.002
2452335	15.006	0.003
2452336	15.038	0.002
2452337	15.067	0.002
2452338	15.071	0.002
2452339	15.067	0.004
2452621	15.268	0.042
2452622	15.247	0.042
2452703	15.284	0.005
2452704	15.278	0.002

Continued on Next Page...

Table. B.3 – Continued

JD	R Mag	Err
2452705	15.286	0.002
2452706	15.313	0.002
2452707	15.340	0.002
2452708	15.347	0.003
2452752	14.861	0.033
2452753	14.841	0.013
2452754	14.857	0.030
2452755	14.872	0.011
2453059	15.336	0.002
2453117	15.492	0.013
2453120	15.464	0.018
2453269	15.098	0.015
2453282	15.287	0.010
2453429	15.241	0.013
2453430	15.240	0.020
2453653	15.728	0.012
2453654	15.729	0.016
2453656	15.672	0.012
2453714	15.603	0.011
2453715	15.545	0.012
2453783	15.411	0.009
2453784	15.412	0.009
2453785	15.406	0.013
2453847	15.235	0.012
2454079	16.080	0.003
2454081	16.105	0.001
2454139	15.969	0.006
2454140	16.017	0.025
2454217	15.597	0.014
2454421	15.388	0.005
2454422	15.377	0.003
2454423	15.399	0.001
2454424	15.400	0.002
2454520	15.971	0.010
2454521	16.014	0.003
2454522	16.084	0.002
2454523	16.129	0.003
2454524	16.070	0.002

Continued on Next Page...

Table. B.3 – Continued

JD	R Mag	Err
2454537	16.229	0.008
2454581	15.446	0.010

B.4 0851+203

Table. B.4: 0851+203 - Optical Data

JD	R Mag	Err
2448652	15.478	0.014
2449371	15.627	0.014
2449372	15.655	0.014
2449373	15.695	0.014
2449374	15.774	0.014
2449375	15.752	0.014
2449376	15.878	0.014
2449815	15.513	0.017
2449816	15.949	0.031
2449817	15.635	0.015
2450174	13.813	0.010
2450175	13.887	0.015
2450198	14.083	0.010
2450420	14.450	0.009
2450422	14.287	0.008
2450424	14.351	0.011
2450425	14.317	0.010
2450718	14.606	0.013
2450879	15.730	0.015
2451164	15.752	0.008
2451491	15.933	0.010
2451494	15.901	0.002

Continued on Next Page...

Table. B.4 – Continued

JD	R Mag	Err
2451547	16.066	0.010
2451549	16.008	0.001
2451842	14.597	0.010
2451843	14.111	0.010
2452326	14.920	0.008
2452577	13.934	0.009
2452752	15.178	0.016
2452753	15.126	0.011
2452754	15.083	0.011
2452755	15.126	0.011
2452779	14.487	0.011
2452976	15.877	0.014
2452977	15.556	0.010
2452978	14.862	0.010
2453117	14.870	0.010
2453118	14.738	0.016
2453120	14.989	0.016
2453146	14.788	0.010
2453430	14.402	0.015
2453431	14.285	0.009
2453497	15.029	0.011
2453498	14.911	0.010
2453499	14.909	0.019
2453714	13.895	0.012
2453715	13.912	0.020
2453783	15.087	0.005
2453784	14.990	0.008
2453785	14.904	0.003
2453847	15.021	0.008
2454081	15.353	0.008
2454107	15.329	0.023
2454110	15.352	0.015
2454112	15.290	0.022
2454116	15.542	0.019
2454120	15.161	0.018
2454122	15.064	0.018
2454127	15.589	0.027
2454133	15.286	0.015

Continued on Next Page...

Table. B.4 – Continued

JD	R Mag	Err
2454136	15.388	0.021
2454139	15.510	0.012
2454140	15.573	0.009
2454146	15.545	0.018
2454149	15.151	0.021
2454152	15.169	0.021
2454155	15.148	0.022
2454161	15.175	0.019
2454164	15.200	0.022
2454167	15.252	0.025
2454171	15.166	0.022
2454176	15.139	0.022
2454188	15.115	0.026
2454191	14.644	0.017
2454196	14.519	0.020
2454199	14.806	0.018
2454215	14.633	0.020
2454217	14.572	0.001
2454218	14.711	0.018
2454223	14.700	0.023
2454231	14.097	0.014
2454240	14.328	0.017
2454243	14.288	0.017
2454246	14.276	0.019
2454253	14.021	0.017
2454256	14.128	0.018
2454422	13.964	0.003
2454423	13.869	0.002
2454424	13.725	0.001
2454439	13.660	0.012
2454442	13.812	0.016
2454447	13.822	0.017
2454450	13.685	0.016
2454451	13.720	0.020
2454453	13.754	0.016
2454454	13.637	0.017
2454456	13.753	0.018
2454464	14.075	0.017

Continued on Next Page...

Table. B.4 – Continued

JD	R Mag	Err
2454466	14.078	0.023
2454469	14.210	0.018
2454472	13.789	0.019
2454474	13.558	0.018
2454478	13.545	0.016
2454480	13.656	0.017
2454484	13.388	0.015
2454490	13.735	0.015
2454495	13.803	0.019
2454498	14.001	0.016
2454501	13.996	0.014
2454504	14.063	0.017
2454508	14.216	0.018
2454511	14.296	0.018
2454516	14.350	0.014
2454519	14.422	0.018
2454522	14.752	0.015
2454523	14.823	0.008
2454524	14.829	0.008
2454526	14.772	0.021
2454534	15.149	0.021
2454537	14.960	0.004
2454538	14.939	0.001
2454539	14.887	0.002
2454540	14.830	0.003
2454541	14.766	0.006
2454543	14.768	0.017
2454546	14.593	0.019
2454550	14.325	0.020
2454553	14.331	0.020
2454556	14.094	0.021
2454558	14.088	0.018
2454561	14.478	0.018
2454564	14.817	0.019
2454571	14.933	0.021
2454574	14.881	0.016
2454577	14.741	0.017
2454581	15.120	0.007

Continued on Next Page...

Table. B.4 – Continued

JD	R Mag	Err
2454584	15.202	0.020
2454589	14.443	0.019
2454592	14.395	0.018
2454595	14.389	0.021
2454598	14.368	0.018
2454601	14.252	0.018
2454606	14.427	0.015

B.5 1253−055

Table. B.5: 1253−055 - Optical Data

JD	R Mag	Err
2450200	15.232	0.019
2450880	14.255	0.002
2450881	14.556	0.002
2450882	14.694	0.002
2450948	13.673	0.029
2450950	14.187	0.009
2450951	14.452	0.013
2451226	14.015	0.004
2451227	13.977	0.007
2451228	13.957	0.017
2451229	14.181	0.003
2451230	14.327	0.004
2451575	14.373	0.012
2451577	14.425	0.005
2451646	14.651	0.009
2451647	14.661	0.004
2451648	14.664	0.003

Continued on Next Page...

Table. B.5 – Continued

JD	R Mag	Err
2451649	14.585	0.005
2451850	14.569	0.016
2452016	14.234	0.001
2452049	14.014	0.001
2452050	14.089	0.001
2452051	14.166	0.001
2452052	14.115	0.001
2452053	14.066	0.004
2452075	13.478	0.009
2452250	14.353	0.017
2452413	14.338	0.005
2452704	16.742	0.017
2452705	16.758	0.017
2452706	16.835	0.017
2452708	16.852	0.017
2452752	16.479	0.017
2452753	16.888	0.017
2452754	16.940	0.017
2452755	16.987	0.017
2453059	15.075	0.015
2453062	15.082	0.015
2453070	15.227	0.015
2453077	15.240	0.015
2453096	15.652	0.018
2453101	15.759	0.017
2453104	15.800	0.015
2453107	15.816	0.015
2453111	15.809	0.015
2453114	15.632	0.015
2453117	15.658	0.017
2453121	15.580	0.014
2453124	15.864	0.018
2453129	15.758	0.015
2453133	15.649	0.016
2453136	15.688	0.023
2453139	15.442	0.086
2453143	15.347	0.017
2453146	15.085	0.005

Continued on Next Page...

Table. B.5 – Continued

JD	R Mag	Err
2453149	15.020	0.015
2453152	14.948	0.029
2453157	15.174	0.016
2453160	15.101	0.019
2453163	15.171	0.022
2453167	15.012	0.015
2453173	14.854	0.015
2453176	14.521	0.015
2453183	14.492	0.015
2453187	14.037	0.016
2453190	14.322	0.016
2453193	14.426	0.016
2453196	14.581	0.015
2453201	14.985	0.015
2453205	15.298	0.018
2453211	15.646	0.019
2453222	15.466	0.015
2453224	15.532	0.017
2453229	15.791	0.018
2453242	15.607	0.018
2453377	15.062	0.018
2453380	15.612	0.016
2453383	15.423	0.019
2453396	15.137	0.015
2453398	15.335	0.015
2453413	15.208	0.020
2453424	14.570	0.015
2453430	14.615	0.025
2453436	15.505	0.030
2453445	14.682	0.024
2453449	14.536	0.015
2453459	14.969	0.030
2453461	14.960	0.015
2453464	15.125	0.015
2453467	15.111	0.019
2453474	14.809	0.026
2453476	14.766	0.015
2453489	14.984	0.015

Continued on Next Page...

Table. B.5 – Continued

JD	R Mag	Err
2453494	15.154	0.015
2453497	15.163	0.004
2453498	15.185	0.009
2453499	15.267	0.008
2453500	15.166	0.011
2453501	15.207	0.018
2453506	14.508	0.015
2453511	14.944	0.021
2453517	14.637	0.015
2453521	14.958	0.016
2453524	14.904	0.014
2453527	15.151	0.019
2453532	14.998	0.016
2453543	14.634	0.020
2453550	15.273	0.029
2453749	14.892	0.016
2453754	15.248	0.016
2453760	15.128	0.015
2453765	14.356	0.019
2453775	14.100	0.015
2453785	14.226	0.008
2453786	14.222	0.016
2453792	14.459	0.019
2453799	14.365	0.015
2453802	14.421	0.016
2453812	13.997	0.016
2453815	14.013	0.015
2453826	14.174	0.015
2453832	14.910	0.019
2453839	14.905	0.016
2453843	14.675	0.015
2453847	14.749	0.005
2453848	14.673	0.016
2453852	14.559	0.015
2453855	14.600	0.025
2453860	14.425	0.023
2453861	14.503	0.027
2453866	14.569	0.019

Continued on Next Page...

Table. B.5 – Continued

JD	R Mag	Err
2453871	14.285	0.016
2453874	14.264	0.015
2453879	14.326	0.018
2453881	14.370	0.016
2453885	14.261	0.016
2453893	14.369	0.021
2453901	14.166	0.017
2453905	14.250	0.016
2453924	14.221	0.015
2453931	14.078	0.026
2453935	14.228	0.026
2454081	13.626	0.007
2454117	13.294	0.017
2454121	13.389	0.015
2454124	13.393	0.016
2454127	13.509	0.015
2454132	13.708	0.016
2454133	13.595	0.017
2454136	13.675	0.017
2454148	14.130	0.015
2454151	14.369	0.018
2454154	14.395	0.020
2454157	14.338	0.021
2454163	14.154	0.021
2454167	14.012	0.016
2454170	14.129	0.015
2454172	14.238	0.015
2454176	14.237	0.015
2454180	14.103	0.015
2454190	14.650	0.015
2454194	14.945	0.047
2454198	15.548	0.015
2454202	15.620	0.015
2454204	15.619	0.015
2454212	15.891	0.014
2454213	15.899	0.006
2454214	15.940	0.014
2454215	15.958	0.011

Continued on Next Page...

Table. B.5 – Continued

JD	R Mag	Err
2454216	15.891	0.018
2454217	15.815	0.048
2454221	15.790	0.016
2454224	15.680	0.015
2454229	16.004	0.015
2454233	16.285	0.019
2454239	16.032	0.017
2454242	15.686	0.029
2454251	15.457	0.015
2454254	15.289	0.015
2454257	14.971	0.015
2454258	14.998	0.019
2454260	14.829	0.051
2454262	14.998	0.015
2454271	15.135	0.015
2454275	15.095	0.032
2454278	15.105	0.016
2454284	14.488	0.017
2454291	14.268	0.015
2454296	14.145	0.015
2454299	13.917	0.015
2454303	13.896	0.015
2454305	14.397	0.007
2454423	15.271	0.005
2454521	16.415	0.002
2454522	16.429	0.001
2454523	16.444	0.001
2454524	16.413	0.001
2454525	16.450	0.002
2454538	16.432	0.001
2454539	16.426	0.004
2454540	16.467	0.004
2454552	16.298	0.020
2454554	16.307	0.015
2454557	16.407	0.015
2454563	16.365	0.015
2454566	16.200	0.015
2454569	16.192	0.017

Continued on Next Page...

Table. B.5 – Continued

JD	R Mag	Err
2454572	16.407	0.015
2454577	16.537	0.015
2454581	16.431	0.015

B.6 1510−089

Table. B.6: 1510−089 - Optical Data

JD	R Mag	Err
2449913	16.905	0.015
2450880	15.419	0.008
2450881	15.796	0.007
2451311	16.368	0.008
2451701	16.767	0.005
2451702	16.780	0.004
2451703	16.771	0.003
2451704	16.764	0.005
2452051	17.125	0.009
2452396	16.881	0.001
2452397	16.871	0.001
2452398	16.873	0.001
2452399	16.900	0.001
2452400	16.909	0.001
2452401	16.917	0.001
2452402	16.909	0.001
2452403	16.936	0.001
2452404	16.904	0.001
2452426	16.790	0.008
2452428	16.773	0.006
2452429	16.807	0.004

Continued on Next Page...

Table. B.6 – Continued

JD	R Mag	Err
2452430	16.784	0.005
2452435	16.785	0.004
2452440	16.781	0.005
2452442	16.736	0.005
2452455	16.669	0.006
2452460	16.646	0.004
2452517	16.227	0.006
2452520	16.553	0.002
2452753	16.931	0.001
2452754	16.954	0.001
2452755	16.950	0.001
2452756	16.945	0.001
2452843	16.672	0.006
2452845	16.730	0.005
2452853	16.584	0.014
2452859	16.741	0.015
2452863	16.653	0.016
2452866	16.642	0.016
2452869	16.627	0.016
2452872	16.662	0.016
2452875	16.646	0.016
2452878	16.681	0.016
2452882	16.688	0.010
2453120	16.758	0.012
2453123	16.728	0.013
2453126	16.729	0.013
2453130	16.777	0.014
2453133	16.485	0.012
2453136	16.517	0.012
2453139	16.686	0.014
2453144	16.700	0.012
2453148	16.729	0.012
2453152	16.675	0.012
2453154	16.644	0.011
2453158	16.643	0.014
2453161	16.692	0.013
2453164	16.678	0.012
2453168	16.646	0.013

Continued on Next Page...

Table. B.6 – Continued

JD	R Mag	Err
2453174	16.553	0.012
2453177	16.542	0.012
2453181	16.466	0.013
2453185	16.548	0.014
2453188	16.510	0.013
2453194	16.357	0.020
2453198	16.458	0.015
2453202	16.436	0.014
2453206	16.220	0.014
2453216	15.707	0.014
2453223	15.665	0.016
2453228	16.148	0.013
2453241	16.366	0.015
2453246	16.384	0.015
2453253	16.424	0.014
2453263	16.571	0.012
2453267	16.590	0.013
2453448	16.675	0.012
2453453	16.701	0.017
2453460	16.709	0.014
2453463	17.780	0.014
2453465	16.747	0.017
2453468	16.760	0.010
2453471	16.720	0.012
2453475	16.744	0.013
2453488	16.762	0.014
2453491	16.739	0.012
2453496	16.740	0.012
2453500	16.745	0.016
2453503	16.749	0.013
2453509	16.868	0.002
2453510	16.861	0.002
2453515	16.794	0.010
2453519	16.793	0.014
2453522	16.793	0.013
2453525	16.765	0.013
2453541	16.764	0.021
2453546	16.774	0.015

Continued on Next Page...

Table. B.6 – Continued

JD	R Mag	Err
2453553	16.783	0.015
2453558	16.761	0.012
2453561	16.740	0.012
2453570	16.809	0.017
2453575	16.731	0.014
2453578	16.716	0.014
2453581	16.706	0.016
2453584	16.704	0.017
2453588	16.669	0.012
2453592	16.701	0.014
2453784	16.564	0.005
2453824	16.363	0.016
2453832	16.359	0.012
2453834	16.370	0.014
2453841	16.302	0.013
2453845	16.291	0.013
2453848	16.129	0.013
2453853	16.194	0.014
2453856	16.165	0.016
2453879	16.343	0.015
2453885	16.324	0.015
2453892	16.348	0.004
2453895	16.118	0.016
2453899	16.169	0.016
2453900	16.297	0.037
2453904	16.285	0.012
2453907	16.254	0.012
2453915	16.150	0.022
2453926	16.372	0.016
2453932	16.416	0.012
2453936	16.382	0.014
2453948	16.474	0.006
2453955	16.419	0.013
2453958	16.388	0.013
2453962	16.451	0.013
2453973	16.508	0.005
2453974	16.523	0.005
2453975	16.502	0.005

Continued on Next Page...

Table. B.6 – Continued

JD	R Mag	Err
2454215	16.740	0.005
2454217	16.742	0.005
2454218	16.791	0.007
2454225	16.748	0.014
2454232	16.698	0.017
2454238	16.632	0.014
2454243	16.770	0.015
2454245	16.734	0.010
2454247	16.696	0.011
2454253	16.718	0.016
2454257	16.666	0.015
2454258	16.821	0.009
2454260	16.663	0.016
2454268	16.415	0.015
2454273	16.457	0.013
2454277	16.411	0.012
2454280	15.905	0.034
2454282	16.087	0.015
2454289	16.578	0.015
2454294	16.357	0.015
2454297	16.183	0.012
2454300	16.357	0.014
2454307	16.366	0.016
2454314	16.422	0.015
2454331	15.685	0.005
2454520	15.561	0.001
2454521	15.717	0.002
2454522	15.606	0.007
2454525	15.845	0.006
2454538	15.847	0.005
2454539	15.761	0.001
2454540	15.802	0.001
2454552	16.118	0.017
2454555	15.667	0.013
2454558	15.930	0.016
2454563	15.638	0.016
2454567	15.294	0.015
2454569	16.088	0.016

Continued on Next Page...

Table. B.6 – Continued

JD	R Mag	Err
2454573	15.826	0.010
2454576	16.003	0.015
2454579	16.401	0.018
2454582	16.404	0.005
2454583	16.161	0.001
2454584	16.435	0.001
2454585	16.333	0.001
2454586	16.123	0.001
2454588	16.294	0.012
2454592	16.187	0.014
2454594	16.132	0.019
2454597	16.211	0.017
2454600	16.256	0.015
2454605	16.342	0.018

B.7 2200+420

Table. B.7: 2200+420 - Optical Data

JD	R Mag	Err
2448517	14.684	0.059
2448648	14.904	0.023
2448744	15.225	0.038
2448782	15.265	0.047
2448867	14.539	0.043
2448868	14.502	0.042
2448869	14.504	0.044
2448926	14.709	0.043
2448927	14.702	0.050
2448928	14.623	0.049

Continued on Next Page...

Table. B.7 – Continued

JD	R Mag	Err
2448929	14.605	0.041
2449209	14.662	0.036
2449210	14.718	0.046
2449211	14.713	0.015
2449212	14.673	0.042
2449213	14.732	0.016
2449214	14.676	0.016
2449501	14.282	0.024
2449912	14.881	0.091
2449974	14.980	0.005
2449975	14.734	0.003
2449976	14.712	0.004
2449977	14.936	0.003
2449978	14.891	0.003
2449979	14.886	0.010
2450020	14.844	0.005
2450176	14.502	0.022
2450202	14.722	0.022
2450344	14.738	0.019
2450345	14.765	0.003
2450346	14.565	0.005
2450420	14.856	0.022
2450421	14.853	0.027
2450424	14.636	0.022
2450425	14.782	0.024
2450647	13.512	0.008
2450717	14.144	0.013
2450718	14.217	0.011
2450719	14.443	0.002
2450950	13.373	0.024
2450951	12.954	0.026
2451024	13.320	0.200
2451027	13.580	0.200
2451035	13.400	0.200
2451103	13.274	0.019
2451104	13.455	0.010
2451105	13.514	0.023
2451490	13.356	0.020

Continued on Next Page...

Table. B.7 – Continued

JD	R Mag	Err
2451700	14.124	0.024
2451770	13.970	0.020
2451772	14.163	0.009
2451773	14.173	0.010
2451774	14.148	0.007
2451775	13.912	0.034
2451794	14.090	0.036
2451797	13.916	0.048
2451798	13.232	0.050
2451842	13.206	0.022
2452049	13.662	0.019
2452073	12.745	0.003
2452074	12.771	0.010
2452075	12.948	0.020
2452076	12.992	0.017
2452077	13.274	0.015
2452078	13.267	0.017
2452249	14.001	0.021
2452298	13.183	0.013
2452426	13.981	0.021
2452517	13.746	0.017
2452518	13.641	0.022
2452519	13.552	0.017
2452520	13.528	0.020
2452521	13.558	0.016
2452575	12.889	0.018
2452576	13.189	0.020
2452577	13.357	0.018
2452620	12.827	0.024
2452621	12.927	0.030
2452622	13.175	0.027
2452780	13.822	0.020
2452844	13.153	0.027
2452885	13.967	0.020
2452975	13.582	0.023
2452976	13.743	0.025
2452977	13.797	0.025
2453120	13.626	0.020

Continued on Next Page...

Table. B.7 – Continued

JD	R Mag	Err
2453146	12.889	0.031
2453268	13.311	0.012
2453269	13.348	0.011
2453270	13.328	0.014
2453271	13.316	0.027
2453281	13.481	0.013
2453282	13.786	0.009
2453283	13.762	0.012
2453284	13.764	0.012
2453285	13.641	0.011
2453286	13.744	0.012
2453497	14.571	0.028
2453498	14.089	0.021
2453500	14.322	0.028
2453545	14.415	0.052
2453546	14.021	0.027
2453547	13.895	0.027
2453548	14.236	0.027
2453624	13.846	0.019
2453652	13.602	0.022
2453653	13.628	0.020
2453655	13.773	0.030
2453713	13.720	0.044
2453714	13.706	0.027
2453948	14.838	0.021
2453973	13.780	0.018
2453974	13.887	0.024
2453975	13.875	0.033
2454019	13.731	0.018
2454020	13.744	0.007
2454080	13.517	0.022
2454082	13.784	0.024
2454256	13.855	0.021
2454258	13.953	0.017
2454259	13.901	0.026
2454329	14.345	0.022
2454330	14.502	0.022
2454420	13.895	0.021

Continued on Next Page...

Table. B.7 – Continued

JD	R Mag	Err
2454421	13.980	0.021
2454422	13.872	0.028
2454423	13.830	0.019
2454424	13.756	0.033

B.8 2251+158

Table. B.8: 2251+158 - Optical Data

JD	R Mag	Err
2449210	15.923	0.010
2449975	15.936	0.006
2450421	16.060	0.008
2450424	16.137	0.005
2450425	16.130	0.006
2450586	16.569	0.054
2450717	16.055	0.012
2450718	16.108	0.011
2450950	15.468	0.010
2450951	15.375	0.017
2451050	16.027	0.005
2451051	16.006	0.002
2451052	16.010	0.003
2451053	16.009	0.003
2451054	16.021	0.002
2451104	15.922	0.003
2451105	15.979	0.011
2451490	15.892	0.005
2451700	15.962	0.005
2451770	16.173	0.002

Continued on Next Page...

Table. B.8 – Continued

JD	R Mag	Err
2451772	16.187	0.006
2451774	16.178	0.002
2451775	16.157	0.007
2451794	16.145	0.005
2451797	16.160	0.009
2451798	16.152	0.008
2451842	15.452	0.008
2452249	13.610	0.015
2452298	14.197	0.005
2452426	15.592	0.005
2452516	15.101	0.002
2452517	15.039	0.007
2452518	14.916	0.003
2452519	14.710	0.001
2452520	14.818	0.001
2452521	14.221	0.001
2452575	15.592	0.004
2452576	15.640	0.005
2452621	15.358	0.005
2452622	14.973	0.026
2452885	15.117	0.004
2452976	14.826	0.004
2453269	14.832	0.012
2453497	11.837	0.004
2453498	11.892	0.001
2453499	12.264	0.001
2453500	12.325	0.001
2453502	12.877	0.021
2453508	12.220	0.017
2453514	13.109	0.019
2453520	13.846	0.021
2453524	13.635	0.013
2453527	13.657	0.014
2453540	13.341	0.020
2453543	13.242	0.016
2453545	13.657	0.006
2453546	13.841	0.001
2453547	14.084	0.001

Continued on Next Page...

Table. B.8 – Continued

JD	R Mag	Err
2453548	14.098	0.006
2453550	14.428	0.016
2453553	14.359	0.020
2453559	14.086	0.019
2453562	13.439	0.064
2453575	14.322	0.035
2453580	14.281	0.012
2453584	14.889	0.019
2453588	14.641	0.017
2453591	14.790	0.017
2453596	14.990	0.014
2453607	14.860	0.017
2453618	15.719	0.015
2453624	15.591	0.001
2453625	15.612	0.002
2453626	15.614	0.001
2453627	15.650	0.001
2453628	15.685	0.001
2453633	15.690	0.017
2453637	15.636	0.017
2453641	15.596	0.016
2453644	15.533	0.014
2453652	15.151	0.002
2453653	15.266	0.002
2453654	15.165	0.020
2453655	15.419	0.002
2453663	15.033	0.016
2453669	14.638	0.018
2453679	14.881	0.018
2453689	15.762	0.015
2453699	15.866	0.018
2453707	15.880	0.017
2453713	15.858	0.015
2453714	15.740	0.020
2453715	15.671	0.012
2453716	15.712	0.009
2453973	15.799	0.021
2453974	15.722	0.020

Continued on Next Page...

Table. B.8 – Continued

JD	R Mag	Err
2453975	15.618	0.022
2453993	15.179	0.015
2453998	15.552	0.017
2454002	15.599	0.019
2454006	15.853	0.012
2454010	15.672	0.023
2454014	15.652	0.017
2454019	15.498	0.012
2454020	15.508	0.002
2454023	15.562	0.013
2454026	15.732	0.019
2454030	15.851	0.033
2454037	15.949	0.015
2454040	15.978	0.014
2454043	16.106	0.013
2454046	16.091	0.013
2454051	15.981	0.015
2454057	16.005	0.012
2454065	15.863	0.017
2454071	15.984	0.021
2454078	16.224	0.014
2454080	16.220	0.021
2454082	16.218	0.010
2454257	14.279	0.051
2454295	13.961	0.017
2454298	13.482	0.017
2454299	12.958	0.014
2454301	13.116	0.016
2454303	13.934	0.015
2454304	13.807	0.015
2454306	14.269	0.013
2454308	13.803	0.015
2454309	13.918	0.014
2454314	13.689	0.015
2454318	13.598	0.014
2454319	13.497	0.011
2454325	13.437	0.015
2454327	13.649	0.014

Continued on Next Page...

Table. B.8 – Continued

JD	R Mag	Err
2454329	13.691	0.001
2454330	13.543	0.001
2454331	13.250	0.001
2454332	13.068	0.001
2454334	13.280	0.085
2454335	13.287	0.011
2454337	13.211	0.013
2454339	13.724	0.016
2454340	13.914	0.015
2454341	14.273	0.014
2454342	14.349	0.013
2454343	14.655	0.017
2454345	14.705	0.014
2454346	14.651	0.012
2454347	14.922	0.013
2454349	14.985	0.013
2454351	15.142	0.013
2454353	15.120	0.014
2454355	15.098	0.014
2454357	15.146	0.019
2454359	14.963	0.012
2454364	15.164	0.010
2454366	15.350	0.015
2454369	14.467	0.025
2454371	15.167	0.016
2454372	14.988	0.008
2454374	15.169	0.012
2454375	14.671	0.014
2454376	14.461	0.011
2454377	14.570	0.011
2454379	14.690	0.016
2454380	14.471	0.015
2454381	14.241	0.014
2454382	14.129	0.013
2454383	14.568	0.013
2454384	14.618	0.014
2454386	14.929	0.015
2454387	14.992	0.014

Continued on Next Page...

Table. B.8 – Continued

JD	R Mag	Err
2454389	14.887	0.012
2454390	14.969	0.019
2454391	15.068	0.013
2454392	14.837	0.021
2454393	14.992	0.017
2454394	14.700	0.020
2454395	14.897	0.020
2454396	15.009	0.015
2454397	14.623	0.014
2454398	14.903	0.015
2454399	14.548	0.015
2454400	14.463	0.085
2454401	14.488	0.014
2454402	14.476	0.018
2454406	14.736	0.015
2454407	14.785	0.013
2454408	15.078	0.015
2454409	14.750	0.011
2454411	15.216	0.013
2454412	14.985	0.013
2454414	15.197	0.012
2454416	14.709	0.054
2454418	14.128	0.016
2454420	14.493	0.017
2454422	14.718	0.014
2454424	14.257	0.013
2454426	14.697	0.011
2454428	14.722	0.015
2454430	14.414	0.013
2454432	14.430	0.017
2454435	12.999	0.013
2454436	13.573	0.013
2454438	14.220	0.013
2454439	14.153	0.015
2454440	14.020	0.015
2454441	14.307	0.015
2454442	14.481	0.013
2454443	14.543	0.015

Continued on Next Page...

Table. B.8 – Continued

JD	**R Mag**	**Err**
2454444	14.713	0.014
2454445	14.935	0.017
2454446	14.457	0.014
2454447	14.770	0.015
2454448	14.981	0.015
2454449	15.068	0.014
2454450	15.117	0.020
2454451	14.978	0.013
2454452	14.501	0.023
2454453	15.031	0.027